Technische Universität München
TUM School of Engineering and Design

TUM

L-phenylalanine production with *Escherichia coli* reporter strains in a novel two-compartment bioreactor

Manh Dat Hoang

Vollständiger Abdruck der von der TUM School of Engineering and Design der Technischen Universität München zur Erlangung eines

Doktors der Ingenieurwissenschaften (Dr.-Ing.)

genehmigten Dissertation.

Vorsitz: Prof. Dr.-Ing. Jörg E. Drewes

Prüfende der Dissertation:

    1. Prof. Dr.-Ing. Dirk Weuster-Botz
    2. Prof. Dr. Anna-Lena Heins

Die Dissertation wurde am 12.01.2024 bei der Technischen Universität München eingereicht und durch die TUM School of Engineering and Design am 30.04.2024 angenommen.

Acknowledgements

ideas and solutions. Moreover, the support of Markus Amann and Nelson Vogel regarding technical inquiries in the laboratory and Patrick Meins for bureaucratic matters is appreciated, as well.

The fantastic support of the students I supervised in the laboratory is also acknowledged.

Contents

1. Introduction

Biotechnological production processes exploit genetically optimized microorganisms for the versatile production of bio-based compounds such as vitamins, amino acids or pharmaceuticals. They utilize cheap and renewable resources while keeping the potential amount of hazardous and non-decomposible waste streams low, which ultimately contribute to a reduced carbon footprint (Erickson *et al.* 2012, Mutanda *et al.* 2020, Usmani *et al.* 2021, Boodhoo *et al.* 2022). Due to a greater awareness of customers and consumers for a more sustainable lifestyle and environment to counter the current ecological damage and worsening of the global warming, bio-derived products become more and more popular (Teng & Wu 2019). As a result, the market size of biotechnological applications increased since 2005 and reached a market volume of 295 billion dollars in 2019 (Martin *et al.* 2021). One example is L-phenylalanine, which is an essential amino acid for the food and feed industries and part of the human diet. It is often used as a precursor molecule for the production of the low-calorie sweetener aspartame, an important ingredient for diet drinks and foods (Ager *et al.* 1998, Sprenger 2007). In 2010, the annual demand of L-phenylalanine was estimated to be more than 30 000 tons with an overall increasing trend for all essential amino acids (Li *et al.* 2010, Becker & Wittmann 2012, Rodriguez *et al.* 2014). Until now, L-phenylalanine is mainly produced in microbial fermentations using glucose as a carbon source (Liu *et al.* 2018a, Sun *et al.* 2023). Alternatively, there are also bioprocesses utilizing glycerol, a by-product of the bio-diesel production, as a carbon source (Yazdani & Gonzalez 2007, Yazdani & Gonzalez 2008, Weiner *et al.* 2014a).

To meet the growing demands of the food, feed and many other industries because of the increasing world population, novel and more efficient biotechnological production processes need to be established and continuously enhanced (Calicioglu *et al.* 2019, Molotoks *et al.* 2021). In general, the preliminary conceptualization of new bioprocesses is mainly carried out in parallelizable small-scale vessels such as shake flasks, microbioreactors or microtiter plates with working volumes in the milliliter to microliter range. Combined with a proper design of experiments, this allows a high-throughput screening of ideal process parameters in relatively simple experimental setups with low capital expenses (Kasli *et al.* 2019, Reis *et al.* 2006, Puskeiler *et al.* 2005, Kensy *et al.* 2009). After

successful proof-of-concept of a robust bioprocess setup and strategy, these bioprocesses are transfered and operated at larger scales. For example, the industrial production of pharmaceuticals are conducted with a working volume of up to 20 m^3, whereas the production of fine or bulk chemicals apply even higher volumes of up to 50 m^3 and 800 m^3, respectively (Chmiel & Weuster-Botz 2018). The benefit of using larger scales is the higher generation of product quantities per unit time.

Scale-up procedures often follow certain rules and criteria such as the geometric similarity described by the ratios of the liquid heights at maximum vessel working volume to the bioreactor diameters and bioreactor diameters to impeller diameters or the constant power input per unit volume for the design and operation of industrial bioprocesses. These guidances shall support the efficient transfer of ideal environmental conditions identified in small-scale studies to large-scale bioprocesses as the producing strains perform at their best when surrounded by optimum cultivation conditions. Ideally, the resulting key performance indicators such as the biomass yields and volumetric productivity of the upscaled bioprocesses are equivalent to those of their precursor counterparts (Chmiel & Weuster-Botz 2018).

2. Challenges and motivation

Assuring ideal and homogeneous conditions in large-scale bioprocesses inevitably demands for identical mixing times compared to the corresponding small-scale system. This parameter is defining the time necessary to provide a certain degree of homogeneity (often 95% or higher) of the fermentation broth (You *et al.* 2014). To compensate the increased volume and maintain identical mixing times, a higher volumetric power input has to be applied in large-scale bioprocesses. At some point however, the mandatory power input reaches the technical limitations and becomes impractical. As a result, the mixing times inevitably rise, leading to mixing insufficiencies, mass transfer limitations and ultimately to spatio-temporal process gradients within the bioreactor suspension (Lara *et al.* 2006). This is further exacerbated by the rigid positions for the supply of gases and liquids. For example, oxygen is often sparged from the bottom of the bioreactor, whereas pH titrating agents and feeding solutions are added from the top (Langheinrich & Nienow 1999, Kuschel & Takors 2020). Hence, the likelihood of co-existing microenvironments increases. Consequently, each of the producing cells within the bioreactor experience a random order of these microenvironments that contribute to their expression of different cellular characteristics (Haringa *et al.* 2017). Therefore, single-cell phenotypes can strongly differ in a microbial population though they derive from the same isogenic culture (Hoang *et al.* 2023a). This phenomenon, which is known as population heterogeneity, is expected to negatively influence key performance indicators of large-scale bioprocesses as these are often concomitant with lower volumetric productivities and an overall loss of yields (Bylund *et al.* 1998, Enfors *et al.* 2001). Nonetheless, differences of single-cell phenotypes in a microbial population also resemble a great chance for a better survival of some cells under uncertain environments and potentially lead to subpopulations expressing more robust and superior cellular characteristics (Tanaka *et al.* 2003, Travis & Travis 2002). Despite the awareness of population heterogeneity in bioprocesses, the mechanistic understanding in cells and the underlying biological coherences remain uncertain (Delvigne & Goffin 2014).

With the objective to better comprehend cell-to-bioreactor interactions and provide more information on the mechanistic understanding of subpopulation formation, this work investigates the impact of fluctuating conditions on the process performances and the level

of population heterogeneity of specific cellular characteristics during the L-phenylalanine production process with recombinant *Escherichia coli* FUS4 (pF81$_{kan}$). It is a fed-batch process using a chemically defined minimal medium with glycerol as a sole carbon source that can be divided into three phases: an initial batch phase, a biomass production phase with exponential feeding and a product formation phase with constant feeding. The host strain harbours two auxotrophies towards L-phenylalanine and L-tyrosine due to the genomic deletion of the *pheA*, *aroF* and *tyrA* genes encoding for essential enzymes along the aromatic amino acid biosynthesis (Sprenger 2007). At the same time, the former two genes and the *aroL* and *aroB* genes were inserted into the pF81$_{kan}$ plasmid under the control of a tac promoter to allow the inducible recombinant protein expression with subsequent L-phenylalanine formation (Weiner *et al.* 2016). Together with different feeding solutions, both growth and product formation can be decoupled. This process was originally designed and conducted in stirred-tank bioreactor cultivations with a starting volume of 15 L and proved to be a well-described, reproducible and robust process. Therefore, the general process strategy was adapted from Weiner *et al.* (2016) for the here conducted experiments.

To elucidate potential emergences of different subpopulations during the L-phenylalanine production, the host strain *Escherichia coli* FUS4 shall be transformed to a multiple reporter strain. This is a genetically modified strain, in which synthetic copies of fluorescent reporter molecules are integrated into targeted functional units of the host strains genome or plasmid. Assuming that the expression of these genes are related to distinctive cellular phenotypes, such a strain allows the *at-line* monitoring of these cellular traits by detection of the corresponding reporter molecules. This approach facilitates the unveiling of occurring subpopulations, that become visible through different expression levels of the reporter molecules in single cells. Single reporter strains have been proven to be a non-invasive tool to effectively reflect specific cellular characteristics. For example, Han *et al.* (2013) established an *E. coli* strain expressing a green fluorescent protein for monitoring of the cell growth, whereas Martinez *et al.* (2012) developed an intracellular pH imaging system in both *E. coli* and *Bacillus subtilis* (Han *et al.* 2013, Martinez *et al.* 2012). However, these single reporter strains enable the access to only one specific cellular characteristic at a time. Hence, a more efficient strategy is the integration of multiple synthetic copies of reporter molecules to simultaneously gain insights and information of multiple cellular phenotypes, which can be further correlated to each other (Heins *et al.* 2020, Hoang *et al.* 2023a, Hoang *et al.* 2023b). In this work, a quadruple reporter strain shall be established to display the four cellular characteristics general stress response, growth behaviour, oxygen limitation and product formation of single cells in the microbial popu-

lation. While the former three enable the reflection of the elementary physiological state of single cells, the latter shall reveal the L-phenylalanine forming capacity of each cell. Suitable reporter molecules are selected based on relatively low maturation times, high brightnesses, an monomeric state with the least optical cross-sections between each other and optical compatibility with the measuring device. While three of them shall be integrated genomically into the *E. coli* FUS4 strain targeting the *rpoS* gene, the *rrnB* operon and the *narGHIJ* operon to display the general stress response, growth behaviour and oxygen limitation of single cells (Heins *et al.* 2020), the fourth reporter molecule will be integrated into the pF81$_{kan}$ plasmid to monitor the inducible recombinant protein expression. Because the expression of the encoded genes *aroF*, *aroB*, *pheA* and *aroL* on this plasmid are mandatory for the L-phenylalanine production, the fourth reporter molecule can be seen as the marker for product formation. The functionality of the established *E. coli* reporter strains will be investigated in simple batch cultivations in either shake flasks or in a stirred-tank bioreactor at laboratory scale.

Typically, studies on population heterogeneities in bioprocesses are often investigated in scale-down bioreactors. These are capable of simulating dynamic environmental conditions, which occur in large-scale bioprocesses, at laboratory scale (Neubauer & Junne 2016, Heins & Weuster-Botz 2018). One of the most popular approach is a two-compartment bioreactor using a stirred-tank bioreactor providing well-mixed and controlled bioprocess conditions paired with a continuous tubular reactor as a bypass, in which different gradients can be simulated (Limberg *et al.* 2016, Ziegler *et al.* 2021). To establish a similar two-compartment bioreactor in this work, the L-phenylalanine production process described by Weiner *et al.* (2016) needs to be transferred from stirred-tank bioreactor cultivations with a starting volume of 15 L to a tenfold lower initial volume of approximately 1.0 L to 1.5 L. In a first set of L-phenylalanine production processes using the *E. coli* FUS4 (pF81$_{kan}$) as well as the here established *E. coli* reporter strains, the resulting process performances elaborate on the potential impact of genetic modifications and the additional expression of reporter molecules during the bioprocesses. Furthermore, the expressed fluorescence intensities of the microbial population will be correlated to the related process state variables to verify their functionality. The further transformation of the here used stirred-tank bioreactor to a two-compartment bioreactor demands for a continuous tubular reactor providing mean hydraulic residence times between 10 s to 250 s in the bypass, which corresponds to the expected mixing times in industrial bioprocesses (Vrábel *et al.* 2000). As a prerequisite to simulate process gradients along the continuous tubular reactor, the prevailing flow regimes in the bypass have to provide good radial mixing while keeping the axial dispersion poor. Instead of using a straight tubular

reactor, a helical tube reactor with repetitive integration of 90° bends (known as a coiled flow inverter) will be designed and constructed as a promising alternative to meet all the requirements (Klutz *et al.* 2015). The operating range of the coiled flow inverter will be approximated by preliminary step input experiments to determine the mean hydraulic residence times and the mixing characteristics at different volumetric flow rates. After finding optimal operating conditions to provide good radial mixing and poor axial dispersion as well as the demanded mean hydraulic residence times between 10 s to 250 s, the coiled flow inverter can be integrated to the stirred-tank bioreactor for the experimental simulation of dynamic environments.

Finally, the *E. coli* quadruple reporter strain will be cultivated in the novel two-compartment bioreactor. In this instance, the stirred-tank bioreactor resembles a well-mixed environment with controlled process parameters, whereas there will be no temperature and pH control in the coiled flow inverter with no aeration or supply of feeding solution. Thus, it represents a limitation zone with dynamic environmental conditions. Consequently, a further major objective of this study is to investigate the impact of fluctuating conditions with different mean hydraulic residence times in the coiled flow inverter on key process performance indicators during the L-phenylalanine production process. Besides the consideration of the general courses and maximum achieved biomass and product concentrations, the biomass specific product formation rates will be included for the evaluation, as well. Moreover, single-cell fluorescence intensities will be analyzed and compared to reveal potential differences regarding the general stress response, growth behaviour, oxygen limitation and product formation of single cells within and between the conducted bioprocesses. Histograms and density plots will be utilized for visualization of potential subpopulations. While the former show the distributions of measured signals of single cells, the latter allow a correlative representation of expressed fluorescence levels and support the deciphering of potential coherences between certain cellular characteristics (Herzenberg *et al.* 2006). Both the general process performances and the level of population heterogeneity in two-compartment bioreactor cultivations will be compared to the outcome of L-phenylalanine production with the *E. coli* quadruple reporter strain in an ideal stirred-tank bioreactor with expectably well-mixed and controlled process parameters.

To achieve the above mentioned objectives of this work, the design and establishment of an *E. coli* quadruple reporter strain is mandatory as a tool to reflect the general stress response, growth behaviour, oxygen limitation and product formation of cells during L-phenylalanine production processes. In combination with a novel two-compartment

bioreactor consisting of a stirred-tank bioreactor with a coiled flow inverter as a bypass, dynamic environments can be simulated with various exposure times. With the main focus to elaborate the impact of fluctuating environmental conditions on the cell growth and productivity as well as the level of population heterogeneity regarding the above mentioned characteristics, these findings potentially contribute to a better understanding of industrial-scale bioprocesses and facilitate future scale-up procedures in general. To do so, the following work packages are targeted:

a) Design and establishment of an *E. coli* quadruple reporter strain

    1. Screening and selection of suitable fluorescent reporter molecules

    2. Preliminary characterization of the selected fluorescent reporter molecules

    3. Design and genetic engineering of an *E. coli* triple reporter strain with subsequent analysis of the functionality

    4. Enhancement the *E. coli* triple reporter to a quadruple reporter strain with subsequent analysis of the functionality

b) Process transfer of the L-phenylalanine production process to a two-compartment bioreactor setup

    1. Experimental validation of the reference process (Weiner *et al.* 2016) in a stirred-tank bioreactor with approximately tenfold lower starting volume

    2. L-phenylalanine production with *E. coli* reporter strains in the stirred-tank bioreactor at laboratory scale to approximate potential metabolic burdens due to additional expression of reporter molecules

    3. Design and establishment of a coiled flow inverter with subsequent characterization of mean hydraulic residence times and fluid dynamics at different volumetric flow rates

c) Investigation of the impact of fluctuating environmental conditions on the process performances during L-phenylalanine production processes and the level of population heterogeneity using the *E. coli* quadruple reporter strain

    1. L-phenylalanine production in a stirred-tank bioreactor with well-mixed and homogeneous bioprocess conditions

    2. L-phenylalanine production in a two-compartment bioreactor at different mean hydraulic residence times in the bypass to simulate fluctuating environmental conditions

3. Theoretical background

3.1. Microbial strains in biotechnological production processes

Prokaryotic microorganisms are among the smallest forms of life with particle sizes in the micrometer range (Shehata & Marr 1975, Nakai 2020). Although they are not visible to the naked human eye, microorganisms constitute a major cornerstone in nature and life as they can be encountered all over the biospher catalyzing various reactions, for example in the bioremediation or the human gut (Li *et al.* 2011, Abatenh *et al.* 2017). Additionally, they have a great reputation for the production of various bio-based goods using natural resources as a starting material. Especially the targeted exploitation of bacteria, a subgroup of microorganisms, already began in the fourth millenium before christ for the production of consumable foods such as alcohol, bread or yoghurt (Soomro *et al.* 2002, Hammes *et al.* 2005). Nowadays, bacteria are often optimized by modification of their genetic information to give them artificial biological features (Plavec & Berlec 2020, Hoang *et al.* 2023a). To fully exploit their capabilities and potential, bacteria still demand for environments with specific conditions.

3.1.1. Media components and process conditions

Nutrients are fundamental for any living organisms to maintain metabolism and enable growth. Bacterial cells are generally able to produce a variety of biomolecules themselves. But those that cannot be synthesized are called essential nutrients and must be taken up from the surrounding culture media. In general, a solution enriched with nutrients can be categorized into complex and chemically defined medium. The former is characterized by the utilization of complex nutrients such as peptone or yeast extract, in which the exact chemical composition is uncertain and differs based on the used raw materials and their formulation procedure. As these sources often derive from waste streams, complex media is considered to be cheap. Simultaneously, these media allow short-term rapid growth of bacteria because of the presence of all mandatory nutrients in abundance (Lapierre *et al.* 2020, Allikian *et al.* 2019). However, the variation of nutrient composi-

tions can affect cellular growth, product yields as well as product quality, thus hindering reproducible results (Diederichs *et al.* 2014, Lapierre *et al.* 2020).

In contrast, chemically defined media consist of pure chemical substances in precisely known proportions. Consequently, the nutrient composition can be prepared matching with the exact demands of the used bacteria to enhance the productivity and ensure process reproducibility (Pfeifer *et al.* 1996, Zhang *et al.* 1998a). Moreover, fermentation processes with chemically defined media facilitate process validation as they comply with the requirements of the good manufacturing practice (GMP), but with the drawback of higher costs compared to complex media (Zhang & Greasham 1999). Corresponding requirements on the culture medium vary for bacteria based on their elemental compositions. For example, carbon and oxygen occupy the largest proportion of the cell dry weight in *Escherichia coli* with approximately 45% and 30%, respectively. Furthermore, these bacteria harbour a considerable amount of nitrogen, hydrogen and phosphate (Enfors 2011, see Table 3.1). Besides major elements, trace elements including minerals are also required, but at comparably low concentrations (Allikian *et al.* 2019).

Table 3.1: Elemental composition of *Escherichia coli* with common sources containing these elements (Enfors 2011, Allikian *et al.* 2019).

Element	Proportion of cell dry weight, %	Common sources
Carbon	45	Sugars
Oxygen	30	Air
Nitrogen	12	Ammonia-containing salts
Hydrogen	7	Ammonia-containing salts
Phosphor	3	Mineral salts
Sulfur	1	Mineral salts
Potassium	1	Mineral salts
Magnesium	0.5	Mineral salts

With plenty of sources for carbon and nitrogen, mineral salts, amino acids and many other components, media development and the ideal composition of nutrients can be challenging and time-consuming, but also harbours the potential of process improvements (Weuster-Botz 2000). Allikian *et al.* (2019) elucidated the roles of the most important nutrients, which will be summarized in the following:

Carbon sources: The presence of carbon sources in culture media is decisive for the microbial growth and product formation of cells, as this element is metabolized for the

biosynthesis of complex biomolecules and energy generation. Though photoautotrophic and photoheterotrophic organisms both utilize light as the primary energy source, they still demand for carbon sources. While the former solely employs carbon dioxide, the latter uses organic compounds as a main carbon source. In contrary, chemoautotrophic and chemoheterotrophic organisms directly utilize carbon dioxide or organic compounds for the chemical energy synthesis (Kampen 2014). The most common carbon source used in microbial fermentations is the sugar glucose, which is also preferred by most chemoheterotrophic bacteria. Nonetheless, alternative sources such as glycerol, a by-product of the bio-diesel production, become more attention in the recent years due to their abundance and lower prices (Yazdani & Gonzalez 2007, Yazdani & Gonzalez 2008).

Nitrogen sources: The constant supply of nitrogen is mandatory as this element serves as a key component for anabolic reactions building, amongst others, nucleic acids, amino acids and proteins. In biotechnological applications, ammonia is mainly offered as a nitrogen source, either in ammonia-containing salts or directly as a titrating agent. Although some cells can tolerate nitrogen limited environments for some time, a rapid supply of abundant amounts of ammonia can be problematic as it leads to a so-called ammonia shock. As a result, cells try to counter the rapid internal alkalinization by a strongly reduced ammonium uptake into the cell (Javelle *et al.* 2004, van Heeswijk *et al.* 2013).

Mineral salts: Minerals can be divided into macro-minerals including chemical elements such as phosphor, sulfur and potassium, whereas micro-minerals comprise substances like manganese, zinc and copper. Both comply versatile roles within the cells, mostly for stabilization and maintenance of protein structures and as cofactors for enzymes. In comparison to carbon and nitrogen sources, the necessary amount of minerals in cultivation media is considerably lower. Nevertheless, certain minerals have a decisive role in cellular growth and metabolism and thus remain essential.

Amino acids: These biomolecules consist of the chemical elements carbon, nitrogen, oxygen and hydrogen. Amino acids are characterized by an α-carbon atom paired with a carboxyl group and an amino group, but with varying side-chains. Differences in the side-chains lead to various physicochemical properties regarding the net charge and chemical reactivity. Based on their side-chain, the existing 20 amino acids can be categorized into aliphatic, aromatic or polar groups. They are the basic building unit of all proteins, which occupy the most proportion in cellular mass and are universally involved in a majority of biological reactions within the cells. Therefore, the supply and availability of all essential amino acids is paramount for all cells (Damodaran 1996).

Besides the nutritional requirements for the culture media, bacterial fitness and their physiological state are also determined by the prevailing process conditions. Especially the temperature plays a major role for the microbial growth. Bacteria have different preferences regarding their ideal growth temperature. While psychrophiles demand for rather cool environments between -5 °C to 15 °C, mesophilic bacteria grow best at moderate temperatures of 10 °C to 45 °C. Only cells belonging to the thermophilic and hyperthermophilic groups can grow at even higher temperatures. Environments with small deviations from the optimum temperature slow down microbial growth, whereas larger deviations lead to cellular inactivity or even induce cell death (Behera *et al.* 2019). Additionally, this parameter also contributes to the intracellular reaction rates (Xiong *et al.* 2015). Oxygen is a further crucial parameter deciding the survival of a microbial population. The presence of this chemical element can be a strict prerequisite for some cells, but also strongly toxic to others. For example, aerobic bacteria need high oxygen levels for survival and growth, while microaerophiles prefer lower oxygen levels. There is also a group of bacteria known as facultative anaerobic, which utilize oxygen if present. Nevertheless, they also survive and grow under anoxic conditions. Pure toleration of environments enriched with oxygen without the capability of converting it is typical for aerotolerant anaerobes, whereas strict anaerobic cells are damaged by the presence of this chemical element (Karakashev *et al.* 2003, Grishchenkov *et al.* 2000, Archer *et al.* 1988). A third important parameter is the pH value, which is an indicator for acidity (pH < 7) or alkalinity (pH > 7) of a liquid solution. This parameter is strongly dependent on the chemical composition as well as the temperature of the environment. Bacteria are capable of sensing the surrounding pH value and respond by adjusting intracellular reactions and their physiological state. While neutrophilic bacteria prefer a pH value of 5 to 8, acidophiles and alkaliphiles grow best at very acidic (pH < 5.5) or alkaline (pH > 8.5) conditions. In any case, large deviations from the optimum pH value have detrimental effects on cellular growth and other basic biological functions (Olson 1993, Behera *et al.* 2019).

3.1.2. Microbial growth phases

Assuming the inoculation of bacteria into a new environment with an ideal nutritional composition and optimum process parameters, cells initially show low metabolic activity and no macroscopic conversion of substrates or other media components. This phase is known as the lag phase, in which cells show marginal growth but rather adapt to the new environmental conditions (Madar *et al.* 2013). After a certain period of time, cells become fully acclimatized and begin the uptake and conversion of substrates and other nutritions. As a consequence, the cellular metabolism is activated and cell growth is initiated (Riedel *et al.* 2013, Beg *et al.* 2007). This is rather slow during the acceleration

phase, but rises rapidly during the exponential growth phase, which is concomitant with the maximum specific growth rates μ_{max} (Long *et al.* 2017). In bacteria, biomass is formed by asexual reproduction, in which a single cell divides into two daughter cells (Osella *et al.* 2014). As a preparation for this event, fast growing cells show high expression levels of the *rrnB* operon. This genetic element encodes for a ribosomal ribonucleic acid (RNA), an important precursor for the assembly of ribosomes to enable protein expression (Murray *et al.* 2003, Hernandez & Bremer 1990). A rapid increase of biomass comes along with a fast depletion of highly abundant substrates as well as the formation of potential toxic by-products. Both and other factors can induce the transition to the deceleration phase, in which further cell growth is slowed down. With the complete consumption of substrates and potentially inhibitory concentrations of certain by-products in the environment, the proportion of growing cells and dying cells reach an equilibrium. Therefore, the cell number of a microbial population reaches a threshold in the stationary phase (Luli & Strohl 1990). The shift from exponential to stationary phases is especially accompanied with elevated general stress response levels of the cells indicated by high expression levels of the *rpoS* gene. It encodes for the sigma factor RpoS, which is mainly expressed with the onset of substrate scarcity and induces the expression of up to 500 different genes to cope with substrate-limiting conditions. Consequently, cells become more resistant towards the stressful conditions they encounter (Battesti *et al.* 2011, Saint-Ruf *et al.* 2007, Weber *et al.* 2005). In worst case however, the environmental conditions become harmful so that cell death is inevitable (Figure 3.1).
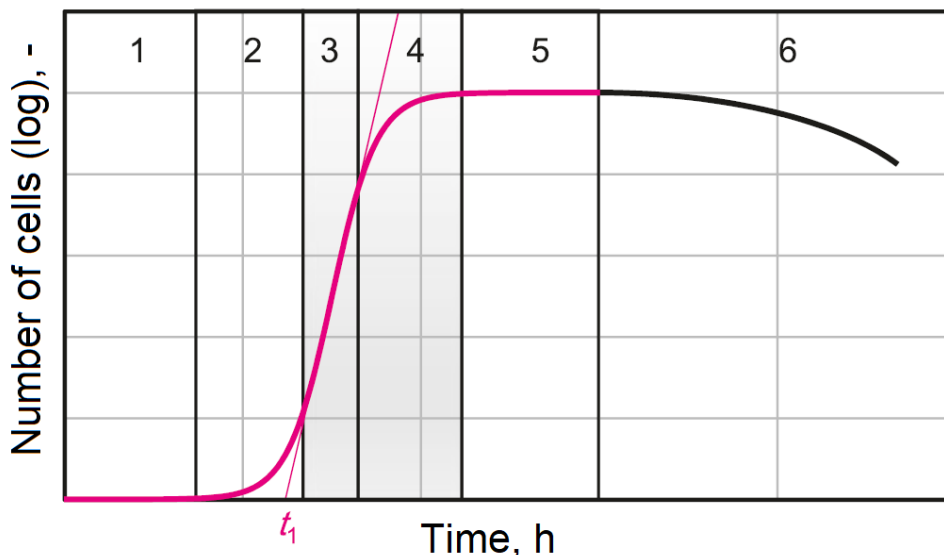
Figure 3.1: Typical growth phases microbial populations undergo after inoculation into a new environment. The time stamp t_1 marks the process time, in which the cell population reaches the maximum specific growth rate. 1 - Lag phase, 2 - Acceleration phase, 3 - Exponential phase, 4 - Deceleration phase, 5 - Stationary phase, 6 - Death phase (adapted from Weuster-Botz & Takors 2018).

The specific growth rate μ of a microbial population is described in relation to biomass changes with the following definition:

$$\mu \equiv \frac{dc_X}{dt} \cdot \frac{1}{c_X} \tag{3.1}$$

μ	Specific growth rate	h^{-1}
c_X	Biomass concentration	$g\ L^{-1}$
t	Time	h

The integration of this equation with the assumption of exponential growth at the maximum growth rate leads to the following result:

$$c_X(t) = c_{X,0} \cdot e^{\mu_{max} \cdot (t-t_0)} \tag{3.2}$$

$c_{X,0}$	Initial biomass concentration	$g\ L^{-1}$
μ_{max}	Maximum growth rate	h^{-1}
t_0	Starting time	h

Growth rates of a microbial population are strongly connected to the availability of substrates. As reported by Monod (1949), the correlation of both parameters follows a saturation curve. This means that growth rates rise with higher substrate abundance. However, this relation recedes at higher substrate concentrations. At some point, the specific growth rates remain constant regardless of the substrate amount in the cultivation medium. This can be described by the following equation with the saturation constant K_S representing the substrate concentration, in which the specific growth rate equals half of its maximum value (Monod 1949)

$$\mu = \mu_{max} \cdot \frac{c_S}{c_S + K_S} \tag{3.3}$$

c_S	Substrate concentration	$g\ L^{-1}$
K_S	Saturation constant	$g\ L^{-1}$

Besides the uptake of substrates for cellular growth, it is also needed for cellular maintenance and the potential product formation. Consequently, the substrate uptake rate q_S is the sum of uptake rates for the biomass production $q_{S,\mu}$, maintenance $q_{S,m}$ and product formation $q_{S,p}$.

$$q_S = \frac{1}{c_X} \cdot \frac{dc_S}{dt} \tag{3.4}$$

$$q_S = q_{S,\mu} + q_{S,m} + q_{S,p} \tag{3.5}$$

q_S	Substrate uptake rate	$g\ g_{CDW}^{-1}\ h^{-1}$
$q_{S,\mu}$	Substrate uptake rate for growth	$g\ g_{CDW}^{-1}\ h^{-1}$
$q_{S,m}$	Substrate uptake rate for maintenance	$g\ g_{CDW}^{-1}\ h^{-1}$
$q_{S,p}$	Substrate uptake rate for product formation	$g\ g_{CDW}^{-1}\ h^{-1}$

The corresponding biomass and product yields can be calculated as the ratio of changes in biomass dc_X to metabolized substrates dc_S and changes of product amount dc_P to metabolized substrates dc_S

$$Y_{X/S} = \frac{dc_X}{dc_S} \tag{3.6}$$

$$Y_{P/S} = \frac{dc_P}{dc_S} \tag{3.7}$$

$Y_{X/S}$	Biomass yield	$g\ g^{-1}$
$Y_{P/S}$	Product yield	$g\ g^{-1}$

Additionally, the biomass specific product formation rate q_P is a further variable to describe the product generation in bioprocesses

$$q_P = \frac{dc_P}{dt} \cdot \frac{1}{c_X} \tag{3.8}$$

q_P	Biomass specific product formation rate	$g\ g_{CDW}^{-1}\ h^{-1}$

All equations are derived from Weuster-Botz & Takors (2018).

3.1.3. Genetic modification of microorganisms

Deoxyribonucleic acids (DNA) are the universal carrier of genetic information in all living organisms. It constitutes a sequence of bases of the four nucleotides cytosine, guanine, adenine and thymine connected by phosphodiester bonds, which are arranged in a double-stranded helix formation with complementary strands (Watson & Crick 1953, Zhang *et al.* 2019). Since the entire genetic information of organisms are contained in the cellular genome, it reaches an extraordinary size, even in comparably simple microorganisms such as bacteria. For example, the basic genome of an *Escherichia coli* strain has a size of around $4 \cdot 10^6$ basepairs (Dixit *et al.* 2015). Despite this length, the progress in high-throughput sequencing enabled whole-genome sequencing, which opened the ac-

cess to various prokaryotic genomes in a short time. Detailed insights into these genetic sequences initiated the deciphering of genotype-phenotype associations as a prerequisite to understand and predict the expression of specific cellular characteristics. Unveiling of what is naturally present and the identification of limitations and drawbacks led to the demand for optimization strategies, which is often realized by genetic modifications (Buron-Moles *et al.* 2019).

Genetic engineering relies on the alteration of the base sequence either by insertion, mutation or deletion of single, multiple nucleotides or even entire genetic elements. The purpose is to modify the genotype of a host strain to dictate the properties of the related proteins. This will affect the corresponding cellular reactions and characteristics according to the demands of a given experimental setup (Khan 2019). One way to alter the chromosomal DNA is the introduction of mutations at random positions induced by ultraviolet light (Shibai *et al.* 2017). Conversely, directed approaches for the targeted modifications are more complex as profound knowledge of the host strains' genome is mandatory to precisely plan and conduct the modification procedures and avoid unwanted biological consequences. Additionally, these modifications have to be executed *in vivo*. One traditional technique is the λ Red mediated Flp/FRT recombineering, which utilizes homologous recombination reactions paired with the subsequent modification executed by the flippase recombinase (Flp). In detail, a double-stranded DNA (dsDNA) sequence is prepared with homologous regions at both ends to the genetic element of interest to be exchanged in the host genome. Furthermore, this DNA sample harbours the genes to be inserted together with a selection marker encoding for a specific resistance gene, which are flanked by the flippase recognition target (FRT) sites 5'-GAAGTTCCTATTC-3'. In case of a targeted deletion, the FRT sites only flank the selection marker. After insertion of this DNA sequence into the cell, the λ Red system provides the three proteins γ, β and an exonuclease (exo). While γ prevents the complete degradation of the inserted dsDNA, exo degrades a single strand of the dsDNA from 5' to 3' manner leaving a single-stranded DNA (ssDNA). This ssDNA gets exchanged with the native homologous genomic target site by recombination facilitated by β. Cells with successful genome modification can be identified by their gained resistance. A subsequent removal of this resistance is possible by the flippase recombinase, which recognizes the FRT sites and cut out the resistance marker together with one of the FRT sites. Consequently, a single FRT scar remains in the genome of the host strain (Mosberg *et al.* 2010, Schweizer 2003, Datsenko & Wanner 2000, Murphy 1998). Nowadays, more advanced systems are available such as the CRISPR/Cas9-mediated genome editing, in which no genetic scars remain in the host genome (Perkel 2013, Zhao *et al.* 2016).

Besides of the chromosomal DNA in bacteria, they optionally harbour a plasmid vector. Basically, this is a circular dsDNA with three general features including the origin of replication, the selection marker and a multiple cloning site (MCS). Especially the latter is of major interest for genetic engineering as plenty of unique restriction sites accumulate at that region. Thus, the MCS is the preferred spot for cutting with various restriction enzymes. Recombinant DNA with compatible overhanging ends can then be inserted and joined by different molecular techniques such as ligation or Gibson assembly. Consequently, the host strain receives certain biological features as long as the cells maintain this vector. The pronounciation of these biological features rely on the expression levels of this recombinant DNA, that is dictated by the genetic design including the selection of promoter and terminator as well as the sequence of the ribosome binding site (RBS). In comparison to chromsomal editing, modifications of plasmids can be conducted *in vitro* with subsequent transformation into bacteria (Idalia & Bernardo 2017, Hoheisel 1989, Santos-Moreno & Schaerli 2019).

Regardless of genome editing or the use of altered plasmids, genetic engineering is a revolutionary approach, which has been extensively exploited and developed since the 1970s as a versatile and powerful tool in different applications (Khan 2019). Until now, numerous successful examples have been reported, in which certain biological functions and features were added, improved or even removed in cells (Priebe *et al.* 2021, Gomez de Santos *et al.* 2021). In biotechnological production processes, this technique is mostly used for the controlled overexpression of native or recombinant genes in an appropriate host strain to elevate the overall productivity. For example, Bokinsky *et al.* (2011) engineered an *E. coli* strain, which was capable of converting lignocellulosic biomass by recombinant expression of cellulases, xylanases, β-xylanases and xylobiosidases for the production of biofuel precursors (Bokinsky *et al.* 2011). Further process relevant modifications include the integration of tags on specific proteins of interest to mark them or simplify later purification steps with His tags being the most extensively used ones (Ederth *et al.* 2009). Moreover, the recombinant expression of biosensors becomes a standard approach for visualization and monitoring of certain events during bioprocesses (Heins *et al.* 2020, Hoang *et al.* 2023a, Hoang *et al.* 2023b). Despite the seemingly unlimited opportunities, genetic modifcations also come with potential drawbacks and risks. Direct alterations of the host strains' genome potentially jeopardize the integrity of native genes and the cells in general. Particularly the unwanted introduction of a frameshift should be avoided as this can lead to the deactivation of certain genes (Cupples *et al.* 1990, Oppenheim *et al.* 2004). Moreover, the additional recombinant expression of certain proteins as well as the spent resources for their biocatalytic activities potentially represent a metabolic burden for the

host strains, which can affect other metabolic pathways (Ow *et al.* 2006, Liu *et al.* 2018b, Lozano Terol *et al.* 2021). This can be exemplified with bacteria containing plasmids, which permanently have to tolerate the presence of antibiotics to maintain plasmid stability. As a consequence, plasmid-free cells often exhibit higher growth rates than the same cells with plasmids (Sieben *et al.* 2016).

3.1.4. *Escherichia coli* as model organism for biotechnological applications

E. coli is a gram-negative and rod-shaped bacillus with a length of around 1 µm and a diameter of approximately 0.35 µm. It belongs to the group of *Enterobacteriaceae* and is naturally habitating the gastrointestinal tract in warm-blooded animals. Although there are pathogenic variants of this strain causing diseases in animals and humans, *E. coli* variants used in biotechnological production processes such as the K-12 strain are harmless laboratory workhorses. Due to its classification into the biosafety level 1, this strain has low chances to cause any diseases in healthy adult humans (IGEM 2014). It is a mesophilic bacterium exhibiting optimum growth at 37 °C under aerobic conditions. Nevertheless, *E. coli* tolerates and grow under anoxic conditions as this strain belongs to the group of facultative anaerobic bacteria. In terms of the pH of the environment, neutral values of around 7.0 are optimal for biotechnological production processes (Croxen & Finlay 2010, Croxen *et al.* 2013, Zilberstein *et al.* 1984, Idalia & Bernardo 2017). As a member of the chemoheterotrophic bacteria, *E. coli* is reliant to take up and convert organic carbon sources for the chemical energy synthesis (van Elsas *et al.* 2011).

E. coli is among the most important model organisms in molecular biology based on the extensive knowledge of its genome, which was fully sequenced in 1997 (Blattner *et al.* 1997). Since then, plenty of studies progressively deciphered the genotype-phenotype associations making this strain among the best described microorganisms (Wei *et al.* 2001, Bochner 2003, Munavar *et al.* 2005). This fundamental basis initiated the establishment of versatile cloning tools and expression systems around this strain with a proven track record for recombinant expression of a vast pool of biomolecules (Priebe *et al.* 2021, Bokinsky *et al.* 2011, Hoang *et al.* 2023a). Apart from the extensive knowledge from a genetical point of view, *E. coli* has low demands on culture media with high flexibility to grow in either complex or chemically defined nutrient solutions. Despite the low-cost media, this strain reportedly exhibit rapid growth at easy-to-provide process conditions in both small-scale and large-scale bioprocesses paired with high-yield production. Therefore, this bacterium can rightly be called as one of the most important model organisms for biotechnological applications (Idalia & Bernardo 2017, Huang *et al.* 2012).

3.1.4.1. Metabolism of *Escherichia coli*

The central metabolic pathways in *E. coli* always begin with the uptake of an organic carbon compound, which then gets converted to biological energy in a chain of enzymatic reactions. Additionally, metabolic precursors are formed during these reactions that serve as fundamental building blocks to create more complex biomolecules. Among the central metabolic pathways in *E. coli* are the glycolysis, the gluconeogenesis, the tricarboxylic acid cycle, the glyoxylate cycle and the pentose phosphate pathway (Romano & Conway 1996, Kornberg 1966). All the mentioned pathways will be briefly presented in the following:

Glycolysis and gluconeogenesis: The glycolysis is also known as the Embden-Meyerhof-Parnas (EMP) pathway, in which a single glucose molecule is converted into two molecules of pyruvate (PYR) in a 10-step reaction in the cytosol of the bacteria. Along this pathway is the production of energy by formation of two adenosine triphosphate (ATP) molecules. Prior to conversion to the final PYR, the important intermediates glucose 6-phosphate (G6P), fructose 6-phosphate (F6P), glyceraldehyde 3-phosphate (G3P) and phosphoenolpyruvate (PEP) are produced, which branch into multiple metabolic pathways. The reverse process of the glycolysis is called gluconeogenesis, in which PYR gets converted back to glucose following the same 10-step reactions, but in reverse direction (Chandel 2021).

Glycerol pathway: Alternatively to the uptake of glucose as an organic carbon source, *E. coli* is capable of utilizing glycerol. After uptake via passive diffusion, this carbon source is initally converted to glycerol 3-phosphate (GLY3P) by an ATP-dependent glycerol kinase. Afterwards, two glycerol 3-phosphate dehydrogenases catalyze the reaction of GLY3P to dihydroxyacetone phosphate (DHAP), which enters the glyolytic or gluconeogenetic pathways under aerobic conditions. In case of anaerobic conditions, glycerol is transformed to dihydroxyacetone (DHA) that further reacts to either DHAP or PYR. Both reactions are catalyzed by the type II glycerol dehydrogenase and a phosphoenolpyruvate-dependent DHA kinase (Durnin *et al.* 2009, Heller *et al.* 1980, Gottlieb *et al.* 2014).

Tricarboxylic acid cycle and glyoxylate cycle: Pyruvate is among the key metabolites during the central carbon metabolism in *E. coli*. Under aerobic conditions, PYR derives from the glycolysis or the glycerol pathway and is oxidized to acetyl-Coenzym A (AcCoA) by a pyruvate dehydrogenase. This AcCoA molecule then enters a series of further reactions in a closed loop, in which it is stepwise converted to citrate, isocitrate, 2-ketoglutarate, succinyl-Coenzym A (SuCCoA), succinate, fumarate, malate and

ultimately to oxalacetate. The produced oxalacetate then reacts with another AcCoA molecule to start the tricarboxylic acid cycle (TCA), again. The metabolic intermediates produced along this pathway are necessary for the biosynthesis of several amino acids and other complex biomolecules. Furthermore, the full oxidation of a single molecule of Ac-CoA in the TCA, in which two molecules of carbon dioxide emerge, is an energy-producing step leading to one molecule ATP, three molecules of nicotinamide adenine dinucleotide (NADH) and one molecule of flavin adenine dinucleotide ($FADH_2$). Especially the two latter products are of major importance for the energy generation in the cells as they are further utilized during the oxidative phosphorylation of the respiratory chain under the consumption of oxygen. Alternatively to the TCA, cells can follow the glyoxylate bypass, in which isocitrate is immediately converted to succinate with glyoxylate as a by-product. This by-product is then metabolized to malate under the presence of a malate synthase (Brown *et al.* 1994, Cronan & Laporte 2005, Martínez-Reyes & Chandel 2020).

Pentose phosphate pathway: The pentose phosphate pathway (PPP) can be separated into the oxidative branch and the non-oxidative branch. Under aerobic conditions, G6P of the glycolysis gets oxidized to 6-phosphate gluconate (6PG) under the presence of a glucose 6-phosphate dehydrogenase and a phosphogluconolactonase. In a second oxidation reaction, 6PG is converted to ribulose 5-phosphate (Ru5P) by the 6-phosphogluconate dehydrogenase. During these reactions, important equivalents of nicotinamide adenine dinucleotide phosphate (NADPH) are formed together with carbon dioxide. In contrary, the non-oxidative branch is characterized by the degradation of pentose phosphates. First, Ru5P is converted to either ribose 5-phosphate (R5P) by the ribose 5-phosphate isomerase or to xylulose 5-phosphate (X5P) by the ribulose 5-phosphate epimerase. Transketolases then mediate the formation of sedoheptulose 7-phosphate (S7P), which are further converted to erythrose 4-phosphate (E4P) by transaldolases. Alternatively, R5P will be metabolized to G3P, that re-enters the glycolysis or gluconeogenesis, respectively. Furthermore, transketolases also catalyze the interconversion of X5P to E4P or F6P. All metabolic intermediates produced in the PPP are paramount for the anabolism of amino acids, vitamins or nucleotides. For example, E4P is a fundamental building block for the aromatic amino acid biosynthesis (Sprenger 1995, Stincone *et al.* 2015, Sharkey 2021).

Mixed-acid fermentation: When cells are exposed to anaerobic conditions, PYR is not converted to AcCoA. Instead, other metabolic pathways are activated for the energy production. This includes the conversion of PYR to formate mediated by the pyruvate formate lyase, lactate by the lactate dehydrogenase, ethanol by the alcohol dehydrogenase and acetate by the phosphate acetyltransferase and acetate kinase. Lactate and ethanol production are accompanied by NADH consumption, whereas ATP is formed during ace-

tate production. Additionally, PEP is converted to succinate in a series of reactions, in which NADH is consumed. In comparison to the respiratory chain, energy yields in mixed-acid fermentations are at least ten times lower compared to the oxidative phosphorylation (Ciani *et al.* 2008, Förster & Gescher 2014, Kargeti & Venkatesh 2017).

Aromatic amino acid biosynthesis: *E. coli* is capable of producing the amino acids L-tyrosine, L-phenylalanine and L-tryptophane during the aromatic amino acid biosynthesis (AAA). Mandatory precursors to initiate this metabolic pathway are the molecules E4P and PEP originating from the PPP or glycolysis. In a first reaction, E4P and PEP are converted to 3-deoxy-D-arabino-heptulosonate 7-phosphate (DAHP) under the presence of three isoenzymes of the DAHP synthase encoded by the *aroF*, *aroG* and *aroH* genes. All three enzymes are sensitive to one of the aromatic amino acids with feedback regulation of their expression. While AroF is tyrosine-sensitive, AroG and AroH are sensitive to elevated concentrations of phenylalanine and tryptophane, respectively. Afterwards, DAHP is dephosphorylated to 3-dehydroquinate (3DHQ) under the presence of a 3DHQ synthase (encoded by *aroB*) followed by the conversion to 3-dehydroshikimate (3DHS) with a 3DHQ dehydratase (corresponding gene is *aroD*). Shikimate (SHK) is then produced from 3DHS mediated by the shikimate dehydrogenase (encoded by *aroE*) under the consumption of NADPH. Subsequently, the ATP-dependent shikimate kinases I and II (*aroK* and *aroL*) introduce a phosphate group into SHK leading to 3-phosphoshikimate (SHK3P). It is reported that the shikimate kinase II (AroL) has a 100-fold higher affinity for SHK than AroK, making this isoenzyme the dominant variant in this phosphorylation reaction (DeFeyter & Pittard 1986). SHK3P is then further converted to 5-enolpyruvylshikimate 3-phosphate (5EPS3P) under the degradation of PEP by the 5EPS3P synthase. Ultimately, the chorismate synthase utilizes 5EPS3P and it produces chorismate. From this central precursor molecule, there are three branching pathways for either L-tryptophane, L-tyrosine or L-phenylalanine production. The former is synthesized in a five-step reaction, whereas L-tyrosine and L-phenylalanine are produced in a three-step reaction. The formation of L-tyrosine begins with the conversion of chorismate to prephenate (PRE) mediated by a chorismate mutase followed by the elimination of carbon dioxide under the presence of NAD^+ to form 4-hydroxyphenylpyruvate (HPP). Both reactions are catalyzed by enzymes encoded by the *tyrA* gene. For the L-phenylalanine biosynthesis, chorismate is also converted to PRE by the chorismate mutase in the first step, which gets further tranformed to phenylpyruvate (PHPYR) mediated by a prephenate dehydratase (both encoded by *pheA*). At the end, the same tyrosine aminotransferase (encoded by the *tyrB* gene) catalyzes the final conversion of HPP and PHPYR to either L-tyrosine or L-phenylalanine with simultaneous consumption of glutamate and the formation of α-ketoglutarate (Sprenger 2007, Weiner *et al.* 2014a, Pittard & Yang 2008).

3.1.4.2. Production of amino acids with recombinant *Escherichia coli* strains

Among the three aromatic amino acids L-tryoptophane, L-tyrosine and L-phenylalanine, particularly the latter receives plenty of attention from the food and feed industry due to its versatile spectrum of applications. For example, it is often used as a precursor for the low-calorie sweetener aspartame, a key ingredient for diet drinks or foods (Ager *et al.* 1998). Furthermore, L-phenylalanine occupies an important role as a feed additive and represent a major intermediate for the production of pharmaceuticals such as human immunodeficiency virus protease inhibitors or anti-inflammatory drugs. Logically, its commercial market volume in 1999 was 20-fold higher in comparison to their aromatic amino acid counterparts (Bongaerts *et al.* 2001). The manufacturing of this highly demanded biomolecule can be performed by either chemical synthesis, enzymatic conversion or microbial production processes (Ager *et al.* 1998, Sprenger 2007).

Although amino acids were initially synthesized via chemical synthesis in 1960, these processes led to racemic mixtures from which the correct enantiomer had to be purified. Hence, microbial production processes were established that are capable of producing optically active amino acids (Nakamori 2017, Tonouchi & Ito 2017). To compete with yields achieved in the chemical industry, potential producing strains in microbial production processes need to be optimized by genetic engineering (Sprenger 2007). Based on the given understanding of the aromatic amino acid biosynthesis in *E. coli*, different approaches and producing variants were established and investigated (Backman *et al.* 1990, Liu *et al.* 2014). Among them is the *E. coli* FUS4 strain, which was developed in the laboratory of Georg A. Sprenger and co-workers. Following the so-called FAME approach (Fermentation And Metabolic Engineering), an *E. coli* K-12 derivative called W3110 was used as a host strain due to the profound knowledge of the genomic structures, the available genetic tools to introduce genetic modifications and the ease in handling during bioreactor cultivations (Sprenger 2007). The general concept of this approach is the rational improvement of the L-phenylalanine production during bioprocesses with *E. coli.* This was achieved by identification of limiting reactions by metabolic pathway analysis and subsequent targeted genetic engineering of potential weak links during the L-phenylalanine production. Planned as an iterative procedure, the product formation shall be boosted step by step (Gottlieb *et al.* 2014, Weiner *et al.* 2016). As a preparation for this approach, the gene cluster including *pheA*-*aroF*-*tyrA* was removed by chromosomal deletion. As a consequence, the strain is auxotroph for L-phenylalanine and L-tyrosine. Both the *pheA* and *aroF* were deleted to avoid any unwanted homologous reactions with plasmid-borne variants of these genes. Furthermore, it circumvents the unnecessary accumulation of certain intermediates along the aromatic amino acid biosynthesis. On the other hand,

the *tyrA* gene was removed to restrict any unwanted L-tyrosine formation as this stoichiometrically reduces the E4P and PEP levels in cells, which are also needed for the L-phenylalanine production. Additionally, the double auxotrophy in this strain enables the decoupling of growth with the product formation, which was a relevant factor in the metabolic pathway analysis. The inducible L-phenylalanine production was realized by preparation of a $pF81_{kan}$ plasmid, which encodes for the *aroF*, *pheA^{fbr}*, *aroB* and *aroL* genes under the control of a tac promoter. A feedback resistant variant of the PheA was introduced to circumvent any product inhibition events. Moreover, the plasmid harbours a *lacIq* gene and a kanamycin resistance. Because the expression of the genes encoded on the plasmid are induced by the presence of isopropyl ß-D-1-thiogalactopyranoside (IPTG) and structural analogues such as lactose, the *lacIZYA* in the genome was replaced by another *aroFBL* gene cluster under the control of the same tac promoter (Sprenger 2007, Weiner *et al.* 2014b, Gottlieb *et al.* 2014).

The L-phenylalanine production with the *E. coli* FUS4 ($pF81_{kan}$) strain was extensively studied by Dirk Weuster-Botz and co-workers during fed-batch cultivations in a stirred-tank bioreactor with 15 L of a chemically defined medium as a starting volume. Instead of using glucose as a carbon source, glycerol was used. Besides the ecological benefit of using a major by-product of the bio-diesel production, glycerol has application-oriented advantages such as a higher degree of reduction per carbon than glucose as well as no PEP consumption during the cellular uptake (Yazdani & Gonzalez 2008, Weiner *et al.* 2014a). The conducted process can be divided into three phases including an initial batch phase, a biomass production phase with exponential feeding of glycerol, L-phenylalanine and L-tyrosine and a product formation phase with a constant feeding of glycerol. Maximum achieved product titers were at 22.8 g L^{-1} with maximum biomass specific L-phenylalanine formation rates of 34 mg g^{-1} h^{-1}. The analysis of the metabolic pathways during L-phenylalanine production were conducted in parallel short-term steady-state perturbation experiments (Weiner *et al.* 2014a, Weiner *et al.* 2014b, Weiner *et al.* 2016).

3.2. Design and process control in bioreactors

Bioreactors define an apparatus such as a chamber or a vessel, in which biochemical reactions take place involving enzymes, microorganisms or eukaryotic cells. They fulfill several tasks to provide ideal bioprocess conditions for the desired reactions. Among them is the capability to control certain process parameters by the input of energy and supply of gases and liquid solutions. For example, the energy consumption allows cooling and heating of the bioreactor suspension to maintain a constant temperature, whereas the ad-

dition of titrating agents such as bases and acids are mandatory to control the pH value. Concomitant to this, the homogenization of bioreactor suspensions is achieved by mixing and is important to avoid spatial gradients of pH, temperature, substrate concentrations and other decisive parameters. Accordingly, the distribution of solid particles such as microorganisms (suspension) and the gas transfer into the liquid media is enhanced, as well. Last but not least, the usage of a closed vessel or other containers constitute a sterile barrier from the adjacent environment and thus promote the growth of pure cultures (Chmiel & Weuster-Botz 2018, Mandenius 2016). Therefore, bioreactor cultivations provide ideal conditions and prerequisites to enable the recombinant production of bio-based components with high biomass yields and productivity (Zhu *et al.* 2015, Wang *et al.* 2020, Aro *et al.* 2023, Rantasalo *et al.* 2019). Bioreactors can be operated based on their size at various volumes from microliter scale up to production scales with several thousands of liters (Kirk & Szita 2013, Tonin *et al.* 2021).

Different types of bioreactors have been established, developed and used for various biotechnological applications, each with their own benefits and drawbacks. The choice of bioreactor influences important operational considerations such as the oxygen transfer, mixing efficiency, shear levels, process control, scale-up and total capital expenses. At the same time, the operational parameters provided in the bioreactor need to match with the demands of the producing strains to maximize the biological performance measured by biomass and product yields (Zhong 2010). Available bioreactor types can be categorized based on the energy input for homogenization and mixing of the liquid suspension. Stirred-tank bioreactors are by far the most used bioreactors for biotechnological production processes as mixing is achieved by mechanical forces (Zhong 2010, Chmiel & Weuster-Botz 2018). Nevertheless, homogenization can also be provided by gas bubble expansion, e. g. in flat-panel photobioreactors (Wolf *et al.* 2021, Trivedi *et al.* 2021). Moreover, continuous tubular reactors are often operated with pumps to mix and homogenize the liquid suspensions (Winn *et al.* 2014, Bélafi-Bakó *et al.* 2006).

3.2.1. Stirred-tank bioreactor

Stirred-tank bioreactors often have a cylindrical geometry with a flat or round bottom, in which the culture medium is mixed by agitation of integrated impellers through energy input. Its popularity for biotechnological production processes relies on good fluid mixing and enhanced oxygen transfer from the gas into the liquid, simple scale-up transfers and the facilitated compliance with GMP requirements (Zhong 2010). More importantly, a wide variety of impellers have been designed and developed to enable the efficient mixing of fluids with different rheological properties at different shear levels. Even the mixing in

solid-state cultivations is possible using specifically designed impellers (Karimi *et al.* 2013, Mohamed *et al.* 2009, Ghobadi *et al.* 2017, Dohi *et al.* 2004). Ideal flow regimes can be set by the rational combination of radial and axial mixing impellers based on the given bioreactor geometry (Zlokarnik 1999).
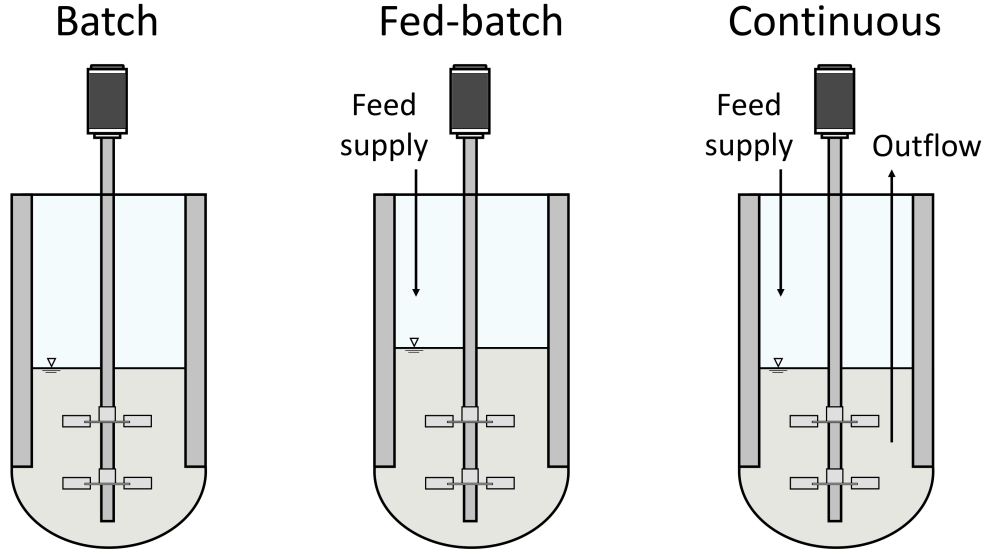
Figure 3.2: Different operation modes in a stirred-tank bioreactor. Batch processes are characterized by a fixed volume of culture medium, which contains all nutrients to enable bacterial growth. In contrast, both fed-batch and continuous cultivations are accompanied by the permanent supply of a feeding solution. There is a further outflow of the cell suspension in the latter operation mode to provide a steady-state environment.

Besides the selection from a pool of impellers, stirred-tank bioreactor cultivations can be operated in three modes: batch, fed-batch or continuous cultivations (Figure 3.2). Under the assumption of an ideal bioreactor, in which a complete homogenization of the biosuspension is expected with no concentration gradients of any components and equal environmental conditions at any spatial position, the general mass balance can be described by the following equation (Takors & Weuster-Botz 2018)

$$V \cdot \frac{dc_i}{dt} = c_{i,0} \cdot \dot{V}_{in} - c_i \cdot \dot{V}_{out} + r_i \cdot V \tag{3.9}$$

c_i	Concentration of component i	$g\ L^{-1}$
$c_{i,0}$	Concentration of component i in feeding solution	$g\ L^{-1}$
$\dot{V}_{in}$	Volumetric flow of feed medium into the bioreactor	$L\ h^{-1}$
$\dot{V}_{out}$	Volumetric flow of culture medium out of the bioreactor	$L\ h-1$
r_i	Reaction rate of component i	$g\ L^{-1}\ h^{-1}$
V	Working volume	L

3.2.1.1. Batch cultivation

Batch processes are characterized by a fixed volume of the culture medium enriched with all necessary nutrients, components and substrates. The abundance of all media components and substrates allow cells to grow exponentially with the maximum specific growth rate μ_{max} until depletion of the limiting substrate. Therefore, a vast amount of biomass can be generated in a short time period (Bolmanis *et al.* 2023, Yee & Blanch 1992, Luli & Strohl 1990). Apart from the marginal addition of the cell inoculum as well as bases and acids for pH regulation and antifoam agents during the process, the volume can be considered as constant. With no influx and no effluent, the concentration of a component c_i is solely dependent from the reaction rate r_i

$$\frac{dc_i}{dt} = r_i \tag{3.10}$$

Although a rapid cell growth is generally preferred, high growth rates are often accompanied by unwanted by-product formation. Studies have shown for *E. coli*, that growth rates above 0.35 h^{-1} induce acetate formation, which was absent at lower rates (Meyer *et al.* 1984, Paalme *et al.* 1990). Additionally, batch processes are limited to rather low cell densities as specific carbon and nitrogen sources cannot be provided at infinitely high concentrations in the starting cultivation medium. Not only all chemicals have a certain solubility limit when dissolving in liquid solutions, they can also contribute to inhibitory effects on the cell growth when surpassing certain concentrations (Kazan *et al.* 1995, Lee 1996, Thompson *et al.* 1985).

3.2.1.2. Fed-batch cultivation

High cell densities can be provided in fed-batch cultivations, in which potential inhibitory effects of media components are circumvented by implementation of a constant or intermittent influx of a highly concentrated nutrient solution. Nevertheless, these processes often start with an initial batch phase to generate a sufficient amount of biomass. Only after the complete depletion of the substrates in the cultivation medium, a rational feeding profile is applied at a specific growth rate below μ_{max} to avoid by-product formation and thereby prolonging the cell growth phase. Their superior performance in terms of biomass yields and productivity with lower waste generation compared to simple batch cultivations made this operation mode the benchmark for biotechnological production processes for several decades (Lee 1996, Riesenberg *et al.* 1991, Bolmanis *et al.* 2023, Muradi *et al.* 2020, Dias Rodrigues *et al.* 2019).

The mass balance of fed-batch processes can be described by the following equation:

$$V \cdot \frac{dc_i}{dt} = (c_{i,0} - c_i) \cdot \dot{V}_{in} + r_i \cdot V \tag{3.11}$$

Assuming a continuous feeding with no feedback control, three strategies can be applied. A constant feeding of a nutrient solution lead to a steady decrease of the specific growth rate of the microbial population due to the rise of the culture volume and biomass concentration over time. This can be temporarily compensated by application of a linearly increasing feeding method. A theoretically unlimited growth of biomass can be achieved by an exponential feeding strategy when neglecting limitations of the oxygen transfer into the cultivation medium. In this instance, the specific growth rate of the microbial population equals a constant value μ_{set}. To calculate the corresponding exponential feeding rate $\dot{V}_{in}$, the general mass balance (equation 3.11) needs to be specified regarding the substrate concentration:

$$V \cdot \frac{dc_S}{dt} = (c_{S,0} - c_S) \cdot \dot{V}_{in} + r_S \cdot V(t) \tag{3.12}$$

$c_{S,0}$	Substrate concentration in feeding solution	$g\ L^{-1}$
c_S	Substrate concentration in bioreactor suspension	$g\ L^{-1}$
r_S	Reaction rate of substrate	$g\ L^{-1}\ h^{-1}$

The reaction rate r_S is equivalent to the product of the substrate uptake rate q_S and the biomass concentration c_X

$$r_S = q_S \cdot c_X = -\left(\frac{\mu}{Y_{X/S}} + m_S\right) \cdot c_X \tag{3.13}$$

q_S	Substrate uptake rate	$g\ g_{CDW}^{-1}\ h^{-1}$
c_X	Biomass concentration	$g\ L^{-1}$
μ	Specific growth rate	h^{-1}
$Y_{X/S}$	Biomass yield	$g\ g^{-1}$
m_S	Substrate consumption for maintenance	$g\ g_{CDW}^{-1}\ h^{-1}$

Assuming a set growth rate μ_{set} of the microbial population due to the exponential feeding and ideal bioreactor conditions with no spatio-temporal concentration gradients within the biosuspension, the substrate concentration c_S is constant, as well.

$$\mu = \mu_{set} = constant \tag{3.14}$$

$$c_S = constant \tag{3.15}$$

$$\frac{dc_S}{dt} = 0 \tag{3.16}$$

With further neglection of the substrate consumption for the maintenance m_S, equation 3.12 transforms to the following

$$0 = (c_{S,0} - c_S) \cdot \dot{V}_{in} - \left(\frac{\mu_{set}}{Y_{X/S}} \right) \cdot c_X \cdot V(t) \tag{3.17}$$

The biomass concentration c_X is expected to increase according to the set specific growth rate μ_{set}. Hence, it can be approximated with the following term

$$c_X \cong c_{X,0} \cdot e^{\mu_{set} \cdot t} \tag{3.18}$$

$c_{X,0}$	Initial biomass concentration	$g\ L^{-1}$
t	Time	h

When integrating equation 3.18 into equation 3.17 and neglecting the changes in volume ($V(t) = V_0 = constant$), the exponential feeding rate $\dot{V}_{in}$ can be approximated as

$$\dot{V}_{in} \cong \frac{\mu_{set} \cdot c_{X,0} \cdot V_{R,0}}{Y_{X/S} \cdot (c_{S,0} - c_S)} \cdot e^{\mu_{set} \cdot t} \tag{3.19}$$

$V_{R,0}$	Initial bioreactor volume	L

3.2.1.3. Continuous cultivation

Continuous cultivations combine an influx of fresh culture medium into the bioreactor with the simultaneous efflux of biosuspension from the bioreactor. As both fluxes are identical, the application of suitable feeding and dilution rates theoretically allow an infinite growth of the cells at a constant volume level. Similarly to the fed-batch operation, the supply of substrates control the specific growth rates of the cell population while keeping the limiting substrate concentrations rather low. Furthermore, product accumulation and possible inhibitory effects can be circumvented due to a constant removal through the efflux. This enables a constant product formation over a longer period of time with higher biomass productivities and optimized space-time yields for the product formation (Ling *et al.* 2006, Göksungur & Güvenc 1997, Fernandes *et al.* 2015). In research applications, continuous cultivations offer an effective platform for single parameter studies on

specific cell physiologies and productivities as they provide a steady-state environment with constant process parameters. To reach this state, continuous cultivations have to undergo through at least five retention times, which describes the duration to exchange the entire volume of the bioreactor. By alteration of a single parameter, this steady-state is perturbated, from which the corresponding effects can be monitored and clearly attributed to the changed parameter (Hoskisson & Hobbs 2005, Adamberg *et al.* 2015). Assuming ideal conditions in the operating bioreactor, the concentration of a component i remains constant over time. Therefore, the mass balance transitions to the following equation with $\dot{V}_{in} = \dot{V}_{out} = \dot{V}$

$$0 = \frac{\dot{V}}{V} \cdot (c_{i,0} - c_i) + r_i \tag{3.20}$$

3.2.2. Continuous tubular reactor

Bench scale tubular reactors are cylindrical tubes with a constant diameter that are operated at a constant flow (Monge *et al.* 2013). With similarities to continuous stirred-tank bioreactor cultivations, a mixture of reactant and reagent enters the reactor on one side, moves along the tube with a distinctive residence time and leaves it on the other end (Tabatabaei *et al.* 2019). Due to their comparably simple design and easy operation mode, these types of reactors are often utilized for chemical kinetic studies and continuous conversion reactions (Brown 1978, Monge *et al.* 2013, Takors & Weuster-Botz 2018). Especially for the bio-diesel production, tubular reactors remain a popular choice because of the steady-state operation (Harvey *et al.* 2003, Tabatabaei *et al.* 2019). Until now, various configurations have been developed for this type of reactor. But still, a straight tubular reactor remains the most characterized and used type of continuous tubular reactors (Kurt *et al.* 2017, Kováts *et al.* 2020, Jaibiba *et al.* 2020).

3.2.2.1. Straight tubular reactor

Assuming an empty cylindrical pipe with a fixed diameter and length, the selection of an appropriate flow rate for steady-state operation is paramount to dictate the reaction rates and its extent of a chemical reaction. In general, three different flow profiles can be observed based on the applied flow rates. For low flow rates, a parallel stream of fluid elements evolve along the pipe axis. However, the fluid motions adjacent to the walls are immediately slowed down owing the surface friction forces, which is also known as no-slip conditions. In contrary, fluid elements in the center of the tube move faster

with a constant cross-sectional mass flow rate at any axial location, which ultimately lead to the typical parabolic profile for laminar flow in pipes (Figure 3.3, Durst *et al.* 2005, Surek & Stempin 2014). Elevating the applied superficial velocity, the laminar state becomes increasingly susceptible to perturbations as the parallel fluid layers start to intertwine with rather chaotic trajectories. These counter-rotating vortices and other eddying motions are the result of dynamic changes of each fluid element regarding the magnitude of its speed and direction. As a consequence, the velocity profile for turbulent flow regimes strongly flattens for most of the cross-sectional area. The boundary layers with comparably low velocities close to the pipe wall remain present, but to a remarkably lower extent (Figure 3.3, Meisner & Rushmer 1963, Eckhardt *et al.* 2007, Kühnen *et al.* 2018). These boundary layers become more irrelevant at even higher superficial velocities. With the simultaneous assumption of ideal conditions with no friction loss on surfaces, plug flow occurs with each fluid particle having the exact same flow rate along the cross-sectional area (Figure 3.3, Takors & Weuster-Botz 2018).
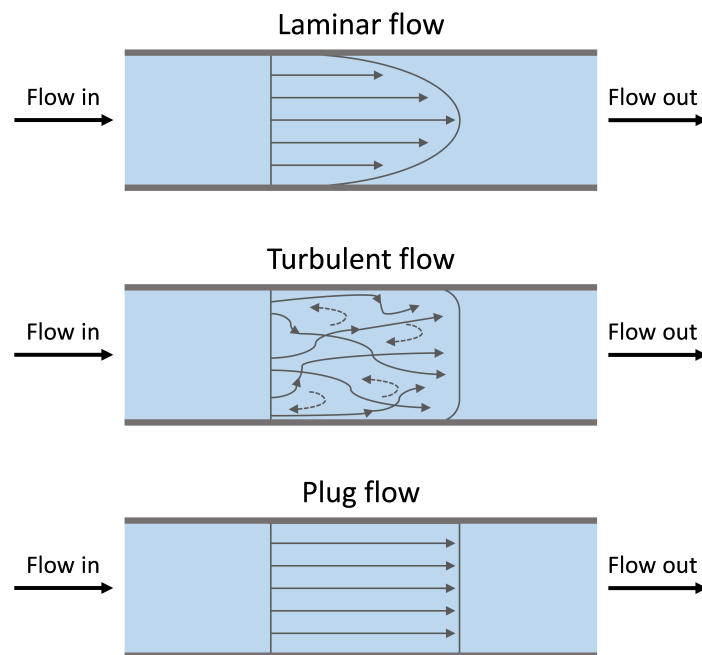
Figure 3.3: Flow rate profiles in a straight pipe at different flow regimes. The upper depicts the typical parabolic profile for laminar flows, while the middle represents the flow profile for turbulent regimes. In the bottom, ideal conditions are assumed so that a plug flow results.

Instead of determining the prevailing flow regimes in a pipe by visualization of the flow profiles, the transition from laminar to turbulent regimes can be calculated with the dimensionless Reynolds number. It describes the ratio of inertial to viscous forces (equation 3.21). Despite of some divergent outcomes regarding the exact number, studies often show the transition from laminar to turbulent regimes at Reynolds numbers of around

$Re_{crit} = 2300$, while full turbulences in a straight pipe can be assumed with Reynolds numbers above 10 000 (Hlushkou & Tallarek 2006, Schlichting & Gersten 2017, Darbyshire & Mullin 1995, Basse 2021, Hattori *et al.* 2022).

$$Re = \frac{d \cdot u \cdot \rho}{\eta} \tag{3.21}$$

Re	Reynolds number	$-$
d	Characteristic length	m
u	Superficial velocity	$m\ s^{-1}$
ρ	Density of the fluid	$kg\ m^{-3}$
η	Dynamic viscosity	$Pa\ s$

The mass balance of a component i in pipe flows is determined as the sum of convection, dispersion and the reaction rate for the cross-sectional area A for a specific distance dz. Under the consideration of a Taylor approximation, the following equation can be used:

$$\frac{d(V_L \cdot c_i)}{dt} = -dV_L \cdot u_z \cdot \frac{\partial c_i}{\partial z} - dV_L \cdot D_i \cdot \frac{\partial^2 c_i}{\partial z^2} + r_i \cdot dV_L \tag{3.22}$$

V_L	Volume	L
c_i	Concentration of component i	$mol\ L^{-1}$
t	Time	s
z	Axial distance	m
D_i	Dispersion coefficient	$m^2\ s^{-1}$
r_i	Reaction rate of component i	$mol\ L^{-1}\ s^{-1}$

Assuming no changes of the balanced volume element $\frac{dV}{dt} = 0$ and steady-state operations ($\frac{dc_i}{dt} = 0$), the equation can be simplified to

$$u_z \cdot \frac{\partial c_i}{\partial z} + D_i \cdot \frac{\partial^2 c_i}{\partial z^2} = r_i \tag{3.23}$$

The ratio between convection and dispersion in a pipe is also described by the dimensionless Bodenstein number (Bo)

$$Bo = \frac{u_z \cdot L}{D_i} \tag{3.24}$$

Bo	Bodenstein number	$-$
L	Length of the tube	m

For Bodenstein numbers above 100 ($Bo \gg 100$), the mass transport by convection becomes superior while the dispersion processes can be neglected. Integrating this into equation 3.23, the fraction resembling the dispersion vanishes and the concentration of the component i is solely dependent on the reaction rate r_i and the superficial velocity u_z (Takors & Weuster-Botz 2018). Minimizing the extent of dispersion for the chemical synthesis in a pipe is important to reliably predict and determine the residence time distribution (RTD) of particles. Strong deviations potentially lead to incomplete or unwanted reactions. Broader distributions are especially promoted in a laminar flow due to poor radial mixing and the increasing magnitude of dispersion processes, which enhance axial dispersion (backmixing). Consequently, a turbulent flow tremendeously improves radial mixing, diminishes the impact of dispersion to make axial dispersion negligible and ultimately ensure narrow RTDs (Levenspiel 2012, Monge *et al.* 2013, Tabatabaei *et al.* 2019).

Despite the long history of straight pipes in flow chemistry, there are applications demanding for specific requirements, which cannot be fulfilled by this type of reactor. Among them are chemical reactions with slow kinetics that demand for residence times of several hours (Johnson *et al.* 2012, Chapman *et al.* 2017). Lowering the flow rate to prolong the residence time most certainly lead to the transition from turbulent to laminar flow regimes and thus improper mixing, which negatively impacts the product quality and yield. Conversely, extending the pipe length seems rather impractical and at some point impossible (Kumar *et al.* 2006). In general, straight pipes lack of compactness and flexibility in terms of scalability as they are often build of rigid and expensive materials such as stainless steel, which make later modifications of the reactor rather challenging (Klutz *et al.* 2015, Adschiri *et al.* 1992, Watkins & McCarthy 1995). Active mixing devices such as stirrers or ultrasonic micromixers can be beneficial to improve radial mixing under laminar flow regimes (Longis *et al.* 2023, Yang *et al.* 2001), but they elevate the operational costs and complexity. In contrary, passive mixing methods are superior to keep the operational expenses as low as possible as mixing is solely enhanced by targeted distraction of the fluid motion (Klutz *et al.* 2015). Especially static mixers with various geometries have been extensively studied and have proven their beneficial impact on enhanced radial mixing (Hobbs & Muzzio 1997, Hirech *et al.* 2003, Jilisen *et al.* 2013, Kreimer *et al.* 2019). Conversely, the use of static mixers comes with more complex structures and higher pressure drops (Khot *et al.* 2019). Additionally, static mixing devices automatically increase the surface area, thus making these systems vulnerable for (bio-)fouling and clogging, particularly with biosuspensions at very low flow rates (Citulski *et al.* 2009).

3.2.2.2. Helical tube reactor

In 1927 and 1928, Dean investigated the steady motion of fluid flowing through a circular pipe coiled around a circular geometry. According to his studies, he predicted that fluid elements started to deviate from their parallel streamlines when entering a curved pipe with a specific ratio of the tube diameter to circle diameter. In fact, he described the emergence of double helical vortices in the plane of the cross-section superimposing the known streamline velocity distributions in straight pipes (Dean 1927, Dean 1928a, Dean 1928b, White 1929). These assumptions were approved by more advanced experimental setups such as the laser-incduced fluorescence measurements of resorufin that allows the exact monitoring of fluid motion in the cross-section of pipes (Kováts *et al.* 2020). The magnitude of this type of secondary flow is described by the dimensionless Dean number (Dn) and is dependent of the prevailing Re number as well as the inner tube diameter d_i and the coil diameter d_c (Kumar *et al.* 2006)

$$Dn = Re \cdot \sqrt{\frac{d_i}{d_c}} \tag{3.25}$$

Dn	Dean number	$-$
d_i	Inner tube diameter	m
d_c	Coil diameter	m

Dean vortices are the result of centrifugal forces. The radial counter-rotating circulations improve radial mixing in tubes, especially at laminar flow regimes (Trivedi & Vasudeva 1975, Saxena & Nigam 1981). Due to the fact, that mixing is solely enhanced by the motion of fluids induced by the curvature, helical tube reactors are interesting aspirants for passive mixing reactor concepts (Klutz *et al.* 2015). However, other studies revealed the importance of the interface angles of two liquids at the inlet of the curved pipe, which have to be perfectly aligned with the coil axis. In worst case, the mixing efficiency can tremendeously decline as fluids or particles can be separately trapped in one of the counter-rotating vortices (Mansour *et al.* 2017, Khot *et al.* 2019).

3.2.2.3. Coiled flow inverter

To circumvent the permanent formation of two separate mixing zones in a coiled tube, fully developed Dean vortices need to be repeatedly disturbed. This can be accomplished by the frequent introduction of bends. The idea is to re-orientate the acting centrifugal forces based on the change of coil direction and thus the rotation of evolving Dean vortices in the cross-sectional plane. As a consequence, the beneficial radial mixing can be

maintained while hindering the permanent existence of two isolated mixing zones and ultimately promote narrow RTDs (Saxena & Nigam 1984, Rossi *et al.* 2017, Khot *et al.* 2019, Kováts *et al.* 2020). Additionally, these kind of reactors feature a very compact design as bends enable the occupation of a third spatial dimension. One example of a specialized helical tube reactor with a permanent re-orientation of the acting centrifugal forces and a compact design is the coiled flow inverter (CFI), in which frequent bends of 90° are implemented (Klutz *et al.* 2015, Khot *et al.* 2019).

The degree of mixing efficiency in coiled flow inverters is strongly linked to specific design parameters such as the coil diameter d_c or the number of bends n. All of them influence the feasibility and the compactness of this reactor type. Klutz *et al.* (2015) summarized the most important design parameters of a CFI and elucidated the best performance design space for narrow RTDs under laminar flow (Klutz *et al.* 2015):

Inner tube diameter d_i: The inner tube diameter is of great importance due to its connection with the tube length. Given a reaction system with a fixed flow rate and a fixed required residence time, the decrease of d_i can be only compensated by extending the tube length to maintain the desired residence time. Therefore, a compact design is more accessible with larger inner diameters. Furthermore, any changes of the inner tube diameter affects the corresponding Reynolds number and thus the magnitude of Dean vortices.

Coil diameter d_c: Cylindrical rods are often used as a supporting framework for helical tube reactors. The outer diameter of this rod contributes the most to the coiling diameter d_c and directly influences the presence and magnitude of occurring secondary flow in the tube. The lower the coiling diameter, the higher the ratio of d_i to d_c and thus the stronger the Dean vortices (Dean 1927, Dean 1928a, Dean 1928b, White 1929, Saxena & Nigam 1984). However, reducing the coil diameter of the rod decreases its available surface area at the same time, which is counterintuitive for a compact design.

Tube wall thickness: The wall thickness of a tube is the difference of the outer tube diameter d_o to d_i, which marginally elevates the coil diameter. In terms of a compact design, a rather small thickness is beneficial.

Pitch distance p: This parameter describes the distance of the pole centers of two adjacent tubing parts coiled around the same cylindrical rod. The pitch distance should be kept as low as possible and ideally equals the outer tube diameter d_o.

Dean number Dn: As mentioned previously, the dimensionless Dean number indicates the magnitude of the prevailing secondary flow in helical pipes. It is strongly dependent on the Re number, the inner tube diameter d_i and the coil diameter d_c. Plenty of studies investigated the minimum mandatory Dn number to fully develop secondary vortices for a narrow RTD at laminar flow. As a rule of thumb, Dean numbers should be at least higher than 3 to exploit the acting centrifugal forces for a better radial mixing (Saxena & Nigam 1984).

Modified torsion parameter T*: The torsion parameter T is a further dimensionless number describing the geometrical ratio of the pitch distance p to the length of a single turn of a helical coil. Therefore, this parameter is strongly defined by the pitch distance p, the coil diameter d_c and the Re number. The modified torsion parameter T^* results by multiplicative inversion of the torsion number T. According to Saxena & Nigam (1983), the torsion number in coiled pipes should be below 0.001 to allow secondary flow patterns to evolve. Consequently, the modified torsion parameter T^* should surpass values higher than 500.

$$T = \frac{p}{2 \cdot \pi \cdot d_c \cdot Re} \tag{3.26}$$

$$T^* = \frac{2 \cdot \pi \cdot d_c \cdot Re}{p} \tag{3.27}$$

T	Torsion parameter	$-$
T^*	Modified torsion parameter	$-$
p	Pitch distance	m
d_c	Coil diameter	m

Number of turns in a coiling element N: One of the problems with straight helical tubes is the formation of two isolated counter-rotating mixing zones in the cross-sectional plane, which can be circumvented by the introduction of bends. However, these bends should be implemented soon after the Dean vortices are fully developed to provide optimum radial mixing. Based on the studies of Saxena & Nigam (1984), at least two helical turns are mandatory. Therefore, a coiling element, which defines a section of adjacent coiled hoses with no bends, should have 2 to 4 turns before a bend is introduced.

Bend angle α_b: Coiled flow inverters are known to have repetitive bends with an angle of 90°, which lead to their characteristic hollow square design. Khot *et al.* (2019) approved this bend angle to provide the best mixing efficiencies and narrow RTDs.

Number of bends n_{bends}: Generally speaking, the implementation of more bends always improves the mixing characteristics in helical tubular reactors. Nevertheless, the number of bends should be defined and set in accordance to the number of turns in a coiling element as they ultimately define the final design of a coiled flow inverter, especially regarding the number of necessary layers. According to Saxena & Nigam (1984), RTDs drastically narrowed for bend numbers higher than 3.

3.2.2.4. Fluid dynamic characterization of tubular reactors

The golden standard for monitoring of residence time distributions in any kind of tubular reactors is the use of the tracer technology. In accordance with the name, tracers are injected at the inlet of a pipe and the spreading of this tracer is measured at the exit. Based of the acquired signal intensities and distribution, the fluid dynamics of a given system can be approximated for the applied operational setup (Levenspiel 2012).

The choice of tracers is strongly dependent on the mobile phase of the experiments. In best case, the tracer is chemically inert and has the same density as the mobile phase. Additionally, tracers should be injected across the cross-sectional area with the same flow rate of the flowing fluid to ensure reliable and reproducible results. Simultaneously, the monitoring devices should be capable of covering the whole cross-sectional area of the eluted mobile phase at the exit with an appropriate time resolution (Levenspiel 2012). In most cases, concentrated solutions of bases such as sodium hydroxide or potassium hydroxide can be used in combination with pH electrodes with short response times of a few seconds (Papagianni *et al.* 2003, Mørup *et al.* 2015). Alternatively, dyeing solutions such as a pink cobalt nitrate(II) hexahydrate solution or a red vitamin B12 solution also qualify as tracers together with a colorless mobile phase (Santacesaria *et al.* 2012, Klutz *et al.* 2015, Kurt *et al.* 2015).

Tracers can be injected in two ways. The first approach is the pulse injection of a comparably low volume of tracer ($V_{tracer} < 0.01 \cdot V_{reactor}$) into the inlet of a pipe flow. With the acquired data of tracer concentration at a specific point downstream the injection port, values of the exit age distribution $E(t)$, the mean residence time τ and the variance σ can be calculated (Levenspiel 2012, Mørup *et al.* 2015).

$$E(t) = \frac{c(t)}{\int_0^\infty c(t)dt} \tag{3.28}$$

$$\tau = \int_0^\infty t \cdot E(t)dt \tag{3.29}$$

$$\sigma^2 = \int_0^\infty (t - \tau)^2 \cdot E(t)dt \tag{3.30}$$

$E(t)$	Exit age distribution	s^{-1}
$c(t)$	Tracer concentration	$mol\ L^{-1}$
τ	Mean hydraulic residence time	s
t	Time	s
σ^2	Variance	s^2

Experimentally determined mean hydraulic residence times τ should be approximately similar with the theoretical residence time $t_{theoretical}$ calculated by the ratio of reactor working volume V to the applied volumetric flow rate $\dot{V}$ (equation 3.31). In cases of $t_{theoretical} < \tau$, unwanted dead or stagnant zones exist, whereas $t_{theoretical} > \tau$ indicate a hold back of the tracer, e.g. by adsorption to the inner tube wall. On the other hand, the variance σ of the measured RTD is a good indicator of the prevailing axial dispersion as small σ values indicate very narrow distributions and *vice versa* (Levenspiel 2012).

$$t_{theoretical} = \frac{V}{\dot{V}} \tag{3.31}$$

V	Working volume	L
$\dot{V}$	Volumetric flow rate	$L\ s^{-1}$

The second method of injection is the step input. In contrary to the previous approach, the tracer solution is fed into the reactor by a sudden switch from an ordinary mobile phase to the tracer solution. This automatically ensures the complete coverage of the tracer solution to the cross-sectional area of the pipe with a constant flow rate. Consequently, the step input method is less apparative, easier to handle and reduces the chances of handling errors. In this instance, the obtained RTD is a cumulative distribution curve $F(\theta)$, which monitors the outbreak of the tracer solution at a specific point of the system. The dimensionless time θ is calculated as the ratio of the time t to the mean hydraulic residence time τ, whereas the dimensionless values of $F(\theta)$ can be determined by division of the concentration $c(t)$ to the maximum measured concentration of a run

c_{max} (Kurt *et al.* 2015, Levenspiel 2012).

$$F(\theta) = \frac{c(t)}{c_{max}} \tag{3.32}$$

$$\theta = \frac{t}{\tau} \tag{3.33}$$

$F(\theta)$	Dimensionless concentration	$-$
θ	Dimensionless time	$-$
$c(t)$	Concentration	$mol\ L^{-1}$
c_{max}	Maximum tracer concentration	$mol\ L^{-1}$

Assuming the validity of using the dispersion model, which is applicable for systems with small deviations from plug flow (Bo > 100), the axial dispersion of the tubular reactor can be approximated with the following equation

$$F(\theta) = \frac{1}{2} \cdot \left[erf\left(\frac{1}{2} \cdot \sqrt{Bo} \cdot (\theta - 1) \right) + 1 \right] \tag{3.34}$$

Other models such as the tanks-in-series model or the convection model can be used according to the given experimental setup (Levenspiel 2012).

3.2.3. Scale-up and scale-down in biotechnological production processes

The development of novel biotechnological production processes is mainly conducted at rather small scale using parallelizable platforms such as shake flasks, micro-bioreactors or microtiter plates with working volumes ranging from milliliters to microliters. This allows a high-throughput screening of optimal cultivating conditions in simple experimental setups at low costs (Reis *et al.* 2006, Puskeiler *et al.* 2005, Kensy *et al.* 2009). After the successful proof-of-concept, these bioprocesses need to be transfered to larger scales to maximize the generated product amount per unit time (Lee & Kim 2015). Based on the product of interest, industrial production processes often range from 5 m^3 to 20 m^3 for pharmaceuticals, 5 m^3 to 50 m^3 for fine chemicals and 100 m^3 to 800 m^3 for bulk chemicals. Different scale-up criteria exist such as the geometrical similarity of bioreactors or the constant volumetric power input between small-scale and large-scale bioprocesses, which have proven to be useful guidelines (Chmiel & Weuster-Botz 2018).

Ideally, the environmental conditions in upscaled bioprocesses should be identical to those provided in the small-scale setup. Only then, cells probably develop the same cellular physiologies to achieve similar product yields and quality. However, chances are high that only a few operational parameters can be kept constant after the scale-up (Lara *et al.* 2006). On the one hand, this relies on the differences during bioprocess preparation. While pure chemicals and de-ionized water are usually used for the cultivation media of bioprocesses at laboratory scale, cheap media components with lower purities are often dissolved in non-filtered tap water to keep the operational costs at large-scale bioprocesses low. Additionally, the production strains have to undergo further preliminary cultivation steps owing the higher needed amount of cell suspension for the inoculation of higher working volumes. Consequently, the number of generations during the seed train increases, which elevates the chances of mutations and differences in phenotypes (Kimura & Ohta 1969, Chmiel & Weuster-Botz 2018).

From an operational point of view, key process variables such as the mass transfer of gases into the liquid or the mixing times should remain identical to small-scale cultivations. However, mixing of a larger volume needs to be compensated with an increase of the volumetric power input. Unfortunately, the theoretically needed power input for large scale bioprocesses quickly reaches the technical limitations and become simply impractical. As a result, mixing and circulation times inevitably increase, which is concomitant with the occurence of environmental process gradients (Lara *et al.* 2006). Dissolved oxygen levels, pH values as well as the temperature spatially differ within the bioreactor. This is further exacerbated by the limited supply of gases and other liquid solutions at single positions in traditional bioreactors. For example, spargers for oxygenation are only present at the bottom, whereas the titration of acids and bases is solely provided from the top of the bioreactor. The same applies to the provision of a feeding solution during fed-batch or continuous cultivations that lead to potential substrate concentration gradients (Langheinrich & Nienow 1999, Haringa *et al.* 2017, Kuschel & Takors 2020). Hence, the prevailing bioprocess conditions deviate from ideal environments for the producing strains that possibly induce pertubation of the cellular metabolism and affect the development of cellular physiologies. For example, Bylund *et al.* (1999) reported an increase of respiration in high glucose concentration zones during fed-batch cultivations of *E. coli* in a 12 m^3 bioreactor. Compared to identical bioprocesses at laboratory scale, metabolic overflow was induced accompanied by the unwanted formation of acetate (Bylund *et al.* 1999, Lara *et al.* 2006). Another example was stated by Ozturk 1996 during a high cell density cultivation of myeloma cells in a 15 L bioreactor, in which cell lysis was observed owing the addition of a concentrated base solution (Ozturk 1996). Further complexity is added

by the fact that each cell experiences different microenvironments in a random order. As a result, the related metabolic responses potentially vary, which ultimately promote a diverge pool of single-cell physiologies of producing strains from an isogenic culture (Müller *et al.* 2010). In some cases, this negatively impacts the mean productivity of the cells as biotechnological production processes at large scale often suffer from lower yields in comparison to their smaller counterparts (Bylund *et al.* 1998, Enfors *et al.* 2001). However, conventional production processes often mask the occurrence of population heterogeneity because the acquired data often reflect average product yields and rates (Avery 2006). Nonetheless, dynamic environmental conditions in bioprocesses also harbour the chance to generate cells with robust and superior cellular characteristics (Tanaka *et al.* 2003, Travis & Travis 2002).

3.3. Population heterogeneity in bioprocesses

With the rapid progress of novel tools and methods to precisely analyze single cells, the ubiquity of differences in expressed cellular physiologies is becoming increasingly apparent in microbial populations. This phenomenon is known as population heterogeneity, which is defined by the co-existence of subpopulations with unequal cellular characteristics although they originate from the same isogenic culture. Concerning decisive process state variables such as the cell growth or product formation, outliers with strong deviations from the mean physiological state of the main population complicate accurate predictions of the outcome of biotechnological production processes. Nevertheless, the existence of both weaker, but also potentially stronger producing cells remain uncertain due to the insufficient mechanistic understanding of this phenomenon. Therefore, further insights of the underlying sources of population heterogeneity during microbial cultivations are paramount to design better and more consistent bioprocesses (Lidstrom & Konopka 2010, Rugbjerg *et al.* 2018, Rugbjerg & Sommer 2019).

3.3.1. Mechanistic understanding of population heterogeneity in bioprocesses

Assuming an identical state between two cells originating from the same isogenic culture, any stochastic fluctuations of certain intracellular events such as the gene expression or metabolic reactions would lead to deviations of their identical physiological state. Especially gene expression events including transcription and translation are vulnerable to a certain degree of randomness regarding the produced protein titers. This is due to the complexity of such processes as transcription and translation rely on specific initiating

events of various factors and elements that are not deterministic but rather depend on probabilities. Additionally, noises on molecular level can arise at different stages of multi-step reactions (Kœrn *et al.* 2005, Swain *et al.* 2002, Kiviet *et al.* 2014, Norman *et al.* 2015). The same stochasticity applies to metabolic reactions within the cell because the conversion of specific molecules is strongly related to the accessibility to the active site of the corresponding biocatalyst. These and other factors such as the age distribution and cell cycle states can be categorized as intrinsic factors, which potentially promote the emergence of population heterogeneity, even under homogeneous conditions (Norman *et al.* 2015, Dewachter *et al.* 2019). In contrary, extrinsic factors refer to intercellular variations of global factors. This includes the numbers of ribosomes, polymerases and other key enzymes as a result of preliminary differences in their genetics or expression levels of certain biocatalysts (Assaf *et al.* 2013, Avery 2006, Swain *et al.* 2002). Genetic variations in cells originating from an isogenic culture is due to the omnipresence of mutations, which defines the spontaneous or induced alteration of bases in a genetic sequence. Mutations tend to be deleterious rather than beneficial. But both elevate uncertainties as they lead to unpredictable genotypes in some cells of a microbial population (Woo *et al.* 2018, Eyre-Walker & Keightley 2007). In bacteria, they naturally arise during the replication of bacterial DNA at cell separation events. Although the corresponding DNA polymerases harbour proofreading domains, they are prone to mismatches and errors when duplicating DNA strands (Oller & Schaaper 1994, Moser *et al.* 1997). Interestingly, the mutation rates in cells particularly increase when microbial populations are facing highly fluctuating or uncertain environmental conditions (Tanaka *et al.* 2003, Travis & Travis 2002). In any case, extrinsic factors are strongly affected by the surrounding environment due to the semi-permeability of the cell membrane. This enables the interaction of the periplasm and cytoplasm of the cells to extracellular conditions. In worst case, these conditions jeopardize the cellular integrity by perturbation of fundamental intracellular processes such as the DNA replication or protein biosynthesis. As a matter of fact, it is not surprising that extrinsic factors mainly contribute to heterogeneity in bacterial populations rather than intrinsic noises (Avery 2006).

Despite the awareness of intrinsic and extrinsic factors to induce population heterogeneity in bioprocesses, it remains unclear whether the co-existence of cells with various phenotypes in a microbial population is the result of a cellular function or just randomly occurring fitness advantages of certain mutants. Hence, novel experimental setups and further practical studies are mandatory to better understand this phenomenon (Heins & Weuster-Botz 2018, Delvigne & Goffin 2014). Some research studies already found several adaptation strategies of microbial populations in different bioprocess setups.

Bet-hedging: Among the most common explanation for the constant adapation of a microbial population is the bet-hedging strategy. It is a risk-spreading approach of a microbial community by the random emergence of cells with co-existing phenotypes. Of course, cells that have developed cellular characteristics for rather challenging environmental conditions will suffer in stable environments and under ideal conditions. However, bet-hedging is especially effective for microbial populations experiencing unpredictable, dynamic or harsh conditions as a broad diversification to elevate the chances of successful adaptation and survival of at least some individuals. Examples for such circumstances are the temporal depletion of substrates or the presence of antibiotics (Heins & Weuster-Botz 2018, Norman *et al.* 2015, Wielgoss *et al.* 2013, Sniegowski *et al.* 1997).

Persistance: Deriving from the bet-hedging approach, bacterial survival in environments enriched with antibiotics can be described by persistance. Persisting cells, which only resemble a small fraction of an isogenic culture of around 1%, survive treatments with antibiotics because of their differences in expressed phenotypes compared to the non-persisting cells. Although persisters are not capable of performing cell separation under these harsh conditions, they ensure the survival of some cells of a bacterial population. Lowering the presence of antibiotics can transform persister cells back to antibiotic-sensitive variants and initiate the formation of a new population, again with a small fraction of persisting cells (van den Bergh *et al.* 2017, Dewachter *et al.* 2019).

Noise in gene expression: Due to the complexity of gene expression events in bacteria, in which plenty of activating factors and enzymes are involved, the resulting gene product titers are sensitive to stochastic fluctuations (Kœrn *et al.* 2005, Swain *et al.* 2002, Kiviet *et al.* 2014, Norman *et al.* 2015). They can be triggered by four different sources: (i) the inevitable stochasticity of biochemical processes that are dependent on certain molecular events, (ii) different internal states of cells in an isogenic population, (iii) subtle environmental differences each cell is experiencing or (iv) ongoing genetic mutations (Raser & O'Shea 2005).

Division of labour: This kind of strategy is based on a direct cell-to-cell interaction, which can be catalyzed via diffusible molecules. The idea is having a group of cells with phenotypes, which sacrifice their own fitness to improve the outcome of the remaining population. This can be exemplified during starvation phases of a cell population as some cells lyse and release important nutrients for a better survival of the residual cells (Heins & Weuster-Botz 2018, Norman *et al.* 2015).

3.3.2. Investigation of population heterogeneity in bioprocesses

Due to the increasing demand for a better mechanistic comprehension of population heterogeneity in bioprocesses, novel tools and sophisticated experimental setups have been advanced in recent years. Especially the importance of single-cell technologies was emphasized as a prerequisite to understand complex cell-to-cell and cell-to-environment interactions. Future studies will surely focus on further progression and development of the currently available technology in this field (Teichmann & Efremova 2020).

3.3.2.1. Omic technology

The most direct approach to analyze cellular characteristics is the utilization of omic technologies. It is a collective term for biological disciplines ending with the suffix -omics. For example, transcriptomics define the monitoring of expression levels of RNA molecules of a sample, while proteomics focus on the analysis of already expressed proteins inside the cells. Considering other existing fields in omic technologies, they all provide detailed information of complex biological processes of a microbial population at different stages. Thus, they support the general understanding of existing networks and further operational principles within the cells. Additionally, multimodal omics provide comprehensive molecular profiles and enlighten dynamic relationships based on direct quantitative correlations of certain molecules with their precursors and derivates. One example is the correlation of messenger RNA (mRNA) concentrations to the corresponding protein amount. Together with approaches to analyze one cell at a time, average masked data can be avoided. Hence, single-cell multimodal omics tools have a great potential to shed light on the sources, mechanisms and consequences of population heterogeneity in bioprocesses. Despite the bright future to come, it is worth mentioning that these tools are still limited in throughputs and suffer from high per-cell costs. Furthermore, experimental procedures of some omics disciplines struggle to distinguish noises from cell signals (Rinke *et al.* 2014, Zhu *et al.* 2020, He *et al.* 2020). Therefore, alternative approaches are necessary that allow reliable and fast detection of single-cell differences during bioprocesses.

3.3.2.2. Fluorescence proteins and reporter strains

Molecular groups harbouring aromatic compounds are capable of absorbing energy from light at specific wavelengths. This is based on the excitation of the electrons to lift them to an excited state. However, these high-energetic electrons are rather unstable and thus emit lower-energy as photons to return to their stable ground state after a short period of time. As a result, an optical signal emerges, which is called fluorescence. Each fluorescent molecule has its own distinct excitation and emission spectra dependent on

the characteristics of the containing chromophor group. Chromophors can occur in an isolated state, but are rather embedded in whole proteins called fluorescence proteins (Herman 1998, Cohen 2010, Wong *et al.* 2020).

Nowadays, fluorescent proteins are among the most used reporter molecules in research applications in the field of life sciences (Shaner *et al.* 2007). They can be expressed in almost any organism due to the easy access to genetic information of such reporter proteins that can be inserted into a host strains' genome or plasmid by genetic engineering. After transcription and translation processes as well as correct protein folding, fluorescent proteins undergo a maturation process for chromophor formation. The very first proposed reaction was reported by the group of Roger Tsien in 1994 and 1995, followed by new insights by Zhang *et al.* (2006).

Originally, *in vivo* maturation of a green fluorescent protein (GFP) in *E. coli* was proposed as an interaction between the three chromophore-forming residues Ser65, Tyr66 and Gly67 (serine, tyrosine and glycine at the positions 65, 66 and 67) and is initiated by a nucleophilic attack of the amide nitrogen (N) of Gly67 towards the carbonyl carbon (C) of Ser65. This cyclization reaction leads to a five-membered ring formation, followed by a loss of water (H_2O) during an oxidation reaction to form an imidazolin-5-one intermediate with a double bond between C65 and N66. To close the π-conjugation between the phenolic group with the imidazolin-5-one ring, the hydroxybenzyl side chain of Tyr66 gets oxidized, which leads to a double bond between $C_\alpha 66$ and $C_\beta 66$. It is proposed that atmospheric oxygen (O_2) is required for the final reaction, as it gets converted to hydrogen peroxide (H_2O_2). Therefore, Tsien and coworkers assumed full restrictions of *in vivo* maturation reactions of chromophors under anaerobic conditions. As a consequence, fluorescence signals do not evolve under such circumstances (Heim *et al.* 1994, Cubitt *et al.* 1995, Zhang *et al.* 2006). Zhang *et al.* (2006) reported an alternative pathway, in which the initial cyclization reaction remains the same and the backbone form a cyclic tetrahedral intermediate. In contrary to the assumptions of Tsien and co-workers, the ring is initially oxidized by molecular O_2 to form a cyclic imine and H_2O_2. Afterwards, the elimination of a hydroxyl group establishes the π-conjugated system under the formation of H_2O and leads to the maturated chromophore (Zhang *et al.* 2006). Despite the differences, both pathways rely on the presence of molecular O_2 and produce H_2O_2 in return. Normally, the maturation procedure endure in the double-digit minute range (Cubitt *et al.* 1995, Zhang *et al.* 2006). However, both reactions were never approved so that the exact mechanism is not clearly defined until now (Bartkiewicz *et al.* 2018).

With the ongoing advances in protein engineering and higher resolution of protein crystal structures, maturation times of fluorecent proteins can be shortened significantly. For example, Bevis & Glick (2002) engineered a DsRed variant by combination of random and directed mutagenesis steps to reduce the maturation time from 11 h to 0.71 h (Bevis & Glick 2002). Nowadays, plenty of fluorescent proteins are available with tailored characteristics to match specific research interests. They especially differ regarding the following aspects (Shaner *et al.* 2005):

Excitation and emission: The wavelength λ_{Ex} at which a fluorescent protein gets excitated the best and emits photons at the maximum wavelength λ_{Em} are the most decisive characteristics to consider. In fact, they have to be compatible with the given optical setup because any miscalculation can lead to either no excitation of the fluorescent proteins or no detection of the emitted photons. Fortunately, being capable of modifying the chromophor group has led to a plethora of different proteins with various fluorescence properties. This milestone arranged the simultaneous use of multiple reporter molecules with low overlapping emission signals (Shaner *et al.* 2004, Wang *et al.* 2004, Tsien 2009).

Brightness: From a physical point of view, brightness can be understood as the product of the molar absorption coefficient $\epsilon(\sigma)$ and the luminescence quantum yield $\Phi(\sigma)$. In practical terms however, the perceived brightness of a fluorescent protein is strongly dependent on various factors such as the maturation times, the extinction coefficient as well as the optical properties of the imaging setup including the laser configuration and the used detection filters. Consequently, this characteristic is rather relative than absolute (Shaner *et al.* 2005, Wong *et al.* 2020).

Photostability: Due to the extended exposure of fluorescent proteins to high-energy light sources, they suffer from photobleaching, which is concomitant with the progressive loss of fluorescence. Whether highly photostable proteins are preferred or not depends strongly on the research application. Similar to the brightness however, photostability measurements can strongly differ given the experimental setup and optical equipment (Lichtman & Conchello 2005, Shaner *et al.* 2005).

Oligomerization state: In most applications, fluorescent proteins with a monomeric state are preferred over higher oligmerization states. This is due to the higher tendency of dimeric or tetrameric reporter molecules to aggregate with other proteins, leading to the formation and accumulation of inclusion bodies (Shaner *et al.* 2005, Shemiakina *et al.* 2012).

Moreover, fluorescent proteins can be extended with certain tags. On the one hand, degradation tags can be inserted, which can be recognized by intracellular proteases. Different degradation tags have been successfully investigated to allow a faster and controllable protein degradation after a defined time (McGinness *et al.* 2006, Gur & Sauer 2009). On the other hand, the addition of fusion tags allow the precise and directed marking of specific proteins, tissues or other molecular structures. Together with a palette of fluorescent proteins exhibiting different colours, these reporter molecules remain superior in terms of visualization (Chalfie *et al.* 1994, Shaner *et al.* 2004, Tsien 2009). In addition, they can signalize the occurrence of certain chemical reactions or events such as the expression of specific genes of interest. The latter idea has already been implemented in so-called reporter strains that are mainly used for a better comprehension of population heterogeneity in bioprocesses. In detail, a synthetic copy of a reporter molecule is integrated into a certain genetic element of the host strains' genome or plasmid, which is associated to a specific cellular phenotype of interest. Assuming the expression of this genetic element based on a triggering event, cells start to develop this phenotype together with the expression of the integrated fluorescent protein. As a result, specific cellular traits of cells can be reflected by the expressed fluorescence signals at single-cell level. Furthermore, differences between single cells in a microbial population can be detected by disparities in expressed fluorescence intensities, thus allowing the unveiling of potential subpopulations during bioprocesses. The successful usage of reporter strains has already been proven in numerous studies. For example, Han *et al.* (2013) constructed an *E. coli* reporter strain for the monitoring of cell growth. This was achieved by integration of a synthetic copy of a destabilized GFP variant downstream the *rrnB* P1 and P2 promoter. As the *rrnB* promoters are activated during cell growth, the monitoring of expressed GFP molecules correlated with the increasing biomass amount (Han *et al.* 2013). There are also reporter strains for screening of the general stress response or even cells sensing extracellular pH (Garcia *et al.* 2009, Martinez *et al.* 2012). However, the potential of reporter strains can be maximized by integration of multiple reporter molecules into a host strain to monitor several cellular characteristics at the same time. Moreover, the fluorescent responses and the expressed phenotypes could be correlated to each other, which would tremendeously elevate the comprehension of possible cell-to-cell or cell-to-environment interactions (Hoang *et al.* 2023a, Heins *et al.* 2020). In contrary, it is important to bear potential drawbacks of genetic modifications such as the elevated genetic load as well as the increased metabolic burden due to additional expression of fluorescent proteins. Both can affect the cellular physiology and other key process parameters, for instance biomass yield and productivities (Ow *et al.* 2006, Liu *et al.* 2018b, Lozano Terol *et al.* 2021).

3.3.2.3. Microscopy and flow cytometry

To correctly visualize and evaluate the expressed fluorescences of reporter strains, optical systems are demanded. Their basic tasks include the excitation of the probe with an appropriate wavelength λ_{Ex} at sufficient energy levels, the collection of the emitted photons of the fluorescent proteins and the visualization of the gained data as an image. Microscopes are among those optical systems, which already existed in the 17th century. The basic elements of this apparatus comprise a light source with special lenses integrated in the condenser, the objective and the ocular. While the condenser fixates the light beam of a lamp to the specimen of interest, the objective and the ocular are mandatory for the magnification and correct visualization of the specimen for the naked human eyes (Singer 1914, Davidson & Abramowitz 2002). In comparison to the standard equipment of microscopes, fluorescence microscopes integrate further adjustable optical filters and dichroic mirrors. Filters at different positions inside the device ensure the transmission of exciting light at the correct wavelengths, whereas dichroic mirrors reflect the light at shorter wavelengths from the lamp to the specimen and transmit the emitted fluorescence signals from the excitated specimen back to the ocular or detector (Lichtman & Conchello 2005). Confocal microscopies even allow the optical sectioning of a specimen leading to high-contrast and high-resolution images. Together with a digital camera, spatio-temporal recordings of emerging intensities can be generated. Additionally, the advancing automatization and guidances of available softwares of digital cameras as well as the microscopes simplify the procedures and allow high-quality and reproducible imaging (Jonkman *et al.* 2020, Fazeli *et al.* 2020). Despite the impressive progress in the field of microscopies, they become impractial for high-throughput screening of large samples.

Similar to microscopes, flow cytometers can measure optical characteristics of a particle such as cells, as well. Known as a high-throughput platform, they allow quantitative measurements of thousands of events in seconds. This is realized by the three main components of this technology including the fluidic system, the optical system and the electronic network. The former enables the transport of particles of interest from the sample to the flow cell by pressurized air or pumps. Inside the flow cell, the particles are singulated by hydrodynamic focusing. By continuous injection of the sample stream into a surrounding sheath flow with a higher flow rate, the particles align into an isolated sequence of the resulting coaxial stream. This is mandatory to ensure a uniform illumination of each particle when they reach the optical system (Jaroszeski & Radcliff 1999, Adan *et al.* 2017, Reggeti & Bienzle 2011, Wilkerson 2012, Veal *et al.* 2000).
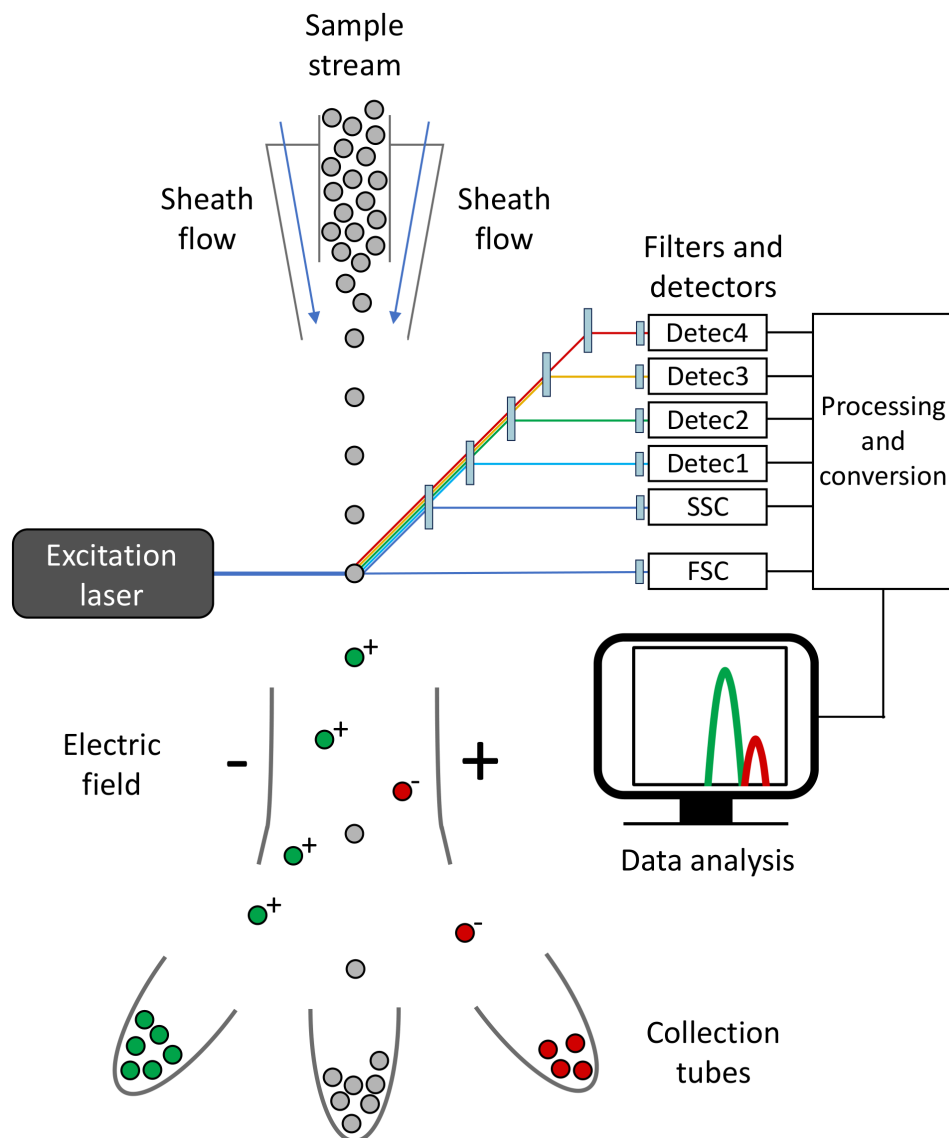
Figure 3.4: General work flow of a flow cytometer with sorting of particles. Particles in the sample stream are singulated by hydrodynamic focussing using sheath fluid. Each particle gets excited consecutively with a laser and the corresponding deflection of the light is monitored by a set of detectors equipped with a filter. These signals are amplified and converted to digital signals to visualize them for data analysis. Optionally, particles are sorted based on their optical characteristics using an electric field.

Flow cytometers are always equipped with at least one laser that is orthogonally positioned to the sample stream. Focused by an optical lens, they excite the singulated particles with high energy photons at a specific wavelength λ_{Ex}, in which the light gets deflected in different directions. The diffracted light along the same axis as the laser beam is called Forward scatter (FSC), whereas light scattered at an angle of around 90° to the laser beam is called Side scatter (SSC). Both provide important information regarding the cell-surface area and cell size (FSC) as well as the cell granularity and internal complexity (SSC). Each optical detector has their own filters and ensure the permanent monitoring

of scattered light at a specific wavelength range λ_{Em}. This also includes the potential emission of fluorescences of the particles. The energy of scattered lights and fluorescences are first converted to an electric current, followed by the transformation to a voltage pulse by either photodiodes or photomultiplier tubes (PMT). Finally, the analog signal of the obtained voltages are converted to the digital equivalent by the electronic network so that the acquired data can be plotted and evaluated (Figure 3.4, Jaroszeski & Radcliff 1999, Adan *et al.* 2017, Reggeti & Bienzle 2011, Wilkerson 2012, Veal *et al.* 2000).

Flow cytometry data are often visualized as histograms, which display a distribution of measured events exhibiting different intensities at a certain detection range. The x-axis is separated into bins ranging between specific, pre-determined intensity values. Based on the measured intensity of an event, it gets assigned to the respective bin. The smaller the bin range and the higher the bin numbers of an histogram, the higher the resolution of the data. An even more detailed display of flow cytometry data can be achieved with density plots, in which the distributions of two optical parameters of the measured events are plotted correlatively. The more events accumulate at a certain position, the more it gets highlighted in the plot by colour codes. Besides revealing potential subpopulations of a sample, coherences can be concluded between two optical signals (Herzenberg *et al.* 2006). To support the visual evaluation of population heterogeneity in bioprocesses, different values can be considered for the analysis, as well. For example, the coefficient of variance (CV) is a popular choice in many research studies (Heins *et al.* 2020, Hoang *et al.* 2023a, Hoang *et al.* 2023b), which is defined as the standard deviation divided by the mean of a distribution.

$$\text{Coefficient of variance} = \frac{\sigma}{\overline{x}} \tag{3.35}$$

σ	Standard deviation of a distribution	-
$\overline{x}$	Mean of a distribution	-

While the mean defines the average value of a sample by dividing the sum of all collected values with the sample number, the standard deviation indicates the level of variation of a measured sample. It is the square root of the variance.

$$\overline{x} = \frac{\sum x_i}{n} \tag{3.36}$$

x_i	Value of sample i	-
n	Total number of samples	-

$$\sigma = \sqrt{\frac{\sum (x_i - \overline{x})^2}{n - 1}} \tag{3.37}$$

While CV values close to 0 indicate a perfectly-narrow distribution of a homogeneous population, higher values indicate the exact opposite. Hence, this parameter can be exploited to find particularly broad histograms that reflect cells with deviating expression levels and cellular characteristics. Additionally, mean-to-median ratios (MMR) of measured samples proved to be an effective parameter for the identification of bimodal distributions. The median value marks the 50th percentile of a distribution, in which half of the events have values below and the other half above the median value. While a MMR of 1 represents an unimodal histogram, higher values indicate a strong shift between the mean and the median values, which is often applicable for a bimodal distribution. Bimodal distributions are generally a good indicator for the co-existence of two subpopulations (Delvigne *et al.* 2017).

$$\text{Mean-to-median ratio} = \frac{\overline{x}}{\widetilde{x}} \tag{3.38}$$

$\widetilde{x}$	Median of a distribution	-

The measured events can be further separated based on their optical characteristics. This specific approach in flow cytometry is called fluorescence-activated cell sorting (FACS). For this technique, the coaxial flow is transitioned to a stream of uniform droplets by a vibrating sorting nozzle integrated into the flow cell. In each droplet, a single particle gets isolated and flows through the laser. Based on its measured optical characteristics, the single droplet gets a positive or negative charge and enters an electrostatic field. Accordingly, it is deflected from the main stream and gets collected in a collection tube (Hodne & Weltzien 2015, Adan *et al.* 2017). Flow cytometry paired with the ability of sorting represents a great tool for the investigation of population heterogeneity in bioprocesses (Park *et al.* 2005, Miao *et al.* 2009). Not only it enables *at-line* monitoring of specific cellular phenotypes via fluorescences, but also the identification and sorting of possibly occurring subpopulations for further investigations such as transcriptomics or proteomics. Moreover, the detected signals can be correlated with each other, thus allow-

ing an in-depth analysis of complex coherences. With the upcoming trend for automated real-time flow cytometers, optical cell information can be permanently collected during bioprocesses at high throughputs. Additionally, there are already efforts to automate specific steps during the processing of flow cytometric measurements such as the data analysis or gating of certain events (Heins *et al.* 2022, Monaco *et al.* 2016, Yu *et al.* 2017, Sarkar *et al.* 2008).

3.3.3. Experimental simulation of industrial bioreactor conditions at laboratory scale

The anticipated omnipresence of population heterogeneity in bioprocesses is often investigated in specialized small-scale setups. These are designed to simulate dynamic environments and fluctuating conditions, which most likely occur in large-scale bioprocesses. Using such scale-down systems instead of directly investigating this phenomenon in industrial bioprocesses have the benefits of drastically saving resources, time and ultimately reducing the total capital expenses (Sweere *et al.* 1987). Moreover, large-scale bioreactors are not designed for the detailed monitoring and analysis of the prevailing spatio-temporal process conditions. In addition, these are generally not available for such studies, but are rather occupied for the large-scale production of bio-based goods (Noorman 2011, Chmiel & Weuster-Botz 2018).

Scale-down systems are rated on how precise they resemble and simulate the existing dynamic environmental conditions of large-scale bioprocesses at smaller scale. Although the experimental design of scale-down bioreactors are often supported by theoretical modeling approaches (Wei *et al.* 2023), still there is no ideal experimental setup that perfectly simulates the fluid dynamics. Instead, each system specializes on a specific hydrodynamic aspect, leading to a variety of scale-down approaches. Among them is the oscillated pulse-feeding in a continuous stirred-tank bioreactor or bioreactors with internal disks for inner compartmentalization (Figure 3.5, Heins *et al.* 2020, Gaugler *et al.* 2023, Simen *et al.* 2017, Neubauer & Junne 2016).

Of all the scale-down systems available, two-compartment devices are the most preferred choice for the simulation of dynamic environmental conditions. The idea is to provide two distinctive environments that cells alternately encounter for a certain duration by the permanent transfer of the cell suspension between both compartments. While one of them often represents a well-mixed environment with controlled process parameters, the other compartment is mainly exploited to simulate certain deviating process conditions. Based on the flexible design of the individual compartments, a wide range of process conditions

and gradients can be simulated and the corresponding metabolic responses of microbial populations can be investigated. Parameters of major interests are gradients of dissolved oxygen levels, pH or substrate concentrations (Limberg *et al.* 2016, Nieß *et al.* 2017, Cortés *et al.* 2016, Käß *et al.* 2014). Setups combining two stirred-tank bioreactors are particularly used for the simulation of complex gradients as they generate a high degree of backmixing. Consequently, the RTDs are rather broad, which lead to heterogeneous oscillations of the cells (Limberg *et al.* 2016). In contrast, the combination of a stirred-tank bioreactor with a tubular reactor as a bypass provides a narrow RTD. Under the assumption of an ideal flow regime within the tubular reactor with good radial mixing and poor axial dispersion (Bo > 100), gradients of a specific process parameter can be simulated in the bypass. The integration of multiple sampling ports along the tubular reactor enables the precise space-time resolution of occurring gradients and their impact on cellular physiologies (Limberg *et al.* 2016, Junne *et al.* 2011).
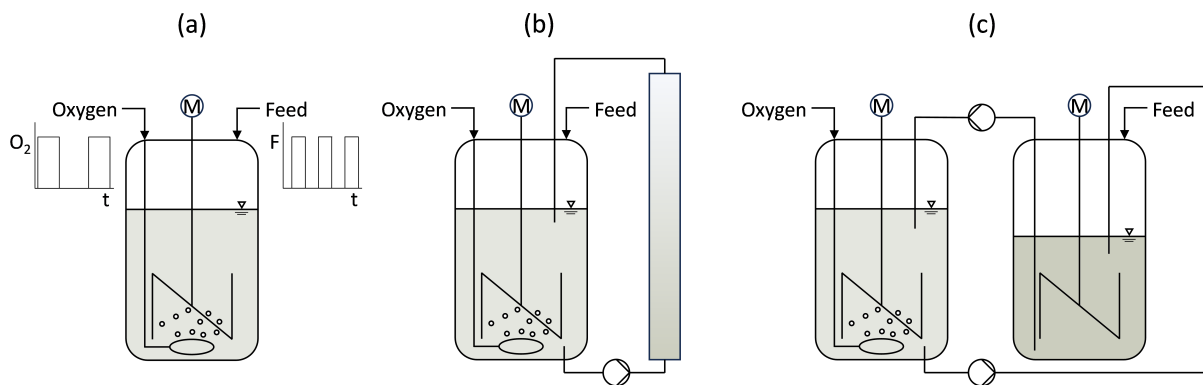
Figure 3.5: Selection of scale-down approaches used for the simulation of dynamic environmental conditions, as they occur in industrial bioprocesses, at small scale. (a) depicts a stirred-tank bioreactor operated as a continuous cultivation with oscillatory pulse-feeding. Two-compartment bioreactors are depicted in (b) and (c) combining a stirred-tank bioreactor with a tubular reactor or two stirred-tank bioreactors.

4. Material and methods

4.1. Chemicals, disposables and devices

The lists of all used chemicals, disposables and devices in this work can be found in the supplementary material (section A.1).

4.2. Media and buffers

In this work, complex and different chemically defined media and buffers were used for the cultivation and preparation of cells. If not stated otherwise, heat autoclavation of liquid solutions was done at 121 °C for 20 min. Filters used for the filtration of liquids always had a pore size of 0.22 µm. Aseptic works such as the filtration of liquids, the addition of sterile stock solutions to unfinished media and other transfer procedures were executed in a laminar flow cabinet (BDK Klasse 1, Luft- und Reinraumtechnik GmbH, Germany).

Stocks, titrating agents and antibiotics
Concentrated stock solutions of single chemical components were prepared to complete media and buffers. A list of all stock solutions is given in Table 4.1. Futhermore, the here used trace element solution 1 for the chemically defined minimal medium consisted of 10 g L^{-1} aluminium chloride hexahydrate, 0.5 g L^{-1} boric acid, 7.33 g L^{-1} cobalt(II) chloride hexahydrate, 1 g L^{-1} copper(II) chloride dihydrate, 11.2 g L^{-1} manganese(II) sulfate monohydrate, 2 g L^{-1} sodium molybdate dihydrate and 2 g L^{-1} zinc sulfate heptahydrate. Due to poor solubility of some components, hydrochloric acid (HCl, 3 M) was added until complete dissolvation of all components. The trace element solution 1 was filtrated and stored at 4 °C (see Table 4.2).

Table 4.1: Concentrated stock solutions, titrating agents and antibiotics with their concentration and the sterilization method.

Stock solution	Concentration	Sterilization method
Calcium chloride dihydrate	15 g L^{-1}	Filtration
Iron(II) sulfate heptahydrate dissolved in tri-sodium citrate dihydrate	22.5 and 300 g L^{-1}	Filtration
Magnesium sulfate heptahydrate	250 or 300 g L^{-1}	Filtration
Thiamine hydrochloride	7.5 or 337.3 g L^{-1}	Filtration
L-phenylalanine	10 g L^{-1}	Filtration
L-tyrosine*	15 g L^{-1}	Filtration
Ammonium sulfate	400 g L^{-1}	Filtration
Diammonium phosphate	400 g L^{-1}	Filtration
Glucose	180 or 500 g L^{-1}	Filtration
Glycerol	1000 g L^{-1}	Heat autoclavation
Ampicillin	100 g L^{-1}	Filtration
Kanamycin	50 g L^{-1}	Filtration
IPTG	0.3 mol L^{-1}	Filtration
Acetic acid	20%	not sterilized
Ammonia	25%	not sterilized
Hydrochloric acid (HCl)	3 mol L^{-1}	not sterilized
Potassium hydroxide (KOH)	5 mol L^{-1}	not sterilized
Sodium hydroxide (NaOH)	5 mol L^{-1}	not sterilized

* titrated with KOH (5 M) for dissolvation

Table 4.2: Components of the trace element solution 1. HCl (3 M) was added until complete dissolvation of all components. The solution was filtrated and stored at 4 °C.

Component	Chemical formula	Concentration, g L^{-1}
Aluminium chloride hexahydrate	$AlCl_3 \cdot 6\ H_2O$	10
Boric acid	H_3BO_3	0.5
Cobalt(II) chloride hexahydrate	$CoCl_2 \cdot 6\ H_2O$	7.33
Copper(II) chloride dihydrate	$CuCl_2 \cdot 2\ H_2O$	1
Manganese(II) sulfate monohydrate	$MnSO_4 \cdot H_2O$	11.2
Sodium molybdate dihydrate	$Na_2MoO_4 \cdot 2\ H_2O$	2
Zinc sulfate heptahydrate	$ZnSO_4 \cdot 7\ H_2O$	2

Lysogeny broth medium

Complex lysogeny broth (LB) medium was prepared by dissolving 10 g L^{-1} of peptone, 5 g L^{-1} of yeast extract and 10 g L^{-1} of sodium chloride in de-ionized water (diH$_2$O). The pH value was adjusted to 7.0 by adding sodium hydroxide (NaOH, 5 M). Then, the cultivation medium was filled up to the final volume and heat autoclaved. LB agar plates were prepared by addition of 20 g L^{-1} agar prior to heat sterilization (see Table 4.3). After autoclavation, the LB agar solution was cooled down to approximately 60 °C followed by the optional addition of antibiotics (0.05 g L^{-1} kanamycin or 0.1 g L^{-1} ampicillin) and immediate pouring into petri dishes under aseptic conditions. The solidified plates were stored at 4 °C until usage.

Table 4.3: Components of the complex lysogeny broth (LB) medium for cultivation of cells. The pH value of the medium was adjusted to 7.0 with NaOH (5 M) prior to heat sterilization.

Component	Chemical formula	Concentration, g L^{-1}
Peptone	-	10
Yeast extract	-	5
Sodium chloride	NaCl	10
Agar[*]	C$_{14}$H$_{24}$O$_9$	20

[*] only added for LB agar

Super optimal broth with catabolite repression (SOC medium)

This nutritionally rich culture medium is also a complex medium, which is especially used after bacterial cell transformations. It contained 20 g L^{-1} peptone, 10 g L^{-1} yeast extract, 0.584 g L^{-1} sodium chloride and 0.186 g L^{-1} potassium chloride, which were dissolved in diH$_2$O and the pH value was adjusted to 7.0 with NaOH (5 M). After heat sterilization, the suspension was cooled down and stocks of 300 g L^{-1} magnesium sulfate heptahydrate and 180 g L^{-1} glucose were added to a final concentration of 4.9 g L^{-1} and 3.6 g L^{-1}, respectively. This complex medium was completed by addition of sterile diH$_2$O to its final volume (see Table 4.4)

Table 4.4: Components of the super optimal broth with catabolite repression (SOC). The pH value of the medium was adjusted to 7.0 with NaOH (5 M) prior to heat sterilization. Stocks of magnesium sulfate heptahydrate and glucose were added thereafter.

Component	Chemical formula	Concentration, g L^{-1}
Peptone	-	10
Yeast extract	-	5
Sodium chloride	NaCl	0.584
Potassium chloride	KCl	20
Magnesium sulfate heptahydrate	MgSO$_4$ · 7 H$_2$O	4.9
Glucose	C$_6$H$_{12}$O$_6$	3.6

Chemically defined minimal medium

The chemically defined minimal medium is based on the works of Albermann *et al.* (2008) and Gottlieb *et al.* (2014). First, a basic solution was prepared by mixing 5 g L^{-1} ammonium sulfate, 3 g L^{-1} monopotassium phosphate, 12 g L^{-1} dipotassium phosphate and 0.1 g L^{-1} sodium chloride in diH$_2$O. The pH value was adjusted to 7.0 with hydrochloric acid (HCl, 3 M). After heat sterilization, 1 mL L^{-1} calcium chloride dihydrate (15 g L^{-1}), 5 mL L^{-1} iron(II) sulfate heptahydrate (22.5 g L^{-1}), 1 mL L^{-1} magnesium sulfate heptahydrate (300 g L^{-1}), 1 mL L^{-1} thiamine hydrochloride (7.5 g L^{-1}), 7.5 mL L^{-1} L-phenylalanine (10 g L^{-1}) and 5 mL L^{-1} L-tyrosine (15 g L^{-1}) were added to the basic solution. Minimal medium assigned for the preliminary cultivation in shake flasks were enriched with 7 mL L^{-1} glycerol (1000 g L^{-1}), whereas the minimal medium for stirred-tank or two-compartment bioreactor cultivations was enriched with 4 mL L^{-1} glycerol (1000 g L^{-1}) and 1 mL L^{-1} trace element solution 1. After addition of all chemical components, the medium was complemented with sterile diH$_2$O to the final volume.

Agar plates of this chemically defined medium were prepared by the separate heat sterilization of an agar solution (20 g L^{-1}) and the basic minimal medium solution. After cooling to about 60 °C, all stocks were added as described for minimal medium for the preliminary cultivation. The minimal medium solution was complemented with diH$_2$O to its final volume and mixed together with the agar solution. Subsequently to the addition of antibiotics (0.05 g L^{-1} kanamycin), the liquid minimal medium agar solution was poured into petri dishes and these were stored at 4 °C after solidification (see Table 4.5).

Table 4.5: Components of the chemically defined minimal medium for the cultivation of cells. The pH value of the medium was adjusted to 7.0 with HCl (3 M) prior to heat sterilization. The formulation is based on Albermann *et al.* (2008) and Gottlieb *et al.* (2014).

Component	Chemical formula	Concentration, g L^{-1}
Ammonium sulfate	$(NH_4)_2SO_4$	5
Monopotassium phosphate	KH_2PO_4	3
Dipotassium phosphate	K_2HPO_4	12
Sodium chloride	NaCl	0.1
Calcium chloride dihydrate	$CaCl_2 \cdot 2H_2O$	0.015
Iron(II) sulfate heptahydrate	$Fe(II)SO_4 \cdot 7H_2O$	0.1125
Magnesium sulfate heptahydrate	$MgSO_4 \cdot 7H_2O$	0.3
Thiamine hydrochloride	$C_{12}H_{17}ClN_4OS \cdot HCl$	0.0075
L-phenylalanine	$C_9H_{11}NO_2$	0.1
L-tyrosine	$C_9H_{11}NO_3$	0.075
Glycerol	$C_3H_8O_3$	7 or 4*
Trace element solution 1*	-	1 mL L^{-1}

* only added for minimal medium for bioreactor cultivation

Feed media

The L-phenylalanine production processes in bioreactors were conducted as fed-batch processes. Therefore, three different feed media were prepared based on Weiner *et al.* (2014a). Feed medium 1 and 2 contained 120 g L^{-1} and 400 g L^{-1} glycerol, 2.5 g L^{-1} and 1.11 g L^{-1} L-phenylalanine, 3.6 g L^{-1} and 3.8 g L^{-1} L-tyrosine and 60 g L^{-1} and 25 g L^{-1} ammonium sulfate, respectively. While the former was titrated with ammonia (25%), potassium hydroxide (KOH, 5 M) was added to the latter until complete dissolvation of L-tyrosine. Sterile diH$_2$O was added up to the final volume. In contrary, feed medium 3 had no amino acids, but only 800 g L^{-1} glycerol, 8 g L^{-1} ammonium sulfate and 8 g L^{-1} diammonium phosphate. This medium was complemented with the basic minimal medium stock (no glycerol and no amino acids) to its final volume. Kanamycin was added to all three feed media to a final concentration of 0.1 g L^{-1} (Table 4.6).

Table 4.6: Feed media used in fed-batch processes for the L-phenylalanine production in bioreactors based on Weiner *et al.* (2014a). Ammonia (25%) and KOH (5 M) were added to the feed media 1 and 2 for complete dissolution of L-tyrosine. Additionally, both media were complemented with sterile diH$_2$O to their final volume, whereas feed medium 3 was supplemented with the basic minimal medium containing no glycerol and no amino acids.

Component	Feed 1*, g L^{-1}	Feed 2**, g L^{-1}	Feed 3, g L^{-1}
Glycerol	120	400	800
L-phenylalanine	2.5	1.11	-
L-tyrosine	3.6	3.8	-
Ammonium sulfate	60	25	8
Diammonium phosphate	-	-	8
Kanamycin	0.1	0.1	0.1

* titrated with ammonia (25%)

** titrated with KOH (5 M)

Defined minimal medium according to Riesenberg

Another chemically defined medium used in this work is the Riesenberg medium (Riesenberg *et al.* 1991). It was prepared by dissolving 13.3 g L^{-1} monopotassium phosphate, 4 g L^{-1} diammonium phosphate and 1.7 g L^{-1} citric acid in diH$_2$O. The pH of this solution was adjusted to 6.7 using KOH (5 M). After heat sterilization and cooling to room temperature, 0.48 mL L^{-1} magnesium sulphate heptahydrate (250 g L^{-1}), 0.4 mL L^{-1} glucose (500 g L^{-1}), 0.11 mL L^{-1} thiamine hydrochloride (337.3 g L^{-1}) and 2 mL L^{-1} of the trace element solution 2 containing 0.15 g L^{-1} boric acid, 0.125 g L^{-1} cobalt(II) chloride hexahydrate, 0.075 g L^{-1} copper(II) chloride dihydrate, 0.42 g L^{-1} ethylenediaminetetraacetic acid, 3 g L^{-1} iron(III) citrate, 0.75 g L^{-1} manganese(II) chloride dihydrate, 0.125 g L^{-1} sodium molybdate dihydrate and 4 g L^{-1} zinc acetate dihydrate. The trace element solution 2 was filtrated and stored at 4 °C. Prior to cultivation of *E. coli* cells, the Riesenberg medium was enriched with 0.05 g L^{-1} kanamycin. The compositions of the Riesenberg medium and the corresponding trace element solution 2 are summarized in Table 4.7 and 4.8.

Table 4.7: Components of the chemically defined Riesenberg medium for the cultivation of cells (Riesenberg *et al.* 1991). The pH value of the medium was adjusted to 6.7 with KOH (5 M) prior to heat sterilization.

Component	Chemical formula	Concentration, g L^{-1}
Monopotassium phosphate	KH_2PO_4	13.3
Diammonium phsophate	$(NH_4)_2HPO_4$	4
Citric acid monohydrate	$C_6H_8O_7 \cdot H_2O$	1.86
Magnesium sulfate heptahydrate	$MgSO_4 \cdot 7\ H_2O$	1.2
Glucose monohydrate	$C_6H_{12}O_6 \cdot H_2O$	2.2
Thiamine hydrochloride	$C_{12}H_{17}ClN_4OS \cdot HCl$	0.38
Trace element solution 2	-	12 mL L^{-1}

Table 4.8: Components of the trace element solution 2. The solution was filtrated and stored at 4 °C.

Component	Chemical formula	Concentration, g L^{-1}
Boric acid	H_3BO_3	0.15
Cobalt(II) chloride hexahydrate	$CoCl_2 \cdot 6\ H_2O$	0.125
Copper(II) chloride dihydrate	$CuCl_2 \cdot 2\ H_2O$	0.075
Ethylenediaminetetraacetic acid	$C_{10}H_{16}N_2O_8$	0.42
Iron(III) citrate	$FeC_6H_5O_7$	3
Manganese(II) chloride tetrahydrate	$MnCl_2 \cdot 4H_2O$	0.75
Sodium molybdate dihydrate	$Na_2MoO_4 \cdot 2\ H_2O$	0.125
Zinc acetate dihydrate	$Zn(CH_3COO)_2 \cdot 2\ H_2O$	2

Phosphate-buffered saline (PBS)

For the short preservation or dilution of cellular suspensions, a phosphate-buffered saline (PBS) solution was used to provide a non-toxic environment with essential ions and a neutral pH. A 10x concentrated PBS solution was prepared by mixing 2 g L^{-1} potassium chloride, 2.4 g L^{-1} monopotassium phosphate, 80 g L^{-1} sodium chloride and 14.4 g L^{-1} disodium phosphate in diH$_2$O (Table 4.9). For usage, the stock solution was diluted with diH$_2$O to a 1x PBS solution. If sterilization was necessary, both heat autoclavation and filtration were used.

Table 4.9: Components of a 10x concentrated phosphate-buffered saline (PBS) solution. Prior to usage, the solution was diluted with diH_2O to a 1x concentrated buffer solution.

Component	Chemical formula	Concentration, g L^{-1}
Potassium chloride	KCl	2
Monopotassium phosphate	KH_2PO_4	2.4
Sodium chloride	NaCl	80
Disodium phosphate	Na_2HPO_4	14.4

Transformation buffer to prepare rubidium chloride competent cells

For the preparation of rubidium chloride competent cells, two transformation buffers (Tfb I and Tfb II) were used in this work. Tfb I was a mixture of 2.95 g L^{-1} potassium acetate, 12.1 g L^{-1} rubidium chloride, 1.45 g L^{-1} calcium chloride, 10 g L^{-1} manganese(II) chloride tetrahydrate and 315 g L^{-1} glycerol with an adjusted pH value of 5.8 by titration of acetic acid (20%). On the other hand, Tfb II was prepared by dissolving 2.1 g L^{-1} 3-(*N*-morpholino)propanesulfonic acid (MOPS), 1.2 g L^{-1} rubidium chloride, 11 g L^{-1} calcium chloride and 315 g L^{-1} glycerol in diH_2O. The pH value of Tfb II was adjusted with NaOH (5 M) to 6.5. After both solutions were complemented with diH_2O to their respective final volume, they were filtrated and stored at 4 °C until usage. Table 4.10 and 4.11 summarize the components of the transformation buffers.

Table 4.10: Components of the first transformation buffer (Tfb I) to prepare rubidium chloride competent cells. The pH value was adjusted to 5.8 using an acetic acid solution (20%). This buffer was filtrated and stored at 4 °C.

Component	Chemical formula	Concentration, g L^{-1}
Potassium acetate	CH_3COOK	2.95
Rubidium chloride	RbCl	12.1
Calcium chloride	$CaCl_2$	1.45
Manganese(II) chloride tetrahydrate	$Mn(II)Cl_2 \cdot 4\ H_2O$	10
Glycerol	$C_3H_8O_3$	315

Table 4.11: Components of the second transformation buffer (Tfb II) to prepare rubidium chloride competent cells. The pH value was adjusted to 6.5 using NaOH (5 M). This buffer was filtrated and stored at 4 °C.

Component	Chemical formula	Concentration, g L^{-1}
3-(N-morpholino)propanesulfonic acid (MOPS)	$C_7H_{15}NO_4S$	2.1
Rubidium chloride	RbCl	1.2
Calcium chloride	$CaCl_2$	11
Glycerol	$C_3H_8O_3$	315

4.3. Strains and cryopreservation

Escherichia coli FUS4 is a well-described strain characterized by Gottlieb *et al.* (2014) and Weiner *et al.* (2016). It is a derivative of the *E. coli* K-12 strain with genomic deletions of the *pheA*, *tyrA* and *aroF* genes encoding for a bifunctional chorismate mutase / prephenate dehydratase, a T-protein and a phospho-2-dehydro-3-deoxyheptonate aldolase along the aromatic acid biosynthesis. Additionally, the *lacIZYA* genes (lactose operon repressor, β galactoside, lactose permease and galactose-6-phosphate isomerase subunit) were replaced by an *aroFBL* gene cluster under the control of a tac promoter. By transformation of the pF81$_{kan}$ plasmid (derived from pJF119EH), cells received a kanamycin resistance. Moreover, this plasmid encodes for the *aroF*, *pheA*, *aroB* (3-dehydroquinate synthase) and *aroL* (shikimate kinase 2) genes under the control of the same tac promoter to enable the IPTG inducible L-phenylalanine synthesis (Gottlieb *et al.* 2014, Weiner *et al.* 2014a, Weiner *et al.* 2014b, Weiner *et al.* 2016).

Based on this strain, two reporter strains were engineered by the integration of synthetic copies of fluorescent proteins into specific genetic elements of the host strains' genome or plasmid. In a first round of genetic modifications, the synthetic copies of the three fluorescent proteins mTagBFP2, mEmerald and CyOFP1 were inserted into the genome of the *E. coli* FUS4 strain by a series of knock-in recombination reactions using the λ-red and Flp/FRT mediated recombination system (Zhang *et al.* 1998b). A synthetic cassette with a monocopy of mTagBFP2 was integrated downstream the *rpoS* gene with a ribosome binding site (RBS) 5'-AAAGAGGAGAAA-3' derived from Elowitz & Leibler (2000). The synthetic cassettes with monocopies of mEmerald and CyOFP1 had the same RBS. While the former was inserted into a synthetic *rrnB* promoter complex, which replaced the native *rhaB* and *rhaS* genes (rhamnose operon), the latter was integrated into the *narGHIJ* gene cluster downstream all native genes. These genetic modifications led to an *E. coli* triple

reporter strain (3RP) that was established in cooperation with Gen-H (Gen-H Genetic Engineering Heidelberg GmbH, Germany, Hoang *et al.* 2023a).

Table 4.12: All strains used in this work with information of their genotypes and the corresponding selection marker. Additionally, the used plasmids are listed with their genetic information and their selection marker.

Strain name	Genotyp	Selection marker
E. coli FUS4	$\Delta pheA$-$tyrA$-$aroF$, $\Delta lacIZYA$	None
E. coli FUS4 pF81$_{kan}$	$\Delta pheA$-$tyrA$-$aroF$, $\Delta lacIZYA$, pF81$_{kan}$	Kanamycin
E. coli FUS4 3RP	$\Delta pheA$-$tyrA$-$aroF$, $\Delta lacIZYA$, $\Delta rhaS$-$rhaB$, $rpoS$::$mTagBFP2$, $rrnB$::$mEmerald$, $narGHIJ$::$CyOFP1$, pF81$_{kan}$	Kanamycin
E. coli FUS4 4RP	$\Delta pheA$-$tyrA$-$aroF$, $\Delta lacIZYA$, $\Delta rhaS$-$rhaB$, $rpoS$::$mTagBFP2$, $rrnB$::$mEmerald$, $narGHIJ$::$CyOFP1$, pF81$_{kan, mod}$	Kanamycin
E. coli DH5 α pJL1[*]	pJL1	Kanamycin
E. coli BL21 pF81$_{kan, mod}$	pF81$_{kan, mod}$	Kanamycin
E. coli BL21 (DE3) pET28a	pET28a	Kanamycin
E. coli DH5 α pNCS1[**]	pNCS1	Ampicillin
E. coli DH5 α pNCS2[***]	pNCS2	Kanamycin

Plasmid name	Genotyp	Selection marker
pF81$_{kan}$	P_{tac}::$aroF$, $pheA^{fbr}$, $aroB$, $aroL$	Kanamycin
pF81$_{kan, mod}$	P_{tac}::$aroF$, $pheA^{fbr}$, $aroB$, $aroL$, $mCardinal2$	Kanamycin
pJL1	P_{T7}::$mTagBFP2$	Kanamycin
pET28a	P_{T7}::$eGFP$	Kanamycin
pNCS1	P_{T7}::$CyOFP1$	Ampicillin
pNCS2	P_{T7}::$mCardinal2$	Ampicillin

[*] provided by Michael Jewett via Addgene (item number 102638, Stark *et al.* 2018)

[**] provided by Michael Lin via Addgene (item number 74278, Chu *et al.* 2016)

[***] provided by Michael Lin via Addgene (item number 52631, Chu *et al.* 2014)

Furthermore, a synthetic copy of a far-red fluorescent protein mCardinal2 was inserted

into the pF81$_{kan}$ by a series of amplification, restriction and assembly reactions. A detailed description on the engineering and establishment of the *E. coli* quadruple reporter strain can be found in section 5.4 (Hoang *et al.* 2023b).

Moreover, other *E. coli* strains holding the genetic information of a single fluorescence protein on their plasmid were used for preliminary experiments. These were provided by Michael Jewett and Michael Lin via Addgene (item numbers 102638, 74278 and 52631). All strains used in this work are summarized in Table 4.12.

For the long-term storage of the strains, a single colony grown on LB agar plates was picked and cultivated in 100 mL of liquid LB medium at 37 °C and 250 rpm in 500 mL shake flasks. Cells were harvested during the early exponential growth phase with an optical density at 600 nm (OD$_{600}$) between 0.8 to 1.0. They were mixed with a sterile glycerol solution (60%) in a ratio of 2:1 into a 1.5 mL microcentrifuge tube with safelock. Finally, the cells were then stored at -80 °C until usage.

4.4. Genetic engineering

The pF81$_{kan}$ plasmid was modified using various methods such as amplification, restriction and assembly of specific gene fragments. The planning of gene modification strategies, the design of primers and other gene fragment analysis were done with Benchling (Benchling Inc., USA). Sanger sequencing of DNA samples were assigned to Genewiz (Azenta Life Sciences, USA). The received sequencing files were checked with the BioEdit Sequence Alignment Editor (Version 7.0.5.3).

Polymerase chain reaction
The polymerase chain reaction (PCR) is a standard method for the amplification of specific gene fragments. PCRs were initiated by preparation of a mastermix in a 0.2 mL PCR tube (thin-walled) with a Q5 polymerase solution (2000 U mL^{-1}), the corresponding Q5 reaction buffer, a dNTP mix (10 mM of each base), forward and reverse primer (10 µM each) and the gene template containing at least 20 ng of the fragment of interest. The mastermix was complemented with sterile diH$_2$O (DNAse-free and RNAse-free) to a final volume of 50 µL and was placed into a thermocycler (Labcycler 48, Sensoquest GmbH, Germany). At the beginning of the PCR, the samples were heated to 98 °C for 30 s (phase 1) once. Afterwards, phase 2 was initiated that included the three steps of denaturation at 98 °C for 10 s, annealing with varying temperatures and durations based on the used primers and elongation at 72 °C for 20 s. The annealing temperature and duration were calculated

with the NEB Tm Calculator. Typically, 35 cycles were set for phase 2. At the end, the temperature was set to 72 °C for 120 s (phase 3) once. Afterwards, the samples were cooled down to 4 °C in phase 4 until further processing (Table 4.13).

Table 4.13: Phases and specifications of the polymerase chain reactions conducted in this work. In step two of phase 2, the variable temperature and duration were calculated with the NEB Tm Calculator based on the used primers.

Phase	Cycles	Temperature, °C	Duration, s
1	1	98	30
2	35	98	10
		variable	variable
		72	20
3	1	72	120
4	1	4	∞

Agarose gel electrophoresis

Agarose gels were prepared by dissolving 1% agarose (w/v) in 100 mL of a tris base, acetic acid and ethylenediaminetetraacetic acid buffer solution (1x TAE). To facilitate this step, the mixture was heated in a microwave (MW 781, Clatronic, Germany). Evaporated liquid was compensated by the addition of diH$_2$O. After complete dissolvation, the mixture was cooled down in a water bath for around 2 min and 15 µL of Midori Green was added and homogenized. The agarose solution was then poured into a gel tray (GCT-10-111, C.B.S. Scientific) and a comb with 18 pockets (MBU-1518, C.B.S. Scientific) was inserted into the liquid solution. After solidification of the gel, which took at least 30 min at room temperature, the gel tray was placed into an electrophoresis chamber (MGU-402T, C.B.S. Scientific) filled with 1x TAE. The comb was then removed and the pockets were filled with either DNA ladder samples or loading samples with volumes between 5 µL to 20 µL. All loading samples were prepared by mixing with a 6x concentrated gel loading dye without sodium dodecyl sulfate (SDS, purple) at a ratio of 5:1. After the pockets were filled with samples, the lid was placed on the electrophoresis chamber and the poles were connected to a power source (peqpower 300, Peqlab Biotechnologie GmbH, Germany). Agarose gel electrophoresis was carried out for at least 1 h at a voltage and current of 110 V and 500 mA. After successful DNA separation, the agarose gel was further analyzed using the Gel iX Imager (Intas Science Imaging Instruments GmbH, Germany). This gel analyzing chamber had an ultraviolet (UV) mode to visualize the DNA bands on the gel. Pictures were taken with a Canon EOS 80D (Japan) using the EOS Utility program (Version 3, Canon, Japan) and post-processing of the images were done with the Digital Photo Professional software (Version 4, Canon, Japan).

Restriction and digestion reactions

Single restriction reactions were necessary to open the $pF81_{kan}$ plasmid. By preparation of a mastermix containing 1 µL of HindIII high fidelity (HF), 5 µL of a CutSmart buffer (10x), 5 µL of the $pF81_{kan}$ plasmid (271.4 ng µL^{-1}) and 39 µL of sterile diH_2O (DNAse-free, RNAse-free), the restriction was held at 37 °C for 3 h in a thermoshaker (Thermomixer comfort, Eppendorf SE, Germany) without shaking. The digestion of gene fragments was initated by adding 2 µL of DpnI into 45 µL of samples. The reaction was executed at 37 °C for 30 min with no shaking.

Kits for purification of gene fragments and plasmids

Plasmid DNA of cells were purified using the QIAprep® Spin Miniprep Kit (Qiagen N.V., The Netherlands). All instructions regarding the buffer and sample preparation and handling were followed according to the manual. The used RNAse A (AppliChem GmbH, Germany) had an activity of 151.5 U mg^{-1}. All obtained gene fragments after restriction, digestion or agarose gel electrophoresis were purified with the Monarch® PCR & DNA Cleanup Kit or DNA Gel Extraction Kit (New England Biolabs, USA).

Gibson assembly

After preparation and purification of all gene fragments, they were fused by a Gibson assembly reaction. First, a mastermix was prepared by adding all the complementary gene fragments and 10 µL of a 2x concentrated HiFi DNA assembly master mix (New England Biolabs, USA). Sterile diH_2O (DNAse-free and RNAse-free) was added to a final volume of 20 µL. The assembly reaction was conducted in a thermocycler at 50 °C for 4 h with no shaking. Afterwards, the samples were cooled to 4 °C until further processing. If not immediately used, the samples were stored at -20 °C.

Transformation in chemically competent cells

One approach to make cells competent for plasmid uptake is the rubidium chloride method. First, cryopreserved cells were streaked on a LB agar plate and were incubated at 37 °C overnight. In the next day, a single colony was picked of the incubated LB agar plate and was resuspended in 10 mL of LB medium in a 100 mL shake flask, which was then cultivated at 37 °C and 150 rpm in an orbital shaker (Multitron, Infors HT, Switzerland) overnight. The density of the cell suspension was then measured by determination of the optical density at 600 nm (OD_{600}, Genesys 10UV, Thermo Fisher Scientific, USA) to inoculate a 500 mL shake flask with 100 mL of LB medium at a starting OD_{600} of 0.01. After the OD_{600} of this cell suspension increased to 0.4 to 0.6, cells were harvested and centrifuged at 4 °C and 3200xg for 10 min. The supernatant was discarded and the

cell pellet was resuspended with a pre-cooled Tfb I buffer. After 15 min of incubation on ice, the cell suspension was centrifuged a second time at 4 °C and 3200xg for 10 min. Again, the supernatant was discarded, the cell pellet was resuspended with a pre-cooled Tfb II buffer and was incubated on ice for 15 min. 200 µL of chemically competent cells were then aliquoted in 1.5 mL microcentrifuge tubes with safelock and were immediately stored at -80 °C.

To initiate the transformation, competent cells were thawed on ice together with the plasmid of interest for a minimum duration of 30 min. Then, at least 20 ng of plasmid DNA was added to the cell suspension. After gentle mixing, the sample was incubated on ice for further 30 min. Afterwards, heat shock of the cells was induced in a water bath (ME, Julabo GmbH, Germany) at 42 °C for 45 s. Directly after, the cells were stored on ice for 2 min to 5 min. 800 µL of SOC medium was added to the cell suspension and it was incubated at 37 °C and 700 rpm in a thermoshaker. After 1 h, the cell suspension was streaked on a LB agar plate enriched with 0.05 g L^{-1} kanamycin and was incubated at 37 °C overnight.

Transformation in electrocompetent cells
Another way for the bacterial uptake of plasmid DNA is the electroporation. Fresh cell material was provided by picking a single colony of a LB agar plate and a two-stage shake flask cultivation as described in the previous section. The cells were harvested after reaching an OD_{600} of 0.5 to 0.7 by direct cooling of the whole 500 mL shake flask on ice for 15 min. The cell suspension was then aliquoted in two 50 mL centrifuge tubes and both were centrifuged at 4 °C and 2129xg for 15 min. After discarding the supernatant, each cell pellet was resuspended with 50 mL of a pre-cooled 10% glycerol solution and was stored on ice for 15 min. Then, the cell suspension was centrifuged a second time at 4 °C and 2129xg for 15 min. The previous steps were repeated twice with addition of 25 mL and 4 mL of a pre-cooled 10% glycerol solution. The final cell pellets were then resuspended in 1.5 mL of a pre-cooled 10% glycerol solution and aliquots of 40 µL of electrocompetent cells were prepared in 1.5 mL microcentrifuge tubes with safelock. These were directly stored at -80 °C.

The electroporation was initiated by thawing competent cells and the plasmid of interest on ice for a minimum of 30 min. At least 20 ng of the plasmid DNA was then pipetted into the cell suspension and was incubated on ice for further 30 min. Afterwards, the mixture was transferred into a pre-cooled electroporation cuvette (1 mm gap, Biozym Biotech Trading GmbH, Germany) and the electroporation was executed using the Gene

Pulser Xcell™ (Bio-Rad Laboratories Inc., USA) at a voltage of 1800 V, a capacitance of 25 µF and a resistance of 200 Ω. Directly after the electric shock, 950 µL of SOC medium was added into the cuvette and the cell suspension was then transferred into a 1.5 mL microcentrifuge tube with safelock. The electroporated cells were incubated at 37 °C and 700 rpm for around 1 h, after which they were streaked on LB agar plates enriched with 0.05 g L^{-1} kanamycin. The streaked plates were incubated at 37 °C overnight.

Colony PCR

The colony PCR is a preliminary screening method to check whether the conducted gene modification succeeded. Basically, it is a PCR reaction, in which colonies grown on LB agar plates of freshly transformed cells can be used as the starting material. In this instance, OneTaq polymerases were used instead of Q5 polymerases. The mastermix was prepared by mixing 1 µL of forward and reverse primer (10 µM each), a 2x concentrated OneTaq® Hot Start Quick-Load® Master Mix (New Englands Biolabs, USA) and cells of a single colony of freshly transformed cells on agar plates into a 0.2 mL PCR tube (thin-walled). Sterile diH$_2$O (DNAse-free and RNAse-free) was then added to reach a final volume of 25 µL. The PCR was conducted in a thermocycler with a program consisting out of four phases. Phase 1 heated the samples to 94 °C for 4 min once. Afterwards, phase 2 was initiated including three steps with 30 cycles. While the denaturation step was conducted at 94 °C for 30 s, the temperature and duration for the subsequent annealing step varied based on the used primers. Both parameter values for this step were calculated with the NEB Tm Calculator. The last step of this phase was the elongation, which was held at 68 °C for 91 s. These three steps were repeated for 30 cycles. In phase 3, the samples were kept at 68 °C for further 5 min and were ultimately cooled down to 4 °C in phase 4 until usage (Table 4.14). All samples were then analyzed by agarose gel electrophoresis.

Table 4.14: Phases and specifications of the colony polymerase chain reactions conducted in this work. The variable temperature and duration in phase 2 were calculated with the NEB Tm Calculator based on the used primers.

Phase	Cycles	Temperature, °C	Duration, s
1	1	94	240
2	30	94	30
		variable	variable
		68	91
3	1	68	300
4	1	4	∞

4.5. Experimental setup for L-phenylalanine production

The L-phenylalanine production with different *E. coli* strains was conducted in two different bioreactor setups. First, cells were cultivated in a conventional stirred-tank bioreactor at laboratory scale. Additionally, the L-phenylalanine production with *E. coli* cells was also conducted in a two-compartment bioreactor, in which a stirred-tank bioreactor was coupled to a specialized helical tube reactor as a bypass. The similarities and differences between both bioreactor setups will be elucidated in the following.

4.5.1. Stirred-tank bioreactor

Bioprocesses with well-mixed conditions were conducted in a 3.6 L stirred-tank bioreactor (round-bottom glass vessel, Labfors 5, Infors HT, Switzerland) equipped with three equidistant baffles and six-blade flat-blade turbines ($\varnothing$ 46 mm). For bioprocesses with an initial working volume of 1 L, two stirrers were implemented to the shaft with either 38 mm or 76 mm clearance to the bottom of the glass vessel, respectively. If the initial working volume was set to 1.35 L, a third stirrer was added at 122 mm above the bioreactor bottom. Several ports on the bioreactor lid allowed the implementation of further accessories. Among them is a pocket dip tube for a temperature sensor (Pt 100), a straight dip tube for sampling and a L-shaped sparger connected to an inlet filter (0.2 µm Emflon$^{\mathrm{TM}}$, Acro$^{\circledR}$ 50, Pall Corporation, USA) for the oxygen supply from the bottom of the bioreactor. The straight dip tube was equipped with a T-piece. One ending of the T-piece was connected to a luer activated valve as a sampling port, while the other ending was connected to an one-way luer check valve. Two ports were used for implementation of a pH electrode (EasyFerm Plus PHI Arc 325, Hamilton, USA) and a dissolved oxygen (DO) probe (VisiFerm DO Arc 325 H0, Hamilton, USA). Sterile solutions such as the inoculum were injected through a septum that was fixated by a septum collar. The supply of titrating agents and feeding solutions was realized by a quadruple addition port adapter. The foam formation was controlled by an implemented antifoam sensor. The off-gas was cooled by an exit gas cooler using tap water as a cooling agent. Additionally, the exit gas cooler was connected to a 2 L coated laboratory glass bottle with an exhaust filter (0.2 µm PTFE, Acro$^{\circledR}$ 50 or AcroPak$^{\mathrm{TM}}$ 300, Pall Corporation, USA). The remaining port was occupied by a blanking plug. The threads of the straight dip tube, the blanking port, both pH and DO probes, the L-shaped sparger and the exit gas cooler were wrapped with teflon tape. Furthermore, they were equipped with an O-ring. The bioreactor lid was fixated onto the glass vessel by four knurled screws. The drive hub was positioned at the middle of the top plate. All the remaining openings of the accessories were closed with either female CPC couplings (1/8 " barb valved) or screw caps with silicone tubings

(inner and outer diameter of 3 mm and 6 mm) as a connector. The exact positioning of all accessories on the bioreactor lid is summarized in Figure 4.1.
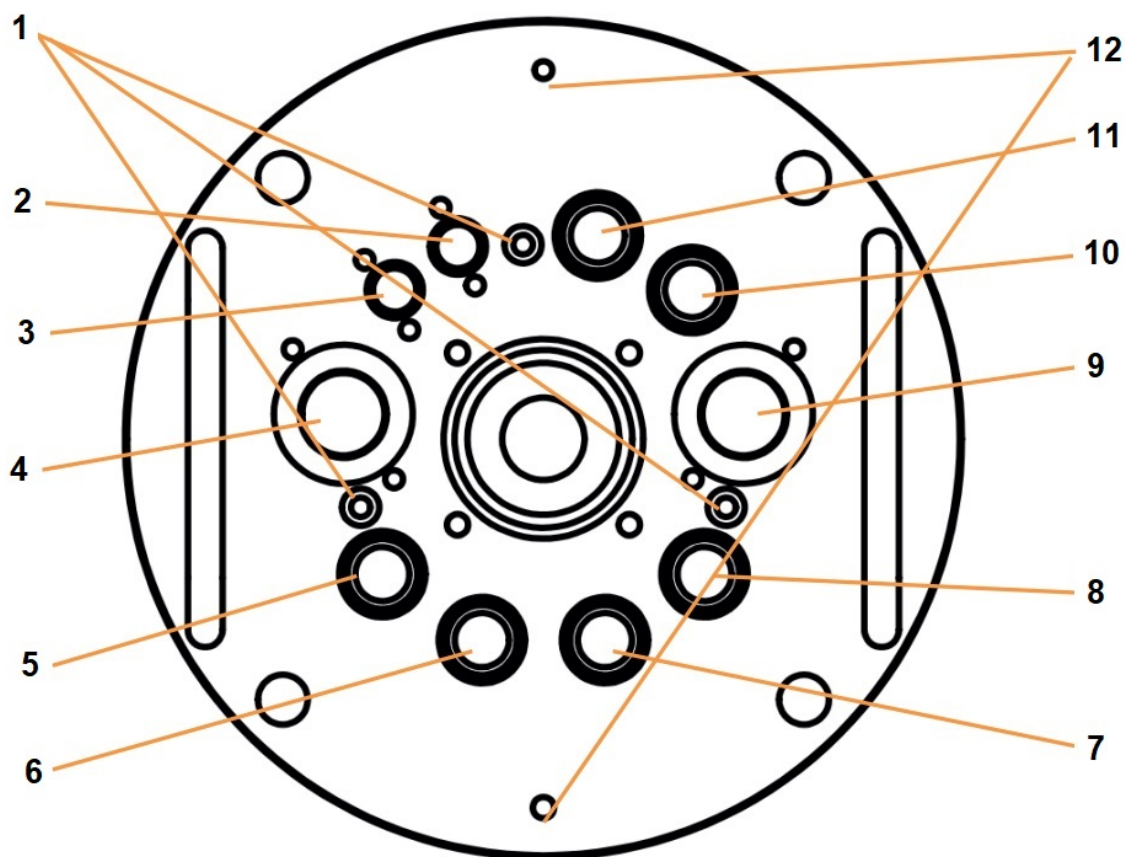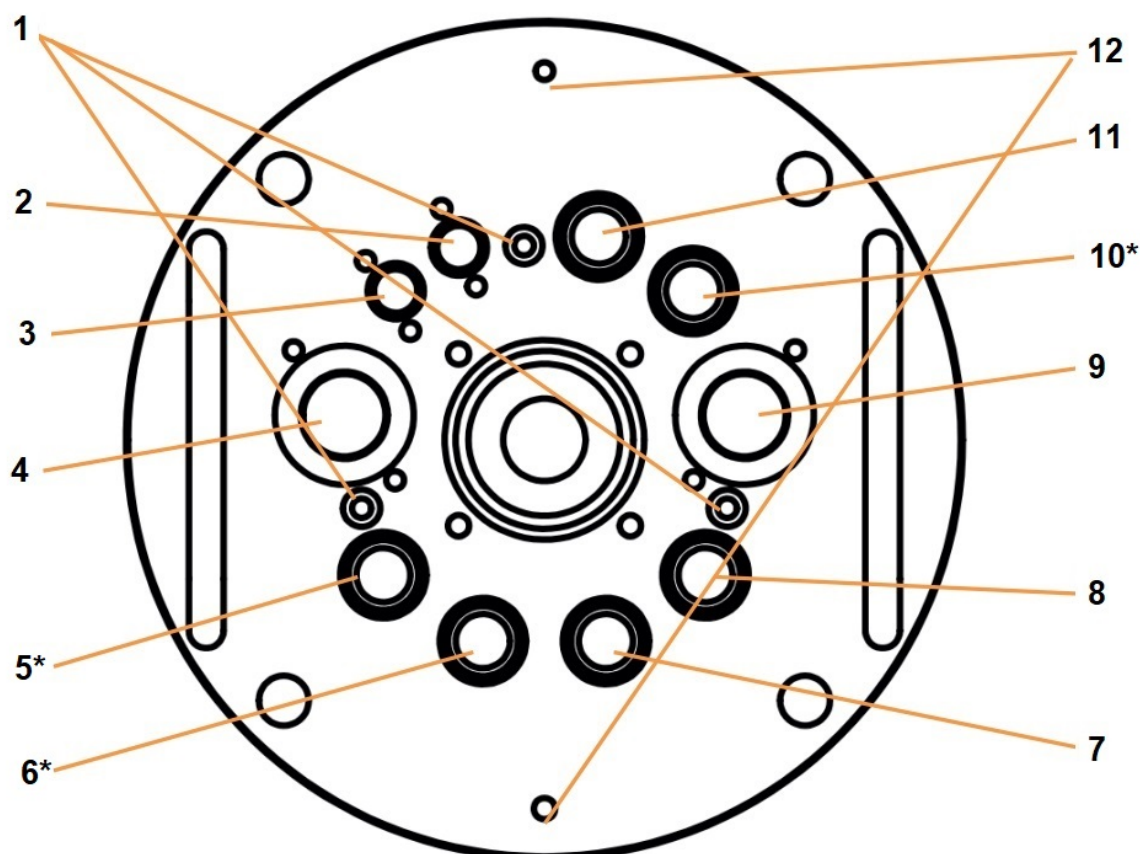

Figure 4.1: Top view of the bioreactor lid (Labfors 5, Infors HT, Switzerland) with the enumeration and occupation of the available ports during stirred-tank bioreactor cultivations: 1 - Baffle fixation, 2 - Pocket dip tube for temperature sensor ($\varnothing$ 10 mm), 3 - Antifoam sensor ($\varnothing$ 10 mm), 4 - Septum collar ($\varnothing$ 19 mm), 5 - Dip tube straight ($\varnothing$ 12 mm), 6 - Blanking plug ($\varnothing$ 12 mm), 7 - DO sensor ($\varnothing$ 12 mm), 8 - pH sensor ($\varnothing$ 12 mm), 9 - Quadruple addition port adapter ($\varnothing$ 19 mm), 10 - Sparger L-shaped ($\varnothing$ 12 mm), 11 - Gas cooler exit ($\varnothing$ 12 mm), 12 - Ground connector for antifoam sensor (modified from Infors AG 2019).

Prior to heat sterilization of the bioreactor, 1 L or 1.35 L of diH$_2$O were poured into the glass vessel. Additionally, the pH probe was calibrated with buffers at pH 4.0 and 7.0. All the accessories were mounted on the bioreactor lid and the top plate was fixated onto the glass vessel. The vessel jacket was filled up to at least half of its maximum volume with diH$_2$O. Approximately 400 mL of diH$_2$O was filled into the coated laboratory glass bottle with a sip of antifoam solution (AF 204, Sigma Aldrich, USA). The bioreactor was then heat autoclaved together with the coated glass bottle at 121 °C for 20 min. Directly after the sterilization, the bioreactor was emptied and re-filled with the chemically defined minimal medium for bioreactor cultivations under sterile conditions. Meanwhile,

the stirrer speed was set to 500 rpm and the aeration rate to 1 vvm using atmospheric oxygen. Additionally, the temperature sensor was inserted into the pocket dip tube and the glass vessel was heated or cooled to 37 °C with tap water for the vessel jacket. The outlet of the exhaust filter was connected to an exhaust gas analyzer for the determination of oxygen and carbon dioxide levels in the off-gas (BlueVary, BlueSens gas sensor GmbH, Germany). After around 4 h of equilibration, the DO probe was calibrated at 100% air saturation using atmospheric oxygen. Furthermore, the oxygen and carbon dioxide sensors of the exhaust gas analyzer were calibrated according to the manual (one-point calibration). Prior to inoculation of the stirred-tank bioreactor, the initial stirrer speed, aeration rate, temperature and pH value were set to 500 rpm, 1 L min^{-1} or 1.35 L min^{-1} (1 L or 1.35 L starting volume), 37 °C and 7.

4.5.2. Design, establishment and fluid dynamic characterization of a coiled flow inverter

Design and establishment

For the establishment of a novel two-compartment bioreactor to investigate the impact of dynamic conditions on the L-phenylalanine production with *E. coli*, the stirred-tank bioreactor shall be connected to a coiled flow inverter (CFI). The CFI is a helical tubular reactor with repetitive integrations of 90° bends. A 495x495x20 mm PVC sheet was used as a stabilizing and supporting platform (Figure 4.2 (1)), in which four mounting foots (Figure 4.2 (2)) were drilled in for the integration of four threaded rods (M10, Figure 4.2 (3)). Two layers of identical hollow square girder frames were anchored on these rods. Each layer consisted of four hollow PVC pipes with an outer diameter of 110 mm (Figure 4.2 (4)). On each of these pipes, two sets of hose clamp brackets were drilled in for the fixation of the hoses. The pipes were connected to a hollow square design by four 3D-printed double pipe sockets with a bend of 90° each (Figure 4.2 (5)). Both layers had a constant distance of 120 mm by implementation of 3D-printed hollow cylinders (Figure 4.2 (6)). Braided silicone hoses were used as tubing material. The design derived from the suggestions stated from Klutz *et al.* (2015).
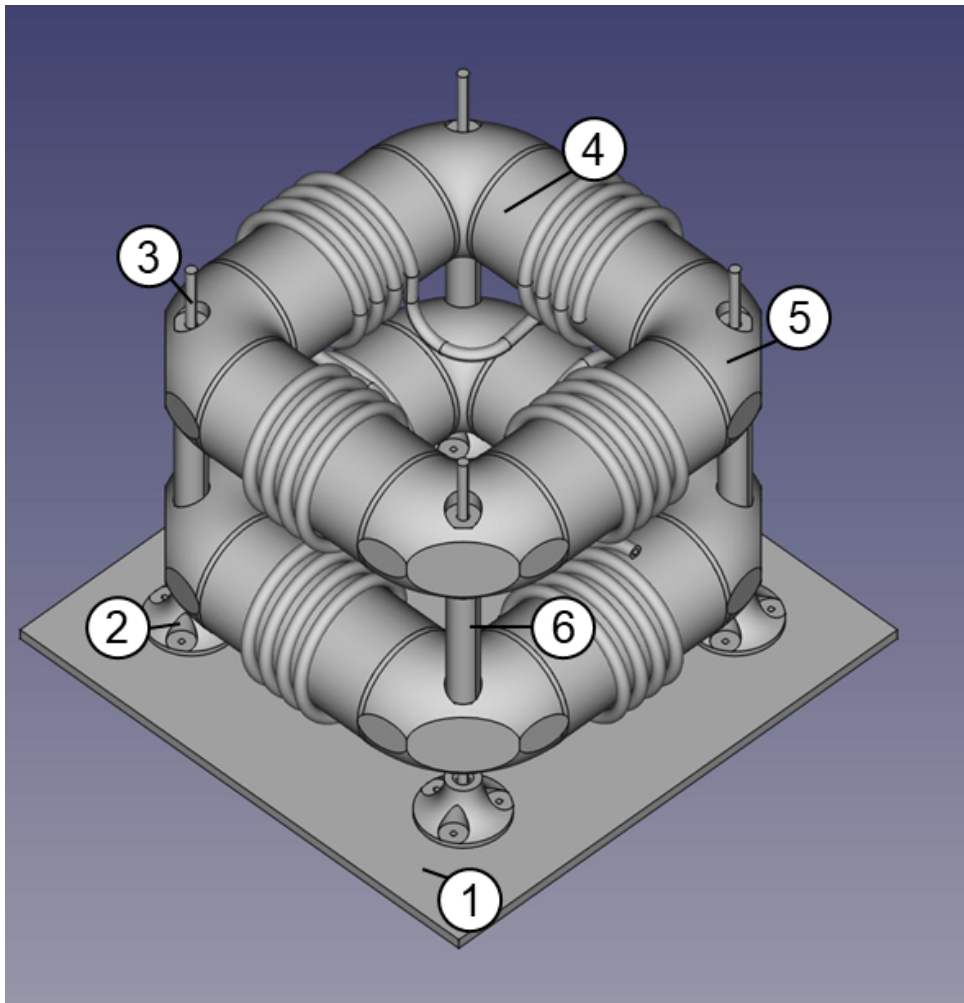
Figure 4.2: Isometrical view of the coiled flow inverter designed with FreeCAD (Version 0.19.2). Important parts for the girder frame are enumerated: 1 - PVC sheet, 2 - Mounting foot, 3 - Threaded rod, 4 - PVC pipe, 5 - Double pipe socket with a 90° bend, 6 - Hollow cylinder as spacer.

Two tubes were used with equal lengths of 6.615 m each, which corresponds to an overall volume of approximately 373 mL. The tubes were coiled around the PVC pipes by inserting them into the hose clamp brackets with a coil diameter of 118 mm and a pitch distance of 20 mm. On each PVC pipe, 3 to 4 turns were introduced (coiling element) after which the tubes were coiled around the next PVC pipe of the same hollow square frame. This automatically led to a 90° bending of the tubes (Figure 4.3).

Tubing material		Braided silicone
Inner tube diameter	d_i	6 mm
Outer tube diameter	d_o	12 mm
Coil diameter	d_c	118 mm
Pitch distance	p	20 mm
Number of turns in one coil	N	$3-4$
Bend angle	α_b	90 °
Length of tubing	L	13.23 m
Number of bends	n_{bends}	6
Levels		2
Distance between the levels	H	120 mm
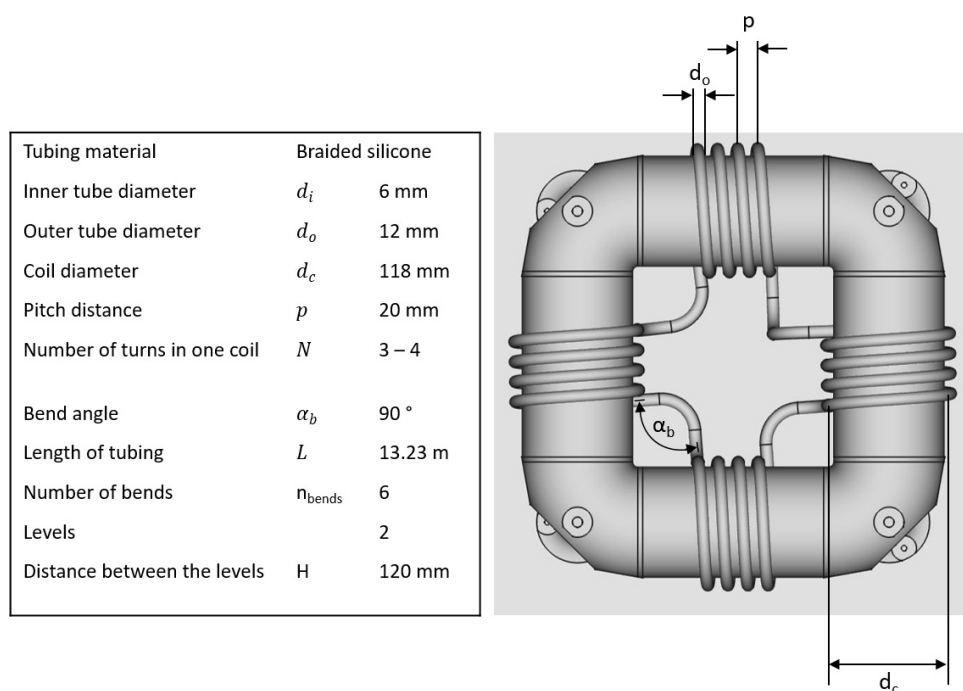
Figure 4.3: Top view of the coiled flow inverter designed with FreeCAD (Version 0.19.2). Key characteristics of the designed coiled flow inverter are listed on the left.

Fluid dynamic characterization

Before the CFI was connected to the stirred-tank bioreactor, key flow characteristics such as the mean hydraulic residence times and the axial dispersion at different flow regimes were measured using the tracer methods described by Levenspiel (2012) and Klutz *et al.* (2015). In detail, step input experiments were conducted with diH$_2$O or different glycerol mixtures ranging between 10% to 50% (v/v) as mobile phases and a 0.025 mg mL^{-1} vitamin B12 solution as a tracer. All solutions were filtrated (0.2 µm) and stored separately in bottle tanks (Figure 4.4 (1) and (2)), which were connected to two piston pumps (Figure 4.4 (4) P-907 and P-908) of an ÄKTA pilot system (GE Healthcare Bio-Sciences AB, USA). Rapid switching between the fluids was realized using a three-way valve (Figure 4.4 (3)). The outlet of the pumps was connected to the entrance of the CFI (Figure 4.4 (5)), while the exit of the CFI was coupled to the UV cell (Figure 4.4 (6)) UV-901) of the chromatography system for monitoring of the absorbance at 280 nm of the outlet flow at data acquisition intervals of 0.1 s to 0.2 s. Five different volumetric flow rates of 1.18 mL s^{-1}, 2.36 mL s^{-1}, 3.54 mL s^{-1}, 4.71 mL s^{-1} and 5.33 mL s^{-1} were investigated and the remote control of the device and data storage was managed by the Unicorn software (Version 5.2).
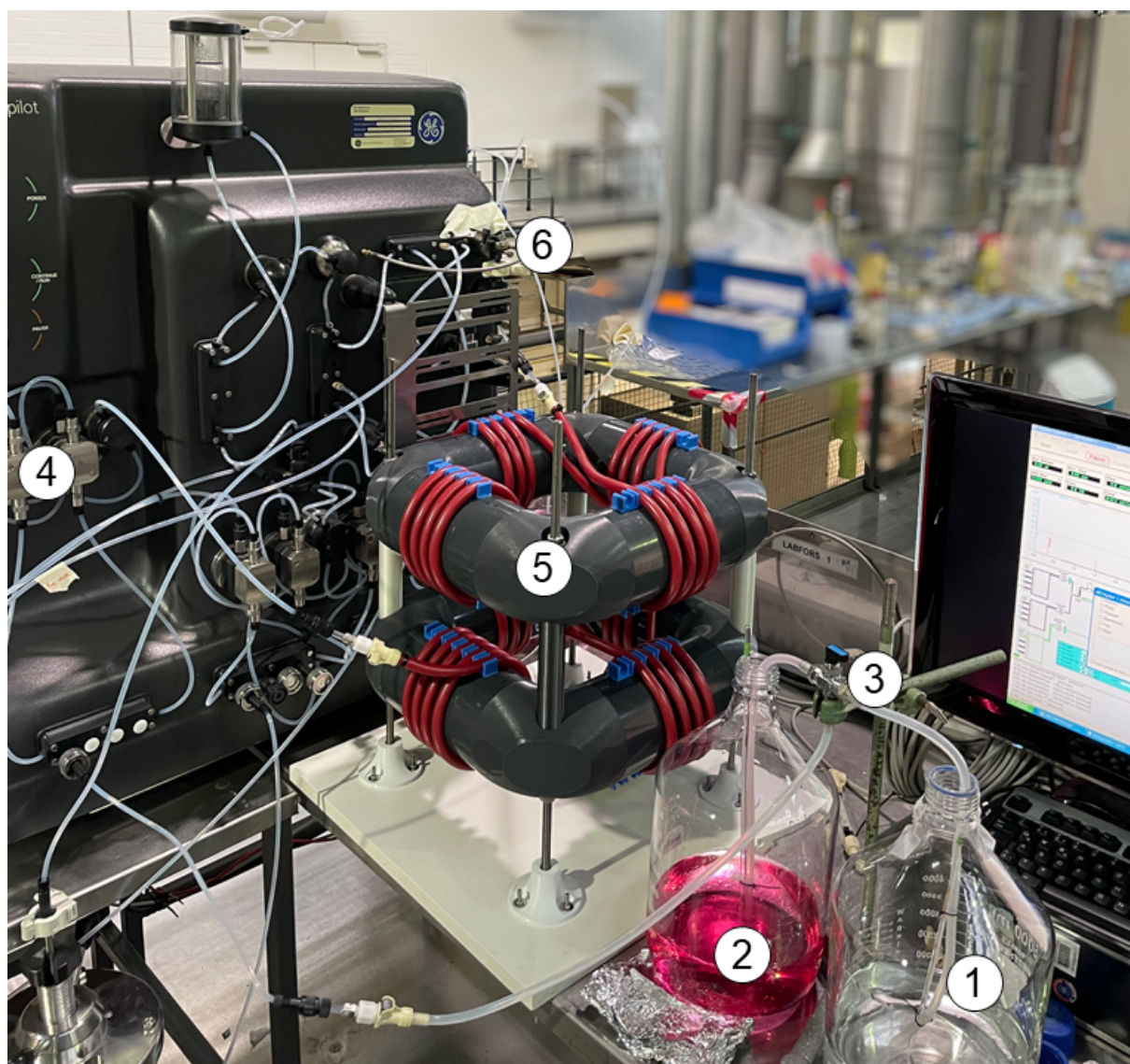
Figure 4.4: Experimental setup for the fluid dynamic characterization of the coiled flow inverter with the following components: 1 - Tank with diH_2O or glycerol mixtures, 2 - Tank with a 0.025 mg mL^{-1} vitamin B12 solution, 3 - Three-way valve, 4 - Piston pumps of the ÄKTA pilot system, 5 - Coiled flow inverter, 6 - UV cell of the ÄKTA pilot system.

In step input experiments, raw data of the monitored absorbance at 280 nm typically lead to a sigmoidal curve, which is known as the F curve. To determine the mean hydraulic residence times and the axial dispersion based on the monitored F curve, it has to be converted to the corresponding exit age distribution (E curve) by differentiation of the data points:

$$E(t) = diff(F(t)) \tag{4.1}$$

By further numerical integration of this equation, the mean hydraulic residence time τ can be calculated by the following formula:

$$\tau = \int t \cdot E(t) dt \tag{4.2}$$

| τ | Mean residence time | s |
| t | Time | s |

The degree of axial backmixing at different volumetric flow rates within the CFI were evaluated by calculation of the dimensionless Bodenstein number (Bo), which describes the ratio of convection to the dispersion current. Based on the dispersion model, which is only applicable for flow regimes with Bo numbers above 100, each time point was divided by the determined mean hydraulic residence time τ leading to the dimensionless time θ. The same was done for the absorbance values A_t by dividing each value by the maximum measured absorbance A_{max} of a run to obtain the dimensionless absorbance F(θ).

$$\theta = \frac{t}{\tau} \tag{4.3}$$

$$F(\theta) = \frac{A_t}{A_{max}} \tag{4.4}$$

θ	Dimensionless time	$-$
A_t	Absorbance at 280 nm	mAU
A_{max}	Maximum absorbance at 280 nm	mAU

After plotting dimensionless absorbance values F(θ) against the dimensionless time θ with subsequent curve fitting, the Bo numbers were calculated by solving equation 4.5 as a minimization problem using the Bo number as a free variable. The curve fitting and solving of the minimization problems were executed with MATLAB (R2017b Version 9.3.0.713579).

$$F(\theta) = \frac{1}{2} \cdot \left[erf\left(\frac{1}{2} \cdot \sqrt{Bo} \cdot (\theta - 1)\right) + 1 \right] \tag{4.5}$$

| Bo | Bodenstein number | $-$ |

4.5.3. Two-compartment bioreactor

After establishing and characterizing the coiled flow inverter, it was integrated to a stirred-tank bioreactor to provide a two-compartment bioreactor for the L-phenylalanine production under dynamic environments. The stirred-tank bioreactor was prepared similarly as

described in section 4.5.1, but with the following adjustments. First, the blanking plug was exchanged by a second bend dip tube. Furthermore, the positioning of the mounted parts on the bioreactor lid were changed to provide the longest distance between both implemented dip tubes (Figure 4.5).

Figure 4.5: Top view of the bioreactor lid (Labfors 5, Infors HT, Switzerland) with the enumeration and occupation of the available ports during two-compartment bioreactor cultivations: 1 - Baffle fixation, 2 - Pocket dip tube for temperature sensor (∅ 10 mm), 3 - Antifoam sensor (∅ 10 mm), 4 - Septum collar (∅ 19 mm), 5 - Dip tube straight (∅ 12 mm), 6 - Sparger L-shaped (∅ 12 mm), 7 - DO sensor (∅ 12 mm), 8 - pH sensor (∅ 12 mm), 9 - Quadruple addition port adapter (∅ 19 mm), 10 - Bend dip tube (∅ 12 mm), 11 - Gas cooler exit (∅ 12 mm), 12 - Ground connector for antifoam sensor (modified from Infors AG 2019). Positions labelled with an asterisk highlight differently occupied ports compared to the stirred-tank bioreactor cultivation.

All two-compartment bioreactor cultivations were conducted with an overall starting volume of 1.35 L. The stirred-tank bioreactor had an initial volume of 0.9 L, whereas the coiled flow inverter together with all connecting tubes (silicone tube with an inner and outer diameter of 4 mm and 8 mm) had a fixed volume of 0.45 L. Due to the partial displacement of the cultivation medium into two compartments, only two 6-blade impellers were fixated to the shaft with clearances of 38 mm and 76 mm to the bottom of the glass

vessel. The continuous transfer of the biosuspension between both compartments was ensured by using a peristaltic pump (Masterflex® L/S® Digital miniflex®, Avantor, USA) with a double pumping tube (Masterflex® Norprene L/S® 16, Avantor, USA). Through the straight dip tube, the fermentation broth inside the stirred-tank bioreactor was pumped into the CFI. The one-way luer check valve on the T-piece was exchanged with a silicone tube that was connected to the pumping tubes of the peristaltic pump. Sampling during bioprocesses was maintained by the remaining luer activated valve at the other ending of the T-piece. The second bend dip tube was used as the entrance of liquids from the CFI back to the stirred-tank bioreactor.

The braided silicone tubes of the CFI were heat sterilized by diving them into an autoclavable box filled with diH_2O. Autoclavation took place at $121\,°C$ for 30 min, after which the remaining liquids within the tubes were removed with atmospheric compressed air through a sterile filter (0.2 µm). Both tubes were then coiled around the hollow square layers of the girder frame. Sterilization of the stirred-tank bioreactor was executed as described in section 4.5.1. After autoclavation, the diH_2O in the bioreactor was exchanged with the chemically defined minimal medium for bioreactor cultivations under sterile conditions. Directly after, the CFI was connected to the stirred-tank bioreactor. The remaining gas bubbles in the CFI were flushed by setting a high volumetric flow rate of around 5 mL s^{-1} for 10 min to 30 min. Afterwards, the volumetric flow rate was reduced to the operating setpoint. The initial stirrer speed, aeration rate, temperature and the pH value were set to 500 rpm, 0.9 L min^{-1}, $37\,°C$ and 7. The calibration of the pH and DO probes and the exhaust gas analyzer were executed as described in section 4.5.1.

4.6. Bioprocess strategy for L-phenylalanine production

Each bioprocess was initiated by thawing of cryopreserved cells on ice for around 30 min, after which they were streaked on chemically defined minimal medium agar plates with 0.05 g L^{-1} kanamycin. Subsequently, the plates were incubated at $37\,°C$ for at least 66 h. To provide enough cell material to inoculate the L-phenylalanine production processes in the stirred-tank bioreactor or two-compartment bioreactor, a two-step preliminary cultivation was conducted in shake flasks.

4.6.1. Preliminary cultivation in shake flasks

A single bacterial colony grown on chemically defined minimal medium agar plates was used for the inoculation of a 100 mL shake flask with 10 mL of the chemically defined minimal medium for precultures enriched with 0.05 g L^{-1} kanamycin. After at least 24 h

of incubation in an orbital shaker at $37\,^\circ$C and 150 rpm, the OD_{600} of the cell suspension was measured. Then, multiple 500 mL shake flasks with 100 mL of the chemically defined minimal medium for precultures with $0.05\,\text{g L}^{-1}$ kanamycin were inoculated with a starting OD_{600} of 0.01. These were further cultivated in the same orbital shaker at $37\,^\circ$C and 250 rpm for a minimum of 24 h. After the cells reached the early or mid exponential growth phase, they were harvested and centrifuged at $10\,^\circ$C and 3260xg for 10 min. The supernatant was discarded and the remaining cell pellets were resuspended using a fresh chemically defined minimal medium solution without amino acids and glycerol. The OD_{600} of the concentrated cell suspension was measured to prepare an inoculation size leading to a starting OD_{600} of 0.05 to 0.1 for the subsequent bioreactor cultivations.

4.6.2. Process strategy in stirred-tank bioreactor cultivations

Bioprocesses in a stirred-tank bioreactor were conducted with controlled process parameters. The temperature was kept at $37\,^\circ$C, whereas the pH value of the fermentation broth was maintained at around 7.0 by the controlled supply of either phosphoric acid (42%) or ammonia (25%). DO levels of above 30% air saturation were preserved by the stepwise increase of the stirrer speed (initial and maximum values at 500 rpm and 1500 rpm) or the aeration rate (initial and maximum values at $1\,\text{L min}^{-1}$ or $1.35\,\text{L min}^{-1}$ for 1 L or 1.35 L of starting volume and $5\,\text{L min}^{-1}$). Antifoam formation was restricted by the addition of a 10x diluted AF 204 solution through the antifoam sensor, if necessary. The exhaust oxygen and carbon dioxide levels were continuously monitored by the BlueVary gas sensor (Figure 4.6). Based on these levels, the oxygen uptake rates (OUR) and carbon dioxide evolution rates (CER) were calculated according to the following equations:

$$OUR = \frac{\dot{V}_{g,in}}{V_M \cdot V_R} \cdot \left(Y_{O_2,in} - \frac{1 - Y_{O_2,in} - Y_{CO_2,in}}{1 - Y_{O_2,out} - Y_{CO_2,out}} \cdot Y_{O_2,out} \right) \tag{4.6}$$

$$CER = \frac{\dot{V}_{g,in}}{V_M \cdot V_R} \cdot \left(Y_{CO_2,out} - \frac{1 - Y_{O_2,in} - Y_{CO_2,in}}{1 - Y_{O_2,out} - Y_{CO_2,out}} \cdot Y_{CO_2,in} \right) \tag{4.7}$$

OUR	Oxygen uptake rate	*mol L^{-1} h^{-1}*
CER	Carbon dioxide evolution rate	*mol L^{-1} h^{-1}*
$\dot{V}_{g,in}$	Inlet gas flow rate	*L h^{-1}*
V_M	Molar volume of ideal gas	*L mol^{-1}*
V_R	Bioreactor volume	*L*
$Y_{O_2,in}$	Molar fraction of oxygen in inlet flow	-
$Y_{CO_2,in}$	Molar fraction of carbon dioxide in inlet flow	-
$Y_{O_2,out}$	Molar fraction of oxygen in exhaust	-
$Y_{CO_2,out}$	Molar fraction of carbon dioxide in exhaust	-

The molar volume of ideal gas was assumed to be at 22.4 L mol^{-1}, whereas the molar fractions of oxygen and carbon dioxide in the inlet flow were set to 0.2095 and 0.0004, respectively.
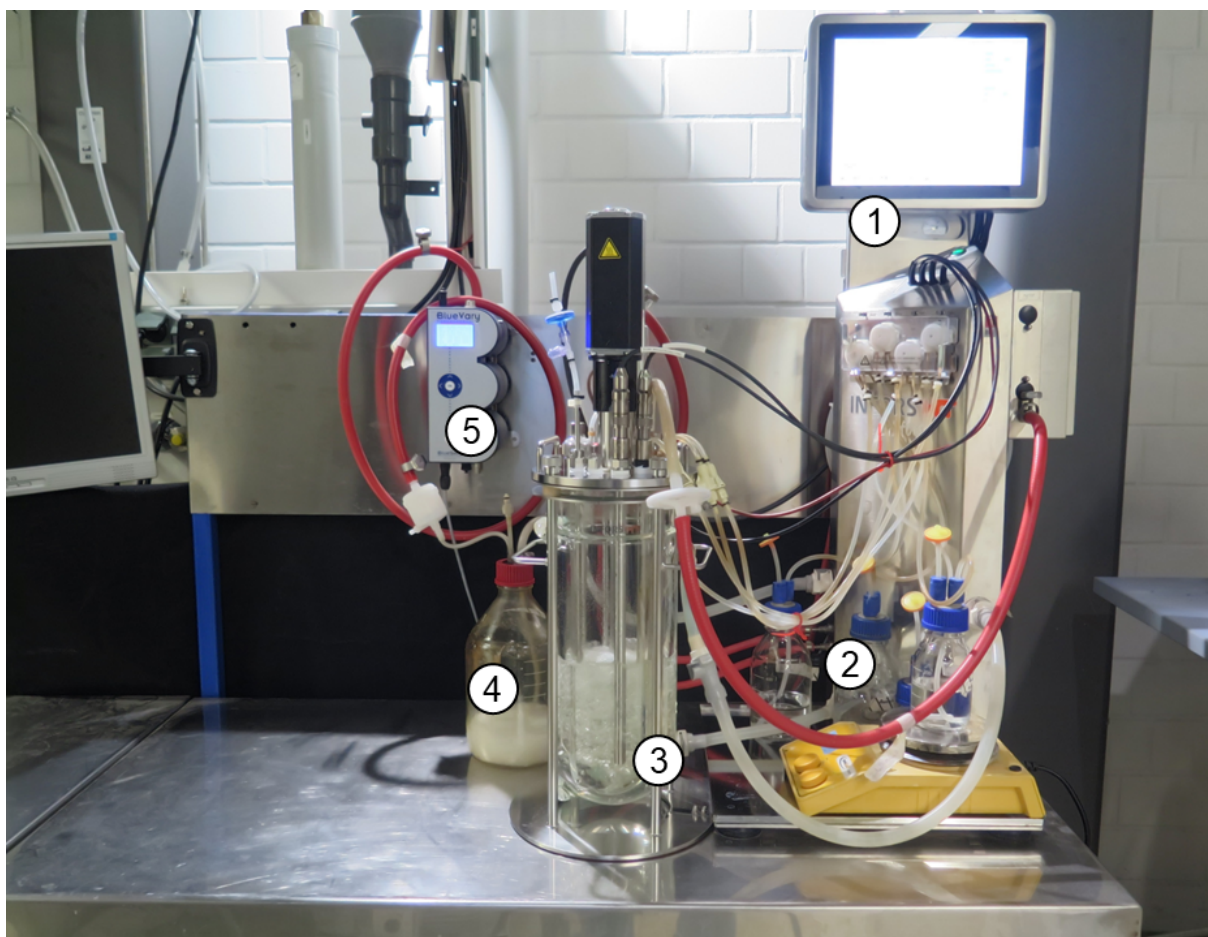
Figure 4.6: L-phenylalanine production process in a stirred-tank bioreactor. 1 - Bioreactor control unit, 2 - Feeding solution, 42% phosphoric acid, 25% ammonia and antifoam solution (AF 204, 1:10 diluted), 3 - Stirred-tank bioreactor, 4 - Foam trap bottle, 5 - BlueVary gas sensor.

The L-phenylalanine production in a stirred-tank bioreactor can be divided into the initial batch phase, the biomass production phase and the product formation phase. The batch phase was initiated by inoculation of the bioreactor with cells derived from the preliminary cultivation in shake flasks. The chemically defined minimal medium in the bioreactor contained 4 g L^{-1} glycerol as a sole carbon source and 0.05 g L^{-1} kanamycin. After complete depletion of the glycerol source, the biomass production phase was initiated by the exponential supply of feed medium 1 with a set growth rate of 0.1 h^{-1}. The derivation of the applied feeding strategy (equation 4.18) is described in section 3.2.1.2.

$$Feed_{1,2}(t) = \frac{V_{R,0} \cdot c_{X,0} \cdot \mu_{set}}{(c_{S,0} - c_S) \cdot Y_{X/S}} \cdot e^{\mu_{set} \cdot t} \tag{4.8}$$

$V_{R,0}$	Initial bioreactor volume	L
$c_{X,0}$	Initial biomass concentration	$g\ L^{-1}$
μ_{set}	Set growth rate	h^{-1}
$c_{S,0}$	Substrate concentration in feeding solution	$g\ L^{-1}$
c_S	Substrate concentration in bioreactor	$g\ L^{-1}$
$Y_{X/S}$	Biomass yield	$g\ g^{-1}$

Simultaneously to the feeding start, 5 mL or 6.75 mL of a 4x concentrated chemically defined minimal medium solution without amino acids, glycerol, trace elements and antibiotics was injected into the bioreactor through the septum (initial working volume of 1 L or 1.35 L, Table 4.5). After around 9 h into the biomass production phase, the feed medium 1 was replaced by feed medium 2 containing higher substrate concentrations (Table 4.6). Thus, the exponential feeding rate was adjusted, but still with a set growth rate of 0.1 h^{-1}. Again, the feeding switch was accompanied by further addition of 10 mL or 13.5 mL of the same 4x concentrated chemically defined minimal medium solution mentioned above into the bioreactor (initial working volume of 1 L or 1.35 L, Table 4.5). The induction of recombinant protein expression for the L-phenylalanine production was initiated after surpassing a biomass target value of at least 20 g L^{-1}. As cell dry weight concentrations could not be determined immediately, OD$_{600}$ values with a correlation factor of 0.5 were used instead. Only in case that the DO levels could not be maintained above 30% air saturation, the product formation phase was initiated earlier regardless of the present biomass concentration. At the beginning of the product formation phase, feed medium 2 was replaced by feed medium 3 (Table 4.6), which was supplied at a constant feeding rate of 0.18 g$_{Substrate}$ g$_{CDW}$$^{-1}$ h^{-1}. Simultaneously, a mixture of 1 mL L^{-1} calcium chloride dihydrate (15 g L^{-1}), 5 mL L^{-1} iron(II) sulfate heptahydrate (22.5 g L^{-1}), 1 mL L^{-1} magnesium sulfate heptahydrate (300 g L^{-1}), 1 mL L^{-1} thiamine hydrochloride (7.5 g L^{-1}) and 1 mL L^{-1} IPTG (0.3 mM) was injected into the bioreactor (Table 4.1). Cell samples were withdrawn frequently for the analysis of the OD$_{600}$, cell dry weight, cell fluorescence levels, specific organic metabolites and amino acids. If not processed immediately, they were stored on ice until analysis (Figure 4.6).

4.6.3. Process strategy in two-compartment bioreactor cultivations

In general, the L-phenylalanine production processes in a two-compartment bioreactor were conducted with the same process strategy as described for stirred-tank bioreactor

cultivations. Process parameters were only monitored and controlled in the stirred-tank bioreactor, whereas the CFI represented a limitation zone with fluctuating process conditions and no supply of oxygen, substrate or pH correcting agents. The peristaltic pump was continuously operated at a constant volumetric flow rate between 1.18 mL s^{-1} and 4.71 mL s^{-1} to circulate the cell suspensions between both compartments. The general feeding strategies and the volumes of injected media components or IPTG were calculated using the combined volume of both compartments. Cell samples were repetitively withdrawn from the stirred-tank bioreactor for the analysis of OD$_{600}$, cell dry weight, fluorescence intensities of the cells, organic metabolites and amino acids. If not processed immediately, withdrawn samples were stored on ice until analysis (Figure 4.7).

Figure 4.7: L-phenylalanine production process in a two-compartment bioreactor. 1 - Bioreactor control unit, 2 - Feeding solution, 42% phosphoric acid, 25% ammonia and antifoam solution (AF 204, 1:10 diluted), 3 - Stirred-tank bioreactor, 4 - Foam trap bottle, 5 - Peristaltic pump, 6 - Coiled flow inverter, 7 - BlueVary gas sensor.

4.7. Analytics and data analysis

Excitation and emission spectra

For the preliminary characterization of fluorescent proteins, the excitation and emission spectra of fluorophore-active components were measured with a photometer (Infinite 200, Tecan Group, Switzerland). Samples were pipetted in a microtiter plate with 96 wells (flat bottom), which was inserted into the device. Prior to the measurements, the plates were shaken with an amplitude of 1 mm and a frequency of 173.9 rpm for 3 s. The excitation spectra of samples were monitored by setting a fixed emission wavelength, whereas the excitation monochromator wavelength varied between 400 nm to 800 nm with a step size of 5 nm. All readings were realized from the top with no lag or settle time and with 20 µs of integration time. The gain was manually set to 100. In contrary, the emission spectra of the samples were screened with a fixed excitation wavelength, while the emission wavelengths changed from 400 nm to 800 nm in steps of 5 nm. The settings for the reading procedures were identical to the excitation measurements. The software Magellan (Version 6.6) was used for the operation of the device and data acquisition.

Rheological measurements

To approximate the viscosity of cell suspensions during the L-phenylalanine production processes, the viscosity of different fluids were monitored with a rotational rheometer (Rheolab QC, Anton Paar, Austria) using a concentric cylinder with a double gap geometry. 10 mL of samples were pipetted into the measuring cup and the cylinder was connected to the device through the rotational bob. The viscosity was monitored using a linearly increasing profile with shear rates from $0\ s^{-1}$ to $300\ s^{-1}$ with 2 s of duration for each data point. During all rheological measurements, samples were tempered to $37\,°C$ by a thermostat connected to the rotational rheometer (rheotherm 115, Contraves, Switzerland). The resulting viscosity values led to a saturation curve, in which the mean of the last 50 data points (from shear rates at $250\ s^{-1}$ to $300\ s^{-1}$) were considered for the calculation of the viscosity of the sample. The device was operated with the Rheoplus/32 software (Version 3.62).

Determination of optical density

The optical density describes the absorbance of light when passing through a sample. This can be defined by the Beer Lambert law as the logarithmic ratio of incident intensity I_0 to the transmitted intensity I. Consequently, a higher cell concentration in a sample is equivalent with a higher optical density. In this work, cell samples were measured with a photometer (Genesys 10S, Thermo Fisher Scientific, USA) at a wavelength of 600 nm. The linear working range of this device was assumed to be between OD_{600} values of 0.05 to

0.3. Samples above the maximum absorbance were diluted with 1x PBS with a maximum dilution factor of 10 per dilution step. Additionally, 1x PBS was used as a blank solution.

$$A_\lambda = log_{10}\frac{I_0}{I} = \epsilon_\lambda \cdot c \cdot d_{cuv} \tag{4.9}$$

A_λ	Absorbance at a wavelength λ	$-$
I_0	Incident intensity	$W\ m^{-2}$
I	Transmitted intensity	$W\ m^{-2}$
ϵ_λ	Molar extinction coefficient at a wavelength λ	$m^2\ mol^{-1}$
c	Concentration	$mol\ L^{-1}$
d_{cuv}	Thickness of the cuvette	m

Cell dry weight measurement

The gravimetric determination of the cell dry weight (CDW) was prepared by drying 2 mL microcentrifuge tubes (round bottom) at 80 °C for at least 24 h. Afterwards, the empty tubes were closed, cooled down to room temperature and weighted with a precision balance (XA204 DeltaRange®, Mettler Toledo, USA). During bioprocesses, the empty tubes were filled with 2 mL of cell suspension and were centrifuged at 4 °C and 21130xg for 20 min. The resulting supernatans were used for later quantification of organic metabolites and amino acids, whereas the cell pellets were dried at 80 °C for at least 24 h. After complete cooldown of the tubes to room temperature, these were weighted with the same precision balance. The corresponding CDW concentration was calculated by the weight difference of filled and empty tubes divided by the applied volume:

$$CDW = \frac{m_1 - m_0}{V} \tag{4.10}$$

CDW	Cell dry weight	$g\ L^{-1}$
m_0	Mass of empty tube	g
m_1	Mass of filled tube	g
V	Volume used	L

Quantification of extracellular organic metabolites

The supernatants of centrifuged cell samples were filtrated (0.2 µm) into glass vials for the later quantification of extracellular organic metabolites with a high performance liquid chromatography (HPLC). In detail, a Prominence-I LC-2030C HPLC (Shimadzu, Japan) was used, which was equipped with an Aminex® HPX-87H ion-exchange column (300 mm x 7.8 mm, Bio-Rad Laboratories Inc., USA) together with a micro-guard cation H guard column (30 mm x 4.6 mm, Bio-Rad Laboratories Inc., USA) inserted in a cartridge holder. An isocratic program was applied with sulfuric acid (5 mM) as mobile

phase and injection volumes of 10 µL per sample. All measurements were conducted at a volumetric flow rate of 0.6 mL min^{-1} and a constant temperature of 60 °C for 30 min. The elution of organic components was monitored by a refractive index detector (RID-20A, Shimadzu, Japan). To allow the quantification of the concentrations of measured components in the samples, two sets of external standard solutions containing glycerol, acetate, citrate, lactate, ethanol, succinate and malate with concentrations between of 0.1 g L^{-1} to 10 g L^{-1} were prepared and measured. All queued samples were cooled to 15 °C. The LabSolution software (Version 5.98) was used for operation of the device and the post-analysis of acquired data.

Quantification of amino acids

The here used quantification of the amino acids L-phenylalanine, L-tyrosine, L-glutamate and L-tryptophane with HPLC is based on a derivatization reaction (Weiner *et al.* 2014a). A bicine buffer (0.04 M, pH 10.2 adjusted with NaOH (5 M)) was used for the preparation of the derivatization agents. Among them is an iodoacetic acid solution, in which 65 mg was dissolved in 10 mL bicine buffer. Additionally, an ortho-phtaldialdehyde solution was prepared by dissolving 100 mg of ortho-phtaldialdehyde in a mixture of 5 mL bicine buffer and 5 mL methanol with subsequent addition of 65 µL 3-mercaptopropionic acid. Lastly, 2.5 µL of 3-mercaptopropionic acid was mixed with 1 mL of bicine buffer for a MCP-bicine solution. The derivatization of the samples were initiated by the transfer of 10 µL of the sample into a destination vial (650 µL bicine buffer mixed with 8 µL MCP-bicine solution). After mixing and incubation for 30 s, 20 µL of the iodoacetic acid solution (1:10 diluted with bicine buffer) was added. At the end, 70 µL of the o-phtaldialdehyde solution (1:7 diluted with bicine buffer) was transferred into the destination vial. After further mixing and incubation, 20 µL of the derivatized sample was injected into the HPLC. A detailed description of all steps of the derivatization reaction is listed in Table 4.15.

In this instance, the HPLC (Knauer, Germany) was equipped with a reversed-phase Gemini® C18 column (150 mm x 4.6 mm x 5 µm, 110 Å, Phenomenex Ltd., Germany) together with a SecurityGuard™ C18 (4 mm x 3.0 mm, Phenomenex Ltd., Germany). A gradient profile was applied using a monosodium phosphate solution (20 mM, pH 7.6 with NaOH (5 M), mobile phase A, filtrated) and a mixture of 45% acetonitrile, 45% methanol and 10% diH$_2$O (mobile phase B, ultrasonicated) at volumetric flow rates between 1.0 mL min^{-1} to 1.2 mL min^{-1} (Table 4.16). During each run, the oven temperature was kept at 40 °C and the components were detected and quantified by a fluorescence detector. The excitation was set to 340 nm, whereas the emission was detected at 450 nm (RF20-A, Shimadzu, Japan). External standard solutions containing L-glutamate,

L-tyrosine, L-phenylalanine (concentrations between 0.02 g L^{-1} and 2 g L^{-1}) and L-tryptophane (concentration between 0.0025 g L^{-1} and 0.25 g L^{-1}) were included in each batch run. The software ChromGate (Version 3.1) was used for the remote control of the device and subsequent data analysis of resulting chromatograms.

Table 4.15: Derivatization protocol for the quantification of amino acids.

Step	Description
1	Transfer of 10 µL of sample to destination vial (650 µL bicine buffer and 8 µL MCP-bicine solution)
2	Mixing (Resuspension with 150 µL for three times)
3	Incubation for 30 s
4	Addition of 20 µL iodoacetic acid solution (1:10 diluted with bicine buffer) to destination vial
5	Mixing (Resuspension with 150 µL for three times)
6	Incubation for 30 s
7	Addition of 70 µL o-phtaldialdehyde solution (1:7 diluted with bicine buffer) to destination vial
8	Mixing (Resuspension with 150 µL for three times)
9	Injection of 20 µL of derivatized sample into the HPLC

Table 4.16: Gradient profile during quantification of amino acids with the Knauer HPLC. Mobile phase A is a monosodium phosphate solution (20 mM, pH 7.6 with NaOH (5 M), filtrated), while mobile phase B is a mixture of 45 % acetonitrile, 45 % methanol and 10 % diH$_2$O (ultrasonicated).

Time, min	Applied flow, mL min^{-1}	Mobile phase A, %	Mobile phase B, %
0.00	1.0	100	0
3.00	1.0	100	0
8.50	1.0	75	25
28.50	1.0	60	40
30.00	1.0	60	40
30.02	1.0	0	100
32.00	1.0	0	100
34.00	1.2	20	80
38.00	1.0	100	0
43.00	1.0	100	0
43.02	1.0	100	0

Flow cytometry analysis

Fluorescence levels of cell samples were measured with the FACSMelody™ (Becton Dickinson, USA), which had three spatially-separated lasers at 405 nm (36 mW), 488 nm (16 mW) and 640 nm (36 mW) with beam spot sizes of 9 µm ($\pm$ 3 µm) x 67 µm ($\pm$ 5 µm) and nine detection filters. Among them are bandpass filters at 448/45 nm (excitated with 405 nm laser), 527/32 nm (excitated with 488 nm laser), 586/42 nm (excitated with 488 nm laser) and 660/10 nm (excitated with 640 nm laser), which suited best for the detection of the here used fluorescent proteins. FACSFlow™ (Becton Dickinson, USA) was used as a sheath fluid. A stream of droplets was enabled by using a sorting nozzle with a diameter of 100 µm.

Samples were prepared by centrifugation of the cell suspension at 13000 rpm for 3 min (Mikro 20, Andreas Hettich GmbH & Co. KG, Germany). The supernatants were discarded and the cell pellets were resuspended with 1x PBS. These were transferred into 5 mL round bottom polystyrene test tubes (Falcon®, Corning, USA) to initiate the measurements. If not stated otherwise, all measurements were conducted with a threshold at 491 V on the width of the side scatter (SSC-W). The event rate was adjusted to 400 events per second to 1000 events per second by regulation of the applied flow rate. For each sample, 100 000 events were recorded and saved. Photomultiplier tube (PMT) voltages for the forward scatter (FSC) and SSC were set to 250 V and 335 V. Moreover, PMT levels of the bandpass filters at 448/45 nm, 527/32 nm, 586/42 nm and 660/10 nm were kept at 500 V, 500 V, 600 V and 600 V, respectively. The flow cytometer was operated with FACSChorus (Version 1.3.3).

Data were saved and exported as FCS3.1 files and the post-analysis was conducted with FCSExpress™ (Version 7.18.0015). Mean, median fluorescence levels, standard deviations of distributions and the coefficient of variances were calculated in this software and were used for data presentation and further analysis. While the mean describes the average value of 100 000 measured events (see equation 3.36), the median value represents the 50th percentile of the measured sample with half of the measured events showing an intensity value above and the other half below the median. To find the median value of a distribution, all 100 000 measured events were ranked based on their corresponding intensity values. The average of the 50 000th and 50 001st entries represented the median value. Higher mean and median levels of a population indicated higher expression levels of fluorescent proteins. The coefficient of variance and standard deviation of a distribution were calculated based on the equations 3.35 and 3.37. High coefficient of variances and standard deviations indicated broad distributions and *vice versa* (Delvigne *et al.* 2017).

The mean-to-median ratios of distributions were calculated according to equation 3.38. Mean-to-median ratios of 1 were understood as unimodal distributions, whereas higher values were interpreted as potentially bimodal distributions (Delvigne *et al.* 2017). Histograms were plotted with a bi-exponential x-axis and a linear y-axis with automatic scale. The smoothing factor of the histograms was set to 10. In contrast, density plots were displayed with double bi-exponential axes.

5. Genetic engineering and preliminary characterization of *Escherichia coli* reporter strains

Population heterogeneity describes the co-existence of cells with different phenotypes within a microbial population, although they originate from an isogenic culture. One approach to identify possible differences of certain cellular physiologies during bioprocesses are fluorescent reporter strains. The concept of these strains is to integrate a synthetic copy of a reporter molecule such as fluorescent proteins into a specific genetic unit of a host strain, which is associated with a certain cellular phenotype of interest. Consequently, cells expressing this specific genetic unit simultaneously produce the integrated reporter molecule. Hence, the expression of certain cellular characteristics can be reflected by fluorescence signals, which further support the elucidation of potential subpopulations by evaluting the single-cell fluorescence intensities. Cells showing strongly deviating fluorescence signals compared to the main population would indicate the presence of outliers with different cellular characteristics. To practically approve these benefits, the *E. coli* FUS4 strain shall be transformed into a quadruple reporter strain by genetic integration of synthetic copies of four different fluorescent proteins into the host strain.

5.1. Excitation and emission spectra of fluorescent proteins

The very first step for the engineering and establishment of a reporter strain is the selection of ideal fluorescent proteins. To provide an efficiently working multiple reporter strain to dynamically reflect single-cell characteristics, the considered fluorescence molecules should have a high brightness to facilitate the detectability, a low maturation time to reduce the time delay from the initiation of its expression to the emerging fluorescence signal and a monomeric state to circumvent the formation of inclusion bodies and avoid any other toxic effects (Shaner *et al.* 2005). Based on these criteria paired with an extensive literature research, the list of potential reporter molecules shrank to the following:

mTagBFP2, mEmerald, CyOFP1 and mCardinal2. According to Subach *et al.* (2011), mTagBFP2 is a blue fluorescent protein with a maturation time of around 13 min, whereas mEmerald fluoresces green with a maturation time of approximately 11 min (Balleza *et al.* 2018). CyOFP1 is described as a bright cyan-excitable orange fluorescent protein by Chu *et al.* (2016) with maturation times of 15 min, while mCardinal2 shows far-red fluorescences with a maturation time of 27 min (Chu *et al.* 2014, Kim *et al.* 2022). All selected reporter molecules are monomeric proteins. Besides these recommended properties, fluorescent proteins can only be monitored if they are excitated with lasers at correct wavelengths and the emitted signals are collected with matching detection filters. Any strong discrepancies potentially lead to a complete loss of detectability. Therefore, the excitation and emission spectra were screened for the pre-selected fluorescent proteins. All fluoresscent proteins were separately expressed in *E. coli* cells. Instead of using mEmerald for this preliminary study, the precursor eGFP was used. Excitation wavelengths of the reporter molecules were measured over the range of 400 nm to 800 nm. The acquired intensities were normalized by dividing each data point with the peak value of a measured fluorescent protein. Consequently, a normalized value of '1' highlighted the wavelength with the highest excitation intensity. In comparison, a value of '0.1' was interpreted as a 90% lower excitation intensity than the peak value. Ideally, the measured peaks of the fluorescent proteins should be equal or close to the wavelengths of the available lasers of the flow cytometer at 405 nm, 488 nm and 640 nm.

According to the measured spectra, the ideal excitation wavelength of mTagBFP2 was at 405 nm (Figure 5.1, blue), which perfectly matches with the first laser of the here used flow cytometer. For eGFP (Figure 5.1, green) and CyOFP1 (Figure 5.1, orange), the highest peak-normalized excitation wavelengths were monitored at 480 nm and 525 nm. The normalized values at 488 nm, which corresponds to the excitation wavelength of the second laser, were at 0.89 and 0.71 for eGFP and CyOFP1, respectively. Last but not least, the ideal wavelength to excite mCardinal2 was at 605 nm. In comparison, the third laser of the here used flow cytometer is at 640 nm, at which the excitation intensity of mCardinal2 was reduced to a normalized value of 0.14 (Figure 5.1, red).
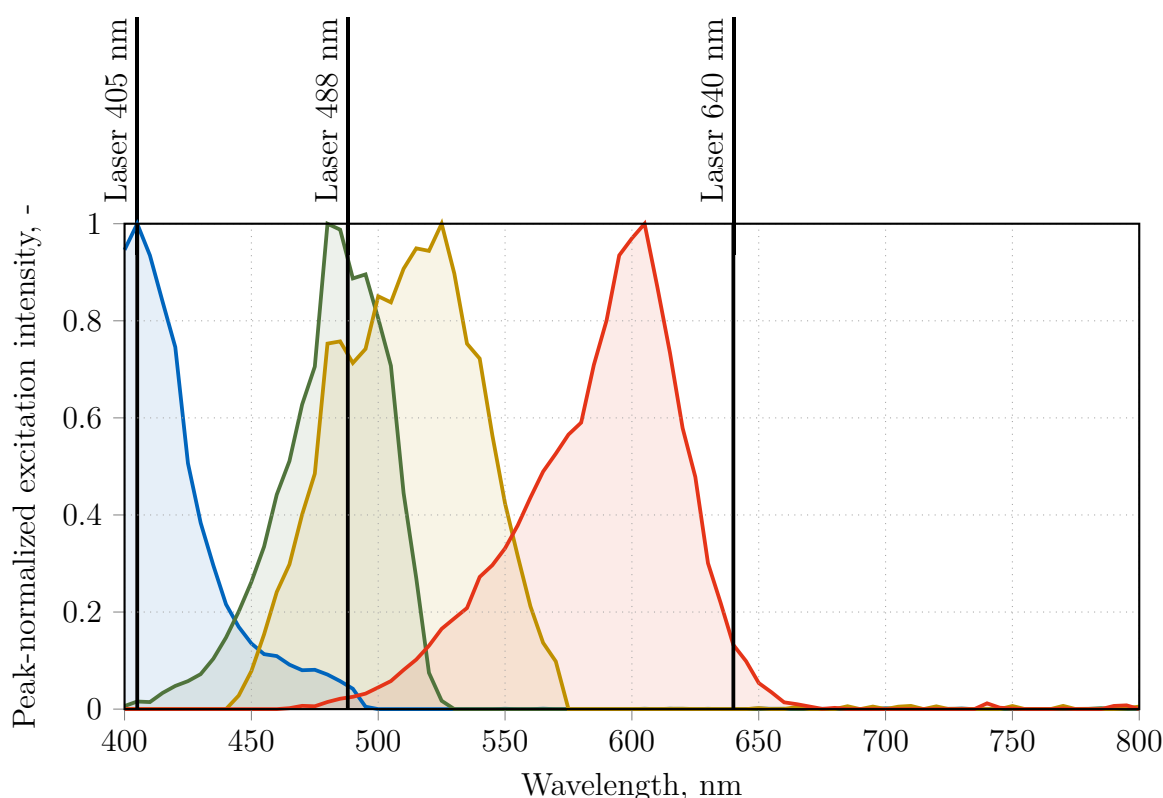
Figure 5.1: Peak-normalized excitation intensities of the four fluorescent proteins mTagBFP2 ——, eGFP ——, CyOFP1 —— and mCardinal2 ——. The measurements were carried out with a photometer at excitation wavelengths between 400 nm to 800 nm. The black verticals mark the excitation wavelengths of the three lasers of the flow cytometer at 405 nm, 488 nm and 640 nm.

Additionally, the emission spectra of mTagBFP2, eGFP, CyOFP1 and mCardinal2 were measured, as well. In this instance, the highest emission intensities of a fluorescent protein should be covered by at least one of the available detection filters of the here used flow cytometer. Overall, the flow cytometer was equipped with nine detection filters. At the same time, each detection filter should receive signals from only one of the fluorescent proteins to minimize fluorescence crossovers. Starting with the emission spectrum of mTagBFP2 (Figure 5.2, blue), its highest emission was monitored at 455 nm, which is covered by the detection filter at 448/45 nm. In contrast, eGFP had its peak-normalized emission intensity at 515 nm. Consequently, the emission of this fluorescent protein is covered by the detection filter at 527/32 nm. However, it is worth mentioning that lower normalized emission intensities of mTagBFP2 between 0.32 and 0.13 were present in this range, as well. Although the next possible detection filter at 586/42 nm even collected emission intensities from all four fluorescent proteins, the highest measured normalized emission intensities derived from CyOFP1 with its peak at 590 nm. In contrast, all the others had normalized emission values below 0.26. At higher wavelengths above 650 nm, only mCardinal2 showed its highest emission at 660 nm. This perfectly matches with the

detection filter at 660/10 nm. However, weak overlapping emission intensities of CyOFP1 were observed in this range (normalized values between 0.25 to 0.35).
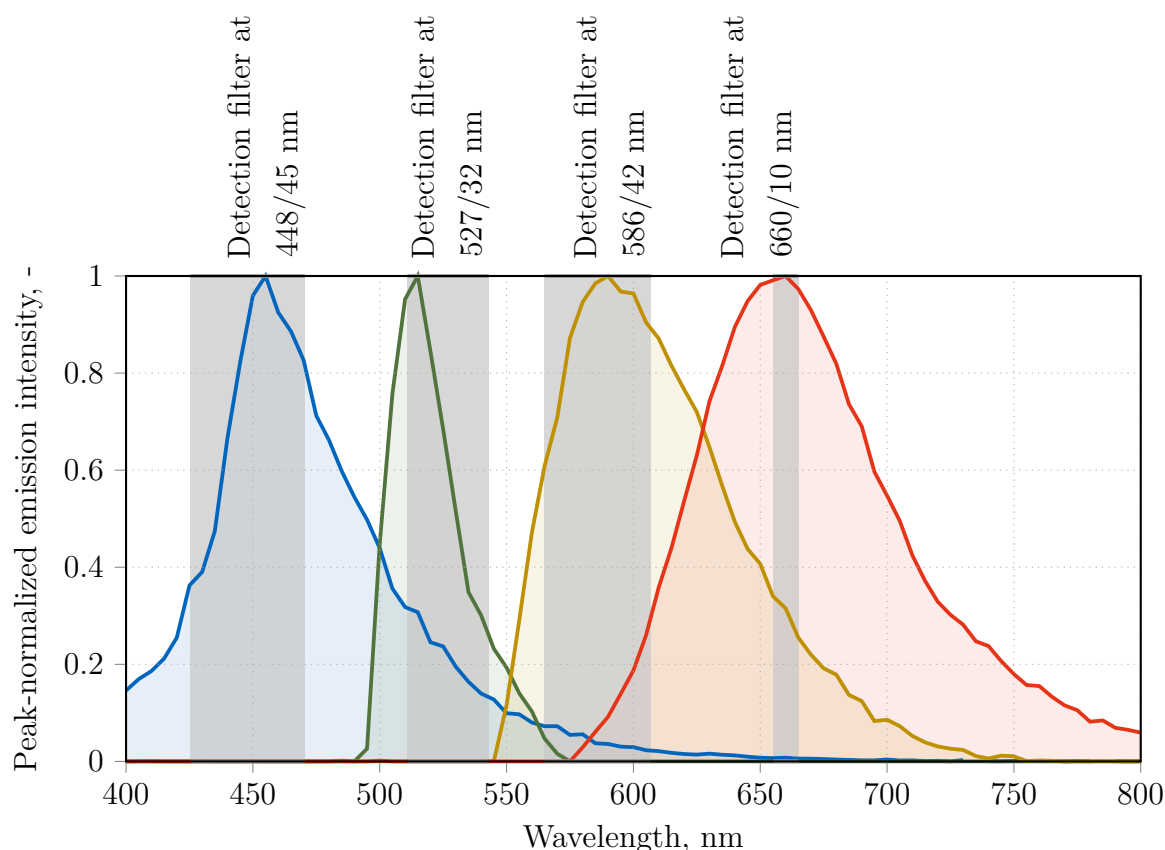
Figure 5.2: Peak-normalized emission intensities of the four fluorescent proteins mTagBFP2 ——, eGFP ——, CyOFP1 —— and mCardinal2 ——. The measurements were carried out with a photometer at emission wavelengths between 400 nm to 800 nm. The grey areas symbolize the wavelenghts covered by the detection filters of the flow cytometer at 448/45 nm, 527/32 nm, 586/42 nm and 660/10 nm.

Discussion

The here acquired excitation and emission spectra of all four fluorescent proteins showed a good agreement with the available data of the same reporter molecules in other studies (Subach *et al.* 2011, Balleza *et al.* 2018, Chu *et al.* 2014, Chu *et al.* 2016). According to the results of this preliminary study, mTagBFP2 can be excited by the first laser at 405 nm, whereas the second laser at 488 nm qualifies for the excitation of eGFP (or mEmerald) and CyOFP1. Though the third laser at 640 nm lies in the range of the measured excitation spectrum of mCardinal2, it is far from the peak excitation wavelength at 605 nm. Hence, the reduced excitation of mCardinal2 potentially complicate the detection of this reporter molecule during bioprocesses. From a positive point of view, cellular autofluorescence in the red spectral range is strongly reduced so that the level of general

noise remains comparably low (Wiedenmann *et al.* 2002). Apart from its lasers, flow cytometers work with optical lenses to provide narrow detection ranges and thus reduce the level of crosstalks (Telford *et al.* 2012). Generally, four filters have been identified with a high level of compatibility to detect the four reporter molecules. However, with the exception of the detection range at 448/45 nm, all the other detection ranges are covered by fluorescence emission signals of more than two different reporter molecules. For example, both eGFP and mTagBFP2 emitted at wavelengths between 527/32 nm, but with higher proportions of the former molecule. According to the measured emission spectra, the detection filter at 586/42 nm would even collect signals of all four fluorescent proteins. The last detection range at 660/10 nm collected the emission signals of CyOFP1 and mCardinal2 with higher measured intensities of the latter.

It is important to mention that eGFP was measured instead of the initially selected mEmerald due to the availability and direct access to eGFP in the laboratory. Both proteins are derivatives of the original green fluorescent protein, but eGFP has two implemented mutations at F64L and S65T, whereas mEmerald also has these two mutations, but further site-directed exchanges of its primary amino acid sequence at S72A, N149K, M153T and I167T. These mutations were mainly implemented to improve the brightness, folding efficiency and to reduce the maturation time, but they had no effects on its excitation and emission characteristics (Cormack *et al.* 1996, Tsien 1998, Iizuka *et al.* 2011). Therefore, both eGFP and mEmerald have the same optical properties, thus legitimizing the representative use of eGFP for mEmerald.

Overall, the optical compatibility between the optical units of the flow cytometer and the properties of the four selected fluorescent proteins was confirmed in a first step. However, potential challenges have been identified, including the possibly weak excitation of mCardinal2 with the third laser exciting at 640 nm. Moreover, there might be a risk of crosstalks between several fluorscent proteins at certain detection ranges.

5.2. *In vivo* fluorescence levels of simple reporter strains

Although the preliminary screening of excitation and emission spectra of the four fluorescent proteins mTagBFP2, eGFP, CyOFP1 and mCardinal2 confirmed a general optical compatibility with the lasers and detection filters of the flow cytometer, possible limitations were revealed. These include the weak excitation of mCardinal2 and possible crosstalks between several fluorescent proteins at certain detection ranges. Thus, the same *E. coli* single reporter strains were cultivated in shake flasks with LB medium at 37 °C

and 250 rpm overnight for the targeted expression of their respective reporter molecules. *E. coli* cells with plasmids for the recombinant production of CyOFP1 or mCardinal2 produced the reporter molecules constitutively. In contrast, cells expressing mTagBFP2 and eGFP were directly induced with 0.3 mM IPTG at the start of the cultivation. After recombinant expression of the fluorescent proteins, whole cells were separately measured with the flow cytometer. This study should further elucidate whether the four fluorescent proteins can be distinctively measured by each of the selected detection filters at 448/45 nm, 527/32 nm, 586/42 nm and 660/10 nm. Furthermore, the *E. coli* FUS4 strain was also included in this experiment to gain first information concerning the autofluorescence levels (Figure 5.3).
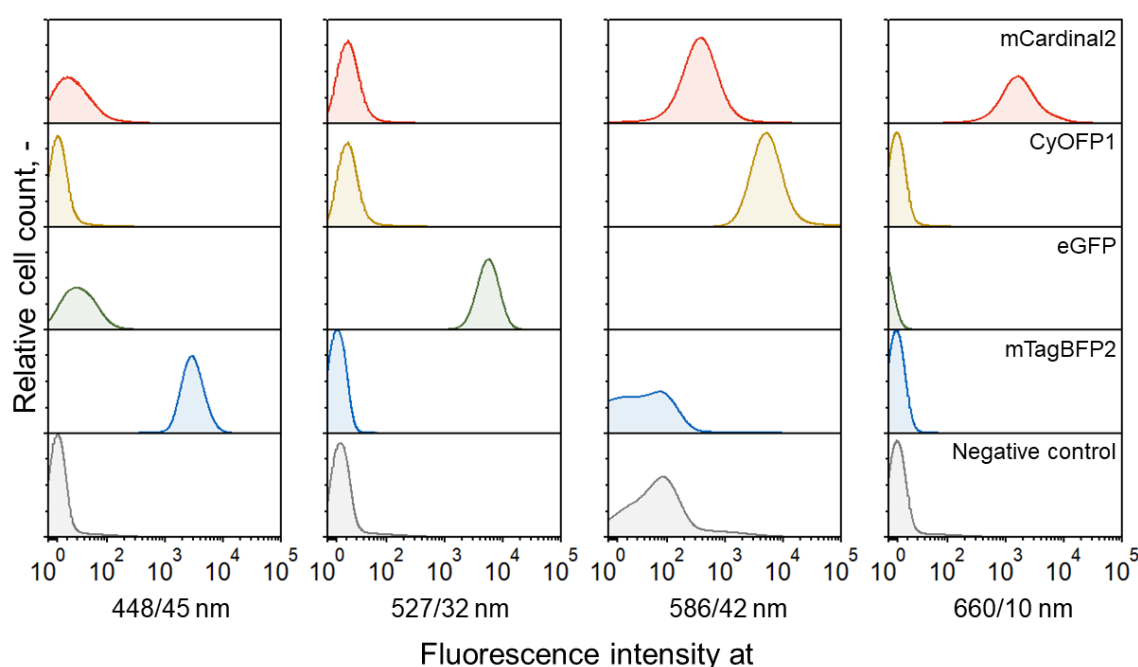
Figure 5.3: Preliminary monitoring of expressed fluorescence signals from four different *Escherichia coli* strains, which produced either mTagBFP2, eGFP, CyOFP1 or mCardinal2 during shake flask cultivations in LB medium at 37 °C and 250 rpm overnight. The LB medium of cells expressing mTagBFP2 and eGFP were enriched with 0.3 mM IPTG from the start of the cultivation. In contrast, CyOFP1 and mCardinal2 were produced constitutively in the respective *E. coli* cells. Whole cells were measured at the four different detection ranges 448/45 nm (PMT at 328 V), 527/32 nm (PMT at 294 V), 586/42 nm (PMT at 425 V) and 660/10 nm (PMT at 447 V). PMT levels of forward scatter (FCS) and side scatter (SSC) were set to 256 V and 348 V. The autofluorescence was measured using *E. coli* FUS4 cells, which expressed no fluorescent proteins. Histograms were plotted with a combined linear and logarithmic x-axis with the transition point at 25. The smoothing factor of the single-cell distributions was set to 50.

Each detection range of the flow cytometer is assigned to a single laser. For example, the first detection range at 448/45 nm monitored the emitted fluorescence intensities of *E. coli*

cells, which were excited by the first laser at 405 nm. Strikingly, only the histogram of cells with mTagBFP2 showed elevated fluorescence intensities at that range with a median value of $2.0 \cdot 10^3$, while all other *E. coli* strains expressed median values below $2.2 \cdot 10^1$. In contrary, cells excited by the second laser at 488 nm showed a different trend at 527/32 nm. In this range, only cells with eGFP had tremendeously higher fluorescence levels with a median value at $3.7 \cdot 10^3$, whereas all the other strains had median values of under $1.2 \cdot 10^1$. The same laser was also used for the excitation of cells, from which their emission signals were collected at 586/42 nm. Interestingly, cells expressing eGFP had a negative median value of $-1.5 \cdot 10^3$. Furthermore, both *E. coli* cells producing either CyOFP1 or mCardinal2 had elevated fluorescence intensities. Although the median value of the former is remarkably higher at $3.1 \cdot 10^3$ compared to the median value of cells with mCardinal2 at $2.2 \cdot 10^2$, a minority of both cell populations seemed to overlap at 586/42 nm. In contrast, cells expressing mTagBFP2 and the *E. coli* FUS4 host strain showed remarkably lower intensities with median values at $1.3 \cdot 10^1$ and $3.9 \cdot 10^1$, respectively. For the last detection filter of interest at 660/10 nm, all cells were excited by the third laser at 640 nm. Similar to the first two detection ranges at 448/45 nm and 527/32 nm, only the histogram of the cells expressing mCardinal2 stood out with elevated fluorescence intensities with a median value of $2.4 \cdot 10^3$, while all the others had median values below $3.0 \cdot 10^0$ (Figure 5.3).

Discussion

Considering the objective to integrate four fluorescent proteins in one strain, they need to be detected distinctively with low levels of crosstalks and background noises caused by autofluorescence. According to the histograms, this was clearly accomplished for the monitoring of mTagBFP2 at 448/45 nm, eGFP at 527/32 nm and mCardinal2 at 660/10 nm. All three stood out with elevated fluorescence intensities at the corresponding detection ranges compared to the other four *E. coli* cells expressing other or no reporter molecules. Only the remaining detection range at 586/42 nm emphasized a potential challenge to selectively detect CyOFP1 because *E. coli* cells expressing mCardinal2 showed elevated fluorescence signals, as well. Indeed, mCardinal2 could be replaced by a fluorescence protein with an excitation spectrum towards higher wavelengths. This would circumvent the residual excitation of the far-red fluorescent protein with the second laser at 488 nm and tremendeously reduce the chances of overlapping signals with CyOFP1 at 586/42 nm. However, it is important to note that mCardinal2 is among the best far-red and monomeric reporter molecules in terms of short maturation times and high brightness. Consequently, any potential substitutes would prolong the maturation times and lower the brightness, which ultimately complicate the detection of the far-red reporter

molecule (Chu *et al.* 2014). Thus, it was decided to rely on the selected four fluorescent proteins, but with the awareness of potential crosstalks between CyOFP1 and mCardinal2 at 586/42 nm. Furthermore, the magnitude of autofluorescence seemed to be the highest when *E. coli* FUS4 cells were excited at 488 nm with their corresponding emission at 586/42 nm. The fact of higher autofluorescence levels of *E. coli* cells when excited at 488 nm is well-described by Renggli *et al.* (2013). Nevertheless, the general magnitude of autofluorescence was comparably low in all considered detection ranges. The negative fluorescence levels measured at 586/42 nm of *E. coli* cells producing eGFP were probably caused by to the automatic compensation of the flow cytometer.

5.3. Design and characterization of the triple reporter strain

Proceeding towards the establishment of a quadruple reporter strain, a triple reporter strain was established as an intermediate step. *E. coli* FUS4 was used as a host strain, which is a derivative of the *E. coli* K-12 strain and well-described by numerous studies (Gottlieb *et al.* 2014, Weiner *et al.* 2014a, Weiner *et al.* 2016). As described in chapter 4.3, this strain was transformed to a triple reporter strain by integration of synthetic copies of mTagBFP2, mEmerald and CyOFP1 downstream the *rpoS* gene, into a synthetic *rrnB* promoter complex and into the *narGHIJ* gene cluster in a series of knock-in recombination reactions utilizing the λ-red mediated Flp/FRT recombination system.

After successful engineering of the *E. coli* triple reporter strain with the pF81$_{kan}$ plasmid (*E. coli* 3RP), two case studies were conducted to evaluate the general functionality and elucidate the impact of additional fluorescent protein expression on the cells. Therefore, batch cultivations in a stirred-tank bioreactor with chemically defined minimal medium enriched with 7 g L^{-1} glycerol and 0.05 g L^{-1} kanamycin were conducted with *E. coli* 3RP and *E. coli* FUS4 (pF81$_{kan}$). Samples during both processes were analyzed by flow cytometry at the relevant detection ranges at 448/45 nm (blue fluorescence), 527/32 nm (green fluorescence) and 586/42 nm (orange fluorescence).

Case study 1:
In case study 1, a conventional batch fermentation was performed under aerobic conditions. The dissolved oxygen levels were kept above 30% air saturation by stepwise increase of the stirrer speed. The purpose was the comparison of the growth behaviour of both strains together with the correlated expression of mEmerald as the marker for growth in the triple reporter strain. Furthermore, the general stress response levels of the reporter

strain shall be elucidated by monitoring of the exhibited blue fluorescences, which were anticipated to rise especially during the transition from the exponential phase to the stationary phase after depletion of the glycerol. At the same time, the oxygen limitation marker indicated by the orange fluorescence at 586/42 nm should not be activated in this case study due to fully aerobic conditions.

Growth of the *E. coli* triple reporter and the *E. coli* FUS4 (pF81$_{kan}$) strains followed the typical course of microbial growth after inoculation into a new environment (Figure 5.4 A). After an initial lag-phase of around 3 h, cells started to increase their biomass. With an initial concentration of 0.05 ± 0.05 g L^{-1} and 0.03 ± 0.03 g L^{-1} for the triple reporter and the host strains at 3 h of process time, the biomass amount rose exponentially within the next 7 h to a maximum cell concentration of 2.88 ± 0.2 g L^{-1} and 2.90 ± 0.05 g L^{-1}. Afterwards, the biomass concentrations started to decrease slightly. The corresponding maximum growth rates were at 0.63 h^{-1} for both strains. Interestingly, the expressed green fluorescence levels of the triple reporter strain particularly increased from 268.6 to 379.6 within the first 3 h of the process. A second, weaker rise from 376.2 to 406.3 was observed between 5 h to 6 h of process time, which simultaneously marked the maximum achieved fluorescence intensities at 527/32 nm. Directly after, the signals decreased to a mean value of 373.1 ± 7.4. In contrary, the expressed fluorescence levels of the host strain at 527/32 nm were between 49.1 and 88.7 and thus consistently lower with no clear trend (Figure 5.4 B).

Data of the glycerol concentrations confirmed the growth trends of the cells. While the substrate concentrations dropped slowly at the beginning of the process, their decrease became more pronounced at later process times. A complete depletion in both bioprocesses was observed at around 10 h (Figure 5.4 C), which matched with the transition of the cells from the exponential growth phase to the stationary phase (Figure 5.4 A). The associated general stress response levels of the triple reporter strain were measured at 448/45 nm. The triple reporter strain actually showed high general stress response levels at the start of the process with a signal intensity of 731.8, which immediately dropped to 600.8 within the first 3 h. During the exponential growth phase between 3 h to 9 h, intermediate fluorescence intensities were observed with an average of 662.6 ± 43.7. However, the signals increased after depletion of glycerol from 607.5 at 9 h of process time to 744.5 at the process end. Again, *E. coli* FUS4 (pF81$_{kan}$) showed remarkably lower fluorescence intensities at 448/45 nm with values below 20 (Figure 5.4 D).
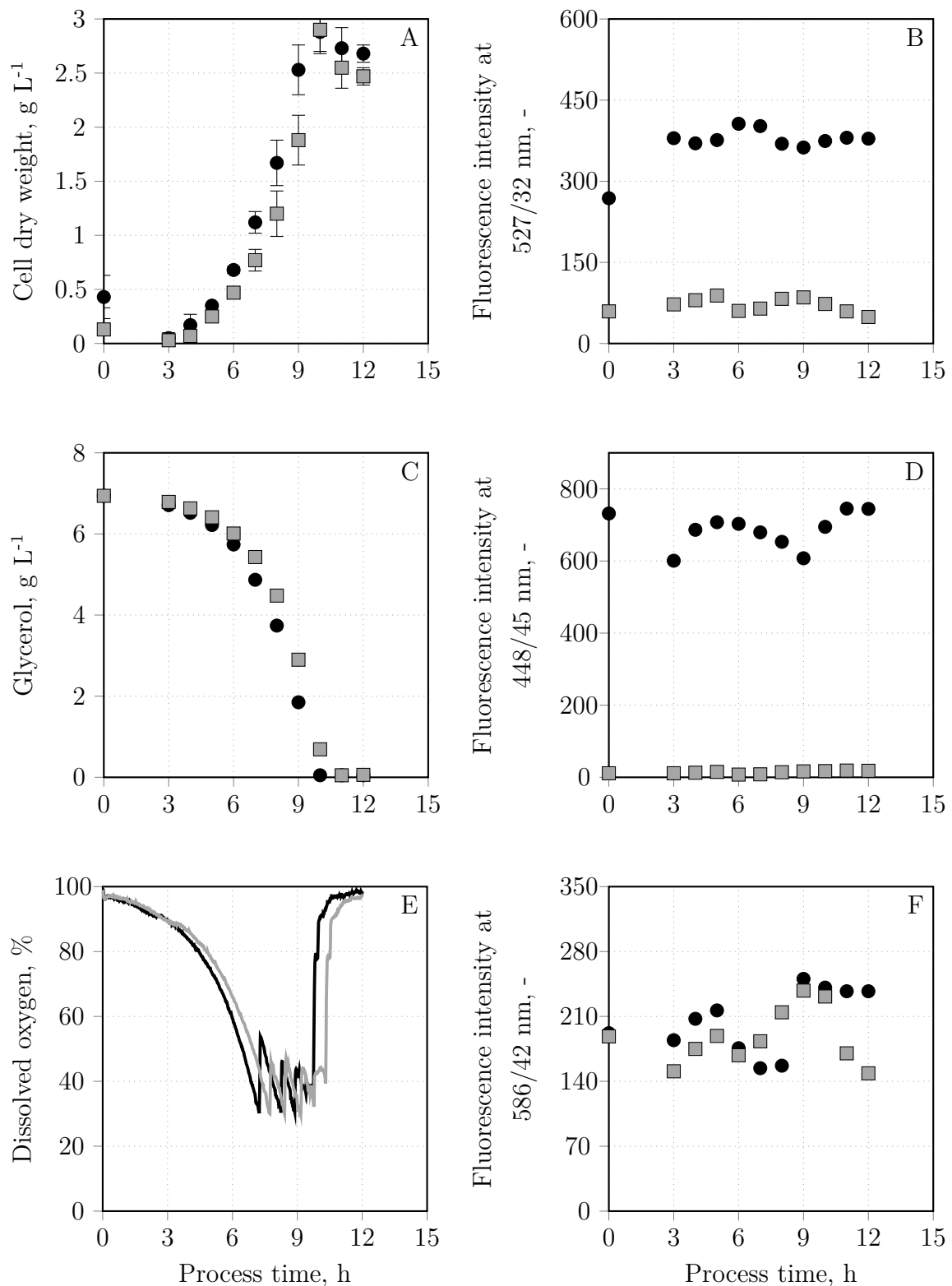
Figure 5.4: Case study 1: Cultivation of the *Escherichia coli* triple reporter strain ($\bullet$, ——) and *Escherichia coli* FUS4 (pF81$_{kan}$) ($\blacksquare$, ——) in a stirred-tank bioreactor as a batch process. (A) depicts the achieved cell dry weight concentrations over time, whereas (B) shows the fluorescence intensities measured at 527/32 nm. Glycerol concentrations are visualized in (C) and the expressed blue fluorescences at 448/45 nm in (D). Subplot (E) and (F) show the dissolved oxygen levels and the monitored fluorescence levels at 586/42 nm.

The dissolved oxygen levels during the batch cultivations with both strains decreased according to the observed trend in substrate concentrations. Between 7 h to 10 h of process time, the lowest dissolved oxygen levels of around 30% air saturation were observed. After the depletion of glycerol, they rose back to 100% air saturation (Figure 5.4 E). The measured fluorescence intensities of *E. coli* 3RP at 586/42 nm for monitoring of CyOFP1 fluctuated between 154.2 and 250.5, but showed no clear trend. This also applied for the fluorescence levels of the host strain, which showed similar fluorescence intensities between 150.8 to 237.9 (Figure 5.4 F).

Case study 2:

Case study 2 implemented a targeted simulation of anaerobic conditions during the conventional batch cultivation with both strains. This was realized by deactivating the increase of stirrer speed regardless of the prevailing dissolved oxygen levels and a further interruption of the aeration between 7 h to 10 h of process time. Hence, *E. coli* cells were temporarily exposed to oxygen limiting conditions to induce the expression of CyOFP1 in *E. coli* 3RP as the oxygen limitation marker.

After an initial lag phase of around 4 h, the biomass concentrations of both strains started to increase exponentially. In detail, cell concentrations rose from 0.20 ± 0.05 g L^{-1} to 1.65 ± 0.10 g L^{-1} for *E. coli* 3RP and from 0.13 ± 0.08 g L^{-1} to 1.12 ± 0.28 g L^{-1} for *E. coli* FUS4 (pF81$_{kan}$) between 4 h to 7 h of process time. This equals growth rates of 0.58 h^{-1} and 0.62 h^{-1} for *E. coli* 3RP and *E. coli* FUS4 (pF81$_{kan}$). Concomitant with the interruption of the oxygen supply at 7 h, the growth of both strains slowed down and the corresponding growth rates were reduced to approximately 0.16 h^{-1} in both cultivations. Accordingly, the biomass concentrations only increased marginally during this period. Directly after re-starting the aeration at 10 h, the cell growth slightly recovered with increased growth rates of 0.24 h^{-1} and 0.35 h^{-1} for *E. coli* 3RP and *E. coli* FUS4 (pF81$_{kan}$). The maximum achieved biomass concentrations were at 3 ± 0.24 g L^{-1} for the triple reporter strain and 2.85 ± 0.05 g L^{-1} for the host strain (Figure 5.5 A). The corresponding fluorescence intensities of the host strain at 527/32 nm remained constant between 43.0 to 75.7. In contrary, the triple reporter strain had higher fluorescence intensities directly at the start of the process with a value of 266.0. Within the first 6 h, the expressed intensities linearly increased to 424.4. However, they stagnated at a mean value of 396.0 ± 18.16 between 6 h to 10 h. Interestingly, a final rise of expressed signal intensities was observed at the process end towards a maximum value of 538.0 (Figure 5.5 B).
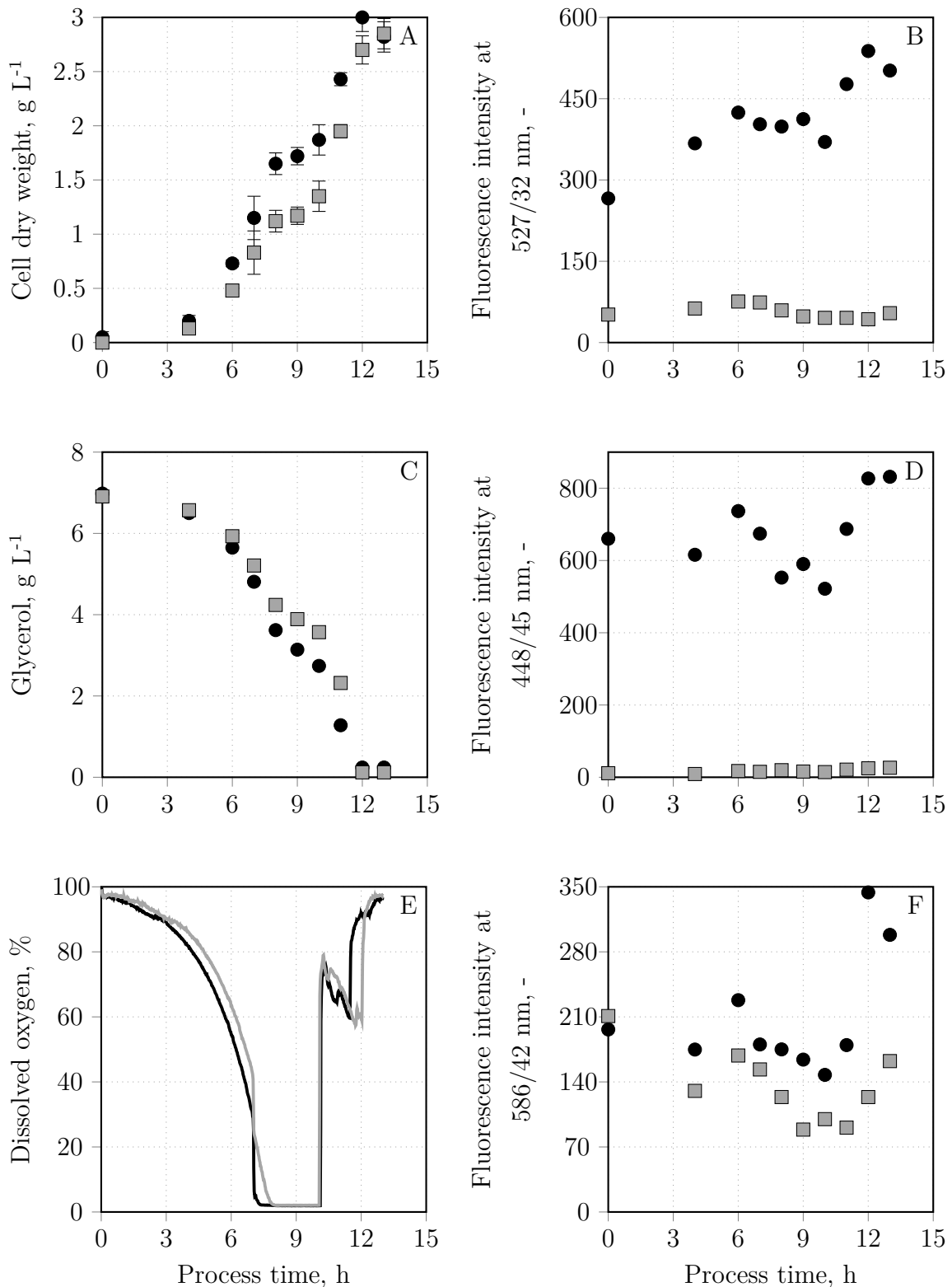
Figure 5.5: Case study 2: Cultivation of the *Escherichia coli* triple reporter strain (●, ——) and *Escherichia coli* FUS4 (pF81$_{kan}$) (■, ——) in a stirred-tank bioreactor as a batch process with targeted interruption of the oxygen supply from 7 h to 10 h of process time. While (A) shows the achieved cell dry weight concentrations over time, (B) depicts the fluorescence intensities measured at 527/32 nm. Glycerol concentrations and the expressed blue fluorescences at 448/45 nm are visualized in (C) and (D). Subplot (E) indicates the dissolved oxygen levels, whereas (F) shows the monitored fluorescence levels at 586/42 nm.

The substrate concentrations in both processes started to decrease slowly at the beginning of the process. Though the logarithmic decay of glycerol was observed for the first 7 h in both processes, the glycerol consumptions seemed to be slower after deactivation of the oxygen supply between 7 h to 10 h. In fact, the glycerol concentrations only sank from 4.81 g L^{-1} to 2.74 g L^{-1} during the cultivation of *E. coli* 3RP and from 5.21 g L^{-1} to 3.57 g L^{-1} with *E. coli* FUS4 (pF81$_{kan}$) during this time period. In comparison, the residual substrate amount was completely consumed after further 2 h in both processes after the oxygen supply was re-started (Figure 5.5 C). The corresponding fluorescence intensities at 448/45 nm indicated intermediate general stress response levels of the triple reporter strain for the first 7 h with a mean value of 671.8 ± 50.0. The fluorescence levels sank concomitant with the presence of anoxic conditions with the lowest value of 370.2 at 10 h of process time. However, re-starting the oxygen supply immediately led to a sharp increase of the expressed fluorescence intensities at 448/45 nm to a maximum value of 831.7 at the process end. In comparison, the *E. coli* FUS4 (pF81$_{kan}$) strain showed consistently lower intensities at 448/45 nm of under 30 (Figure 5.5 D).

Dissolved oxygen levels in both processes decreased within the first 7 h from 100% to around 40% air saturation. After interruption of the aeration at 7 h of process time, they immediately sank to 0%. With the re-activated aeration at 10 h, the dissolved oxygen levels steeply rose to around 80% air saturation in both processes, from where they slowly decreased for the next 2 h. At around 12 h of process time, the dissolved oxygen levels finally elevated to 100% air saturation (Figure 5.5 E). The corresponding fluorescence levels at 586/42 nm of the triple reporter strain and the host strain did not differ remarkably within the first 10 h with values between 88.7 and 228.0. Nevertheless, the fluorescence signals of the triple reporter strain were 22.7% higher compared to the autofluorescence signals of the host strain. The biggest differences were observed after the re-activation of the oxygen supply at 10 h. The fluorescence intensities of the triple reporter strain elevated from 179.6 at 11 h to 345.0 at 12 h, whereas the corresponding fluorescence level of the host strain remained at low levels of around 123.7 (Figure 5.5 F).

Discussion

Generally, the genetic modification of bacteria always requires two prerequisites: a host strain and a clear concept on how to modify the strain. In this instance, the *E. coli* FUS4 strain was used as a host strain, a derivative of the K-12 strain optimized for the inducible L-phenylalanine production. Considering the profound knowledge of the genomic structures of this strain and the available tools for further genetic modifications, it seemed to be a valid candidate to be transformed into a reporter strain (Sprenger 2007,

Gottlieb *et al.* 2014). More importantly, robust and reproducible process strategies for the cultivation of this strain were already established and approved by countless studies in stirred-tank bioreactor cultivations (Weiner *et al.* 2014b, Weiner *et al.* 2016).

Secondly, the triple reporter strain established by Heins *et al.* (2020) was used as a template for the genetic modification of the *E. coli* FUS4 strain. In their study, they integrated synthetic copies of mEmerald, mStrawberry and TagRFP657 downstream to the *rpoS* gene, into a synthetic *rrnB* promoter complex and into the *narGHIJ* operon to monitor the general stress response, growth behaviour and oxygen limitation in cells. While mStrawberry and TagRFP657 were exchanged by mTagBFP2 and CyOFP1 due to lower maturation times and better compatibility to the optical setup of the here used flow cytometer, the integration strategies were kept the same (Heins *et al.* 2020).

The *rpoS* gene was selected as the target gene for monitoring of the general stress response because it encodes for the alternative sigma factor RpoS. It represents a subunit of the RNA polymerase and is known as a global stress response molecule, which regulates the expression of approximately 500 genes related to higher stress resistances in *E. coli.* The expression of the sigma factor is strongly related to the availability of substrate. Consequently, RpoS levels in exponentially growing cells are expected to be rather low, whereas the transition to the stationary phase induce the expression of the *rpoS* gene (Battesti *et al.* 2011, Weber *et al.* 2005). In contrast, studies have shown that exponentially growing cells had elevated levels of ribosomal RNAs (rRNA) derived from the *rrnB* operon. These represent a crucial part of the ribosomes of the cells and thus regulate the translation initiation and the overall protein synthesis. Murray *et al.* (2003) showed that the *rrnB* expression is growth-rate dependent and increases at higher growth rates. Therefore, a synthetic copy of mEmerald was integrated into a *rrnB* promoter complex for monitoring of the growth behaviour of the cells. Regarding the monitoring of oxygen limitation, a synthetic copy of CyOFP1 was integrated into the *narGHIJ* operon, which encodes for major nitrate reductases in *E. coli.* It is especially activated at the presence of nitrate under anaerobic conditions. Hence, CyOFP1 was integrated into this operon for monitoring of the oxygen limitation in cells (Li & DeMoss 1987, Kiley & Reznikoff 1991).

Preliminary studies of the established triple reporter strain during batch cultivations in a stirred-tank bioreactor revealed first interesting insights. According to the biomass formation in both studies, the genetic modification and the additional expression of fluorescent proteins in the triple reporter strain did not affect its growth behaviour with similar (case study 1) or even better trends (case study 2) when compared to the host

strain. Moreover, the clearly elevated fluorescence levels at 527/32 nm during cultivations with the triple reporter strain confirmed the presence of expressed mEmerald molecules. While the fluorescence intensities were lower at the beginning of the batch fermentation, they increased concomitant with the increase of the growth rates. However, maximum intensities at 527/32 nm were often reached in the middle of the process (especially in case study 1), though cells had higher growth rates particularly towards the middle and the end of the process. Consequently, the growth behaviour of the cells can only be approximated by their expressed mEmerald levels, but the precise representation of prevailing growth rates seemed not possible (Murray *et al.* 2003). Nevertheless, plotting of the fluorescence levels at 527/32 nm divided by the corresponding OD_{600} values of the cell samples showed a positive correlation with the prevailing growth rates of the cell population (data not shown). This further underlines the functionality of this marker, which was also exemplified by Heins *et al.* (2020) using a similar *E. coli* reporter strain (Heins *et al.* 2020). The level of autofluorescence at this detection range was remarkably low as signals of *E. coli* FUS4 ($pF81_{kan}$) cells were more than 5 times lower than the expressed signals of the triple reporter strain. The general stress response in the triple reporter strain was signalized by blue fluorescence at 448/45 nm. As described previously, mTagBFP2 expression should arise especially when cells experience nutrient starvation (Dong & Schellhorn 2009, Battesti *et al.* 2011). This was successfully shown in both case studies, in which the expressed fluorescence intensities of the triple reporter strain increased particularly after depletion of the substrate. The level of autofluorescence shown from the host strain was 50 times lower. Finally, the monitoring of CyOFP1 was utilized for reflection of the oxygen limitation in cells. While case study 1 was not particularly designed to approve the functionality of this marker, case study 2 integrated a targeted interruption of the oxygen supply. Thus, anaerobic conditions were provided for 3 h during the batch cultivations in a stirred-tank bioreactor. During this time period, the fluorescence intensities at 586/42 nm did not increase. However, the re-activation of the oxygen supply led to an immediate rise of expressed fluorescence intensities in the triple reporter strain at 586/42 nm. Therefore, the prevailing oxygen limiting conditions were successfully reflected by the CyOFP1 marker despite the delayed occurrence of a signal. It is worth mentioning, that the autofluorescence of *E. coli* FUS4 ($pF81_{kan}$) at 586/42 nm was considerably higher than in other detection ranges. In fact, the fluorescence levels of the host strain were only 40% lower than the triple reporter strain on average, which needs to be considered in future experiments.

Case study 2 enabled further insights on the role of oxygen for the monitoring of fluorescent proteins at anaerobic conditions. Strikingly, fluorescence levels of all three reporter

molecules remained constant or even decreased slightly during the induced anaerobic phase between 7 h to 10 h of process time. Right after the re-activated supply of oxygen, the fluorescence levels of all three reporter molecules immediately increased, but with the steepest slope for CyOFP1. Most likely, molecular oxygen is mandatory for the maturation of fluorescent proteins. As shown by Heim *et al.* (1994) and Cubitt *et al.* (1995), the absence of oxygen postponed the maturation of GFP in *E. coli* cells as this chemical component is strictly required as an oxidizing agent (Heim *et al.* 1994, Cubitt *et al.* 1995, Zhang *et al.* 2006). Consequently, the here observed delay of CyOFP1 maturation might be related to the exposure of the *E. coli* triple reporter strain to anoxic conditions. This hypothesis is further underlined by the measured fluorescence intensities of mEmerald and mTagBFP2 at 527/32 nm and 448/45 nm, which also increased after the re-activated aeration. Hence, the presence of molecular oxygen in the cultivation medium seems to influence the dynamics of fluorescent signals.

A further challenge arise with the fact, that the measured fluorescence intensities at all three detection ranges remained constant even after the depletion of glycerol. Therefore, the expressed fluorescent proteins were not immediately degradated by intracellular proteases of the cells so that the *in vivo* half-life of the fluorescent proteins might be unintentionally long. Indeed, Andersen *et al.* (1998) found out that wildtype GFP variants remain stable in *E. coli* for several hours. However, later L-phenylalanine production processes based on the process strategy established by Weiner *et al.* (2016) are expected to last up to 90 h. Hence, the possibly slow degradation rates of fluorescent proteins might not be a major hindrance. Nevertheless, this aspect needs to be considered in later experiments.

5.4. Design and characterization of the quadruple reporter strain

Besides the already targeted general stress response, growth behaviour and oxygen limitation, the productivity of single cells is a decisive parameter in biotechnological production processes. To better understand the product formation in cells experiencing dynamic conditions and potentially elucidate coherences to the other three cellular characteristics, a last reporter molecule was integrated into the *E. coli* 3RP strain. In detail, the original plasmid was modified by integration of a synthetic copy of mCardinal2 downstream the *aroL* gene, but within the same gene expression cassette. Thus, the addition of IPTG should lead to a combined expression of L-phenylalanine producing enzymes and mCardinal2. As a result, all producing strains expectably show red fluorescence signals (Figure 5.6).
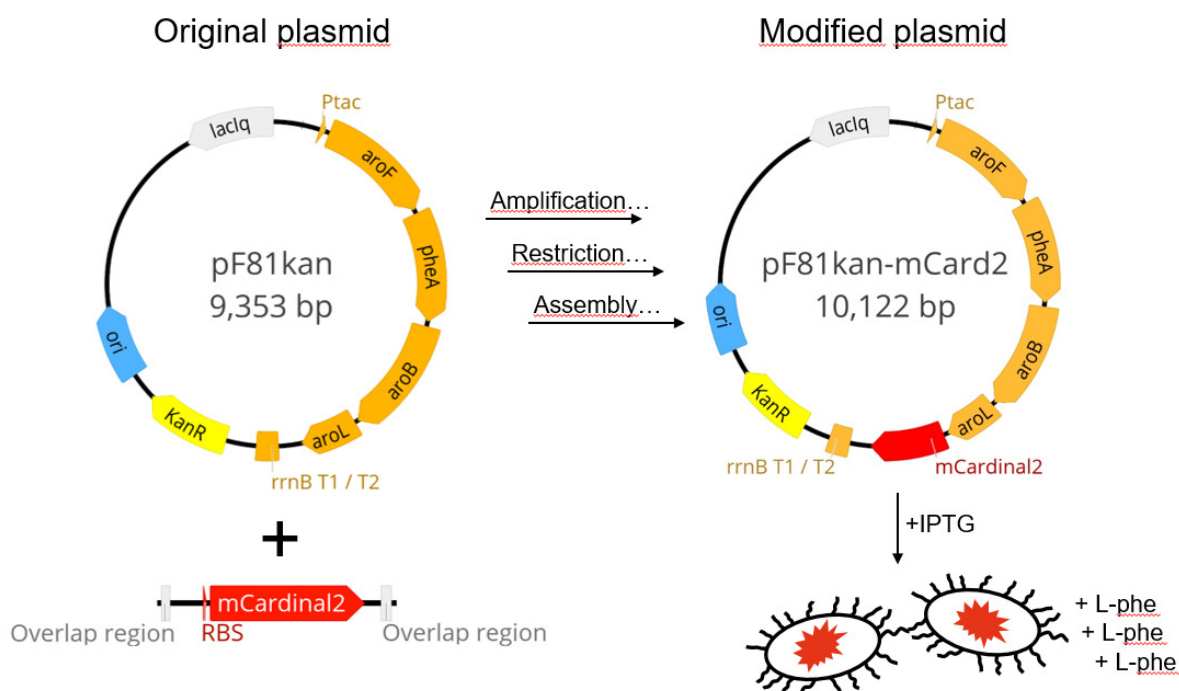
Figure 5.6: Schematic overview of the genetic modification of the pF81$_{kan}$ plasmid. A synthetic copy of mCardinal2 (provided by Chu *et al.* 2016) was inserted downstream the *aroL* gene, but in the same gene expression cassette and thus under the control of the native tac promoter. In a series of amplification, restriction and assembly reactions, the modified pF81$_{kan}$-mCardinal2 plasmid was established. Thus, IPTG addition to cells harbouring this modified plasmid should lead to L-phenylalanine production concomitant with the expression of red fluorescence signals.

Synthetic copies of the coding sequence of mCardinal2 were purified from the pNCS plasmid provided by Chu *et al.* (2016). The precise extraction of the gene sequence of interest was realized by overhang PCRs using the forward and reverse primers 5'-TGT TTA ACT TTA AGA AGG GGA TAT ACA TAT GGT GAG CAA GGG-3' and 5'-CTC ATC CGC CAA AAC AGA CGA ATT CAT TAC TTG TAC AG-3' (variant 1). This variant only targeted the coding sequence of the mCardinal2 protein and included a customized 5'-untranslated region with a ribosome binding site (RBS) to regulate later expression levels to approximately 100 000 according to the UTR designer by Seo *et al.* (2013). Moreover, a second variant was extracted from the pNCS plasmid, which covered the coding sequence of mCardinal2 and the upstream lying His, T7 and Xpress tags. Therefore, the previously used forward primer was substituted with the following primer: 5'-TCG AGC GCA TTT GTT AAC TT TAA GAA GGG-3'. Additionally, the *aroL* gene of the pF81$_{kan}$ plasmid was amplified by a further PCR reaction with the forward and reverse primers 5'-AAT CAG CGT AAC AAC AAG-3' and 5'-GTT AAA CAA ATG CGC TCG AAA ATC-3'. The missing pF81$_{kan}$ backbone without the *aroL* gene was provided by

restriction with HindIII. At the end, all three fragments (pF81$_{kan}$, *aroL* and variant 1 or variant 2 of mCardinal2) were joined by Gibson assembly. The modified plasmids were transformed into competent *E. coli* 3RP strains by electroporation with subsequent streaking of tranformed cells on LB agar plates with kanamycin. Three *E. coli* colonies with variant 1 of the modified plasmid and one colony with variant 2 of the modified plasmid were further analyzed by colony PCR with the primers 5'-AAT CAG CGT AAC AAC AAG-3' and 5'-CTT CTG CGT TCT GAT TTA ATC TG-3', which flank the *aroL* gene and the coding sequence of mCardinal2. Directly after, the genetic material of each PCR was separated on an agarose gel (Figure 5.7).
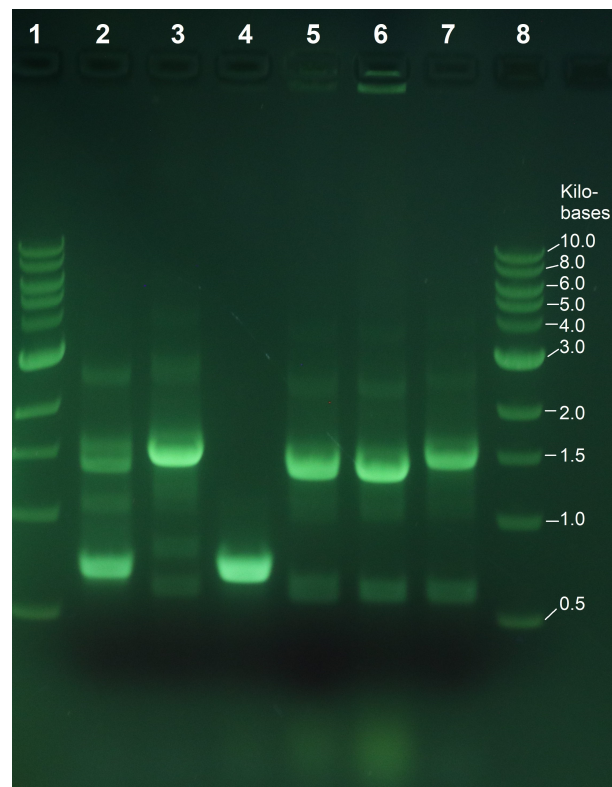
Figure 5.7: Agarose gel of the separated genetic material after colony PCR of *Escherichia coli* 3RP colonies after transformation of two variants of the modified pF81$_{kan}$-mCardinal2 plasmid. Lane 1 and 8 are 1 kb ladder samples with the corresponding kilobases of each band of the ladder on the right side. Lane 2 and 3 represent PCR reactions with the modified plasmid variants 1 and 2 deriving from the Gibson assembly reactions, while lane 3, 4 and 5 show PCR samples of colonies of *Escherichia coli* 3RP after transformation of variant 1 of the modified plasmid. Lane 6 visualize the PCR reaction with *Escherichia coli* 3RP harbouring the variant 2 of the modified plasmid.

Lane 2 and lane 3 represent the PCRs of the Gibson assembly of variant 1 and variant 2 of the modified pF81$_{kan}$ plasmid. While lane 4, 5 and 6 show the results of *E. coli* colonies derived from the transformation with variant 1 of the modified plasmid, lane 7 represents the genetic material from the *E. coli* colony with variant 2 of the modified

plasmid. Lane 1 and lane 8 show the 1 kb DNA ladder. Several bands were visible, but with the strongest at 0.75 kb and 1.5 kb. Most likely, colonies with a band at 1.5 kb had the correctly modified plasmids because only genetic fragments combining the *aroL* gene (591 bp) and the synthetic copy of mCardinal2 (variant 1 and 2 with 800 bp and 899 bp) should result to a band at approximately 1.5 kb. Therefore, the colonies in lane 5 to 7 harboured the correctly modified pF81$_{kan}$ plasmid. Consequently, colonies with bands at 0.75 kb most certainly held the original pF81$_{kan}$ plasmid. Interestingly, the sample derived from the Gibson assembly of variant 1 showed two bands at 0.75 kb and 1.5 kb (Figure 5.7, lane 2), thus indicating that both the original and the correctly modified plasmids were formed during this reaction. At the same time, this would explain why one of the colonies (Figure 5.7 lane 4) had a different band scheme compared to all the other colonies (Figure 5.7 lane 5 to 7). These assumptions were verified by further sequencing of the plasmids of all four colonies (data not shown).

After successful modification of the pF81$_{kan}$ plasmid and transformation into the *E. coli* triple reporter strain, the capability to express red fluorescence was checked by cultivation of the three colonies derived from the transformation of variant 1 of the modified plasmid. These were inoculated in 5 mL of LB medium in sterile cultivation tubes and were incubated at 37 °C and 180 rpm overnight. IPTG was added immediately at the start of the cultivation. The host strain was included in this study as a negative control (Figure 5.8). The *E. coli* strain with variant 2 of the modified plasmid was not further considered due to the presence of the tags that could have led to unwanted reactions with other molecules during later bioprocesses. As this risk was unpredictable, the further studies were continued solely with cells harbouring variant 1 of the modified plasmid. According to the measured fluorescence levels at 660/10 nm (Figure 5.8), colony 2 (V12, lane 5 in Figure 5.7) and colony 3 (V13, lane 6 in Figure 5.7) showed elevated intensities (median values at 515.5 and 512.9), whereas colony 1 (V11, lane 4 in Figure 5.7) exhibited similar fluorescence levels like the negative control (median values at 0.7 and 0). Consequently, only colony 2 and colony 3 had the modified pF81$_{kan}$ plasmid, while colony 1 was transformed with the original pF81$_{kan}$ plasmid.
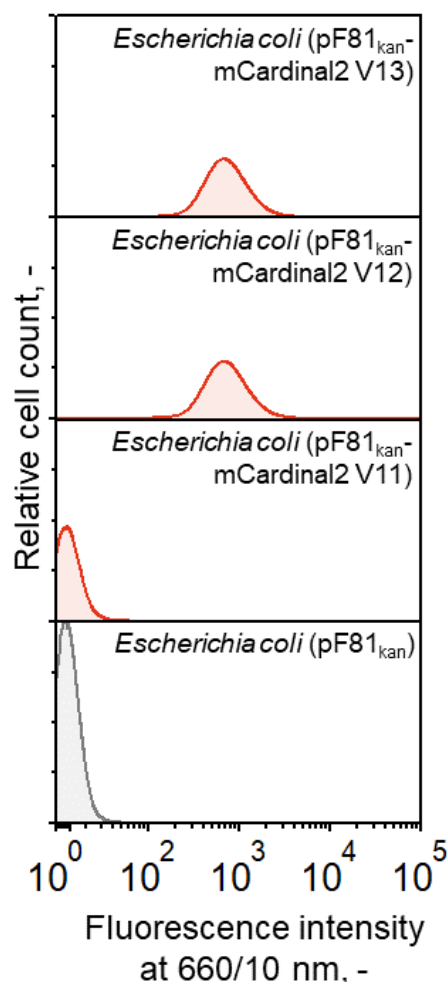
Figure 5.8: Stacked histograms of the three *Escherichia coli* (pF81$_{kan}$-mCardinal2) colonies with variant 1 of the modified plasmid, which were cultivated in sterile tubes with 5 mL of LB medium at 37 °C and 180 rpm overnight. All tubes were supplemented with 0.3 mM of IPTG at the start of the cultivation. Fluorescence intensities were measured at 660/10 nm (PMT at 500 V, FCS and SSC with PMT at 269 V and 337 V).

In a last experiment, the level of basal expression shall be investigated with cells harbouring the modified pF81$_{kan}$ plasmid. For this preliminary study, the modified pF81$_{kan}$ plasmid was transformed into an *E. coli* BL21 strain, which was cultivated in 50 mL Riesenberg medium in 250 mL shake flasks at 37 °C and 200 rpm. While one of the flasks was enriched with 0.3 mM IPTG at the start of the cultivation, the other was free of the inducer molecule. The comparison of the expressed fluorescence levels at 660/10 nm after 26 h of cultivation surprisingly showed high fluorescence intensities of cells, which were not induced with IPTG. In fact, they showed a median value of 68.0. Although the induced cells showed slightly higher intensities with a median value of 139.4, a majority of the induced cells ($> 50\%$) actually overlapped with the non-induced cells (Figure 5.9).
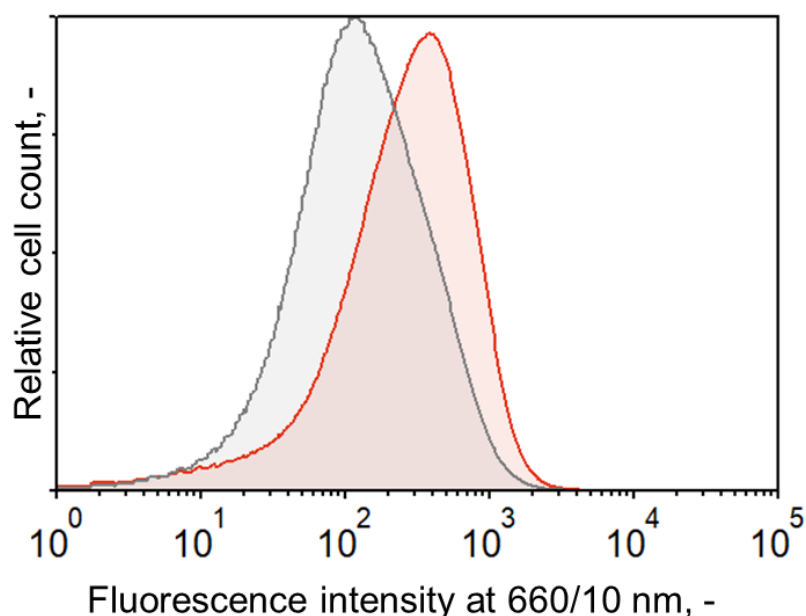
Figure 5.9: Overlaid histograms of *Escherichia coli* BL21 (pF81$_{kan}$-mCardinal2), which were cultivated in 250 mL shake flasks (37 °C, 200 rpm, 26 h) with 50 mL of Riesenberg medium. One shake flask was free of any IPTG (grey histogram), while the other shake flask was supplemented with 0.3 mM IPTG at the start of the cultivation (red histogram). Fluorescence intensities of the corresponding samples were measured at 660/10 nm (PMT at 500 V, FCS and SSC with PMT at 269 V and 337 V).

Discussion

By integration of a synthetic copy of mCardinal2 into the pF81$_{kan}$ plasmid, the intention was to couple the expression of the L-phenylalanine producing enzymes *aroF*, *pheA*, *aroB* and *aroL* to the expression of mCardinal2. To preserve the expression levels of the native genes within the original plasmid, the synthetic copy was inserted downstream all native genes as expression levels can be reduced the farther the gene position from the promoter (Lim *et al.* 2011). Despite the successful modification of the pF81$_{kan}$ plasmid and expression of red fluorescences during cultivations, the observed presence of mCardinal2 in cell suspensions without the addition of IPTG is a strong indicator for an unwanted basal expression. Although the tac promoter remains a popular choice for the design of recombinant strains in biotechnological applications due to the comparably high expression levels, their vulnerability for the unwanted premature expression of recombinant genes seemed well-known and ubiquitous (Terpe 2006, Francis & Page 2010). Indeed, there are plenty of other inducible expression systems available. Nonetheless, the promoter construction was not altered for this study. Exchanging the promoter would lead to completely different expression levels of the encoded genes on the pF81$_{kan}$ plasmid, which would affect the L-phenylalanine production. As a result, this would restrict any comparisons to the extensively characterized original strain (Weiner *et al.* 2016).

All in all, the *E. coli* FUS4 (pF81$_{kan}$) strain was successfully transformed into a quadruple reporter strain by insertion of synthetic copies of mTagBFP2, mEmerald, CyOFP1 and mCardinal2 downstream the *rpoS* gene, into a synthetic *rrnB* promoter complex, the *narGHIJ* operon or the pF81$_{kan}$ plasmid, respectively. While the detection of all reporter molecules was successfully demonstrated with flow cytometric measurements, their functionality will be further approved by application of these reporter strains for the L-phenylalanine production in a stirred-tank bioreactor.

6. L-phenylalanine production with *Escherichia coli* FUS4 strains in a stirred-tank bioreactor at laboratory scale[1]

The L-phenylalanine production described by Weiner *et al.* (2016) is a fed-batch process operated in a stirred-tank bioreactor with chemically defined medium and glycerol as a carbon source. It can be separated into an initial batch phase, a biomass production phase and a final product formation phase (see chapter 4.6.2 for the complete process strategy, Weiner *et al.* 2016). These processes were orignally conducted in a 42 L stirred-tank bioreactor with an initial working volume of 15 L. With the overall objective to establish a scale-down bioreactor for later investigation of the impacts of dynamic environmental conditions in bioprocesses, this reference process shall be transferred to a ten times smaller stirred-tank bioreactor. In the following are fed-batch processes for the L-phenylalanine production in a stirred-tank bioreactor at laboratory scale applying different *E. coli* FUS4 strains. The overall process strategy was adapted from Weiner *et al.* (2016), but with minor deviations described in chapter 4.6.2. Key performance indicators such as the maximum achieved biomass concentrations and L-phenylalanine titers will be evaluated and compared between the conducted cultivations. Moreover, the functionality of reporter strains will be examined to clarify whether the measured fluorescence levels of the cell population are in accordance with the related process state variables and ultimately support the understanding of certain cellular characteristics along the bioprocesses.

---

[1] Parts of the results in this chapter were pre-published in: Hoang *et al.* (2023a): Application of an *Escherichia coli* triple reporter strain for *at-line* monitoring of single-cell physiology during L-phenylalanine production. *Eng Life Sci* **23**: e2100162

6.1. *Escherichia coli* **FUS4 strain**

The first strain to apply for the L-phenylalanine production in a stirred-tank bioreactor with an initial volume of 1 L was the original *E. coli* FUS4 (pF81$_{kan}$) strain. The biomass concentration increased during the initial batch phase to 1.37 ± 0.12 g L^{-1} within the first 16.5 h (Figure 6.1 A) at a maximum growth rate of 0.22 h^{-1}.
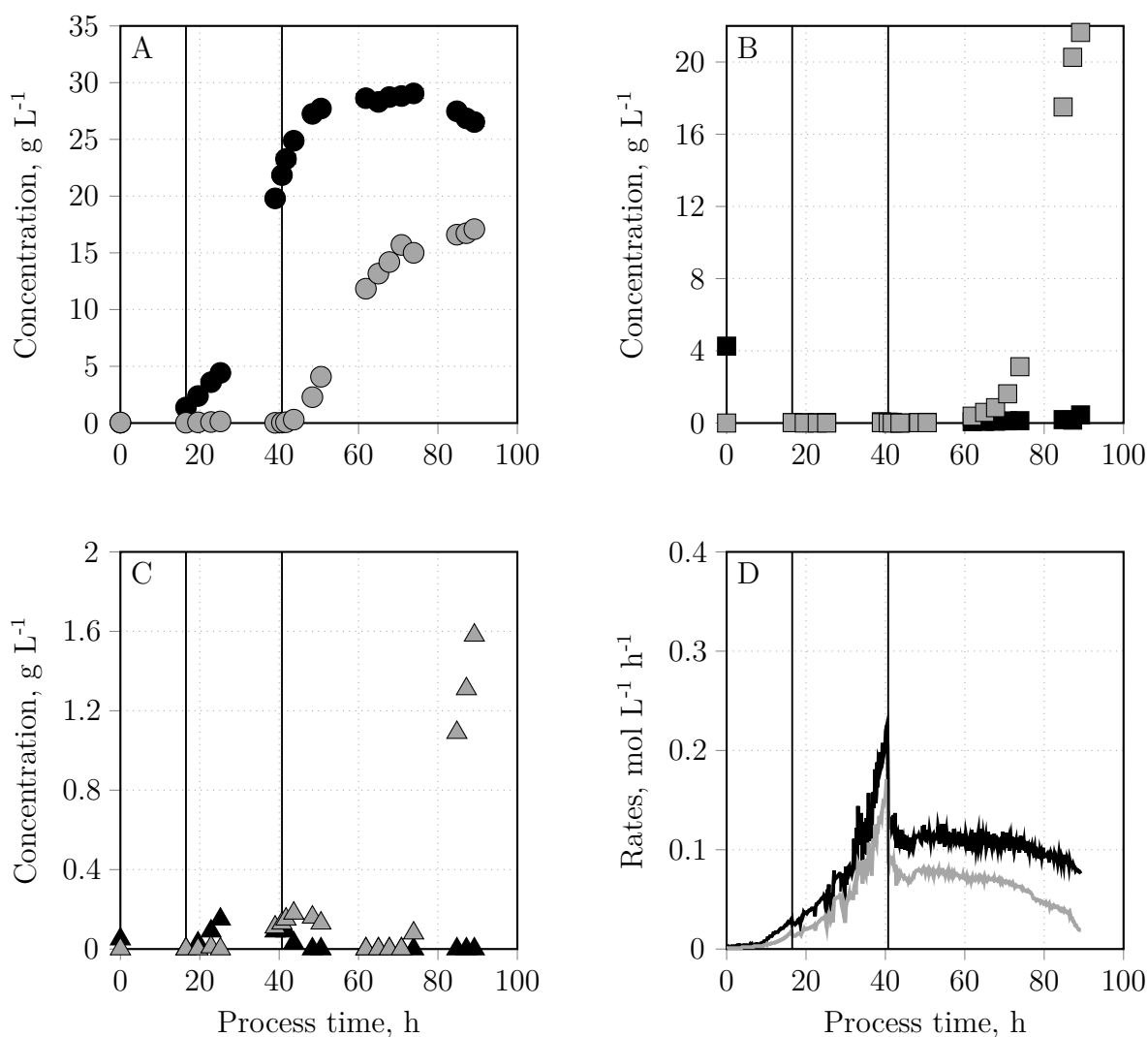
Figure 6.1: L-phenylalanine production with *Escherichia coli* FUS4 (pF81$_{kan}$) in a 3.6 L stirred-tank bioreactor. Subplot A shows the cell dry weight concentrations (●) and L-phenylalanine concentrations (◉), whereas subplot B represents the concentrations of glycerol (■) and acetate (▨). L-tyrosine (▲) and L-glutamate (△) are shown in subplot C, while subplot D shows the oxygen uptake rates (OUR, ———) and carbon dioxide evolution rates (CER, ———). This process was operated as a fed-batch process with an initial batch phase, a subsequent biomass production phase with exponential feeding and a final product formation phase with constant feeding. Verticals at 16.5 h and 40.7 h separate the phases. Process strategy: $V_0 = 1$ L, T = 37 °C, pH = 7, DO $\geq$ 30%, exponential feeding with $\mu_{set} = 0.1$ h^{-1}, constant feeding of 0.18 g$_{substrate}$ g$_{Biomass}$$^{-1}$ h^{-1} after induction of cells with 0.3 mM IPTG.

Concomitant with the cell growth was the complete consumption of 4 g L^{-1} glycerol, so that the exponential feeding was activated directly after (Figure 6.1 B). Accordingly, the biomass concentration further rose linearly, but with a decreased average growth rate of 0.12 $\pm$ 0.04 h^{-1}. The different slopes observed in the early and late biomass production phases were due to the two used feeding solutions with a lower concentrated solution (120 g L^{-1} glycerol) at the start and a higher concentrated solution (400 g L^{-1} glycerol) at the second half of this phase. Accumulations of L-phenylalanine, L-tyrosine or L-glutamate were not found during this phase with concentrations below 0.2 g L^{-1} (Figure 6.1 AC). Additionally, the oxygen uptake rates (OUR) and carbon dioxide evolution rates (CER) exponentially increased from 0.03 mol L^{-1} h^{-1} and 0.01 mol L^{-1} h^{-1} to maximum values of 0.27 mol L^{-1} h^{-1} and 0.16 mol L^{-1} h^{-1} towards the end of the biomass production phase at 40.7 h (Figure 6.1 D). At that time, the cell population reached a biomass amount of 21.85 $\pm$ 0.23 g L^{-1} so that the recombinant protein expression was induced with 0.3 mM IPTG, followed by a constant feeding during the product formation phase. Interestingly, the cell growth still continued until the residual L-tyrosine was completely depleted at 60 h of process time. A maximum biomass concentration of 29.05 $\pm$ 0.43 g L^{-1} was reached at 73.9 h. Simultaneously with the start of the product formation phase, the L-phenylalanine concentration started to increase after an initial lag phase of 3 h into this phase. Afterwards, the product concentration constantly rose until 89 h of process time to a maximum product concentration of 17.09 g L^{-1} (Figure 6.1 A). The corresponding maximum and average biomass specific product formation rates were at 24.68 mg $g_{Biomass}^{-1}$ L^{-1} and 12.52 mg $g_{Biomass}^{-1}$ L^{-1} with a maximum product yield of 0.21 g g^{-1}. During the product formation phase, both the OUR and CER dropped to 0.12 mol L^{-1} h^{-1} and 0.09 mol L^{-1} h^{-1} with a decreasing tendency until the process ended (Figure 6.1 D). It is worth mentioning that the diminishing L-phenylalanine formation at the process end was accompanied by the accumulation of acetate and L-glutamate, which started at around 70 h of process time (Figure 6.1 B).

The autofluorescence levels of _E. coli_ FUS4 (pF81$_{kan}$) at 448/45 nm, 527/32 nm, 586/42 nm and 660/10 nm, which corresponds to the relevant detection ranges for the monitoring of the general stress response (mTagBFP2), growth behaviour (mEmerald), oxygen limitation (CyOFP1) and product formation (mCardinal2) of the _E. coli_ reporter strains, were constantly measured during the L-phenylalanine production process. However, no dynamic trends were observed for all considered detection ranges within the first 80 h of process time. For example, the fluorescence intensities at 448/45 nm were at 28.33 $\pm$ 3.97, while intensities at 527/32 nm fluctuated marginally at around 74.03 $\pm$ 6.47 (Figure 6.2 AB). Relatively elevated fluorescence levels of 264.83 $\pm$ 13.89 were found at

586/42 nm, whereas no red fluorescence signals were measured at all (Figure 6.2 CD). Strikingly, the fluorescence intensities at 448/45 nm, 527/32 nm and particularly at 586/42 nm increased towards the end of the process with maximum values of 58.73, 99 and 466.96. This is equivalent to a 107.3%, 33.7% or 76.3% increase of measured fluorescence intensities compared to the average values of the first 80 h (Figure 6.2 ABC).

Figure 6.2: Expressed median autofluorescence intensities of the *Escherichia coli* FUS4 (pF81$_{kan}$) strain at different detection ranges during the L-phenylalanine production in a stirred-tank bioreactor. Vertical lines separate the initial batch phase, the biomass production phase and the final product formation phase. The threshold of the SSC-W was set to 922 V. PMT levels of FSC, SSC and the 660/10 nm filter were set to 250 V, 335 V and 500 V, respectively.

Discussion

The here conducted L-phenylalanine production process with *E. coli* FUS4 (pF81$_{kan}$) was operated in a stirred-tank bioreactor with a more than ten times lower starting volume of 1 L compared to the reference process described by Weiner *et al.* (2016) with a starting volume of 15 L. Nevertheless, the general trend of the biomass production was similar. For example, the cell dry weight concentration at the end of the biomass production phase was at 21.85 g L^{-1} at 40.7 h in the here shown cultivation, while a biomass concentrations of 21.88 g L^{-1} was observed in the reference process after 43.2 h. Additionally, both bioprocesses were characterized by further cell growth even after the initiation of the product formation phases. Though the applied feeding solution contained no L-tyrosine, the continued cell growth can be explained by the residual L-tyrosine amount in the cultivation medium, which accumulated during the previous biomass production phase. As soon as this aromatic amino acid was fully depleted, the biomass concentration remained approximately constant until the process end. This was also observed by Weiner *et al.* (2016). Hence, the cell growth and L-phenylalanine formation were successfully decoupled (Sprenger 2007). Also, the here observed maximum biomass concentration of 29.05 g L^{-1} was similar to the maximum biomass amount of 31.03 g L^{-1} achieved by Weiner *et al.* (2016), which means a minor reduction of 6.32%.

The L-phenylalanine production can be summarized as a combination of several trends. First, there was an initial lag-phase, probably due to the remaining growth of the cells and thus the further consumption of L-phenylalanine. Afterwards, the product concentration constantly rose for the next 40 h. However, a progressive decline of the product formation was observed towards the process end, which was further accompanied by the accumulation of both acetate and L-glutamate (Weiner *et al.* 2016). The former aspect was recently elucidated by Schoppel *et al.* (2022), in which a similar *E. coli* strain was used for the targeted L-tryptophane production. The vanishing ability of cells to form further product was explained as a result of methylglyoxal accumulation. Cells seemed to produce this metabolite as an adaptation strategy to counter prevailing nutrient imbalances. In fact, it is described that the cellular methylglyoxal production can support cellular survival under certain environmental conditions (Ferguson *et al.* 1998). However, when surpassing a certain titer, methylglyoxal seemed to have toxic effects on *E. coli* cells (Schoppel *et al.* 2022). Assuming similar effects in the here used *E. coli* strain for the L-phenylalanine production, the reduced product formation towards the process end most likely derived due to an increasing number of inhibited or dead cells. Because L-glutamate is an important co-substrate for the L-phenylalanine synthesis, a diminished production of this aromatic amino acid led to the observed accumulation of L-glutamate.

Furthermore, other by-products such as acetate increased at that time. Most likely, the carbon fluxes were directed to other pathways instead of the aromatic amino acid biosynthesis (Weiner *et al.* 2014b, Weiner *et al.* 2016). However, despite having a similar product forming trend, the maximum achieved L-phenylalanine concentration in the here conducted bioprocess was remarkably lower compared to the reference process. In fact, Weiner *et al.* (2016) described a maximum L-phenylalanine concentration of 22.78 g L^{-1}, whereas only 17.09 g L^{-1} of product was produced in a stirred-tank bioreactor with a starting volume of 1 L, which means a loss of almost 25%.

A possible reason could be the differently prepared feeding solutions. Normally, the feeding solutions 1 and 2 in the reference process were enriched with the chemically defined minimal medium. Consequently, components such as calcium chloride, iron-(II) sulfate, magnesium sulfate and thiamine were consistently supplied during the biomass production phase. However, this exact procedure was not applicable for the here conducted L-phenylalanine production process at laboratory scale, because the addition of the chemically defined minimal medium to the feeding solutions 1 and 2 always led to the insolubility of L-tyrosine. While this was no challenge in the reference process as the used diameter of the tubing valves were big enough to circumvent any clogging, tubing valves with smaller diameters had to be used in the here conducted bioprocess to allow lower feeding rates due to the lower working volume. As a result, the insolubility of L-tyrosine always caused an immediate clogging of the tubing valves, thus complicating the feeding strategy. This problem was solved by the addition of either ammonia or potassium hydroxide to the feeding solutions 1 and 2 to completely dissolve L-tyrosine and enable pumping of the solutions through the tubing valves with a small diameter. To compensate the missing supply of chemically defined minimal medium components during the biomass production phase, the corresponding medium components were injected at the start and the middle of the biomass production phase. However, cells were constantly fed with an alkaline feeding solution during the biomass production phase, which synthetically changed the general medium composition with higher ion concentrations and potentially influenced the product formation of the cells.

A further explanation might be the dissolved oxygen levels during the product formation phase. Gottlieb *et al.* (2014) stated higher DO levels of around 60% air saturation to result in a lower L-phenylalanine production for the same *E. coli* FUS4 strain. The authors suggested that DO levels of 20% air saturation would be optimal and assumed higher oxygen levels to enhance the carbon flux towards the tricarboxylic acid cycle. This would favour the by-product formation, whereas the carbon flux towards the pentose phosphate

pathway would be reduced (Gottlieb *et al.* 2014). While the dissolved oxygen levels in the here described process circulated between 40% to 60% air saturation during the product formation phase, the reference process of Weiner *et al.* (2016) also kept the minimum DO levels above 40% air saturation. However, it remains unclear whether the dissolved oxygen levels also circulated between 40% to 60% air saturation or were consistently close to the minimum DO levels as this particular data was not published (Weiner *et al.* 2016). As long as the concrete reasons for the lower product formation cannot be identified, the here established process strategy will be further considered as the template for later cultivations in a stirred-tank bioreactor at laboratory scale.

The intrinsic natural fluorescence of cells, which is known as autofluorescence, originates from the presence of fluorescent components and metabolites (Surre *et al.* 2018). These autofluorescence levels vary based on the considered detection regions. As stated by Wiedenmann *et al.* (2002), the level of autofluorescence is comparably low in the far-red regions, which was approved by the lowest signal intensities of *E. coli* FUS4 (pF81$_{kan}$) cells at 660/10 nm. Additionally, relatively low intensities were also observed at 448/45 nm and 527/32 nm, whereas comparably high levels of autofluorescence were present at 586/42 nm. Most striking was the sudden increase of fluorescence levels at 448/45 nm, 527/32 nm and 586/42 nm towards the end of the bioprocess. Cells that are struggling for survival often show higher autofluorescence levels. This is due to the formation of fluorescent metabolites such as flavins to initiate the energy production and detoxification processes (Renggli *et al.* 2013, Surre *et al.* 2018). In this instance, the here observed rise of autofluorescence levels might have been a response of the cells to the expected nutrient limitation, which additionally induced the methylglyoxal production to toxic concentrations. Therefore, cell viability measurements using DNA-binding dyes such as SYTO9 or propidium iodide could be interesting to confirm this hypothesis in future studies (Lehtinen *et al.* 2004).

6.2. *Escherichia coli* triple reporter strain

With an established process strategy for *E. coli* FUS4 (pF81$_{kan}$) to produce L-phenyl-alanine in a stirred-tank bioreactor at laboratory scale, the same setup was applied for L-phenylalanine production with the *E. coli* triple reporter strain (*E. coli* 3RP). The biomass concentration exponentially increased to 1.42 ± 0.06 g L^{-1} during the initial batch phase with a corresponding growth rate of 0.22 h^{-1} (Figure 6.3 A). This was accompanied by the complete consumption of 4 g L^{-1} glycerol within the first 15 h of process time (Figure 6.3 B). Accordingly, the exponential feeding was started for the biomass production phase. Similiar to the cultivation of the host strain, the cell concentration

rose linearly with a reduced average growth rate of 0.12 ± 0.03 h^{-1}. After 42.2 h of process time, a biomass concentration of 22.13 ± 0.14 g L^{-1} was reached (Figure 6.3 A). While the corresponding concentrations of L-phenylalanine and L-tyrosine remained under 0.22 g L^{-1}, a slightly higher accumulation of L-glutamate at 0.51 g L^{-1} was present in this process (Figure 6.3 AC).

Figure 6.3: L-phenylalanine production with the *Escherichia coli* triple reporter strain in a stirred-tank bioreactor. Subplot A shows the cell dry weight concentration (●) and L-phenylalanine concentration (◐), whereas subplot B represents the concentrations of glycerol (■) and acetate (▨). L-tyrosine (▲) and L-glutamate (△) are shown in subplot C, while subplot D shows the oxygen uptake rates (OUR, ▬) and carbon dioxide evolution rates (CER, ▬). This process was operated as a fed-batch process with an initial batch phase, a subsequent biomass production phase with exponential feeding and a final product formation phase with constant feeding. Verticals at 15.0 h and 42.2 h separate the phases. Process strategy: $V_0 = 1$ L, T = 37 °C, pH = 7, DO $\geq$ 30%, exponential feeding with $\mu_{set} = 0.1$ h^{-1}, constant feeding of 0.18 g$_{substrate}$ g$_{Biomass}$$^{-1}$ h^{-1} after induction of cells with 0.3 mM IPTG.
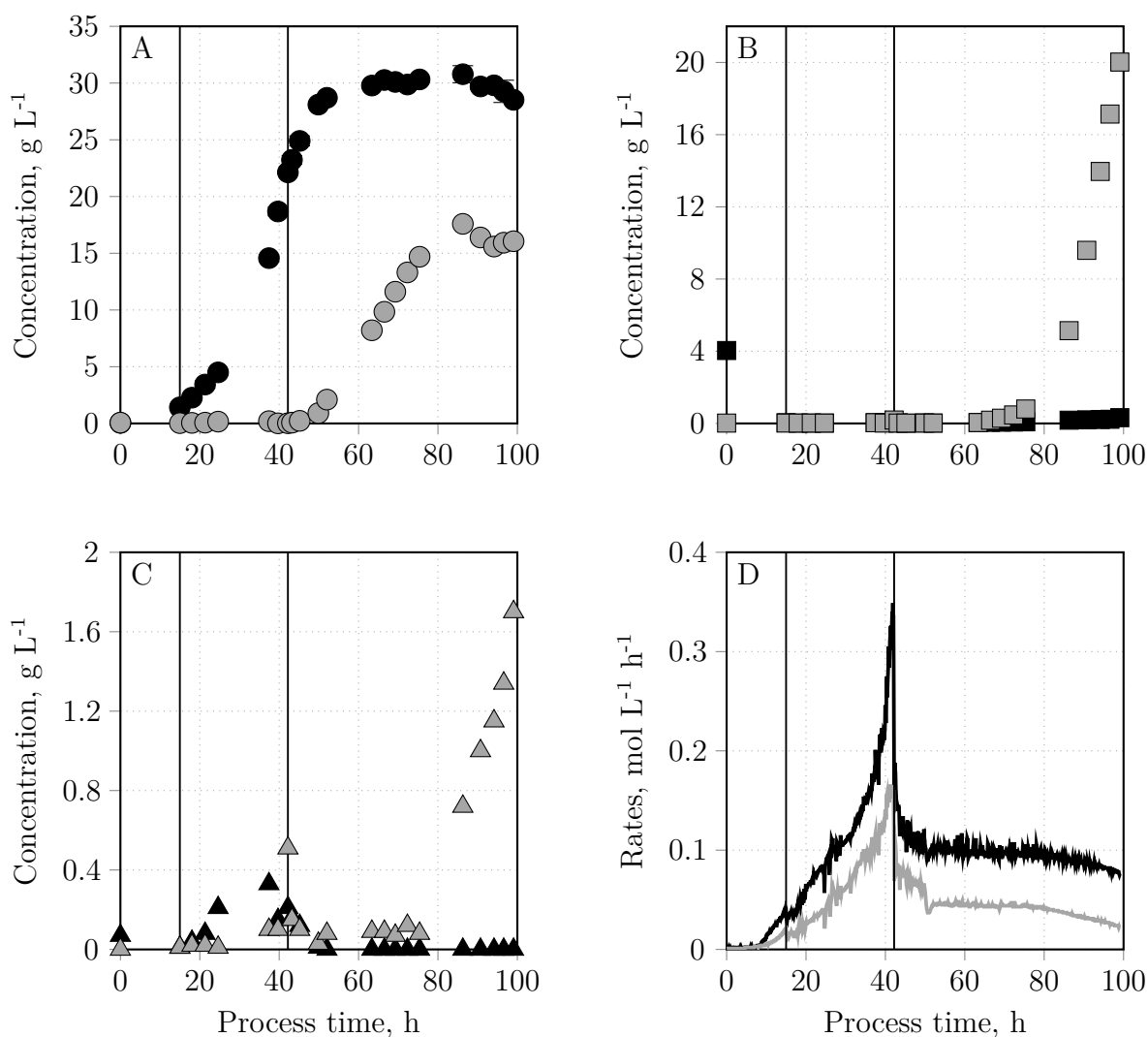
Additionally, this phase was accompanied by the exponential rise of the OUR and CER to their maximum values at 0.35 mol L^{-1} h^{-1} and 0.16 mol L^{-1} h^{-1}, respectively. However, both rates immediately dropped to 0.13 mol L^{-1} h^{-1} and 0.07 mol L^{-1} h^{-1} with the induction of recombinant protein expression with IPTG and the start of the product formation phase at 42.2 h (Figure 6.3 D). At the same time, the cell growth was still present in the first 10 h of this phase, probably due to the residual consumption of L-tyrosine. Maximum cell concentrations of 30.78 $\pm$ 0.75 g L^{-1} were achieved at 86.3 h of process time. The L-phenylalanine production between 42.2 h to 86.3 h led to a maximum L-phenylalanine concentration of 17.59 g L^{-1}. Accordingly, the maximum and average achieved biomass specific product formation rates were at 19.49 mg $g_{Biomass}^{-1}$ h^{-1} and 11.91 mg $g_{Biomass}^{-1}$ h^{-1}, respectively (Figure 6.3 A). The maximum product yield was at 0.22 g g^{-1}. Similarly to the previous process, the L-phenylalanine production slowly diminished at around 86.3 h, which was concomitant with the accumulation of acetate (Figure 6.3 B) and L-glutamate (Figure 6.3 C). Furthermore, a reduction of both the OUR and CER was observed at around 80 h (Figure 6.3 D).

Besides the production of L-phenylalanine, *E. coli* 3RP also expressed the three fluorescent proteins mTagBFP2, mEmerald and CyOFP1 to gain information regarding the general stress response, growth behaviour and oxygen limitation of the cells at different stages of the bioprocess. The general stress response was represented by the expression of mTagBFP2, which was measured at 448/45 nm. At the end of the initial batch phase at 15 h, the blue fluorescence intensity was at 1259.49 $\pm$ 15.91. However, the start of the biomass production phase was accompanied by a steep rise to 1602.75 $\pm$ 18.63 at 24.6 h, which was the maximum measured intensity at this detection range. Towards the end of the biomass production phase, these elevated signal levels decreased strongly from 1487.54 $\pm$ 10.37 at 37.4 h to 972.51 $\pm$ 69.70 at the beginning of the product formation phase at 42.2 h. Directly after induction of the recombinant protein expression with IPTG, the expressed mTagBFP2 levels increased again to a second maximum signal intensity of slightly above 1500 between 69.3 h and 75.4 h. Towards the process end, the monitored signals at 448/45 nm finally dropped to 1096.40 $\pm$ 6.10 (Figure 6.4 A).

The growth behaviour of cells was monitored by the expression of mEmerald2, which was measured at 527/32 nm. At the end of the initial batch phase at 15 h, cells showed their maximum intensity signals of 576.22 $\pm$ 3.93. In the following, the expressed signals slightly diminished, but remained at intermediate levels of around 421.59 $\pm$ 46.83 during the biomass production phase. Prior to induction of the cells, the expressed fluorescence levels at 527/32 nm began to decrease, which was also seen during the monitoring of

the general stress reponse at 448/45 nm. This decreasing trend at 527/32 nm continued after the start of the product formation phase with the lowest average signal values of 272.10 ± 28.03 (Figure 6.4 B).
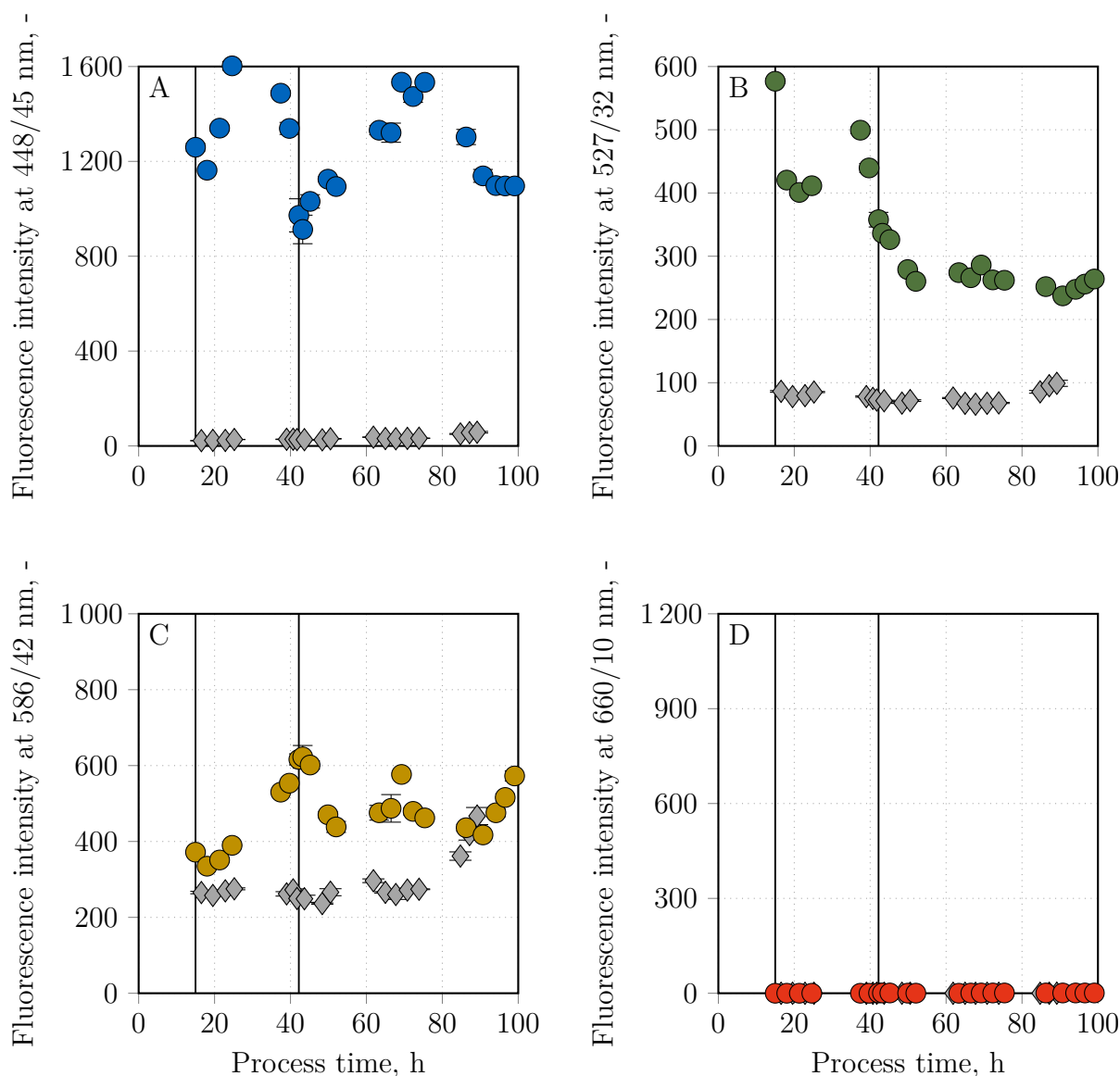
Figure 6.4: Expressed median fluorescence intensities of the *Escherichia coli* triple reporter strain at 448/45 nm (general stress response, ●), 527/32 nm (growth behaviour, ●), 586/42 nm (oxygen limitation, ●) and 660/10 nm (product formation, ●) during the L-phenylalanine production in a stirred-tank bioreactor. Vertical lines separate the initial batch phase, the biomass production phase and the final product formation phase. The threshold of the SSC-W was set to 922 V. PMT levels of FSC, SSC and the 660/10 nm filter were set to 250 V, 335 V and 500 V, respectively. Grey data points (◆) in each subplot represent the measured autofluorescence of the *E. coli* FUS4 (pF81$_{kan}$) host strain at the respective detection range during a separately performed L-phenylalanine production process with the same process strategy (see Figure 6.1 and Figure 6.2).

In contrary, the fluorescence intensities at 586/42 nm are indicators for a possible oxygen limitation. When cells experience such conditions, the signal intensities at this detection range should rise due to the expression of CyOFP1. At the beginning, the measured signals were rather low at 371.73 ± 1.74. However, a constant increase of expressed fluorescence intensities was visible along the biomass production phase with a maximum peak intensitiy of 622.92 ± 30.05 at the end of this phase. Similarly to the green fluorescence marker, the orange fluorescence intensities dropped to an average value of 471.46 ± 45.77 between 49.9 h and 90.7 h. A final rise to 572.72 ± 13.15 was observed at the end of the L-phenylalanine production process (Figure 6.4 C).

No red fluorescence signals were expressed from the triple reporter strain as the average signal intensities at 660/10 nm were at 0.48 ± 0.39 (Figure 6.4 D). This was anticipated because this strain does not harbour a synthetic copy of mCardinal2 in the $pF81_{kan}$ plasmid.

A direct comparison of the expressed fluorescence levels of the *E. coli* triple reporter strain with the autofluorescence levels of the *E. coli* FUS4 ($pF81_{kan}$) strain showed consistently higher fluorescence levels of the modified *E. coli* 3RP cells. For example, the achieved fluorescence levels of the triple reporter strain at 448/45 nm were more than 15 times higher compared to the host strain. Similarly to the results of the preliminary characterization studies described in chapter 5, the autofluorescence levels of *E. coli* FUS4 ($pF81_{kan}$) seemed higher at 527/32 nm and highest at 586/42 nm. Nevertheless, the triple reporter strain showed at least twice as high or equal fluorescence levels at the respective detection ranges (Figure 6.2 and 6.4).

Discussion

Although reporter strains such as the here established *E. coli* 3RP potentially provide insights into certain cellular characteristics based on the expressed fluorescence levels, genetic modifications and the constant production of fluorescent proteins during bioprocesses might endanger the cellular integrity and increase the metabolic burden of the producing cells (Ow *et al.* 2006, Liu *et al.* 2018b, Lozano Terol *et al.* 2021). However, direct comparisons of key process parameters such as maximum biomass concentrations and the achieved product titer between the L-phenylalanine production with the *E. coli* FUS4 ($pF81_{kan}$) host strain and *E. coli* 3RP refuted these concerns. In detail, the maximum biomass concentrations with the triple reporter strain were at 30.78 g L^{-1} and thus 6% higher. Despite the 21% lower maximum and 30% lower average biomass specific product formation rates of the triple reporter strain, the maximum achieved L-phenylalanine concentrations in both processes were at slightly above 17 g L^{-1} with maximum product yields of

0.21 g g^{-1} with *E. coli* FUS4 (pF81$_{kan}$) and 0.22 g g^{-1} with *E. coli* 3RP, respectively. The observed differences in the biomass specific product formation rates might have been a result of the inaccuracies to set the correct feeding rate. While a constant feeding of 0.18 g$_{glycerol}$ g$_{Biomass}$$^{-1}$ h^{-1} was stated as the optimum for the highest L-phenylalanine yield (Weiner *et al.* 2014a), it is important to understand that the calculation of this rate relied on some approximated values. First, the glycerol concentrations within the feeding solution 3 were always assumed to be at 800 g L^{-1}, although the exact concentrations were only measured after the bioprocesses. Secondly, the necessary biomass concentration at the start of the product formation phase were approximated by the measured OD$_{600}$ with a correlation factor of 0.5. In hindsight, the feeding rate during the previously described L-phenylalanine production with *E. coli* FUS4 (pF81$_{kan}$) matched with the optimal value of 0.18 g$_{glycerol}$ g$_{Biomass}$$^{-1}$ h^{-1}, whereas a reduced feeding rate of 0.14 g$_{glycerol}$ g$_{Biomass}$$^{-1}$ h^{-1} was applied during the product formation with *E. coli* 3RP. Hence, the slower product formation was due to the deviation from the optimal feeding rate. Nevertheless, the here shown results emphasized no metabolic burden due to the additional expression of fluorescent proteins as cell growth and product formation were not negatively affected. This fact was also underlined by the identical process trends in general.

The purpose of using reporter strains in bioprocesses is the *at-line* monitoring of cellular characteristics. In the triple reporter strain, the general stress response, growth behaviour and oxygen limitation were followed by expression levels of mTagBFP2 (448/45 nm), mEmerald (527/32 nm) and CyOFP1 (586/42 nm). According to the fluorescence intensities at 448/45 nm, the general stress response levels increased especially during the transition from the initial batch phase to the biomass production phase. In general, the *rpoS* expression is known to be related to the substrate availability. While high substrate concentrations restrict the expression of this gene, a substrate depletion lead to the opposite with high expression levels of this alternative sigma factor (Dong & Schellhorn 2009, Battesti *et al.* 2011). During the L-phenylalanine production process, glycerol was present in abundance during the initial batch phase. After the depletion of glycerol and the start of the biomass production phase however, the substrate availability became scarce. Although glycerol was constantly fed into the bioreactor, the feeding strategies in fed-batch processes are designed to provide the least amount of substrates necessary to keep the cell growth at a certain rate. Therefore, the substrate concentrations often remain close to zero to prevent any substrate accumulation (Lee 1996). This limited access to glycerol potentially simulated nutrient scarcity, to which the cells responded with higher expression levels of the alternative sigma factor RpoS. Consequently, the triple reporter strain also expressed higher levels of the general stress response marker. This effect might have

been promoted by the sudden increase of ammonia concentrations due to the supply of feeding solution 1 at the beginning of the biomass production phase, which contained a considerable amount of ammonia. Though *E. coli* cells can tolerate high concentrations of ammonia and nitrogen in general, a sudden rise of ammonia concentrations potentially induced a so-called ammonium shock, which led to a fast internal alkalization that cells had to cope with (van Heeswijk *et al.* 2013). A further elevation of general stress response levels was observed after induction of the recombinant protein expression during the product formation phase. Potentially, a combination of a higher metabolic burden based on the forced expression of the *aroF*, *pheA*, *aroB* and *aroL* genes and the directed formation of L-phenylalanine with the progressive depletion of certain nutrients might have contributed to higher fluorescence levels at 448/45 nm. Interestingly, the final drop of the general stress response levels of the cells coincidated with the declining product formation ability. Overall, understanding the general stress response levels in bioprocesses remain a challenging task due to the variety of potential triggering factors such as substrate scarcity or other process parameters that deviate from ideal conditions (Battesti *et al.* 2011).

For the monitoring of the growth behaviour at 527/32 nm, three levels of fluorescence intensities were observed during the L-phenylalanine production process. The highest level of mEmerald was measured at the end of the initial batch phase, at which the corresponding growth rate was at 0.22 h^{-1} and thus at its maximum. In the following biomass production phase, the green fluorescence levels decreased slightly, whereas the growth rates also declined to around 0.12 h^{-1}. During the final product formation phase, the cell growth was further diminished and stagnated at around 60 h of process time. This event was accompanied by a further drop of expressed fluorescence signals at 527/32 nm to their lowest measured values. Therefore, mEmerald levels gave a fair approximation of the ongoing growth rates (Murray *et al.* 2003).

Considering the expression of CyOFP1 for the monitoring of cells suffering from oxygen limitation, the highest measured fluorescence intensities at 586/42 nm actually matched with comparably low dissolved oxygen levels at the end of the biomass production phase. In fact, DO levels were on the verge to drop below 30% air saturation because the elevated biomass concentration led to increased oxygen uptake rates of the bacterial population. This concomitant decrease of DO levels during the biomass production phase was well-reflected by the progressive increase of CyOFP1 levels (Li & DeMoss 1987, Kiley & Reznikoff 1991). Importantly, despite the reinforcing presence of oxygen limiting conditions at the end of the biomass production phase, the DO levels never dropped below 20% air saturation. Consequently, this marker seemed to be activated even before com-

pletely anoxic conditions developed. Notably, the expressed fluorescence intensity levels were lower during the product formation phase despite the presence of higher biomass concentrations. This was because of the reduced OUR of the microbial population due to lower growth rates, which led to higher DO levels.

In summary, the monitored fluorescent signals of *E. coli* 3RP at 448/45 nm, 527/32 nm and 586/42 nm gave interesting insights regarding the general stress response, growth behaviour and oxygen limitation during the L-phenylalanine production process. While both the growth marker and oxygen limitation marker were in agreement with their related process state variables, the expressed mTagBFP2 levels revealed reasonable trends concerning the general stress response levels of the cells. It is important to stress out, that the measured fluorescence levels of the *E. coli* triple reporter strain were consistently higher compared to the observed autofluorescence levels of the *E. coli* FUS4 pF81$_{kan}$ host strain at all three above mentioned detection ranges. Furthermore, the measured fluorescence intensities of *E. coli* 3RP cells dynamically changed along the L-phenylalanine production process, thus indicating the intracellular expression and dilution of reporter molecules. Such trends were not seen during the L-phenylalanine production process with the *E. coli* FUS4 pF81$_{kan}$ host strain. In general, the functionality of reporter strains to reflect targeted characteristics of cells in bioprocesses has already been demonstrated in many studies (Garcia *et al.* 2009, Delvigne *et al.* 2009, Han *et al.* 2013). In contrast to the often used single reporter strains, the here established triple reporter strain allows the simultaneous monitoring and analysis of three cellular characteristics in bioprocesses (Heins *et al.* 2020, Hoang *et al.* 2023a). Nevertheless, two aspects must be taken into consideration. First, there might be a time delay from the triggering event for the expression of a certain genetic unit with the integrated reporter molecule to the final capturing of this fluorescent signal. These *in vivo* maturation times of the here used reporter molecules are paramount to re-track the dynamics of fluorescence signals to their triggering events. Secondly, it is unclear whether the decrease of a fluorescent signal is due to cell separation events, the degradation of these reporter molecules by intracellular proteases or the natural loss of fluorescence. This uncertainty further complicates concrete assignments of process events and phases to certain dynamics of fluorescent signals and the corresponding cellular characteristics. In worst case, fluorescent proteins have a long half-life in cells so that the expressed signals are consistently stacked. As a consequence, transient gene expression as a response to fast changing environmental conditions cannot be tracked precisely (Han *et al.* 2013). Hence, future studies should consider the determination of *in vivo* maturation times and half-lifes of the utilized reporter molecules to better understand and interpret the here shown dynamics.

6.3. *Escherichia coli* quadruple reporter strain

After approving the functionality of the *E. coli* 3RP with no drawbacks regarding its growth behaviour and L-phenylalanine production, the last step was to examine the process performance of the *E. coli* quadruple reporter strain (*E. coli* 4RP). In comparison to the triple reporter strain, the quadruple reporter strain harbours a modified $pF81_{kan}$ plasmid, in which a synthetic copy of mCardinal2 was inserted for monitoring of the product formation. To evaluate the impact of this genetic modification, this novel strain was utilized for the L-phenylalanine production in a stirred-tank biorector using the same process strategy as applied for the two precursor strains.

With a maximum growth rate of 0.19 h^{-1} in the initial batch phase, the cell concentration increased to 1.58 ± 0.02 g L^{-1} within the first 14 h (Figure 6.5 A). Due to the complete depletion of glycerol at the same time (Figure 6.5 B), the biomass production phase was started and the cell growth continued with a decreased average growth rate of 0.10 ± 0.03 h^{-1}. Accordingly, the biomass concentration rose to 20.23 ± 0.04 g L^{-1} after 41.1 h of process time (Figure 6.5 A). Again, the OUR and CER increased exponentially during the biomass production phase with maximum rates at 0.26 mol L^{-1} h^{-1} and 0.19 mol L^{-1} h^{-1} (Figure 6.5 D). The corresponding amounts of L-tyrosine and L-phenylalanine were at 0.23 g L^{-1} and 0.07 g L^{-1}, whereas a L-glutamate concentration of 0.54 g L^{-1} was measured at the end of the biomass production phase (Figure 6.5 AC). Directly after induction of the recombinant protein expression at 41.1 h, L-tyrosine and L-glutamate depleted within the first 10 h of the product formation phase (Figure 6.5 C). This was again concomitant with a further cell growth until 63.1 h, after which the biomass concentrations remained constant at around 30 g L^{-1}. The maximum achieved biomass concentration of 31.23 ± 0.40 g L^{-1} was reached at the process end. In contrast, L-phenylalanine accumulated to a final product titer of 16.32 g L^{-1} with a maximum and average biomass specific product formation rate of 23.36 mg $g_{Biomass}^{-1}$ h^{-1} and 10.13 mg $g_{Biomass}^{-1}$ h^{-1}. The highest product yield was at 0.23 g g^{-1} (Figure 6.5 A). The progressive decline of the product formation ability of cells was accompanied by the accumulation of acetate and L-glutamate (Figure 6.5 BC) as well as the further decrease of the OUR and CER, which were already at lower rates of 0.12 mol L^{-1} h^{-1} and 0.09 mol L^{-1} h^{-1} at the start of the product formation phase (Figure 6.5 D).

Figure 6.5: L-phenylalanine production with the *Escherichia coli* quadruple reporter strain in a stirred-tank bioreactor. Subplot A shows the cell dry weight concentration (●) and L-phenylalanine concentration (◉), whereas subplot B represents the concentrations of glycerol (■) and acetate (▣). L-tyrosine (▲) and L-glutamate (△) are shown in subplot C, while subplot D shows the oxygen uptake rates (OUR, ——) and carbon dioxide evolution rates (CER, ——). This process was operated as a fed-batch process with an initial batch phase, a subsequent biomass production phase with exponential feeding and a final product formation phase with constant feeding. Verticals at 14.0 h and 41.1 h separate the phases. Process strategy: $V_0 = 1$ L, T = 37 °C, pH = 7, DO $\geq$ 30%, exponential feeding with $\mu_{set} = 0.1$ h^{-1}, constant feeding of 0.18 g$_{substrate}$ g$_{Biomass}$$^{-1}$ h^{-1} after induction of cells with 0.3 mM IPTG.
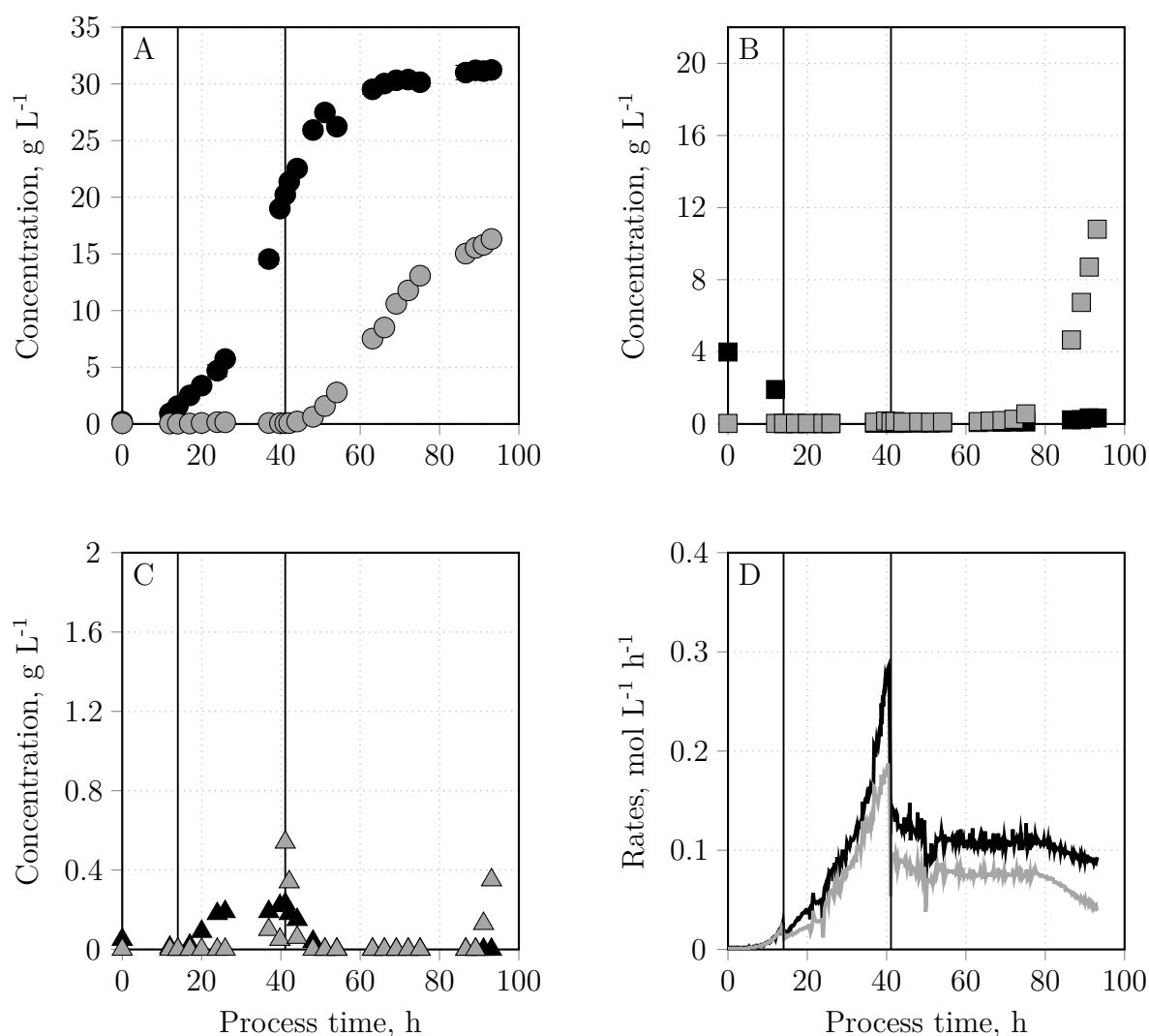
Regarding the expressed fluorescence intensities of the quadruple reporter strain, similar trends were observed for the detection ranges at 448/45 nm, 527/32 nm and 586/42 nm compared to the cultivation with *E. coli* 3RP. Nevertheless, minor deviations were present. For example, the general stress response of the cells indicated by blue fluorescence at 448/45 nm elevated after the transition from the initial batch phase to the following biomass production phase. While the highest levels of 1020.77 $\pm$ 2.10 were reached between 26.0 h and 37.0 h of process time, the expressed fluorescence intensities dropped

towards the start of the product formation phase to 722.19 ± 8.34. In this cultivation however, the general stress response did not increase a second time after induction of the recombinant protein expression with IPTG and the targeted formation of L-phenylalanine. Instead, the measured fluorescence intensities at 448/45 nm remained rather consistent at lower signal intensities of around 649.86 ± 34.65 until the process end (Figure 6.6 A).

In comparison, the growth marker mEmerald was measured at 527/32 nm. A high level of 569.96 ± 4.93 was measured directly at the end of the initial batch phase, which immediately declined with the start of the biomass production phase to 349.19 ± 0.97. However, the expressed green fluorescence intensities of the cells rose between 20.0 h to 37.0 h to the maximum achieved signals at 592.37 ± 7.18. Prior to induction of the recombinant protein expression, the mEmerald levels sharply declined. This trend continued after the start of the product formation phase with the lowest level of 318.17 ± 4.23 at 54.1 h. A slightly rising trend was visible towards the process end, but the expressed fluorescence intensities remained below 400 (Figure 6.6 B).

The expressed levels of the oxygen limitation marker CyOFP1, which were measured at 586/42 nm, constantly increased during the biomass production phase. In fact, the signal intensities rose from 427.48 ± 0.40 at 17.0 h to 798.87 ± 6.53 at 44.1 h (Figure 6.6 C). The same trend was also observed during the cultivation with the triple reporter strain (Figure 6.4 C). In contrast to the previous process, the monitored fluorescence levels at 586/42 nm remained at comparably high signal intensities during the product formation phase with a strong rise to 992.33 ± 25.58 at the process end (Figure 6.6 C).

As a novelty, the *E. coli* 4RP is capable of expressing mCardinal2 as a product formation marker, which is a far-red reporter molecule measured at 660/10 nm. While the starting fluorescence intensities of the cells were already at 494.85 ± 1.42 at the end of the initial batch phase, the signal intensities further increased during the biomass production phase with a slope of 15.5 h^{-1} until 37.0 h. After a temporal drop towards the end of the biomass production phase, the increasing trend continued with induction of the recombinant protein expression to initiate the product formation phase. The highest levels of 1080.62 ± 8.54 were measured between 63.1 h and 75.1 h of process time, which corresponded to a slope of 23.94 h^{-1}. At the end, the measured fluorescence intensity at 660/10 nm slightly decreased (Figure 6.6 D).

Similarly to the *E. coli* triple reporter strain, the *E. coli* quadruple reporter strain expressed considerably higher fluorescence levels at 448/45 nm, 527/32 nm and 586/42 nm

compared to the *E. coli* FUS4 (pF81$_{kan}$) host strain. This aspect was also exemplified at the far-red detection range at 660/10 nm, in which the quadruple reporter strain had more than 1000-fold higher fluorescence levels (Figure 6.1 and 6.4).
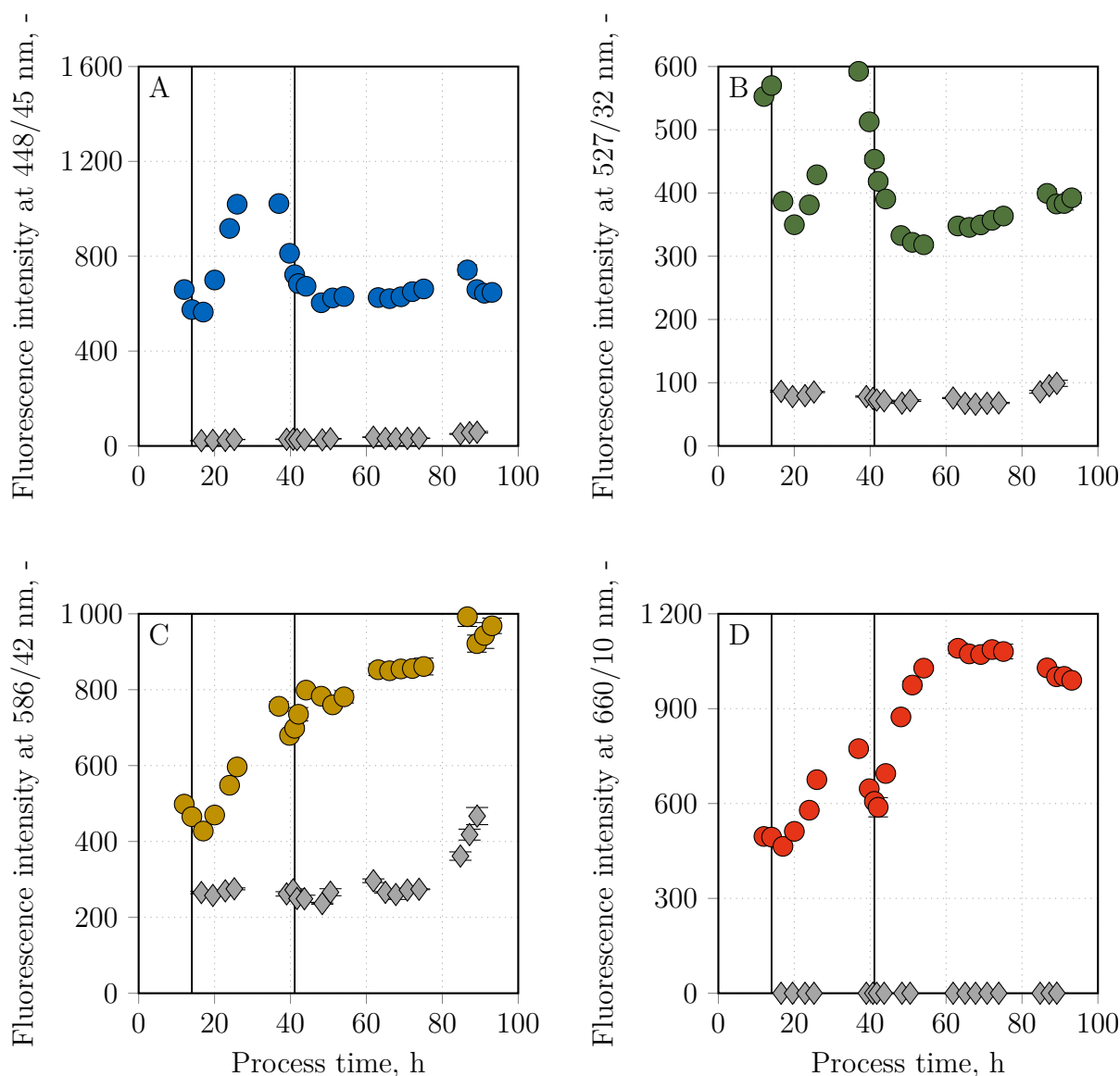
Figure 6.6: Expressed median fluorescence intensities of the *Escherichia coli* quadruple reporter strain at 448/45 nm (general stress response, ●), 527/32 nm (growth behaviour, ●), 586/42 nm (oxygen limitation, ●) and 660/10 nm (product formation, ●) during the L-phenylalanine production in a stirred-tank bioreactor. Vertical lines separate the initial batch phase, the biomass production phase and the final product formation phase. The threshold of the SSC-W was set to 922 V. PMT levels of FSC, SSC and the 660/10 nm filter were set to 250 V, 335 V and 500 V, respectively. Grey data points (◇) in each subplot represent the measured autofluorescence of the *E. coli* FUS4 (pF81$_{kan}$) host strain at the respective detection range during a separately performed L-phenylalanine production process with the same process strategy (see Figure 6.1 and Figure 6.2).

Discussion

The preservance of plasmids within the host strains consumes precursor building blocks and require energy, let alone the corresponding high-level expression of the proteins encoded on the vectors. Consequently, other metabolic pathways are often downregulated due to the resources spent for foreign protein expression (Bentley *et al.* 1990, Carneiro *et al.* 2013). Despite the additional expression of mCardinal2 in the quadruple reporter strain, the cell growth seemed not affected by this burden. While the maximum achieved biomass concentration of the quadruple reporter strain was approximately 7.5% and 1.5% higher compared to the host strain and the triple reporter strain, the lowest maximum L-phenylalanine concentrations were achieved with the quadruple reporter strain. In fact, the final product titer was at 16.32 g L^{-1} and hence 4.5% and 7.2% lower than for the precursor strains. Nonetheless, it is worth mentioning that the process was stopped due to the decreasing OUR and CER, though the L-phenylalanine production was apparently not finished at that time. Therefore, higher maximum L-phenylalanine concentrations could have been achieved with *E. coli* 4RP. In any case, this rather low reduction of the overall product yield was surprising, but might be related to the plasmid copy number. This number describes the amount of plasmids a single cell possess and is driven by the corresponding origin of replication on the plasmid. While high copy numbers in *E. coli* cells (above 100) are known to have a remarkable impact on the cellular growth and expression levels of native proteins, low copy number plasmids (below 20) have a comparably diminished effect on the cellular metabolism. This is due to the lower energy required for the preservance and the corresponding recombinant protein expression (Birnbaum & Bailey 1991, Barghini *et al.* 2007). In this instance, the modified pF81$_{kan}$ belongs to the low copy number plasmids. This aspect might explain, why the additional expression of mCardinal2 had no impact on the cell growth and led to a rather low reduction of L-phenylalanine concentrations in the quadruple reporter strain (Fürste *et al.* 1986, Sun-Gu & Liao 2008, Boros *et al.* 1984).

As a novelty, a synthetic copy of mCardinal2 was inserted into the pF81$_{kan}$ plasmid to monitor the product formation at 660/10 nm. Technically, mCardinal2 only highlights the initiating expression of the *aroF*, *pheA*, *aroB* and *aroL* genes and not the product formation procedure by itself. However, as these enyzmes are mandatory to start the L-phenylalanine production, the expressed red fluorescence levels become an indirect measure to follow the product formation. In best case, red fluorescence should only be visible after induction of the recombinant protein expression. Unfortunately, cells already showed red fluorescence intensities at the end of the initial batch phase, which even increased during the biomass production phase. This is a strong indicator for basal expression of

mCardinal2, despite the lack of inducing agents such as IPTG. As discussed in chapter 5.4, tac promoters are vulnerable to basal expression, thus explaining the unwanted expression of the red reporter molecule prior to induction of the cells. While this would indicate that the other genes *aroF*, *pheA*, *aroB* and *aroL* were also expressed prior to induction, a premature L-phenylalanine accumulation was not observed during the biomass production phase. Therefore, the basal expression might have only occurred for mCardinal2, potentially due to its ribosome binding site (RBS) sequence. Consequently, one approach to reduce the premature expression of mCardinal2 could be the modification of its RBS sequence (Salis *et al.* 2009, Seo *et al.* 2013). Nonetheless, it is important to note that the addition of IPTG led to a steeper elevation of red fluorescence levels of the cells compared to the basal expression during the biomass production phase. Furthermore, the highest red fluorescence levels coincidated with the highest biomass specific product formation rates between 63.1 h and 75.1 h of process time. Hence, the monitored red fluorescence levels of the quadruple reporter strain reflected the L-phenylalanine production in cells to some extent.

Comparing the trends of the expressed fluorescence intensities during the L-phenylalanine production processes with the triple and quadruple reporter strain at population level, a high level of resemblance was observed for the detection regions at 448/45 nm, 527/32 nm and 586/42 nm. While a general reproducibility between both bioprocesses was observed, still some minor deviations were present. For example, the general stress response of the triple reporter strain increased a second time during the product formation phase, while this was trend was attenuated when using *E. coli* 4RP. Another example was observed for the oxygen limitation marker, which remained at high levels during the product formation phase with *E. coli* 4RP, whereas the corresponding orange fluorescence intensities of the triple reporter strain were remarkably lower during this stage of the process. These deviations might have been a result of potentially existing subpopulations. As the presentation and evaluation of expressed median fluorescence intensities mask potential differences of single-cell fluorescence levels, a further consideration of the single-cell data is mandatory to better understand the here shown trends (Delvigne & Goffin 2014).

Overall, a novel *E. coli* quadruple reporter strain was successfully applied for the L-phenylalanine production in a stirred-tank bioreactor at laboratory scale. While the cell growth was not affected by the genetic modifications and the additional expression of fluorescent proteins, marginally lower maximum L-phenylalanine concentrations were observed with *E. coli* 4RP. In return, both the triple and quadruple reporter strains enabled interesting insights on the general stress response, growth behaviour, oxygen limita-

tion and product formation along the here conducted bioprocesses, which approximately matched with most of the ongoing process state variables. Though certain trends were reproducibly seen during the L-phenylalanine production processes, some minor deviations were present. To better understand such outcomes, a further consideration of single-cell fluorescence levels during the L-phenylalanine production could be beneficial.

7. Establishment of a two-compartment bioreactor for investigation of population heterogeneity during L-phenylalanine production[2]

Scale-down bioreactors are specialized small-scale setups with the objective to simulate fluctuating process conditions, which are prevailent in large-scale bioprocesses. These are particularly established to investigate the impact of dynamic environments on the process performances and the level of population heterogeneity in bioprocesses. Due to the smaller working volume, resources, time and total expenses can be saved. In this work, a novel two-compartment bioreactor shall be established by combining a conventional stirred-tank bioreactor at laboratory scale with a so-called coiled flow inverter as a bypass. While the former provides ideal and well-mixed process conditions, the coiled flow inverter represents a limitation zone with dynamic environmental conditions with no temperature control, no aeration and no addition of titrating agents and feeding solutions. By application of the here established *E. coli* quadruple reporter strain for the L-phenylalanine production in the two-compartment bioreactor, the objective is to elucidate the impact of repetitive exposure of the producing cells to rather dynamic and unfavourable conditions on the growth behaviour, productivity and other key cellular physiologies. Furthermore, the evaluation of expressed single-cell fluorescences shall support the identification and characterization of potential subpopulations during the bioprocesses. The outcome of the two-compartment bioreactor cultivations will be compared with the L-phenylalanine production in a stirred-tank bioreactor at well-mixed and controlled bioprocess conditions.

---

[2] Parts of the results in this chapter were pre-published in: Hoang *et al.* (2023b): Impact of mixing insufficiencies on L-phenylalanine production with an *Escherichia coli* reporter strain in a novel two-compartment bioreactor. *Microb Cell Factories* **22**: 153

7.1. Experimental characterization of the coiled flow inverter

To prepare the establishment of the novel two-compartment bioreactor, key characteristics of the coiled flow inverter (CFI) were first determined. This primarily included the mean hydraulic residence time τ and the dimensionless Bodenstein number Bo at different volumetric flow rates. The former number approximates the time a particle spends on average within the CFI, whereas the dimensionless Bo number provides information regarding the prevailent levels of axial backmixing of flowing fluids. These were calculated based on the monitored residence time distributions during step response experiments using a chromatography system (see chapter 4.5.2). Considering the fixed volume of the CFI of approximately 373 mL, the volumetric flow rates were set to 1.18 mL s^{-1}, 2.36 mL s^{-1}, 3.53 mL s^{-1}, 4.71 mL s^{-1} and 5.33 mL s^{-1}. This is equivalent to theoretical residence times between 70 s to 316 s in the bypass (Table 7.1), thus covering the upper range of the anticipated mixing times in large-scale bioprocesses of 10 s to 250 s (Vrábel *et al.* 2000). In comparison, the application of such volumetric flow rates in later two-compartment bioreactor cultivations would lead to theoretical hydraulic residence times of 188 s to 848 s in the stirred-tank bioreactor with a working volume of 1 L.

Table 7.1: Mean hydraulic residence times, variances of the response curves and the Bodenstein number calculated from the step response experiments in the coiled flow inverter at different volumetric flow rates with de-ionized water as a mobile phase and a 0.025 mg mL^{-1} vitamin B12 solution as a tracer solution. Dimensionless Reynolds numbers were calculated assuming a straight pipe, whereas the theoretical residence time was determined by dividing the volume of the CFI (373 mL) to the applied volumetric flow rates.

Volumetric flow rate, mL s^{-1}	Theoretical residence time, s	Mean hydraulic residence time, s	Variance, s^2	Bodenstein number, -
1.18 (Re = 250)	316.10	338.04 ± 0.75	41.06 ± 1.34	164.20 ± 0.53
2.36 (Re = 500)	158.05	166.85 ± 0.18	16.73 ± 1.04	219.97 ± 0.91
3.53 (Re = 750)	105.67	112.37 ± 0.95	11.46 ± 0.48	253.30 ± 5.31
4.71 (Re = 1000)	79.19	86.28 ± 0.62	7.79 ± 0.17	337.37 ± 12.81
5.33 (Re = 1131)	69.98	76.47 ± 0.72	6.50 ± 0.61	403.03 ± 6.57

7.1.1. Measurements of residence time distributions for determination of mean hydraulic residence times and the level of axial dispersion at different volumetric flow rates

First step response experiments were conducted with de-ionized water as a mobile phase and a 0.025 mg mL^{-1} vitamin B12 solution as a tracer. The investigated volumetric flow rates at 1.18 mL s^{-1}, 2.36 mL s^{-1}, 3.53 mL s^{-1}, 4.71 mL s^{-1} and 5.33 mL s^{-1} correspond to Reynolds numbers at 250, 500, 750, 1000 and 1131 (see Table 7.1). According to the calculated mean hydraulic residence times τ, the longest duration of 338.04 $\pm$ 0.75 s was achieved for the lowest applied volumetric flow rate at 1.18 mL s^{-1}. Logically, a further increase of the applied flow rates up to 5.33 mL s^{-1} led to shorter mean hydraulic residence times of 76.47 $\pm$ 0.72. Based on the conducted measurements, the mean hydraulic residence time can be approximated as a power function ($y = 394 \cdot x^{-0.99}$, R^2 = 0.99, Figure 7.1 A). In opposite, the corresponding Bodenstein numbers constantly rose in response to higher applied volumetric flow rates. While a flow rate of 1.18 mL s^{-1} led to a Bodenstein number of 164.20 $\pm$ 0.53, the dimensionless number increased to 403.03 $\pm$ 6.57 at the maximum applied volumetric flow rate. It is worth mentioning, that the determined Bodenstein numbers were consistently above Bo = 100 (Figure 7.1 B).
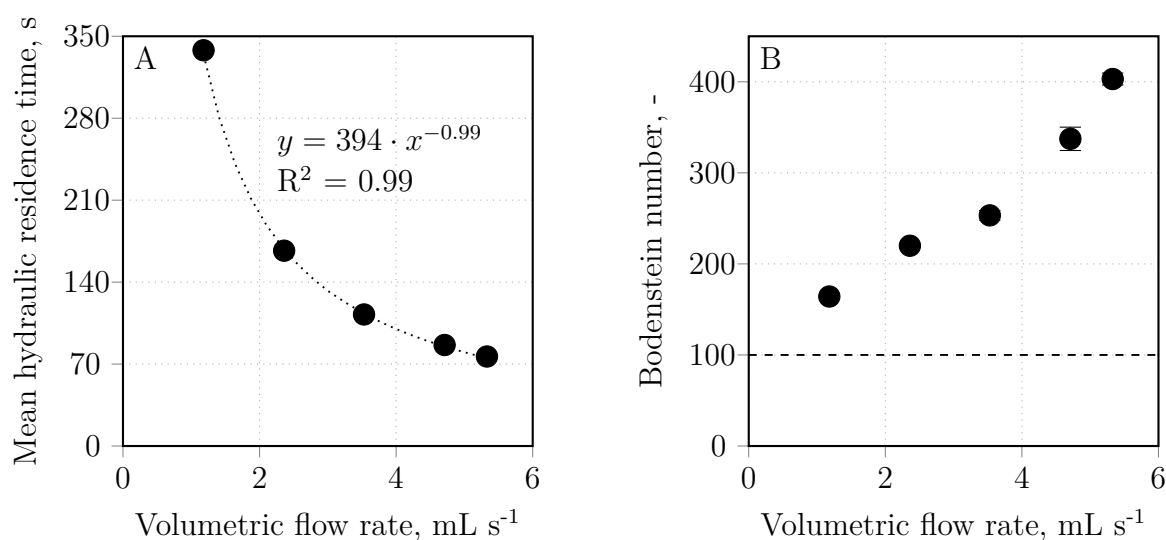
Figure 7.1: Step response experiments for the determination of mean hydraulic residence times (A) and Bodenstein numbers (B) in the coiled flow inverter at different volumetric flow rates between 1.18 mL s^{-1} to 5.33 mL s^{-1}. Filtrated de-ionized water was used as a mobile phase, while a 0.025 mg mL^{-1} vitamin B12 solution was utilized as a tracer for monitoring of the residence time distributions. While the dotted line in (A) displays the fit of the data points ($y = 394 \cdot x^{-0.99}$, R^2 = 0.99), the horizontal dashed line in (B) marks a Bodenstein number of 100.

The corresponding variances of the residence time distributions showed a decreasing trend for higher volumetric flow rates. For example, the variance at a flow rate of 1.18 mL s^{-1} was at 41.06 ± 1.34 s^2, whereas the variance was lowered to 6.50 ± 0.61 s^2 at the maximum applied operating point. Therefore, the distributions became more narrow the higher the applied volumetric flow rates. Direct comparisons of the determined mean hydraulic residence times and the related theoretical residence times, which were calculated by dividing the working volume of the coiled flow inverter (373 mL) to the applied volumetric flow rate, highlighted that τ was consistently higher than their theoretical counterpart. On average, mean hydraulic residence times were 7.41% higher with slightly stronger deviations at higher volumetric flow rates (8.95% and 9.27% at 4.71 mL s^{-1} and 5.33 mL s^{-1}, Table 7.1).

Discussion

Coiled flow inverters represent a specialized variant of helical tubular reactors with repetitive integration of 90° bends (Saxena & Nigam 1984). Though they have a great reputation in the field of flow chemistry (Bittorf *et al.* 2019), coiled flow inverters have never been used in biotechnological applications such as scale-down bioreactors so far. To consider coiled flow inverters as an alternative to continuous tubular reactors for the simulation of process gradients, the prevailing flowing conditions need to be characterized by determination of the Bodenstein number. This dimensionless number derives from the residence time distribution and is often used as a measure to reflect the narrowness of distributions. In fact, Bodenstein numbers above 100 are considered to be an indicator for good radial mixing and poor axial dispersion (Levenspiel 2012, Takors & Weuster-Botz 2018).

During step response experiments with the here established coiled flow inverter, this hurdle was passed for all applied volumetric flow rates. Even at the lowest applied operating point at 1.18 mL s^{-1}, Bodenstein numbers were clearly above 100. At the same time, the increase of volumetric flow rates led to higher Bodenstein numbers of up to 400, thus indicating even more narrow residence time distributions due to better radial mixing and lower axial dispersions. Such findings have been frequently reported in studies that characterized similar coiled flow inverter configurations, even at lower Reynolds numbers between 50 to 100. They all agreed that narrow residence time distributions in coiled flow inverters derived from the prevailent counter-rotating circulations on the plane of the cross-sectional area in tubes (Dean vortices), which are permanently re-orientated by the integrated 90° bends (Saxena & Nigam 1984, Mansour *et al.* 2017, Khot *et al.* 2019, Klutz *et al.* 2015, Kurt *et al.* 2015, Kováts *et al.* 2020). Besides the provision of appropriate mixing conditions, the applied residence times in the coiled flow inverter should

cover conventional mixing times of industrial bioprocesses, which are expected to be between 10 s to 250 s (Vrábel *et al.* 2000). This time frame can be further minimized when considering the findings of Simen *et al.* (2017), who showed that the cellular response times of *E. coli* began at 70 s when exposed to fluctuating conditions (Simen *et al.* 2017). Indeed, the here investigated volumetric flow rates covered the targeted residence times. However, the determined mean hydraulic residence times were always higher than their theoretically calculated counterparts. According to Levenspiel (2012), this indicates a holdback of the tracer during the step response experiments. A possible holdback of the vitamin B12 solution during the step response experiments can not be fully denied as the here used braided silicone tubing is not perfectly smooth. As a result, the frictional drag was increased and a holdback of the tracer molecules became more likely, which ultimately led to a delayed elution (Rothfus *et al.* 1950, Ntengwe *et al.* 2015). Nevertheless, the mean hydraulic residence times deviated only marginally from their theoretically calculated counterpart (< 10%). Additionally, the assumed tracer holdback seemed to have a rather negligible impact on the prevailing mixing characteristics as the Bodenstein numbers still indicated narrow response curves.

All in all, the here established coiled flow inverter was successfully characterized at volumetric flow rates between 1.18 mL s^{-1} to 5.33 mL s^{-1}. Mean hydraulic residence times of 76 s to 338 s were achieved, which correspond to most of the relevant mixing times of large-scale bioprocesses. Moreover, it was shown that the axial dispersion was negligible for the investigated operating points. Thus, all the mandatory requirements were accomplished to provide a scale-down bioreactor for the simulation of dynamic environmental conditions. In comparison to two-compartment bioreactor systems integrating a straight continuous tubular reactor, the exploitation of coiled flow inverters as a bypass particularly qualify for experimental setups demanding for long mean hydraulic residence times with narrow residence time distributions (Bittorf *et al.* 2019, Hoang *et al.* 2023b). Combined with the compact geometrical design and the flexibility in scaling, coiled flow inverters potentially play an important role in future scale-down bioreactors.

7.1.2. Influence of elevated viscosity on mean hydraulic residence times and the level of axial dispersion

Bioprocesses are inevitably accompanied by changes in viscosity as a result of changing compositions of the cultivation medium. It is assumed that especially the increase of the biomass amount contributes to higher viscosities. To verify this assumption, dynamic viscosities of cell samples from the L-phenylalanine production process with *E. coli* FUS4 (pF81$_{kan}$) were measured at different stages of the bioprocess at varying

biomass concentrations. Samples with low biomass concentrations of 0.32 g L^{-1} had a dynamic viscosity of 0.00087 Pa s, whereas samples with the highest achieved cell concentration of 31.47 g L^{-1} simultaneously showed the highest measured viscosity of 0.00176 Pa s. Overall, a clear positive correlation between biomass concentrations in the cultivation medium and the corresponding dynamic viscosity was observed (Figure 7.2 A).
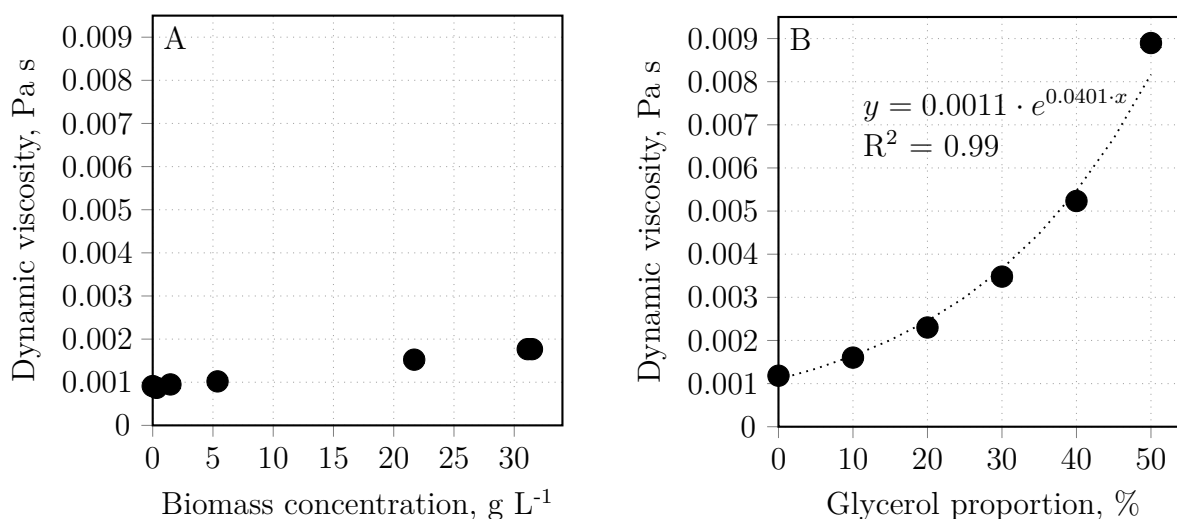
Figure 7.2: Determination of the dynamic viscosity of *Escherichia coli* FUS4 (pF81$_{\text{kan}}$) cell samples at different biomass concentrations (A) and glycerol solutions ranging from 0% to 50% (B). The dotted line in (B) represents the fit of the data points ($y = 0.0011 \cdot e^{0.0401 \cdot x}$, R^2 = 0.99). Viscosities were measured with a rotational rheometer.

Based on this knowledge, the question arises whether the dynamic viscosity of a mobile phase influences the mean hydraulic residence times and the mixing characteristics of flowing fluids in the coiled flow inverter. To elucidate this aspect, step response experiments were conducted using a mixture of glycerol and de-ionized water to simulate the characteristics of cell samples from the L-phenylalanine production process. Hence, dynamic viscosities of different glycerol mixtures were measured, which increased exponentially to higher glycerol proportions of the measured fluids ($y = 0.0011 \cdot e^{0.0401 \cdot x}$, R^2 = 0.99). According to this equation, a glycerol proportion of 12.5% had the same dynamic viscosity as cell samples with biomass concentrations of 31.47 g L^{-1} (Figure 7.2 B).

Using a 12.5% glycerol solution as a mobile phase for the determination of corresponding residence time distributions by step response experiments had no impact on the determined mean hydraulic residence times. Direct comparisons with the measured mean hydraulic residence times with de-ionized water as a mobile phase revealed deviations of less than 2%. Therefore, the increase of dynamic viscosities resulted to the same mean hydraulic residence times between 77.30 s to 339.79 s (Figure 7.3 A). However, the vari-

ances of the response curves were slightly elevated for most of the conducted volumetric flow rates (with exception at 4.71 mL s^{-1}). In comparison to experiments performed with de-ionized water as a mobile phase, variances of the distribution curves with a higher viscous mobile phase were 11.75% higher with stronger deviations at low volumetric flow rates (13.80% and 16.62% at 1.18 mL s^{-1} and 2.36 mL s^{-1}, Table 7.1, Table 7.2).
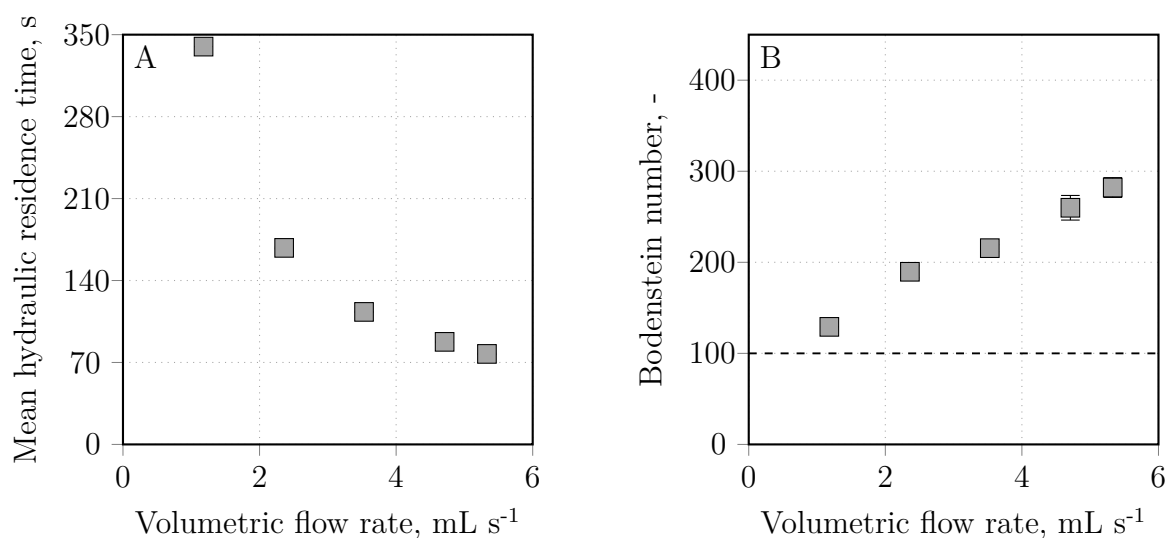
Figure 7.3: Step response experiments for the determination of mean hydraulic residence times (A) and Bodenstein numbers (B) in the coiled flow inverter at different volumetric flow rates between 1.18 mL s^{-1} to 5.33 mL s^{-1}. A 12.5% glycerol mixture was used as a mobile phase with a 0.025 mg mL^{-1} vitamin B12 solution dissolved in a 12.5% glycerol mixture as a tracer for monitoring of the residence time distributions. The horizontal dashed line in (B) marks a Bodenstein number of 100.

Further deviations to the prior measurements were also observed concerning the Bodenstein numbers. Indeed, the calculated Bodenstein numbers increased in step response experiments with a higher viscous mobile phase from 129.10 ± 0.10 at 1.18 mL s^{-1} to 282.13 ± 10.88 at 5.33 mL s^{-1}. However, they were constantly lower compared to the determined Bodenstein numbers during step response experiments with de-ionized water as a mobile phase. In fact, the determined Bodenstein numbers with a higher viscous mobile phase were reduced by up to 30%, but still surpassed a value of 100 (Figure 7.3 B, Table 7.1, Table 7.2).

Table 7.2: Mean hydraulic residence times, variances of the response curves and the Bodenstein number calculated from the step response experiments in the coiled flow inverter at different volumetric flow rates with a 12.5% glycerol mixture used as a mobile phase and a vitamin B12 solution dissolved in a 12.5% glycerol mixture as a tracer solution. Dimensionless Reynolds numbers were calculated assuming a straight pipe, whereas the theoretical residence time is determined by dividing the volume of the CFI (373 mL) to the applied volumetric flow rates.

Volumetric flow rate, mL s^{-1}	Mean hydraulic residence time, s	Variance, s^2	Bodenstein number, -
1.18	339.79 ± 0.05	46.73 ± 0.04	129.10 ± 0.10
2.36	167.87 ± 0.63	19.51 ± 0.07	189.60 ± 6.64
3.53	113.18 ± 0.52	12.51 ± 0.23	215.53 ± 3.77
4.71	87.60 ± 0.58	7.16 ± 2.91	259.90 ± 13.52
5.33	77.30 ± 0.56	7.22 ± 0.50	282.13 ± 10.88

Discussion

The increase of dynamic viscosities in biosuspensions is due to the cell growth and a well-described correlation, which cannot be circumvented. Especially high cell density cultivations are related to this inevitable relationship. Each biological organism affects the viscous properties of a suspension differently, because this coherence mainly relies on their morphology with rather minor effects of the prevailent metabolites (Mori *et al.* 1979, Olsvik & Kristiansen 1994). Hence, the individual determination of dynamic viscosities is mandatory for each producing strain.

The effects of higher viscous biosuspensions are manifold. This includes mass transport properties such as the oxygen or heat transfer, which are often reduced as a result of higher viscosities (Deindoerfer & Gaden 1955, Olsvik & Kristiansen 1994, Lone *et al.* 2020). In terms of flowing fluids through tubes, the viscosity is expected to enhance the overall drag and boundary conditions due to the higher resistance to flow and elevated internal friction. Consequently, velocity gradients are intensified and the particle flow becomes more vulnerable to deviations (Mohammadi & Boodhoo 2012). Therefore, it is not surprising to have seen broader residence time distributions, which were indicated by higher variances and lower Bodenstein numbers, during step response experiments with a 12.5% glycerol mixture compared to de-ionized water as a mobile phase. The same progressive broadening of the residence time distributions with higher viscous mobile phases was also described by Reis *et al.* (2019). Ultimately, mixing characteristics of flowing fluids through the coiled flow inverter were worsened by higher viscous mobile phases. Nonetheless, the determined Bodenstein numbers all surpassed a value of 100, so that the prevailent mixing conditions were sufficient to provide narrow residence time distributions.

All in all, preliminary studies on the coiled flow inverter approved narrow residence time distributions for volumetric flow rates between 1.18 mL s^{-1} to 5.33 mL s^{-1} with mean hydraulic residence times ranging from 76 s to 339 s. These can be applied in later two-compartment bioreactor cultivations as long as the biomass amount will not surpass concentrations of 31 g L^{-1}.

7.2. Two-compartment bioreactor cultivations with the *Escherichia coli* quadruple reporter strain at different mean hydraulic residence times

Preliminary studies on the coiled flow inverter approved narrow residence time distributions at volumetric flow rates between 1.18 mL s^{-1} to 5.33 mL s^{-1}. Applying these flow rates additionally complied with the targeted duration times of 70 s to 250 s within the CFI. Hence, the CFI was integrated to a stirred-tank biroeactor at laboratory scale to establish a novel two-compartment bioreactor. While the stirred-tank bioreactor provides a well-mixed environment with stable process conditions of 37 °C, a pH of 7 and dissolved oxygen levels above 30% air saturation with substrate feeding during the biomass production and the product formation phases, the CFI lacked all these features. Instead, there was no supply of pH correcting agents, feeding solutions or atmospheric oxygen and no temperature control in this compartment. Consequently, the permanent circulation of the cell suspension through both compartments simulated the transition from well-mixed and ideal process conditions in the stirred-tank bioreactor to fluctuating and unfavourable environmental conditions within the bypass. Applying this setup for the L-phenylalanine production with the *E. coli* 4RP shall elucidate the impact of dynamic environments on key process performance indicators as well as the general stress response, growth behaviour, oxygen limitation and product formation of the cell population. Moreover, single-cell fluorescences allow further insights on the effects of dynamic environmental conditions on the level of population heterogeneities during the L-phenylalanine production. The bioprocesses in the two-compartment bioreactor will be compared with the L-phenylalanine production process in a stirred-tank bioreactor as a benchmark.

7.2.1. Process performances of the L-phenylalanine production processes with the *Escherichia coli* quadruple reporter strain in a stirred-tank bioreactor and a two-compartment bioreactor

The L-phenylalanine production processes in the stirred-tank bioreactor (STB) or two-compartment bioreactor (TCB) were conducted with the same process strategy. The overall starting volume of TCB cultivations was at 1.35 L with an initial volume of 0.9 L in the stirred-tank bioreactor and a fixed volume of 0.45 L in the coiled flow inverter with all connecting tubes ($V_{0, STB}$ = 0.9 L and V_{CFI} = 0.45 L). In total, three different two-compartment bioreactor cultivations were performed applying volumetric flow rates of either 4.71 mL s^{-1}, 2.36 mL s^{-1} and 1.18 mL s^{-1}. These corresponded to mean hydraulic residence times of 102.63 s (short, TCB$_S$), 199.50 s (medium, TCB$_M$) and 403.30 s (long, TCB$_L$) in the bypass. Due to the expected narrow residence time distributions of flowing fluids within the CFI, 90% of the cells experienced hydraulic residence times of 102.0 ± 13.0 s (TCB$_S$), 199.5 ± 27.5 s (TCB$_M$) or 403.5 ± 67.5 s (TCB$_L$), respectively. On the other hand, cells in two-compartment bioreactor cultivations also experienced ideal bioprocess conditions in the stirred-tank bioreactor for a certain time, as well. Assuming a volumetric range of 900 mL at the beginning and a maximum of 1350 mL at the process end, the theoretical hydraulic residence times in this compartment would equal 191.1 s to 286.6 s (TCB$_S$), 381.4 s to 572.0 s (TCB$_M$) or 762.7 s to 1 144.1 s (TCB$_L$). A full circulation of each cell of the biosuspension in the stirred-tank bioreactor through the bypass can be assumed after five times of the theoretical hydraulic residence times (955.5 s to 1 433.0 s in the TCB$_S$, 1 907.0 s to 2 860.0 s in the TCB$_M$ or 3 813.5 s to 5 720.5 s in the TCB$_L$). Due to the combined volume of 1.35 L in the the two-compartment bioreactor, the L-phenylalanine production with *E. coli* 4RP in the STB was performed with an initial volume of 1.35 L, as well.

All processes started with an initial batch phase, in which 4 g L^{-1} of glycerol were consumed within the first 14.6 h to 17.6 h of process time (Figure 7.4 BEHK). Accordingly, the biomass concentrations increased to 1.97 ± 0.20 g L^{-1} for the STB cultivation and to 1.65 ± 0.00 g L^{-1} (TCB$_S$), 1.60 ± 0.13 g L^{-1} (TCB$_M$) and 1.50 ± 0.10 g L^{-1} (TCB$_L$) for the TCB cultivations (Figure 7.4 ADGJ). The corresponding maximum growth rates were at 0.26 h^{-1} (STB), 0.34 h^{-1} (TCB$_S$), 0.27 h^{-1} (TCB$_M$) and 0.25 h^{-1} (TCB$_L$). Due to the depletion of substrate in the culture media, the biomass production phases were started with an exponential feeding strategy at a fixed growth rate of 0.1 h^{-1}.
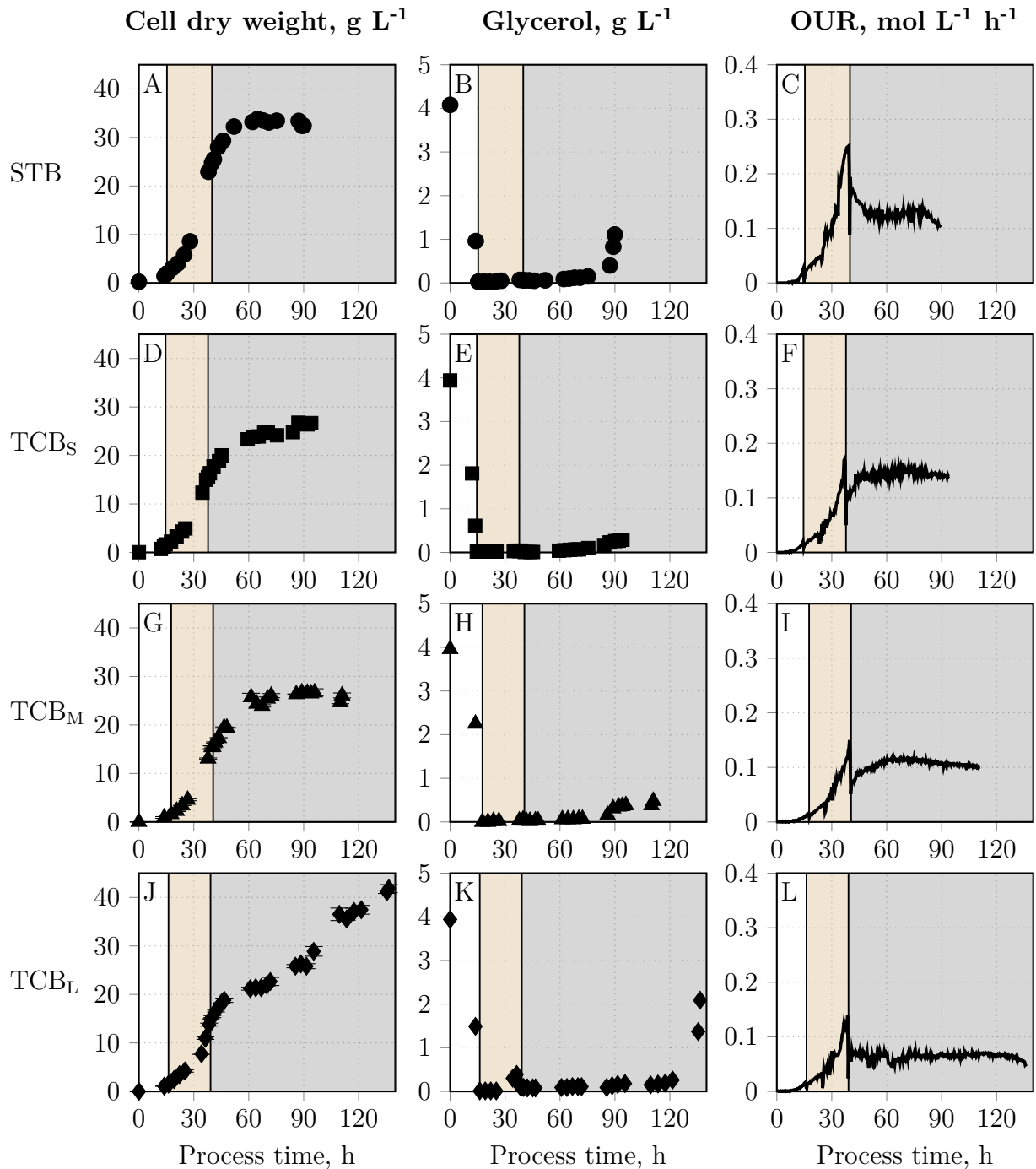
Figure 7.4: L-phenylalanine production with the *Escherichia coli* quadruple reporter strain in a stirred-tank bioreactor (STB) or a two-compartment bioreactor (TCB) with a stirred-tank bioreactor and coiled flow inverter as a bypass. TCB cultivations were conducted with either short (TCB$_S$), medium (TCB$_M$) or long (TCB$_L$) mean hydraulic residence times of 102.63 s (4.71 mL s^{-1}), 199.50 s (2.36 mL s^{-1}) or 403.30 s (1.18 mL s^{-1}). Corresponding cell dry weight concentrations (A, D, G, J), glycerol concentrations (B, E, H, K) and oxygen uptake rates (OUR, C, F, I, L) are plotted along the process time. The initial batch and the biomass production phases are highlighted with a white or orange background, whereas the product formation phase is covered by a grey background. Phases are separated by black verticals (STB: V$_0$ = 1.35 L, T = 37 °C, pH = 7, DO $\geq$ 30%; TCB: V$_{0,\,STB}$ = 0.9 L, V$_{0,\,CFI}$ = 0.45 L, T$_{STB}$ = 37 °C, pH$_{STB}$ = 7, DO$_{STB}$ $\geq$ 30%; exponential feeding with μ_{set} = 0.1 h^{-1}, constant feeding of 0.18 g$_{substrate}$ g$_{Biomass}$$^{-1}$ h^{-1} after induction of the recombinant protein expression with 0.3 mM IPTG).

Nevertheless, the cell growth started to differ between the processes during the biomass production phase. In fact, cells in the STB cultivation showed the strongest growth with a cell concentration of 24.95 ± 0.36 g L^{-1} at the end of the biomass production phase at 39.9 h. In contrary, biomass concentrations above 20 g L^{-1} were not achieved in all TCB setups as the dissolved oxygen levels could have not been kept above 30% air saturation. Consequently, the recombinant protein expression for the L-phenylalanine production were induced at cell concentrations of 15.53 ± 0.25 g L^{-1} (TCB_S) at 37.8 h, 15.50 ± 0.19 g L^{-1} (TCB_M) at 40.5 h and 14.87 ± 0.10 g L^{-1} (TCB_L) at 39.1 h (Figure 7.4 ADGJ). Strikingly, a temporary glycerol accumulation to 0.39 g L^{-1} was observed at the end of the biomass production phase in the TCB_L cultivation (Figure 7.4 K). The biomass production phases were also concomitant with an exponential increase of the OUR in all processes with the highest rates of 0.251 mol L^{-1} h^{-1} during the STB cultivation. In comparison, the oxygen uptake rates in all TCB setups were between 0.125 mol L^{-1} h^{-1} to 0.171 mol L^{-1} h^{-1} and thus lower (Figure 7.4 CFIL). After the addition of IPTG to start the product formation phase, the cell growth continued for the next 10 h to 20 h during the STB, TCB_S and TCB_M cultivations because of the remaining L-tyrosine amount in the culture media (Supplementary material A.2, Table A.13). With the depletion of this aromatic amino acid, the biomass concentrations stagnated at maximum achieved concentrations of 33.83 ± 0.31 g L^{-1} at 64.9 h (STB), 26.75 ± 0.20 g L^{-1} at 87.1 h (TCB_S) and 26.70 ± 0.51 g L^{-1} at 89.0 h (TCB_M) (Figure 7.4 ADG). Although this trend was anticipated for all processes, the biomass concentration in the TCB with long mean hydraulic residence times rose despite the depletion of L-tyrosine (Supplementary material A.2, Table A.13). A maximum biomass concentration of 41.83 ± 0.83 g L^{-1} was achieved at the process end (Figure 7.4 J). In this process, glycerol accumulated towards the end of the process, which was also observed during the STB cultivation (Figure 7.4 BK). In comparison, a glycerol uprise at the process ends were also observed in TCB cultivations with short or medium mean hydraulic residence times, but less pronounced (Figure 7.4 EH). The corresponding oxygen uptake rates during the product formation phases were constant at approximately 0.130 mol L^{-1} h^{-1} (STB), 0.151 mol L^{-1} h^{-1} (TCB_S), 0.117 mol L^{-1} h^{-1} (TCB_M) and 0.067 mol L^{-1} h^{-1} (TCB_L) (Figure 7.4 CFIL).

The accumulation of L-phenylalanine only started with induction of the recombinant protein expression with IPTG combined with a constant feeding of feeding solution 3 at a rate of 0.18 $g_{Substrate}$ g_{CDW}^{-1} h^{-1} in all processes. Prior to that event, the L-phenylalanine concentrations remained below 0.6 g L^{-1} (Figure 7.5 ADGJ). The carbon dioxide evolution rates increased exponentially during the biomass production phase to maximum rates of 0.213 mol L^{-1} h^{-1} (STB), 0.127 mol L^{-1} h^{-1} (TCB_S), 0.118 mol L^{-1} h^{-1} (TCB_M)

and 0.128 mol L^{-1} h^{-1} (TCB_L), but they all dropped to 0.1 mol L^{-1} h^{-1} or lower after the addition of IPTG (Figure 7.5 CFIL). While all processes had a short lag prior to the L-phenylalanine production, cells in the STB and the TCB_S cultivations showed the steepest increase of L-phenylalanine concentrations, especially between 45 h to 70 h of process time with maximum biomass specific product formation rates of 31.53 mg g^{-1} h^{-1} (STB, 67.9 h) and 25.21 mg g^{-1} h^{-1} (TCB_S, 68.4 h). On average, cells in the TCB_S setup showed slightly higher mean product formation rates of 14.68 mg g^{-1} h^{-1} compared to cells during the STB cultivation with 12.95 mg g^{-1} h^{-1}. Nonetheless, the maximum product titers were at 21.46 g L^{-1} (STB) and 20.67 g L^{-1} (TCB_S) and thus almost identical (Figure 7.5 AD). Considering the product formation in the TCB cultivations with medium or long hydraulic residence times, weaker product formations were observed in both cases. In fact, both processes showed lower maximum and mean biomass specific product formation rates of 18.23 mg g^{-1} h^{-1} and 9.55 mg g^{-1} h^{-1} in the TCB_M cultivation as well as 22.52 mg g^{-1} h^{-1} and 9.17 mg g^{-1} h^{-1} in the TCB_L setup. Consequently, the maximum achieved L-phenylalanine concentrations were only at 14.63 g L^{-1} and 15.45 g L^{-1}. Remarkably, the L-phenylalanine concentration of the TCB cultivation with long hydraulic residence times dropped towards the end of the process at a maximum rate of 0.77 g h^{-1} (Figure 7.5 GJ). Despite the different process durations, all maximum L-phenylalanine titers were achieved at around 90 h of process time (Figure 7.5 ADGJ). The corresponding maximum product yields were at 0.24 g g^{-1} (STB), 0.24 g g^{-1} (TCB_S), 0.21 g g^{-1} (TCB_M) and 0.25 g g^{-1} (TCB_L), respectively. The process ends were all accompanied by an acetate accumulation (Figure 7.5 BEHK) and a final decrease of the CER (Figure 7.5 CFIL).

Interestingly, the integral carbon balances of all conducted bioprocesses showed that the proportions of carbon dioxide were higher during the initial and biomass production phases in TCB cultivations compared to the STB setup. For example, carbon dioxide covered 36.4 mol% at the start of the biomass production phase (15.3 h) in the STB cultivation. In contrast, carbon dioxide proportions of 41.0 mol% (14.6 h, TCB_S), 54.6 mol% (17.6 h, TCB_M) or 46.0 mol% (16.2 h, TCB_L) were present in two-compartment bioreactor cultivations. Also the average carbon dioxide proportions were consistently higher during the biomass production phases of TCB cultivations. In the STB setup, carbon dioxide only represented 44.3 ± 9.4 mol% of the carbon balance, whereas elevated proportions of 53.0 ± 8.8 mol% (TCB_S), 60.9 ± 5.9 mol% (TCB_M) or 56.1 ± 6.5 mol% (TCB_L) were present in the two-compartment bioreactor setups (Supplementary material A.3, Tables A.14, A.15, A.16 and A.17).

Figure 7.5: L-phenylalanine production with the *Escherichia coli* quadruple reporter strain in a stirred-tank bioreactor (STB) or a two-compartment bioreactor (TCB) with a stirred-tank bioreactor and a coiled flow inverter as a bypass. TCB cultivations were conducted with either short (TCB_S), medium (TCB_M) or long (TCB_L) mean hydraulic residence times of 102.63 s (4.71 mL s^{-1}), 199.50 s (2.36 mL s^{-1}) or 403.30 s (1.18 mL s^{-1}). Corresponding L-phenylalanine concentrations (A, D, G, J), acetate concentrations (B, E, H, K) and carbon dioxide evolution rates (CER, C, F, I, L) are plotted along the process time. The initial batch and the biomass production phases are highlighted with a white or orange background, whereas the product formation phase is covered by a grey background. Phases are separated by black verticals (STB: $V_0 = 1.35$ L, T = 37 °C, pH = 7, DO ≥ 30%; TCB: $V_{0, STB} = 0.9$ L, $V_{0, CFI} = 0.45$ L, $T_{STB} = 37$ °C, $pH_{STB} = 7$, $DO_{STB} ≥ 30$%; exponential feeding with $\mu_{set} = 0.1$ h^{-1}, constant feeding of 0.18 g$_{substrate}$ g$_{Biomass}$$^{-1}$ h^{-1} after induction of the recombinant protein expression with 0.3 mM IPTG).
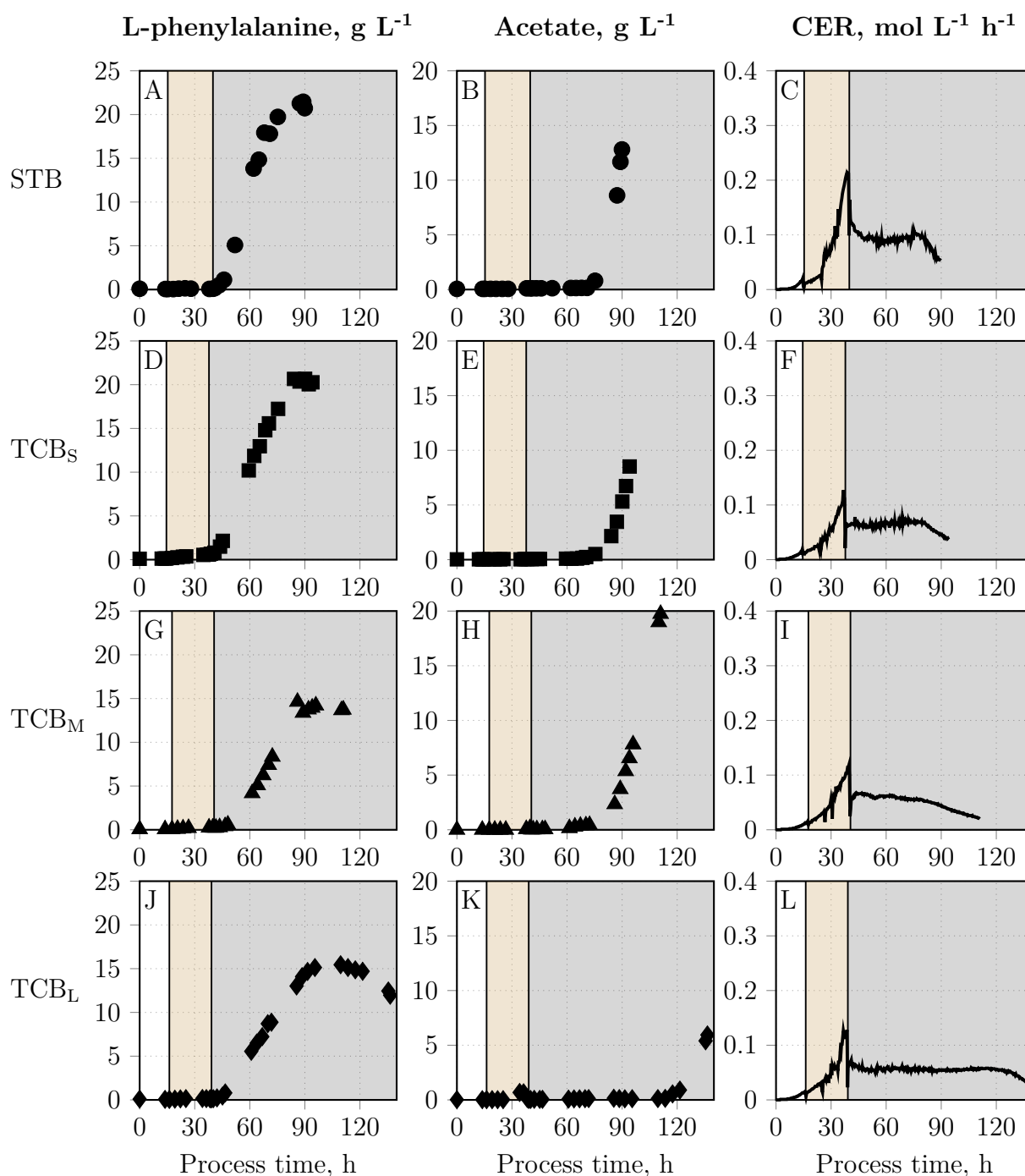
The comparison of key performance indicators of all conducted L-phenylalanine production processes in either STB or TCB is summarized in Table 7.3. According to the achieved biomass concentrations at the beginning of the product formation phases, the cell growth was superior in the STB cultivation, in which the targeted cell concentration of at least 20 g L^{-1} was surpassed. For all the TCB cultivations, such high biomass amounts were not reached (approximately 25% below the target value), because the dissolved oxygen levels were on the verge to fall below 30% air saturation. Simultaneously, the maximum achieved biomass concentration in the STB cultivation was remarkably higher compared to TCB cultivations with exception of the TCB setup with long mean hydraulic residence times. In particular, this process was characterized by a suspicious continuation of cell growth during the product formation phase though L-tyrosine was depleted already. Regarding the product formation, cells in the STB and TCB setup with short mean hydraulic residence times achieved the highest L-phenylalanine titers of slightly above 20 g L^{-1}. Accordingly, both processes showed the highest maximum and mean biomass specific product formation rates. In contrast, the L-phenylalanine production in TCB setups with medium or long hydraulic residence times were remarkably worse with approximately 25% lower maximum achieved product titers (Table 7.3).

Table 7.3: Key process performance indicators of the L-phenylalanine production processes in a stirred-tank bioreactor (STB) or a two-compartment bioreactor (TCB) with a stirred-tank bioreactor and a coiled flow inverter as a bypass. Bioprocesses in the latter setup were conducted at three different hydraulic residence times of 102.63 s (TCB$_S$), 199.50 s (TCB$_M$) and 403.30 s (TCB$_L$) within the bypass.

	STB	TCB$_S$	TCB$_M$	TCB$_L$
Maximum achieved biomass concentration, g L^{-1}	33.83	26.75	26.70	41.83
Maximum product concentration, g L^{-1}	21.46	20.67	14.63	15.45
Maximum product formation rate, mg g$_{Biomass}^{-1}$ h^{-1}	31.53	25.21	18.23	22.52
Mean product formation rate, mg g$_{Biomass}^{-1}$ h^{-1}	12.95	14.68	9.55	9.17

Discussion

The increase of the starting volume from 1 L to 1.35 L in STB cultivations had no major effects on the biomass production. In both processes, the demanded biomass amount of at least 20 g L^{-1} were achieved at the start of the product formation phase and maximum biomass concentrations of slightly above 30 g L^{-1} were observed, regardless of the initial working volume. However, the L-phenylalanine production was positively affected by the volumetric adjustment. Surprisingly, the maximum generated product amounts increased from 16.32 g L^{-1} in the STB cultivation with 1 L of starting volume to 21.46 g L^{-1} with the higher starting volume of 1.35 L. This corresponds to a percentual elevation of 31.5%. Interestingly, the STB cultivation with a starting volume of 1.35 L resulted to comparable maximum achieved product concentrations as in the reference process using the original *E. coli* FUS4 (pF81$_{kan}$) strain in a stirred-tank bioreactor with a starting volume of 15 L. There, a maximum L-phenylalanine concentration of 22.78 g L^{-1} was observed (Weiner *et al.* 2016). Hence, this is a supporting indicator that the genetic modifications conducted on the quadruple reporter strain neither damaged the cellular integrity, nor did the additional expression of the reporter molecules represent a strong metabolic burden to the cells. Nevertheless, this can not be considered as a definitive proof due to the differences in bioprocess scales. Despite this important outcome, the remaining question arises why the product formation was enhanced by the increase of the initial working volume. The media composition, feeding strategy and all other relevant process parameters were adjusted accordingly to the volumetric adjustment. Although a stronger accumulation of toxic by-products such as methylglyoxal or acetate are known to have inhibiting effects on *E. coli* cells (Baronofsky *et al.* 1984, Axe & Bailey 1995, Leone *et al.* 2015, Dharmadi *et al.* 2006), this can be ruled out as the product formation phases in both processes lasted approximately 50 h with the highest product amounts towards the process ends. Additionally, expression levels of the genes *aroF*, *pheA*, *aroB* and *aroL* encoded on the pF81$_{kan}$ plasmid should have not deviated between the processes as the recombinant protein production in *E. coli* cells were induced with the same molar concentration of IPTG. Nonetheless, both the maximum and mean biomass specific product formation rates were 35% and 28% higher in the STB cultivation with 1.35 L starting volume compared to the process with a lower initial working volume of 1 L. Hence, no obvious reasons were found to explain the seemingly positive effect of a higher working volume during the L-phenylalanine production in stirred-tank bioreactors.

The repetitive circulation of the cells from expectably ideal process conditions in the stirred-tank bioreactor to dynamic and partly unfavourable conditions in the CFI during two-compartment bioreactor cultivations led to a reduced cell growth compared to the

STB cultivation, regardless of the applied mean hydraulic residence times in the bypass. Though the *E. coli* cells spent at least twice as long in the stirred-tank bioreactor based on the theoretically calculated hydraulic residence times, still the temporal exposure to limiting and presumably anaerobic conditions in the tubular compartment most likely contributed to the diminished cell growth. Although glycerol is expected to be similarly absorbed by either passive or protein-mediated diffusion under aerobic and anaerobic conditions (Heller *et al.* 1980, Weiner *et al.* 2014a), the observed accumulation of the substrate at the end of the biomass production phase in the TCB$_L$ cultivation hinted towards a slower uptake of glycerol under anaerobic conditions. At the same time, the glycerol conversion might have been disturbed under such conditions. While biomass yields of 0.25 g g^{-1} are expected under fully aerobic conditions (Weiner *et al.* 2014a), Durnin *et al.* (2009) showed strongly reduced biomass yields of slightly above 0.1 g g^{-1} in *E. coli* cells experiencing anaerobic conditions. Potentially, this is due to different metabolic pathways during the respiratory and fermentative utilization of glycerol in *E. coli* (Durnin *et al.* 2009). Additionally, anaerobic conditions often activate alternative fluxes in the central carbon metabolism, thus leading to the formation of by-products such as acetate or ethanol (Förster & Gescher 2014, Kargeti & Venkatesh 2017). However, no premature accumulation of by-products was surprisingly observed in any TCB cultivations. Instead, the integral carbon balances of all three conducted TCB cultivations showed higher proportions of carbon dioxide during the L-phenylalanine production processes compared to the STB setup, especially during the biomass production phases (Supplementary material A.3, Tables A.14, A.15, A.16 and A.17). Carbon dioxide is generally known as a by-product of the central carbon metabolism under the presence of oxygen (Martínez-Reyes & Chandel 2020). Normally, carbon dioxide evolution rates increase when cells experience a high abundance of carbon sources, which lead to higher growth rates (Kayser *et al.* 2005). Though the substrate availability was consistently low during the L-phenylalanine production processes in the two-compartment bioreactor, the return of cells from the coiled flow inverter, in which they suffered from substrate scarcity for at least 100 s, to the stirred-tank bioreactor might have simulated a strong increase of substrate availability for the cells. As a consequence, the carbon dioxide evolution rates particularly rose in TCB cultivations. Furthermore, the overall reduced cell growth in the two-compartment bioreactor might have been enhanced by the potentially lower prevailing temperatures in the coiled flow inverter. As shown by Doyle & Schoeni (1984), the generation times of *E. coli* cells were at the lowest during cultivations in a complex medium at 37 °C, whereas any deviations from that optimal cultivation temperature led to prolonged generation times. To confirm this assumption, data regarding the temperature in the coiled flow inverter needs to be recorded in future cultivations. It is worth mention-

ing that a suspiciously high maximum biomass concentration above 40 g L^{-1} was observed during the TCB cultivation with the longest mean hydraulic residence times. While the often observed cell growth in the first 10 h to 20 h of the product formation phase is due to the residual consumption of accumulated L-tyrosine in the culture medium, the cells in the TCB_L even grew despite the complete depletion of L-tyrosine. As this strain is auxotroph towards L-phenylalanine and L-tyrosine (Sprenger 2007, Weiner *et al.* 2014b, Weiner *et al.* 2016), this outcome was utterly surprising. Indeed, the occurrence of mutated cells, which were capable to produce L-tyrosine, is possible. Mutations often occur in cell populations as a survival strategy to unpredictable and stressful conditions (Tanaka *et al.* 2003, Travis & Travis 2002). The stronger the spread of cells regarding their expressed phenotypes, the higher the chances of at least some cells to survive and adapt to the prevailing conditions (Wielgoss *et al.* 2013, Sniegowski *et al.* 1997, Swings *et al.* 2017, Callens *et al.* 2023, Matic 2019). Additionally, plasmid loss in bacteria is often observed as a response to highly stressful conditions as a further survival strategy of the cells, as well (Smith & Bidochka 1998, Silva *et al.* 2009, Summers 1991). On that note, *E. coli* 4RP cells might have lost the modified $pF81_{kan}$ plasmid during the later stages of the L-phenylalanine production process in the TCB_L setup. Nevertheless, the occurrence of a contamination cannot be excluded, yet. Particularly the surprising increase of the biomass during the product formation phase in combination with the suspicious decrease of the L-phenylalanine concentration towards the process end reinforce this assumption. To better understand the here observed event, further data needs to be considered, for example the expressed fluorescence intensities at single-cell level.

Although the biomass concentrations were consistently lower at the start of the product formation phases in the TCB setups, the L-phenylalanine production of cells seemed to be not affected when applying short mean hydraulic residence times of 102 s in the bypass. In fact, the maximum achieved product titer was at 20.67 g L^{-1} and thus only 4% lower compared to the STB cultivation. However, a longer exposure of cells to the limiting conditions in the coiled flow inverter led to a percentual loss of 29% (TCB_M) and 25% (TCB_L) compared to the achieved product concentration of the STB cultivation. Most likely, the extended absence of glycerol, especially at longer mean hydraulic residence times in the CFI, contributed to rather unfavourable conditions for the L-phenylalanine production. The glycerol uptake and its conversion is mandatory to activate the central carbon metabolism and provide the crucial precursor molecules erythrose 4-phosphate and phosphoenolpyruvate for the aromatic amino acid biosynthesis (Weiner *et al.* 2014b, Weiner *et al.* 2016). Due to no feeding into the bypass, the production of these precursor molecules might have been delayed in the producing cells so that the overall L-phenylalanine production

was slowed down. Furthermore, low dissolved oxygen levels in the CFI might have contributed to unfavourable conditions for the L-phenylalanine production, as well. Though the enzymes along the aromatic amino acid biosynthesis are not directly dependent on the presence of molecular oxygen to catalyze the respective reactions (Pittard & Yang 2008), Khamduang *et al.* (2009) and others stated the importance of aerobic conditions for the production of amino acids such as L-arginine and L-phenylalanine (Utagawa 2004, Khamduang *et al.* 2009, Shu & Liao 2002). This is due to the re-oxidation of coenzymes such as $NADPH_2$ or $FADH_2$, which are directly involved in some reactions along the aromatic amino acid biosynthesis (Utagawa 2004, Pittard & Yang 2008). Additionally, the presence of oxygen also dictates the fluxes within the central carbon metabolism so that its prolonged absence potentially affected the availability of the precursor molecules erythrose 4-phosphate and phosphoenolpyruvate (Förster & Gescher 2014, Kargeti & Venkatesh 2017). Due to the fact that the L-phenylalanine production was not reduced at short exposure times of 102 s to unfavourable conditions in the bypass, the producing cells seemed to be capable to tolerate such conditions for a certain period of time.

In summary, exposing *E. coli* 4RP cells to dynamic conditions in the bypass of the two-compartment bioreactor negatively affected the cell growth regardless of the duration within the coiled flow inverter, whereas longer mean hydraulic residence times simultaneously reduced the product formation ability of the cells. Studies of *Corynebacterium glutamicum* in a two-compartment bioreactor with a stirred-tank bioreactor and plug flow reactor led to the same outcomes of a reduced cell growth (Limberg *et al.* 2016) or a diminished product yield during the lysine production (Lemoine *et al.* 2015). There are also studies on the impact of fluctuating conditions on *E. coli* cells in two-compartment bioreactors with a stirred-tank bioreactor and plug flow reactor. For example, both Löffler *et al.* (2016) and Simen *et al.* (2017) investigated the effects of glucose and nitrogen starvation in the plug flow reactor for up to 110 s, in which cells reacted with the immediate increase of the ppGpp alarmone. Commonly, all of these studies were conducted with mean hydraulic residence times of 180 s or less. Although such durations generally comply with the expected mixing times of large-scale bioprocesses, they can also be remarkably longer (Vrábel *et al.* 2000). However, longer mean hydraulic residence times in conventional two-compartment bioreactors with a straight tubular reactor as a bypass are difficult to realize, as this can mainly be achieved by lengthening the bypass. Instead, the here shown exploitation of coiled flow inverters in scale-down systems becomes a serious alternative due to their compact and flexible design. More importantly, coiled flow inverters provide good radial mixing with poor axial dispersion, even at lower volumetric flow rates (Klutz *et al.* 2015). Thus, they are particularly suitable for bioprocess operations

that demand for longer mean hydraulic residence times (Hoang *et al.* 2023b). Indeed, the here shown setup is far from perfect. Especially strategies to monitor the temperature, pH and dissolved oxygen levels at different positions of the coiled flow inverter would tremendeously elucidate the prevailing process conditions along the bypass. One interesting approach to realize this is the utilization of so-called flow-through cells. They can be easily connected to the used tubes of the coiled flow inverter and allow the optical *in-line* monitoring of the pH or dissolved oxygen levels.

7.2.2. Exhibited fluorescence levels during the L-phenylalanine production processes at population level

To better understand the effects of dynamic conditions on the cell growth and product formation in the performed L-phenylalanine production processes, the expressed reporter molecules of *E. coli* 4RP might reveal relevant information to explain the here observed outcomes. Specifically, deeper insights on the general stress response, growth behaviour, oxygen limitation and the product formation can be obtained by monitoring of fluorescence intensities at distinct wavelength ranges. Samples of all bioprocesses were prepared and measured in the flow cytometer following the same protocol with identical device configurations. If not stated otherwise, the following data show the median fluorescence intensities of the measured samples.

General stress response indicated by blue fluorescence levels
In the *E. coli* quadruple reporter strain, the general stress response of the cells were reflected by the expression of mTagBFP2, which is a blue fluorescent protein measurable at 448/45 nm (Figure 7.6). Interestingly, a reproducible pattern was recognized in all processes. In detail, a strong increase in fluorescence levels were observed during the biomass production phases with their maximum close to the start of the product formation phases. While median intensity levels of the cell population in the STB setup rose from 217.83 ± 8.95 at 15.3 h to 624.81 ± 3.32 at 39.9 h (Figure 7.6 A), they also increased in the TCB_S and TCB_M cultivations from 269.89 ± 3.16 at 14.6 h to 731.54 ± 2.08 at 37.8 h (TCB_S) and 299.82 ± 2.89 at 17.6 h to 627.66 ± 2.76 at 40.6 h (TCB_M) (Figure 7.6 BC). Though the cell population of the TCB_L setup also showed this increasing trend of the general stress response markers during the biomass production phase, it was less pronounced compared to the other bioprocesses (242.67 ± 3.94 at 16.2 h to 449.32 ± 2.07 at 39.1 h, Figure 7.6 D). Nonetheless, the monitored mTagBFP2 levels of all cell populations dropped remarkably right before and after the start the product formation phases. With exception of the STB cultivation, in which a slightly rising trend was observed towards the process end, the expressed median fluorescence levels remained

stable at comparably low levels. On average, the cell populations showed median fluorescence intensities of 449.63 ± 38.89 (STB), 420.65 ± 65.27 (TCB_S), 402.17 ± 31.88 (TCB_M) and 382.32 ± 36.70 (TCB_S) after 60 h until the process end (Figure 7.6).
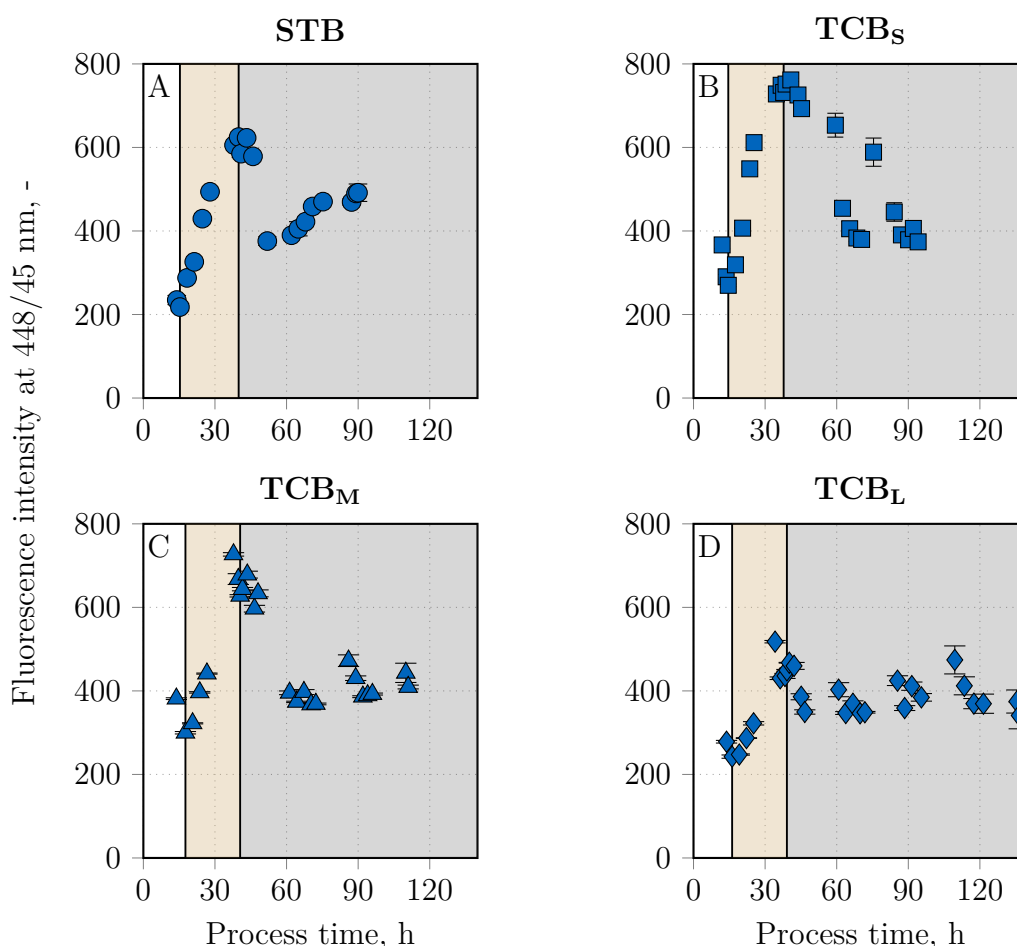
Figure 7.6: Expressed median fluorescence intensities of *Escherichia coli* 4RP cells at 448/45 nm for monitoring of the general stress response during the L-phenylalanine production in a stirred-tank bioreactor (STB) or in a two-compartment bioreactor (TCB) combining a stirred-tank bioreactor and a coiled flow inverter as a bypass. The latter cultivations were conducted with either short (TCB_S), medium (TCB_M) or long (TCB_L) mean hydraulic residence times of 102.63 s (4.71 mL s^{-1}), 199.50 s (2.36 mL s^{-1}) or 403.30 s (1.18 mL s^{-1}) within the coiled flow inverter. Vertical lines indicate the transition from the initial batch phase (white background) to the biomass production phase (orange background) and the final product formation phase (grey background).

Growth behaviour indicated by green fluorescence levels

The growth of cell populations was monitored by expression levels of a green fluorescent protein called mEmerald, which can be measured at 527/32 nm. It is important to mention that the growth rates of the cell population in all processes followed the same pattern: the highest growth rates at the end of the initial batch phases, reduced intermediate growth rates during the biomass production phases and no further cell growth at the mid and

late product formation phases with exception of cells in the TCB_L. Therefore, a step-wise decrease of median fluorescence signals would be expected. Indeed, this anticipated pattern was observed during the L-phenylalanine production processes in the STB and TCB_S setups. On average, cells showed median fluorescence intensities of 212.20 ± 5.75 (initial batch phase), 126.01 ± 29.19 (biomass production phase) and 123.15 ± 12.95 (product formation phase) in the STB, whereas the median green fluorescence levels of the cell population in the TCB_S setup consecutively dropped from 305.17 ± 29.40 (initial batch phase) to 277.40 ± 13.52 (biomass production phase) and ended at 198.44 ± 36.51 (product formation phase) (Figure 7.7 AB).
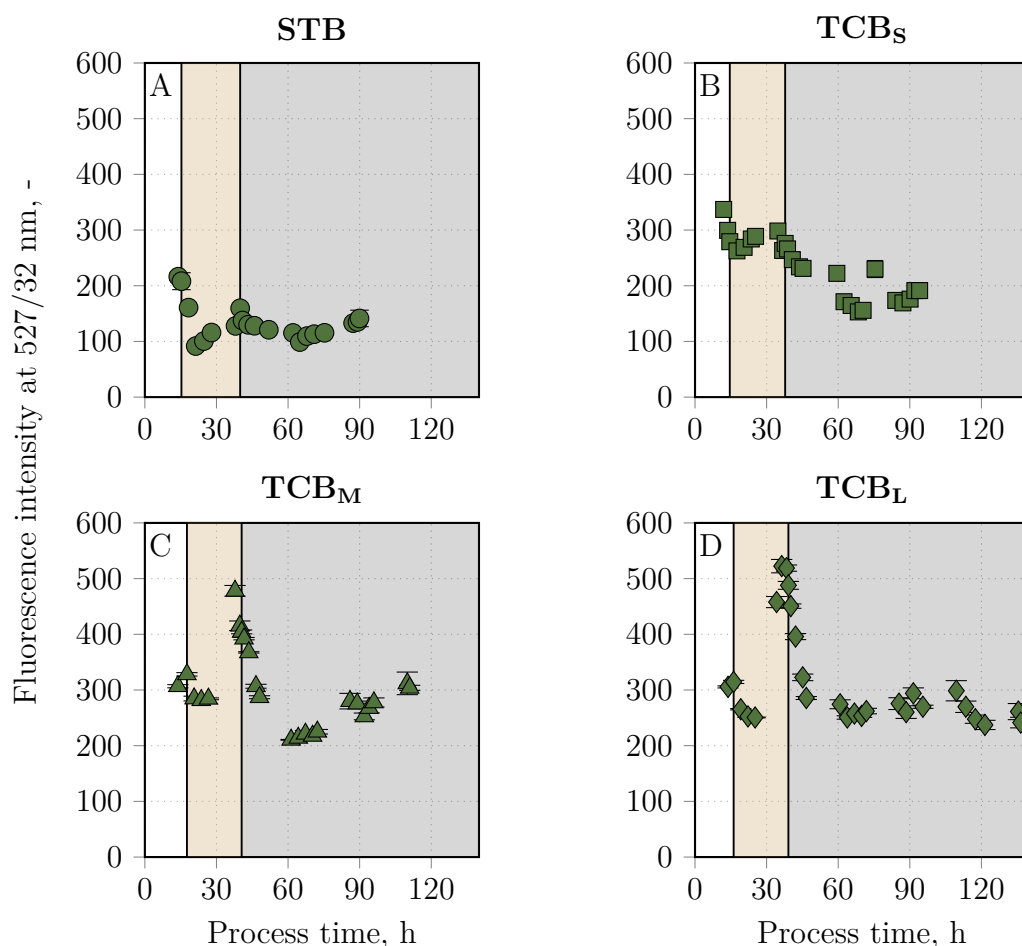
Figure 7.7: Expressed median fluorescence intensities of *Escherichia coli* 4RP cells at 527/32 nm for monitoring of the growth behaviour during the L-phenylalanine production in a stirred-tank bioreactor (STB) or in a two-compartment bioreactor (TCB) combining a stirred-tank bioreactor and a coiled flow inverter as a bypass. The latter cultivations were conducted with either short (TCB_S), medium (TCB_M) or long (TCB_L) mean hydraulic residence times of 102.63 s (4.71 mL s⁻¹), 199.50 s (2.36 mL s⁻¹) or 403.30 s (1.18 mL s⁻¹) within the coiled flow inverter. Vertical lines indicate the transition from the initial batch phase (white background) to the biomass production phase (orange background) and the final product formation phase (grey background).

However, strongly deviating trends were observed in TCB processes with either medium or long mean hydraulic residence times. At the end of the initial batch phases and the early stages of the following biomass production phases, the cell populations in both processes were characterized with comparably low median fluorescence levels of 297.06 ± 20.09 (TCB_M) and 277.73 ± 30.19 (TCB_L). Towards the end of the biomass production phases, the observed signals remarkably increased to a maximum value of 478.05 ± 9.68 (TCB_M) at 37.8 h and 522.41 ± 12.01 (TCB_L) at 36.3 h. These directly dropped right before or after the start of the product formation phases with constant average values of 254.79 ± 36.24 (TCB_M) and 263.61 ± 17.43 (TCB_L) after 60 h of process time and beyond (Figure 7.7 CD).

Oxygen limitation indicated by orange fluorescence levels

The presence of oxygen limitation in cells is indicated by the expression of CyOFP1, which was measured at 586/42 nm. Dissolved oxygen levels in the stirred-tank bioreactor never felt below 30% air saturation for a longer period in all conducted L-phenylalanine production processes. However, the levels of dissolved oxygen within the coiled flow inverter in TCB cultivations were uncertain due to the lack of monitoring devices within the bypass. Again, similar trends of the oxygen limitation marker CyOFP1 were observed during the L-phenylalanine production processes in the STB and TCB_S. The expressed median fluorescence intensities increased particularly during the biomass production phases from 192.81 ± 2.45 at 21.3 h to 358.92 ± 1.79 at 39.9 h (STB) and 426.55 ± 1.24 at 14.6 h to 528.19 ± 2.69 at 37.8 h (TCB_S). After the start of the product formation phases, the cell populations in both processes showed reduced but constant median fluorescence intensities at 318.11 ± 35.27 (STB) and 477.75 ± 54.10 (TCB_S) with rare outliers (Figure 7.8 AB). In contrast, the expressed median fluorescence intensities of cells in the TCB_M and TCB_L setups showed a constantly rising trend during the L-phenylalanine production. In detail, the median fluorescence intensities of the cell population in the TCB_M setup increased from 322.82 ± 2.83 at 17.6 h to 800.22 ± 15.24 at the process end (Figure 7.8 C). Similarly, cells in the TCB_L constantly expressed the oxygen limitation marker, so that the median fluorescence signals rose from 261.30 ± 4.62 at 16.2 h to 836.93 ± 55.5 at the end of the process (Figure 7.8 D).
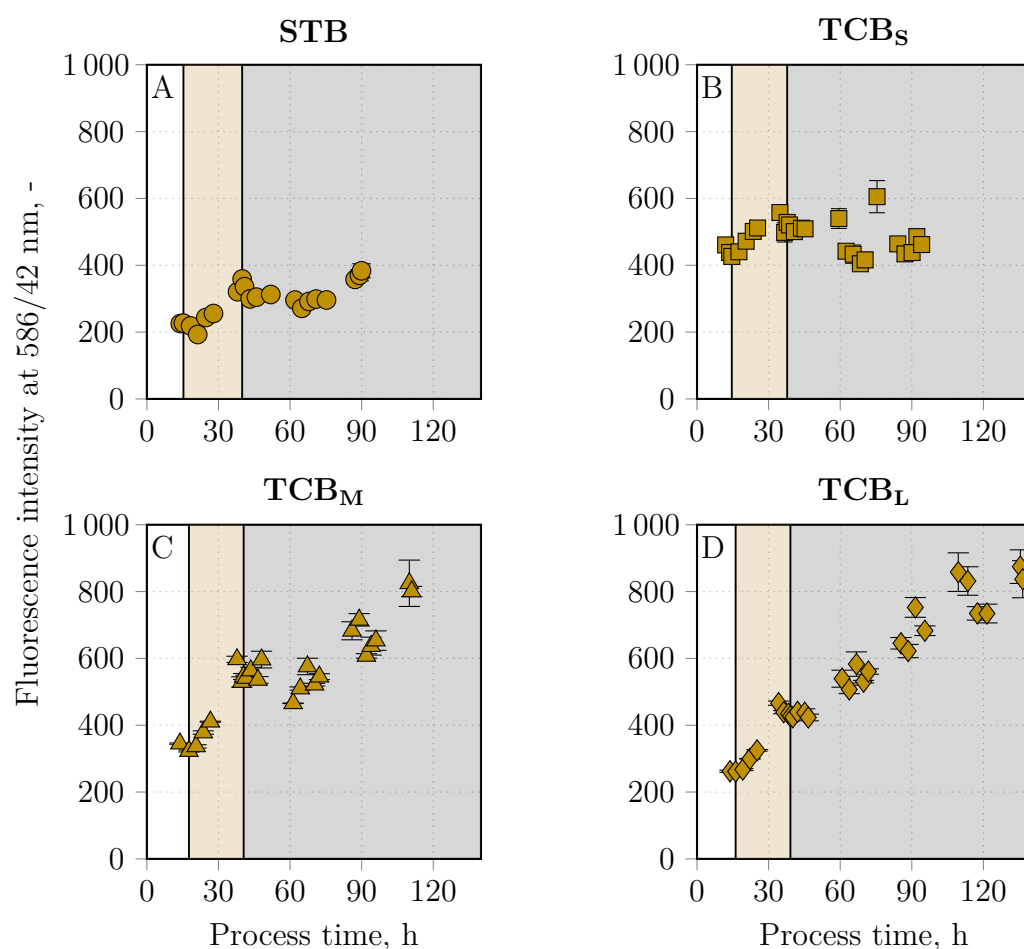
Figure 7.8: Expressed median fluorescence intensities of *Escherichia coli* 4RP cells at 586/42 nm for monitoring of the oxygen limitation during the L-phenylalanine production in a stirred-tank bioreactor (STB) or in a two-compartment bioreactor (TCB) combining a stirred-tank bioreactor and a coiled flow inverter as a bypass. The latter cultivations were conducted with either short (TCB$_S$), medium (TCB$_M$) or long (TCB$_L$) mean hydraulic residence times of 102.63 s (4.71 mL s^{-1}), 199.50 s (2.36 mL s^{-1}) or 403.30 s (1.18 mL s^{-1}) within the coiled flow inverter. Vertical lines indicate the transition from the initial batch phase (white background) to the biomass production phase (orange background) and the final product formation phase (grey background).

Product formation indicated by red fluorescence levels

The product formation of *E. coli* 4RP cells was tracked by monitoring of the mCardinal2 expression, a far-red fluorescent protein measurable at 660/10 nm. During the L-phenylalanine production process conducted in the STB, cells showed the lowest median signals at the beginning of the biomass production phase with values around 220.34 ± 2.68. However, the expressed median fluorescence intensities of the cell population increased from the start until the end of the biomass production phase with a slope of 9.31 h^{-1} to an intensity of 390.61 ± 114.73 at 39.9 h. After a short lag phase, the median red fluorescence levels further increased with the start of the product formation phase from 393.83 ± 1.37 at 43.3 h to a maximum value of 625.71 ± 9.21 at 51.9 h. This corresponded to a slope

of 26.78 h^{-1}. From then on, the median fluorescence signals constantly declined until the process end to a final value of 381.34 ± 19.25 (Figure 7.9 A).
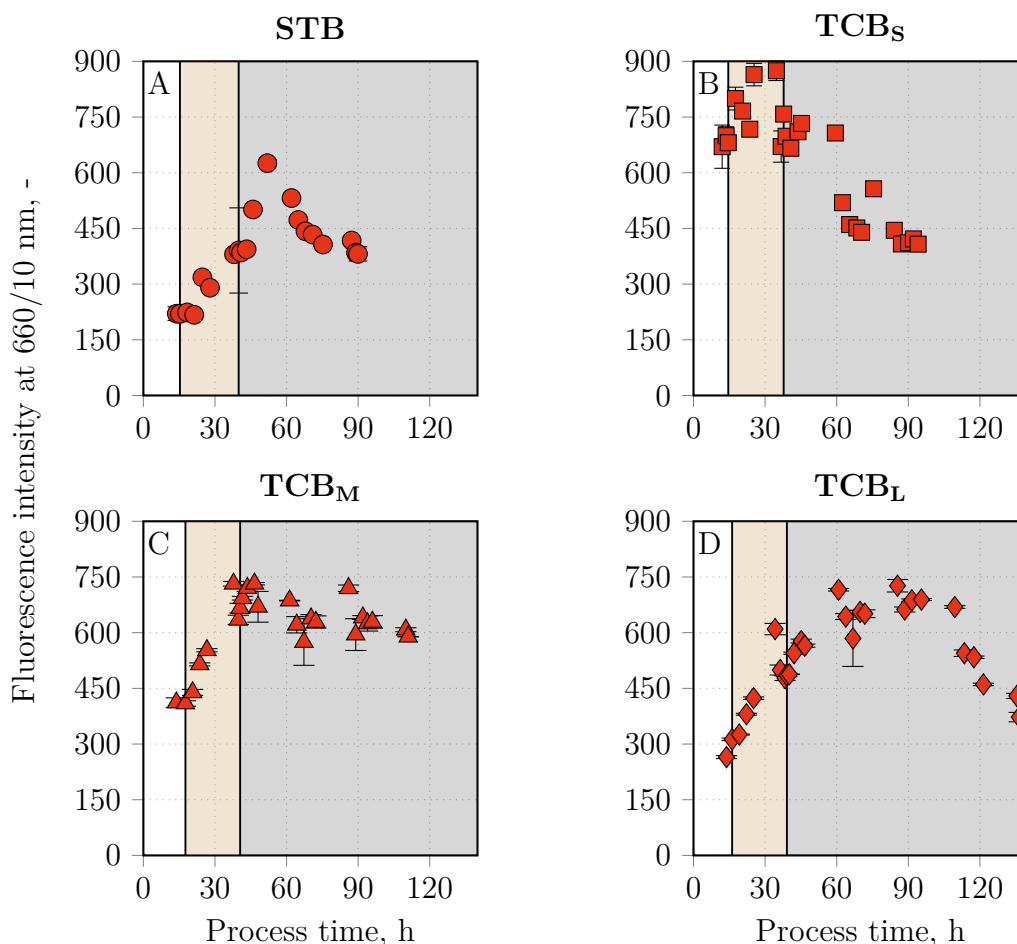
Figure 7.9: Expressed median fluorescence intensities of *Escherichia coli* 4RP cells at 660/10 nm for monitoring of the product formation during the L-phenylalanine production in a stirred-tank bioreactor (STB) or in a two-compartment bioreactor (TCB) combining a stirred-tank bioreactor and a coiled flow inverter as a bypass. The latter cultivations were conducted with either short (TCB$_\text{S}$), medium (TCB$_\text{M}$) or long (TCB$_\text{L}$) mean hydraulic residence times of 102.63 s (4.71 mL s^{-1}), 199.50 s (2.36 mL s^{-1}) or 403.30 s (1.18 mL s^{-1}) within the coiled flow inverter. Vertical lines indicate the transition from the initial batch phase (white background) to the biomass production phase (orange background) and the final product formation phase (grey background).

In contrary, cells in the TCB$_\text{S}$ setup already showed the highest median fluorescence intensities of 869.49 ± 7.27 in the middle of the biomass production phase between 25.4 h to 34.7 h. Prior to the start of the product formation phase, the median signal intensities fell to 757.99 ± 5.88 at 37.8 h and further decreased after the initiation of the L-phenylalanine production to a value of 407.65 ± 7.52 at the process end (Figure 7.9 B). Another unique trend was observed during the L-phenylalanine production in the TCB with medium mean hydraulic residence times in the CFI. During the biomass production phase, the expressed

median fluorescence intensities of the cell population rose from 409.25 $\pm$ 7.27 at 17.6 h to 666.16 $\pm$ 13.02 at 40.6 h (slope of 11.21 h^{-1}). Subsequently, there was a second increase of median fluorescence signals during the first 6 h of the product formation phase to 731.87 $\pm$ 3.10 (slope of 10.95 h^{-1}). Directly after, a slightly declining trend occurred until the process end with a final expressed median intensity of 589.08 $\pm$ 0.04 (Figure 7.9 C). Some similarities were also observed during the TCB cultivation with long mean hydraulic residence times in the bypass. Again, there was an initial increase of expressed median fluorescences of the cell population from 264.72 $\pm$ 3.93 at 13.8 h to 485.95 $\pm$ 4.97 at the end of the biomass production phase at 39.1 h (slope of 8.74 h^{-1}). After induction of the recombinant protein expression and the start of the product formation phase, the expressed median signals at 660/10 nm further rose to 689.16 $\pm$ 2.80 at 95.5 h (slope of 3.61 h^{-1}), which coincided with the maximum achieved L-phenylalanine concentration. Thereafter, a decline of median fluorescence intensities was seen to a final value of 372.56 $\pm$ 12.65 at 136.5 h. The overall trend is reminiscent of an inverted parabola (Figure 7.9 D).

Discussion

The obtained trends of all expressed fluorescent proteins during the L-phenylalanine production process with *E. coli* 4RP in the STB with 1.35 L starting volume were identical to the observed trends in the same bioreactor setup with a lower starting volume of 1 L. Hence, the *E. coli* quadruple reporter strain reproducibly reflected the general stress response, growth behaviour, oxygen limitation and product formation during the L-phenylalanine production under well-mixed process conditions, which presumably matched with the related process state variables.

Dynamic environmental conditions in TCB cultivations had no major impact on the general stress response of the cells during the L-phenylalanine production. In all processes, cells showed the anticipated elevation of blue fluorescence intensities during the biomass production phases with their maximum before the start of the product formation phases. Assuming that higher mTagBFP2 levels can be interpreted as cell populations that mainly suffer from substrate limiting conditions (Battesti *et al.* 2011), the coiled flow inverter in TCB cultivations resembled a limitation zone with no substrate supply. Therefore, higher mTagBFP2 levels could have been expected. However, the substrate concentrations in the STB setup were also relatively low due to the fed-batch operation with a strongly limited glycerol supply (Lee 1996). Therefore, identical trends regarding the general stress response levels in both the STB and TCB setups most certainly derived owing the low availability of substrates during the biomass production phases in any case. The weaker pronounciation of this trend in the TCB$_L$ setup might be related to the unwanted accu-

mulation of glycerol towards the end of the biomass production phase, which increased the abundance of this carbon source and probably dampened the corresponding general stress response levels of the cells.

The growth of *E. coli* cells can be associated with the expression of the *rrnB* operon, which encodes for ribosomal RNA molecules. This also applies for the here used quadruple reporter strain. According to Murray *et al.* (2003), the activation of this operon is growth-rate dependent. Therefore, the integration of a synthetic copy of mEmerald into a *rrnB* promoter complex shall reflect the magnitude of growth of the cell population. In all performed L-phenylalanine production processes, the cell populations always showed the highest growth rates at the initial batch phases, intermediate growth rates during the biomass production phases and almost no cell growth for the whole product formation phases (with exception of the TCB$_L$ cultivation). While this reproducible pattern was well-reflected by the mEmerald levels of the cell populations in the STB and the TCB$_S$ cultivations, prolonging the mean hydraulic residence times to 199.50 s or 403.30 s in the CFI led to a complete different trend. Surprisingly, the cell populations in the TCB$_M$ and TCB$_L$ showed by far the highest fluorescence intensities at 527/32 nm towards the end of the biomass production phases, which clearly did not match with the corresponding growth rates. Additionally, the lowered cell growth in two-compartment bioreactor cultivations were particularly observed during the biomass production phases, which make these trends even more questionable. While Murray *et al.* (2003) stated that the activation of the *rrnB* operon is also dependent on the amino acid availability (stringent control), there were no remarkable differences concerning the concentrations of L-phenylalanine, L-tyrosine, L-glutamate and L-tryptophane between the conducted processes. Indeed, there are 16 other amino acids to consider. Therefore, the detection and quantification of these might clarify this aspect. Additionally, the repetitive exposure of cells to aerobic and anaerobic conditions might have contributed to these unconventional trends, as well. According to Basan *et al.* (2015), the proportions of certain proteome fractions in *E. coli* cells are strongly affected whether the cells follow the fermentative pathway under anaerobic conditions or the oxidative respiration under aerobic conditions for the energy generation (Basan *et al.* 2015). Thus, the longer exposure of *E. coli* cells in the coiled flow inverter might have partly activated the fermentative pathway for the energy generation. As a result, the proteome fractions of the cells changed, thus leading to more irrational trends of biomass-related events such as the *rrnB* expression. However, assuming the prevailence of anoxic conditions in the coiled flow inverter, it is surprising that no accumulation of by-products such as acetate was observed in the TCB cultivations with mean hydraulic residence times of 199.50 s or 403.30 s (see chapter 7.2.1). It is also worth

mentioning that the unexpected cell growth during the TCB cultivation with the longest applied mean hydraulic residence time was not reflected by the measured fluorescence intensities.

Previous L-phenylalanine production processes with the *E. coli* quadruple reporter strain showed the activation of the *narGHIJ* operon when dissolved oxygen levels were on the verge to fall below 30% air saturation, which was coupled to elevated fluorescence signals at 586/42 nm. This was especially observed at the end of the biomass production phases (Hoang *et al.* 2023a, Hoang *et al.* 2023b). The same trend was seen during the L-phenylalanine production processes in the STB and the TCB_S setups. Consequently, a rather short exposure of cells to limiting conditions with expectably anoxic conditions did not promote the oxygen limitation responses. However, prolonging the mean hydraulic residence times to 199.50 s or 403.30 s in the bypass led to constantly increasing CyOFP1 levels from the beginning of the biomass production phases until the process ends. Therefore, cells seemingly suffered from permanent oxygen limiting conditions, most likely due to the longer exposure to anoxic conditions in TCB cultivations. Hence, mean hydraulic residence times of around 200 s or longer seemed to be a decisive turning point to perturbate some of the cellular physiologies. Indeed, this duration was also the turning point for a reduced product formation in *E. coli* cells.

The red fluorescent protein mCardinal2 was integrated into the $pF81_{kan}$ plasmid to monitor the recombinant expression of important enzymes along the aromatic amino acid biosynthesis pathway for the L-phenylalanine production. Despite the successful formation of L-phenylalanine in all conducted processes, the functionality of this reporter molecule was only confirmed in the STB cultivation. Though a basal expression was again observed in the STB setup, there was a stronger increase of signal intensities after addition of IPTG. However, exposing the quadruple reporter strain to dynamic environmental conditions in two-compartment bioreactor cultivations led to completely deviating and partly irrational trends. For example, the expressed fluorescence intensities in the TCB_S setup were higher during the biomass production phase compared to the product formation phase, whereas the mCardinal2 levels in the TCB_M cultivation particularly increased during the biomass production phase, but declined with the start of the product formation phase. Based on the rather random trends obtained during the TCB cultivations, it appears that the repetitive exposure of the *E. coli* 4RP cells to dynamic and rather limiting conditions might have enhanced the level of basal expression. According to Giuliodori *et al.* (2007), fluctuating and unfavourable conditions potentially influence the gene expression events in cells and make them rather unpredictable. To underline

this hypothesis, future processes should consider the measurements of transcriptomics or proteomics. Also, the basal expression of mCardinal2 needs to be controlled in future experiments. Indeed, the tac promoter in the pF81$_{kan}$ plasmid can be exchanged with more reliable promoter systems such as the araBAD promoter for a tighter regulation (Guzman *et al.* 1995, Terpe 2006). However, this would completely alter the expression system of the well-characterized *E. coli* FUS4 (pF81$_{kan}$) strain and would demand for new characterization studies. Alternatively, the ribosome binding site of mCardinal2 can be adjusted to reduce the basal expression during the L-phenylalanine production, while sticking to the original expression system (Salis *et al.* 2009, Seo *et al.* 2013).

Overall, the *E. coli* quadruple reporter strain is capable of reflecting certain prevailing process state variables based on the expression of related reporter molecules in a reproducible and thus reliable way. However, this was only observed in processes with well-mixed and homogeneous environments. As soon as the cells were exposed to dynamic and limiting conditions in the coiled flow inverter of the two-compartment bioreactor, the corresponding trends of the reporter molecules increasingly deviated to their related process state variables. Especially the application of mean hydraulic residence times of above 200 s in the bypass seemed to be a critical turning point. Besides the impact of anoxic conditions on the proteome levels of cells (Basan *et al.* 2015), they might have also affected the development of reporter molecules within the coiled flow inverter in TCB cultivations. As mentioned previously, fluorescent proteins can not mature under oxygen limiting conditions (Heim *et al.* 1994, Cubitt *et al.* 1995). Indeed, the returning of the cells from the coiled flow inverter with expectably anoxic conditions to the stirred-tank bioreactor with dissolved oxygen levels above 30% air saturation should immediately re-activate the initiated maturation processes of all expressed fluorescent proteins. Nonetheless, the maturation reactions might have been delayed or disturbed in the longer term due to the repetitive exposure to limiting conditions in the bypass, thus leading to unexpected trends. To circumvent this obstacle, future reporter strains should consider flavin mononucleotide-based fluorescent proteins, which evolve optical signals under both aerobic and anaerobic conditions (Drepper *et al.* 2007). At the same time, this study emphasizes the urgency to determine *in vivo* maturation and degradation rates of the utilized reporter molecules to better evaluate the general trends. Ultimately, it is worth considering the aspect that cell samples were consistently withdrawn from the stirred-tank bioreactor during the TCB cultivations. Due to the continuous circulation of cells between the compartments, a pool of cells accumulated in the stirred-tank bioreactor that just experienced different cultivating conditions. Some might have spent a non-trackable time under ideal bioprocess conditions, while others re-entered the stirred-tank bioreactor after experiencing the lim-

iting conditions in the bypass. This diversity was further exacerbated by the accompanied increase of the working volume during the fed-batch operations. As a consequence, the collected cell samples contained uncertain proportions of cell fractions with diverse cultivating histories, which might have contributed to the partly unexpected trends of the expressed fluorescence intensities. For a better clarification, future studies in the TCB should implement the simultaneous sampling from the coiled flow inverter to have a direct comparison.

7.2.3. Population heterogeneity during the L-phenylalanine production processes with an *Escherichia coli* quadruple reporter strain in a stirred-tank bioreactor and a two-compartment bioreactor

The median fluorescence levels of reporter strains give a fair approximation regarding the developed cellular characteristics of a microbial population. However, differences between single cells are masked so that the potential occurrence of subpopulations remain uncertain. To elucidate this aspect and ultimately elaborate the level of population heterogeneity in bioprocesses, the expressed fluorescence levels have to be compared at single-cell level. In the following, the single-cell fluorescences of *E. coli* 4RP from the L-phenylalanine production processes in the STB or TCB were compared at 448/45 nm, 527/32 nm, 586/42 nm and 660/10 nm to reveal potential differences between the general stress response, growth behaviour, oxygen limitation and product formation of the cells. Based on the achieved histograms, multimodal, particularly broad or left- and right-skewed distributions indicated a heterogeneous population. Conversely, narrow and unimodal distributions were a sign of a homogeneous population. Besides the consideration of their distributions, the mean-to-median ratios (MMR) and coefficient of variances (CV) were included for the evaluation. The higher the MMR and CV values, the stronger the level of population heterogeneity and *vice versa*. Furthermore, the expressed fluorescence levels of single cells were correlated in density plots, that allow a coherent analysis of two specific cellular physiologies of interest.

Stirred-tank bioreactor cultivation

According to the MMR and CV values of the single-cell fluorescence levels at 448/45 nm (Supplementary material A.4, Tables A.18 and A.19), cells particularly differed in their general stress response levels at the beginning and the process end. The histograms at 14 h and 15 h were characterized by high CV values above 2.00, thus indicating broad distributions (Figure 7.10, blue subplots). However, the distributions seemed even broader

with a left skew between 25 h to 28 h, though the CV values were lower at 1.17 ± 0.02 and 1.00 ± 0.02. Towards the start of the product formation phase, the distributions became comparably narrow with MMR and CV values at 1.08 ± 0.00 and 0.71 ± 0.01 at 40 h. Strikingly, two subpopulations evolved at around 52 h. While one of the cell population contained 54% of the cells with a median fluorescence intensity of $2.9 \cdot 10^2$ at 448/45 nm, the second population represented 46% of the population with elevated stress response levels at a median signal intensity of $1.3 \cdot 10^3$. Both co-existing subpopulations remained present until the end of the process. This bimodal distribution was also indicated by the elevated MMR values of 1.72 ± 0.04 at the process end.

The histograms displaying the growth behaviour at 527/32 nm merely changed concerning their exhibited fluorescence intensities and were mainly characterized by very uniform distributions during the L-phenylalanine production in the STB cultivation (Figure 7.10, green subplots). This was also shown by the MMR and CV values (Supplementary material A.4, Tables A.18 and A.19), which were consistently at 1.20 ± 0.10 and 1.10 ± 0.64. Two exceptions occurred at 21 h and 62 h, in which left-skewed distributions were observed.

A similar trend was seen in the distributions of single cells regarding the expression of CyOFP1 at 586/42 nm. Only unimodal distributions occurred with slight left skews that barely changed during the STB cultivation (Figure 7.10, orange subplots). Accordingly, the MMR and CV neither signalized strong differences between single cells with values at 1.23 ± 0.13 and 1.33 ± 0.35 (Supplementary material A.4, Tables A.18 and A.19).

In contrast, *E. coli* cells seemed to have expressed different levels of red fluorescence intensities during the initial batch phase and the start of the biomass production phase. The histograms were characterized by broad distributions with an average median signal intensity of $2.2 \cdot 10^2 \pm 0.2 \cdot 10^2$ and a standard deviation of $1.2 \cdot 10^3 \pm 0.2 \cdot 10^3$ between 14 h to 21 h (Figure 7.10, red plots). Towards later stages of the biomass production phase, a second population occured. While 72.8% of the cells expressed lower fluorescence intensities of around $2.1 \cdot 10^2$, the smaller fraction of around 27.2% of the population showed higher signal intensities at $1.2 \cdot 10^3$. These observations were underlined by the MMR and CV values. While the latter was above 2.00 between 14 h to 15 h, the mean-to-median ratios also surpassed values of 2.00 between 14 h and 38 h. Both subpopulations converged and fused with the start of the product formation phase to a uniform and more narrow distribution with a median signal intensity of $4.5 \cdot 10^2$ and a standard deviation of $7.8 \cdot 10^2$ at 46 h. Out of this population, again 44% of the cells detached and showed

lower fluorescence intensities of $2.2 \cdot 10^2$, while the remaining 56% of the population had higher signal intensities of $5.9 \cdot 10^2$. Surprisingly, this was not reflected by the MMR and CV values, which decreased towards the process end (MMR of 1.12 $\pm$ 0.02 and CV of 0.66 $\pm$ 0.02, Supplementary material A.4, Tables A.18 and A.19). At the same time, the standard deviations of the histograms consistently sank from a comparably high value of $1.3 \cdot 10^3$ $\pm$ $0.1 \cdot 10^3$ at 14 h to $2.9 \cdot 10^2$ $\pm$ $0.1 \cdot 10^2$ at the process end.
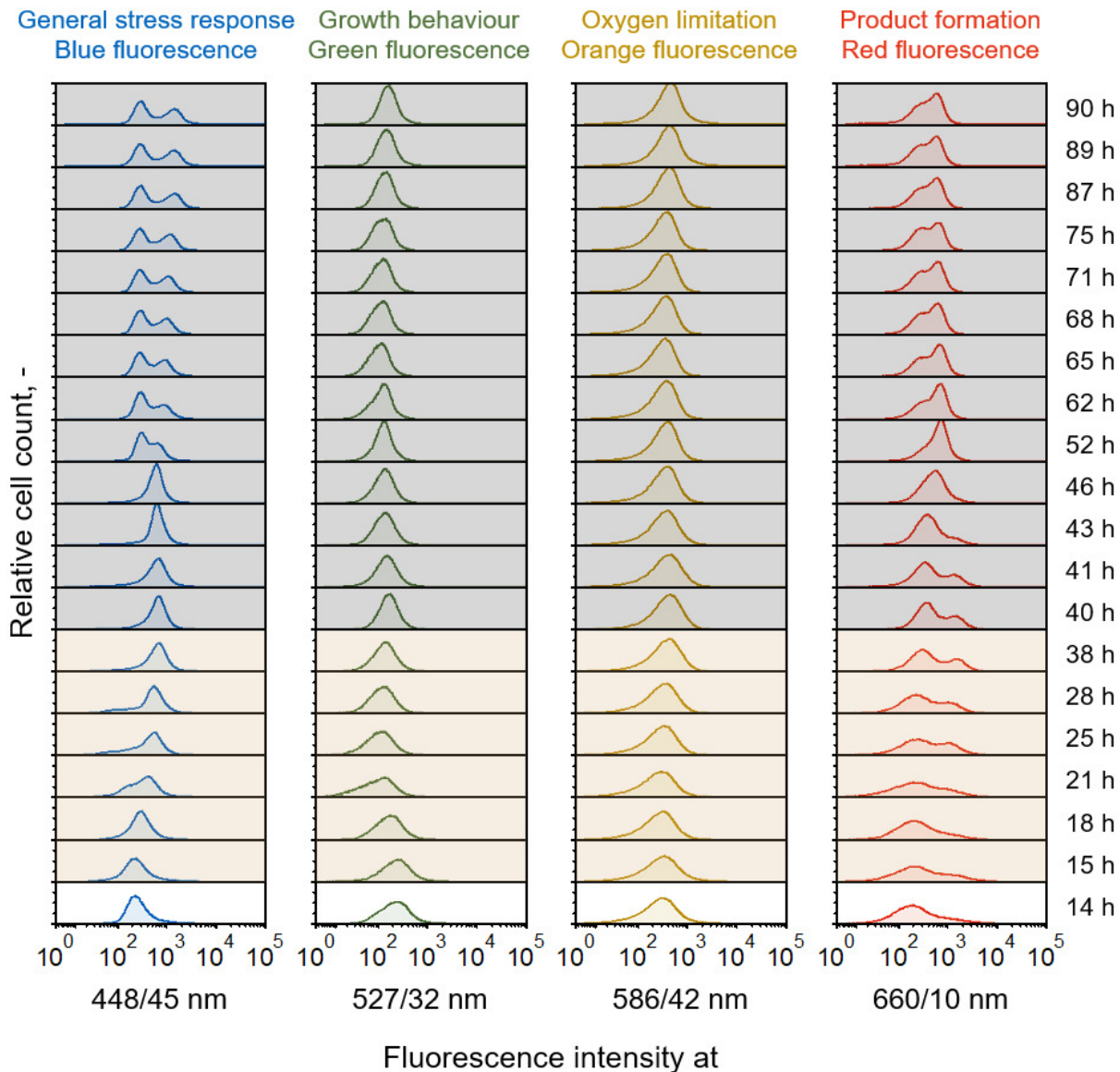
Figure 7.10: Fed-batch process for the L-phenylalanine production with *Escherichia coli* 4RP in a stirred-tank bioreactor: Stacked histograms showing the expressed fluorescence intensities at 448/45 nm (general stress response, blue histograms), 527/32 nm (growth behaviour, green histograms), 586/42 nm (oxygen limitation, orange histograms) and 660/10 nm (product formation, red histograms) against the relative cell count of *at-line* analyzed cell samples. Histograms with a white, orange or grey background derive from samples during the initial batch phase, biomass production phase or product formation phase. The corresponding time stamps of all samples are on the right side.

Two-compartment bioreactor cultivation with short mean hydraulic residence times of 102.63 s in the bypass

Conversely to the single-cell levels of the general stress response marker in the STB setup, the cultivation of *E. coli* 4RP cells in the TCB with short mean hydraulic residence times of 102.63 s showed an unimodal distribution at the end of the initial batch phase. The MMR and CV values were at 1.23 ± 0.00 and 1.24 ± 0.07 at 12 h and remained at these levels until 45 h. Nonetheless, the distributions became relatively broad towards the end of the biomass production phase with an average signal intensity of $7.4 \cdot 10^2 \pm 0.2 \cdot 10^2$ and a standard deviation of $1.1 \cdot 10^3 \pm 0.2 \cdot 10^3$ between 35 h to 44 h. This was not displayed by the supporting indicators. Interestingly, some of the cells detached from the main population towards higher fluorescence intensities at around 62 h. As a result, 72.6% of the cells had lower signal intensities of $4.3 \cdot 10^2$, whereas a minority of 28.2% showed elevated fluorescence intensities of $1.3 \cdot 10^3$. Towards the process end, the MMR increased to a maximum value of 2.16 ± 0.01 with the highest standard deviation of $1.2 \cdot 10^3 \pm 0.0 \cdot 10^3$ (Supplementary material A.4, Tables A.20 and A.21, Figure 7.11, blue plots).

The same trend was observed for the expressed single-cell fluorescence intensities at 527/32 nm for monitoring of the growth behaviour. While cells showed similar expression levels of mEmerald from the end of the initial batch phase at 12 h to the beginning of the product formation phase at 45 h (average MMR and CV of 1.24 ± 0.04 and 0.86 ± 0.19), tendencies towards slightly bimodal and right-skewed distributions occurred at 65 h and beyond. Interestingly, this coincided with the depletion of L-tyrosine at around 60 h (Supplementary material A.2, Table A.13). At the end of the process, 70.8% of the cells showed lower fluorescence intensities of $1.6 \cdot 10^2$, while the rest of the population expressed higher levels at $4.5 \cdot 10^2$. The corresponding MMR values elevated to over 1.40 towards the process end, whereas the CV values remained under 1.00 (Supplementary material A.4, Tables A.20 and A.21, Figure 7.11, green plots).

Again, the expressed single-cell fluorescences of *E. coli* 4RP at 586/42 nm (oxygen limitation marker) did not differ during the whole TCB$_S$ cultivation. Uniform histograms were consistently observed, but with small pronounciations for left skews between 12 h to 25 h. Towards the bioprocess end, the distributions broadened with slight tendencies for right skews. Accordingly, the standard deviation of the histograms almost doubled from $4.6 \cdot 10^2 \pm 0.1 \cdot 10^2$ at 12 h to $8.7 \cdot 10^2 \pm 0.4 \cdot 10^2$ at the process end. This was also reflected by the MMR and CV values, which increased from 1.19 ± 0.01 and 0.84 ± 0.02 at 12 h of process time to 1.57 ± 0.01 and 1.21 ± 0.00 at the process end (Supplementary material A.4, Tables A.20 and A.21, Figure 7.11, orange plots).
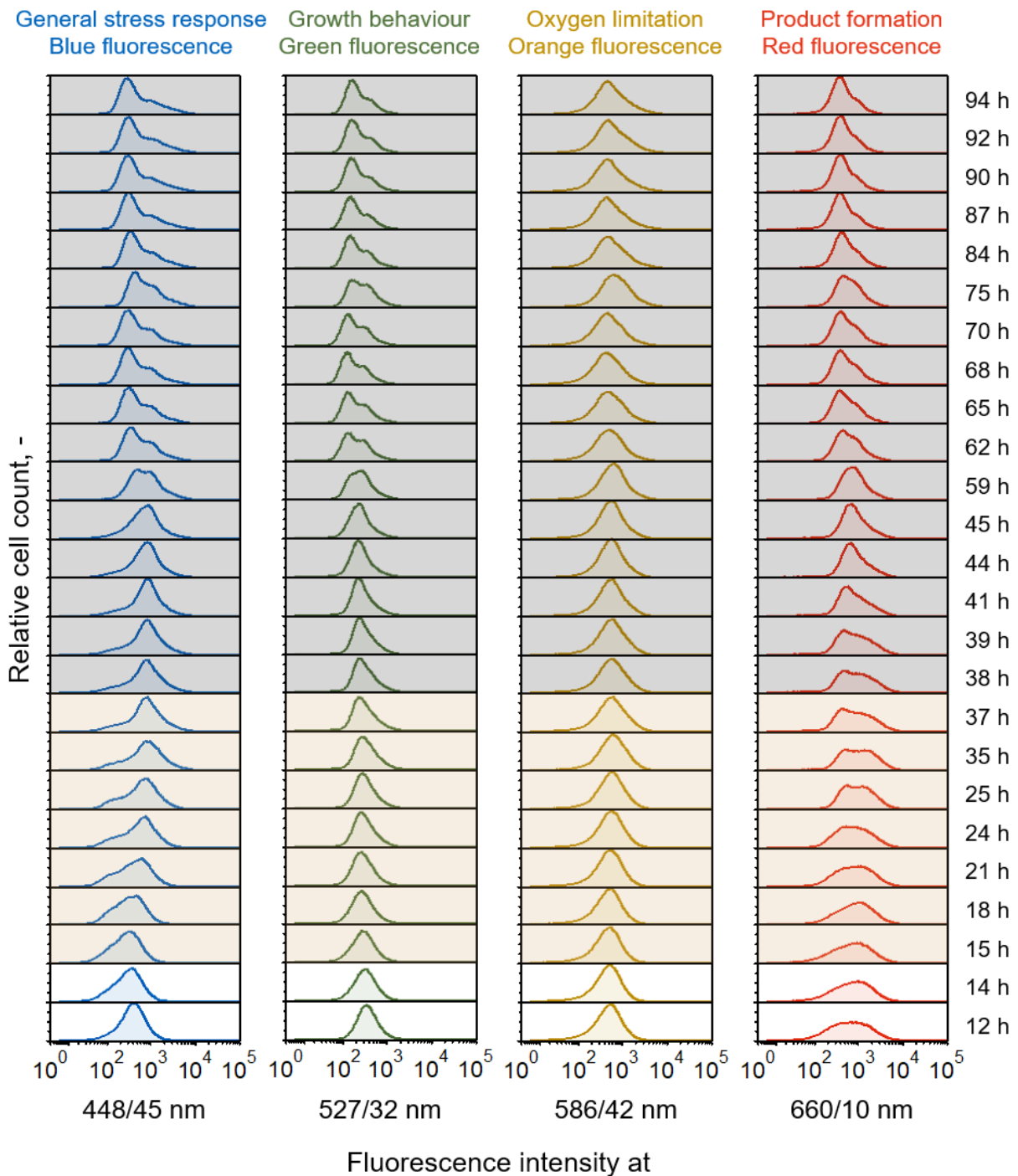
Figure 7.11: Fed-batch process for the L-phenylalanine production with *Escherichia coli* 4RP in a two-compartment bioreactor with a mean hydraulic residence time of 102.63 s (TCB$_S$): Stacked histograms showing the expressed fluorescence intensities at 448/45 nm (general stress response, blue histograms), 527/32 nm (growth behaviour, green histograms), 586/42 nm (oxygen limitation, orange histograms) and 660/10 nm (product formation, red histograms) against the relative cell count of *at-line* analyzed cell samples. Histograms with a white, orange or grey background derive from samples during the initial batch phase, biomass production phase or product formation phase. The corresponding time stamps of all samples are on the right side.

The single-cell fluorescence levels of the product formation marker at 660/10 nm showed broad distributions directly during the inital batch phase and the biomass production phase. Hence, the highest MMR and CV values occurred between 12 h and 37 h with average values of 1.50 $\pm$ 0.07 and 1.03 $\pm$ 0.07. Afterwards, the distributions became more narrow towards the process end. For example, the CV values of the histograms sank to 0.84 $\pm$ 0.03 between 84 h and 94 h of process time. Accordingly, the related histograms were rather unimodal, but with a seemingly minor subpopulation showing higher fluorescence intensities. Similar to the cells in the STB cultivation, the width of the histograms decreased during the L-phenylalanine production process. While the initial standard deviation was at $1.2 \cdot 10^3$ $\pm$ $0.0 \cdot 10^3$ at 12 h, it diminished to $4.3 \cdot 10^2$ $\pm$ $0.0 \cdot 10^2$ at the process end (Supplementary material A.4, Tables A.20 and A.21, Figure 7.11, red plots).

Two-compartment bioreactor cultivation with medium mean hydraulic residence times of 199.50 s in the bypass

At the early stages of the biomass production phase during the TCB cultivation with a hydraulic mean residence time of 199.50 s in the bypass, the histograms at 448/45 nm were characterized by uniform distributions (average MMR and CV values of 1.30 $\pm$ 0.03 and 0.97 $\pm$ 0.29). Accordingly, the average standard deviation of the distributions was at $3.9 \cdot 10^2$ $\pm$ $0.0 \cdot 10^2$ between 21 h to 27 h. Histograms with left skews evolved towards the end of the biomass production phase and the beginning of the product formation phase with elevated standard deviations of $7.7 \cdot 10^2$ $\pm$ $0.1 \cdot 10^2$ between 40 h to 42 h. These then transformed to right-skewed distributions at around 61 h and beyond. This was indicated by both the standard deviation and MMR, which rose to $1.0 \cdot 10^3$ and 1.74 $\pm$ 0.01 at 111 h (Supplementary material A.4, Tables A.22 and A.23, Figure 7.12, blue plots).

Right-skewed distributions were also found concerning the expressed growth marker of *E. coli* 4RP cells at 527/32 nm. Starting with an uniform population with a median signal intensity of $3.1 \cdot 10^2$ and a standard deviation of $3.4 \cdot 10^2$ at 14 h, the histograms became right-skewed at around 38 h. Consequently, the cell population showed relatively broad distributions between 38 h to 61 h with an average standard deviation of $5.0 \cdot 10^2 \pm 0.7 \cdot 10^2$ and varying median signal intensities at around $3.8 \cdot 10^2$ $\pm$ $0.7 \cdot 10^2$. Simultaneously, there were slight tendencies for the formation of a subpopulation showing higher fluorescence intensities compared to the main population between 47 h and 48 h. However, these quickly transformed back to right-skewed distributions (Figure 7.12, green plots). According to the MMR and CV values, no remarkable differences occurred concerning the single-cell fluorescence intensities of this marker as they were consistently between 1.33 $\pm$ 0.07 and 0.91 $\pm$ 0.16 (Supplementary material A.4, Tables A.22 and A.23).
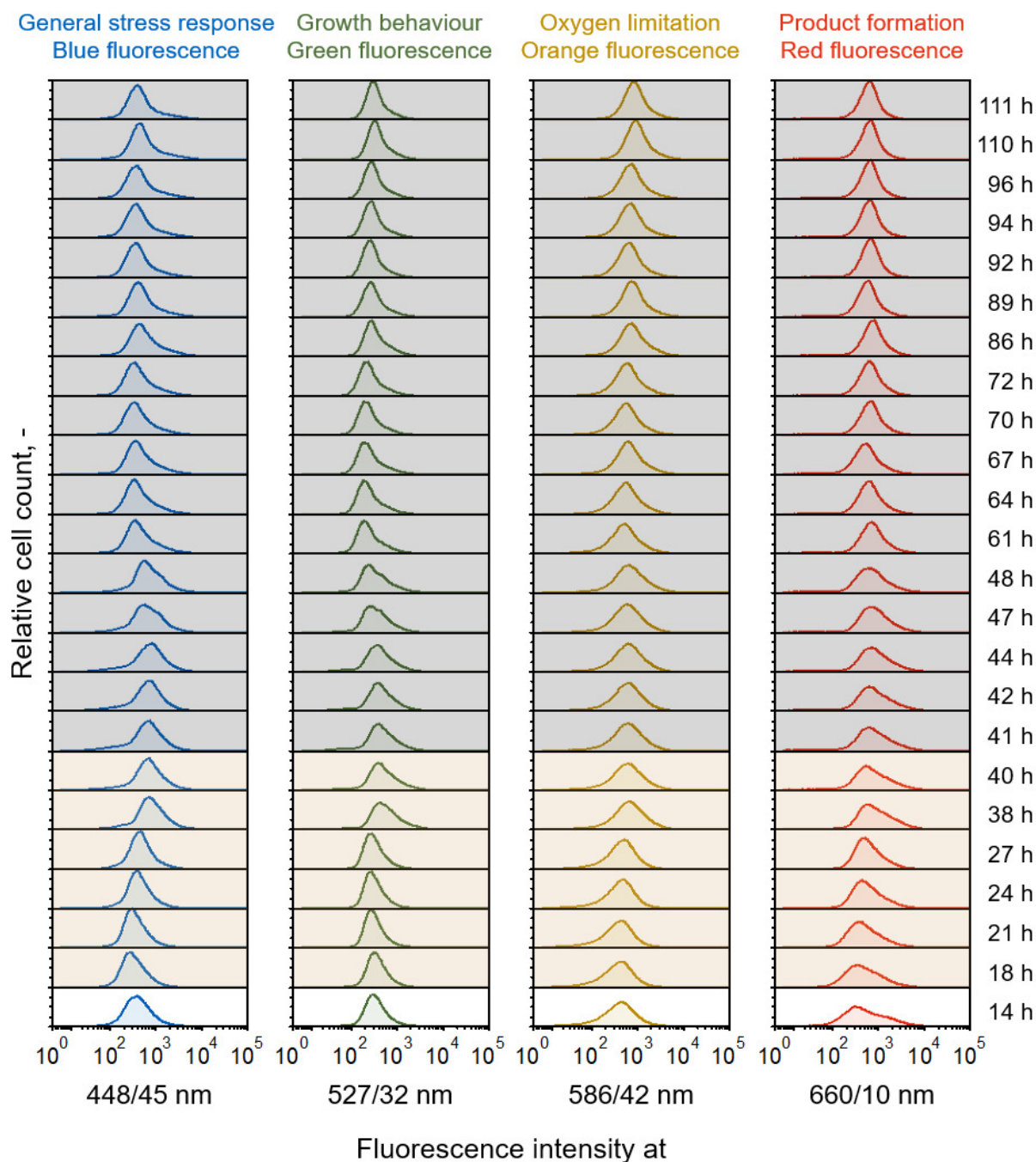
Figure 7.12: Fed-batch process for the L-phenylalanine production with *Escherichia coli* 4RP in a two-compartment bioreactor with a mean hydraulic residence time of 199.50 s (TCB_M). Stacked histograms showing the expressed fluorescence intensities at 448/45 nm (general stress response, blue histograms), 527/32 nm (growth behaviour, green histograms), 586/42 nm (oxygen limitation, orange histograms) and 660/10 nm (product formation, red histograms) against the relative cell count of *at-line* analyzed cell samples. Histograms with a white, orange or grey background derive from samples during the initial batch phase, biomass production phase or product formation phase. The corresponding time stamps of all samples are on the right side.

At 586/42 nm, all histograms were mainly uniform, which was further underlined by constant mean-to-median ratios of 1.32 $\pm$ 0.05 and CV values of 1.19 $\pm$ 0.22. Nonetheless, it is worth mentioning that the distributions of the oxygen limitation marker shifted towards higher fluorescence intensities with an initial median signal intensity of $3.5 \cdot 10^2 \pm 0.0 \cdot 10^2$ at 14 h to $8.0 \cdot 10^2 \pm 0.2 \cdot 10^2$ at 111 h. At the same time, the standard deviation consistently increased from $5.4 \cdot 10^2 \pm 0.3 \cdot 10^2$ to $9.6 \cdot 10^2 \pm 0.1 \cdot 10^2$ (Supplementary material A.4, Tables A.22 and A.23, Figure 7.12, orange plots).

Differences in single-cell expression levels of the product formation marker mCardinal2 were particularly present at the initial batch phase and the start of the biomass production phase between 14 h to 18 h. These were indicated by relatively broad distributions with an average standard deviation of $1.2 \cdot 10^3 \pm 0.0 \cdot 10^3$. Accordingly, the MMR was at 2.09 $\pm$ 0.02 and concomitant with the highest CV value of 1.57 $\pm$ 0.05 at 14 h. Further broad histograms were observed between the end of the biomass production phase and the early product formation phase between 38 h to 47 h with standard deviations of $1.2 \cdot 10^3 \pm 0.0 \cdot 10^3$, but with lower MMR and CV values of 1.53 $\pm$ 0.07 and 1.10 $\pm$ 0.06. Towards the process end, the expressed single-cell fluorescences of the cell population became more narrow with no signs of co-existing subpopulations. This assumption was supported by a reduced standard deviation of $4.5 \cdot 10^2 \pm 0.0 \cdot 10^2$ at 111 h. Additionally, the MMR and CV values sank to 1.12 $\pm$ 0.00 and 0.68 $\pm$ 0.00 (Supplementary material A.4, Tables A.22 and A.23, Figure 7.12, red plots).

Two-compartment bioreactor cultivation with long mean hydraulic residence times of 403.30 s in the bypass

During the L-phenylalanine production in the two-compartment bioreactor applying long mean hydraulic residence times of 403.30 s in the CFI, the general stress response of *E. coli* cells seemed to be homogeneous at the initial batch phase and biomass production phase. This was also reflected by the MMR and CV values, which were between 1.22 $\pm$ 0.04 and 0.82 $\pm$ 0.28. Additionally, the distributions between 14 h to 38 h had an average standard deviation of $3.4 \cdot 10^2 \pm 0.4 \cdot 10^2$. However, the initiation of the product formation phase temporarily affected the distributions. For example, weak signs of a second population were observed between 45 h to 47 h, that showed higher fluorescence intensities compared to the main population. Furthermore, slightly right-skewed distributions occurred towards the process end with elevated standard deviations of $9.0 \cdot 10^2 \pm 0.0 \cdot 10^2$ at 136 h. At the same time, both the MMR and CV values increased to 1.47 $\pm$ 0.04 and 1.79 $\pm$ 0.09 towards the process end (Supplementary material A.4, Tables A.24 and A.25, Figure 7.13, blue plots).
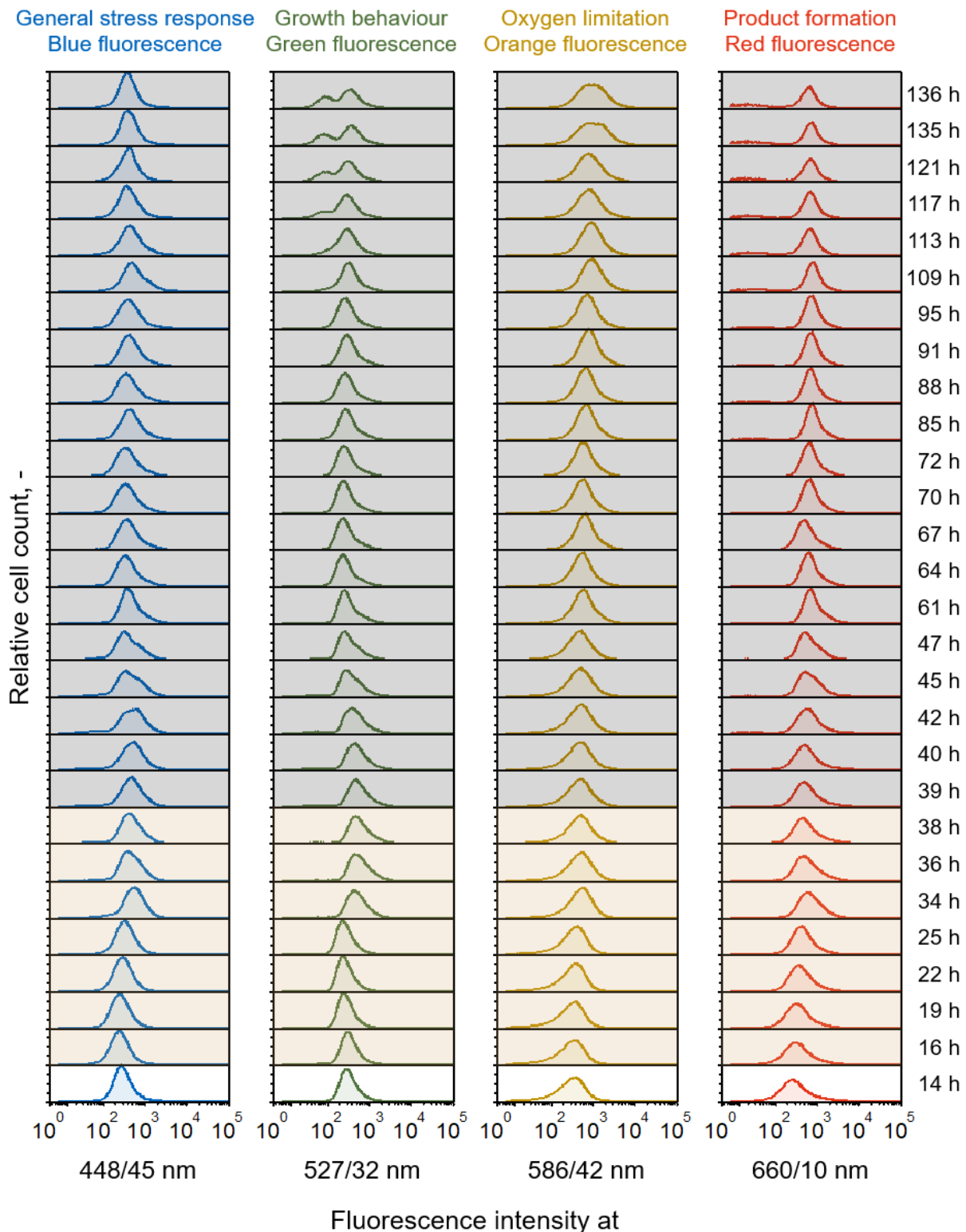
Figure 7.13: Fed-batch process for the L-phenylalanine production with *Escherichia coli* 4RP in a two-compartment bioreactor with a mean hydraulic residence time of 403.30 s ($\mathrm{TCB_L}$): Stacked histograms showing the expressed fluorescence intensities at 448/45 nm (general stress response, blue histograms), 527/32 nm (growth behaviour, green histograms), 586/42 nm (oxygen limitation, orange histograms) and 660/10 nm (product formation, red histograms) against the relative cell count of *at-line* analyzed cell samples. Histograms with a white, orange or grey background derive from samples during the initial batch phase, biomass production phase or product formation phase. The corresponding time stamps of all samples are on the right side.

The histograms at 527/32 nm to reflect the growth behaviour of the cells were also characterized by relatively narrow and uniform distributions with minor right-skewed tendencies between 34 h to 47 h. Accordingly, the standard deviations were at $4.5 \cdot 10^2 \pm 0.7 \cdot 10^2$ (median signal intensity of $4.4 \cdot 10^2 \pm 0.8 \cdot 10^2$) and thus slightly higher compared to the remaining samples with an average standard deviation of $2.8 \cdot 10^2 \pm 0.4 \cdot 10^2$ (median signal intensity of $2.7 \cdot 10^2 \pm 0.2 \cdot 10^2$). Towards the process end at 117 h, a second population arose with a minority of 36.1% of the cells that showed a lower signal intensity of $8.2 \cdot 10^1$. In contrast, the remaining population had elevated fluorescence intensities of $3.6 \cdot 10^2$ (Figure 7.13, green plots). All these deviations from a normally distributed cell population were not highlighted by the respective MMR and CV values, which were stable at around 1.26 ± 0.04 and 0.81 ± 0.09 (Supplementary material A.4, Tables A.24 and A.25).

Similar to the TCB cultivation with medium mean hydraulic residence times, the measured distributions of the oxygen limitation marker at 586/42 nm were characterized by unimodal shapes with a constant shift towards higher intensities. Again, the increase of median fluorescence intensities was concomitant with an increase of the standard deviation of the distributions. While cells showed a median signal intensity of $2.6 \cdot 10^2$ with a standard deviation of $3.8 \cdot 10^2$ at 14 h of process time, both increased to $9.0 \cdot 10^2$ and $1.3 \cdot 10^3$ at the end of the process (Figure 7.13, orange plots). This was not indicated by the MMR and CV values as both were stable at approximately 1.25 ± 0.06 and 0.95 ± 0.17 (Supplementary material A.4, Tables A.24 and A.25).

Broad distributions of the product formation marker at 660/10 nm were especially present at the beginning of the process between 14 h to 16 h (MMR and CV values of 1.69 ± 0.18 and 1.64 ± 0.21) as well as at the start of the product formation phase between 39 h to 47 h (MMR and CV values of 1.41 ± 0.07 and 1.13 ± 0.12). Accordingly, the standard deviations of the distributions were at $7.9 \cdot 10^2 \pm 0.3 \cdot 10^2$ between 14 h and 16 h and $8.5 \cdot 10^2 \pm 0.1 \cdot 10^2$ between 39 h and 47 h. The broader histograms at 39 h to 47 h were also characterized by slight right skews. Similar to all the other conducted bioprocesses, the standard deviation of the distributions sank towards the process end to $4.6 \cdot 10^2 \pm 0.1 \cdot 10^2$. Surprisingly, a second population emerged at around 85 h, but with a considerably lower fluorescence intensity. While these cells made 7.7% of the whole cell population at that time, their population size increased to 43.3% at the end of the process. Compared to the median signal intensity of $6.1 \cdot 10^2$ of the remaining cells, the strongly rising second population showed a suspiciously lower signal intensity of $2.5 \cdot 10^0$ (Supplementary material A.4, Tables A.24 and A.25, Figure 7.13, red plots).

Besides the consideration of histograms to investigate the extent of population heterogeneity in bioprocesses, density plots are another visualization tool, in which two fluorescence parameters are coherently plotted. Hence, potential correlations between two markers can be revealed. In best case, subpopulations can be identified with superior cellular characteristics compared to the remaining cell population. Particularly three distinct process stages of the conducted L-phenylalanine production processes were of major interest. First, the growth marker mEmerald was correlated with the three remaining markers at the end of the biomass production phases with the objective to find coherences for well-growing cells. Secondly, the product formation marker mCardinal2 was further analyzed at the mid product formation phases in each process, where cells showed the highest biomass specific product formation rates. Ideally, cells can be revealed with superior characteristics concerning the L-phenylalanine production. Last but not least, the general stress response marker mTagBFP2 was correlated to all remaining markers at the process ends. During this time, the cell populations expectably experienced challenging conditions, which was reflected by the accumulation of by-products and the diminished product formation. Assuming that cells with a higher general stress response level better anticipated such environments and developed effective strategies to cope with unfavourable conditions, these seemingly more robust cells shall be identified. A positive correlation between two markers indicate the simultaneous increase or decrease of the expressed marker levels, whereas a negative correlation symbolize the rise of one marker amount with the decrease of the other and *vice versa*.

Correlation of the growth behaviour of cells to the general stress response, oxygen limitation and product formation at the end of the biomass production phase

The end of the biomass production phases were characterized by elevated general stress response and oxygen limitation levels of the cell populations. Nevertheless, cell growth was still present. According to the density plots of the fluorescence intensities at 527/32 nm (growth behaviour) to the fluorescence intensities at 448/45 nm (general stress response) in all L-phenylalanine production processes (STB, 38.0 h, TCB_S, 36.7 h, TCB_M, 39.8 h, TCB_L, 38.3 h), cells in the TCB setups showed that stronger growing cells also expressed higher general stress response levels (Figure 7.14 DGJ). Though this coherence also applied for *E. coli* cells in the STB setup, it was less obvious. This was due to a small population of 6.2% of the cells that detached from the main population (91.3%) with lower general stress response levels (median value of $6.1 \cdot 10^1$). Nonetheless, they showed similar growth characteristics (median value of $1.4 \cdot 10^2$) compared to the residual population, which had median values of $6.4 \cdot 10^2$ and $1.3 \cdot 10^2$ at 448/45 nm and 527/32 nm (Figure 7.14 A).

End of biomass production phase
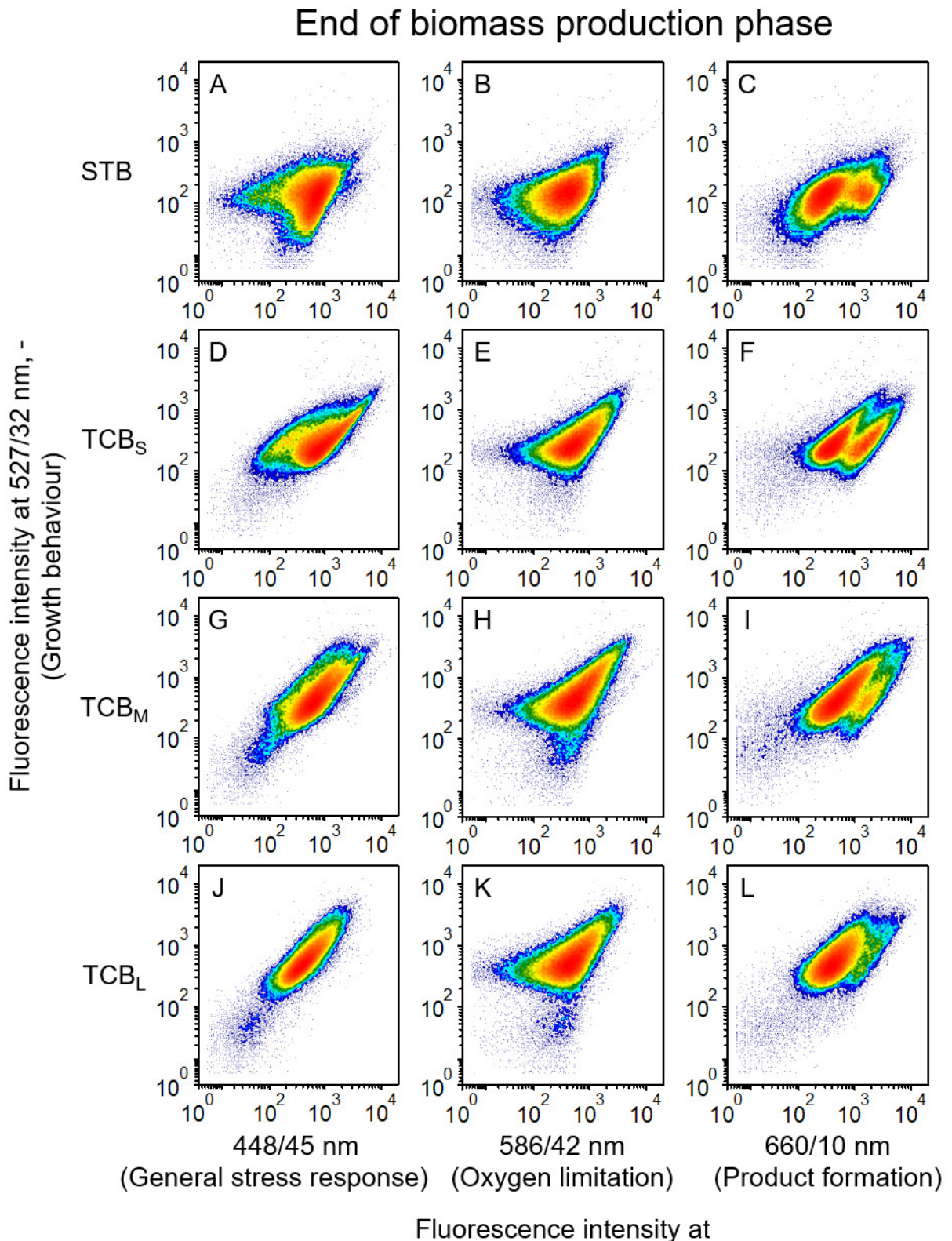
Figure 7.14: Density plots of *Escherichia coli* 4RP cells during the L-phenylalanine production processes at the end of the biomass production phases of the stirred-tank bioreactor cultivation (STB, 38.0 h) and two-compartment bioreactor cultivations with short (TCB$_S$, 36.7 h, 102.63 s), medium (TCB$_M$, 39.8 h, 199.50 s) and long (TCB$_L$, 38.3 h, 403.30 s) mean hydraulic residence times. The fluorescence intensities at 527/32 nm (growth behaviour, y-axis) are plotted against the measured intensities at 448/45 nm (general stress response, x-axis), 586/42 nm (oxygen limitation, x-axis) and 660/10 nm (product formation, x-axis).

Plotting the growth marker of cells with the oxygen limitation marker (586/42 nm), an overall positive correlation was observed in all processes, which was again less pronounced during the L-phenylalanine production process in the STB (Figure 7.14 BEHK). However, no strong indications were observed regarding the existence of subpopulations. Instead, these were found when plotting the growth marker with the product formation marker at 660/10 nm. In general, the expressed single-cell fluorescences followed a positive correlation, again. At the same time, two populations were present, especially during the STB and TCB_S cultivations. In the former, there was a smaller subpopulation of 31.7% showing a higher fluorescence intensity at 660/10 nm (median value of $1.5 \cdot 10^3$) and a slightly higher fluorescence intensity at 527/32 nm (median value at $1.6 \cdot 10^2$) compared to the main population (64.3% of the cell population with median values of $1.2 \cdot 10^2$ and $2.8 \cdot 10^2$ at 527/32 nm and 660/10 nm). The latter showed two equally distributed subpopulations with approximately the same signal intensities at 527/32 nm (52.1% of the cells with a signal intensity of $2.8 \cdot 10^2$ compared to 41.6% of the cells with $2.8 \cdot 10^2$), but different intensities at 660/10 nm (52.1% of the cells with a signal intensity of $4.3 \cdot 10^2$ and 41.6% of the cells with $1.6 \cdot 10^3$). Density plots of the cells from the TCB_M and TCB_L cultivations were characterized with similar patterns like in the TCB_S setup, but with weaker pronounciations of a detaching subpopulation towards higher intensities at 660/10 nm (Figure 7.14 CFIL).

Correlation of the product formation of cells to the general stress response, growth behaviour and oxygen limitation at the mid product formation phase
L-phenylalanine was produced in all performed processes in the STB and TCB. Interestingly, the highest biomass specific product formation rates occurred approximately at the same process times at 67.9 h in the STB, 68.4 h in the TCB_S, 69.8 h in the TCB_M and 72.3 h in the TCB_L. Plotting the expressed fluorescence intensities of single cells at 660/10 nm (product formation) to the fluorescence intensities at 448/45 nm (general stress response) revealed opposing trends between the STB and TCB cultivations. *E. coli* 4RP cells in the TCB cultivations consistently showed a positive correlation between the product formation and the general stress response levels regardless of the operated mean hydraulic residence times. Hence, strong L-phenylalanine producing cells also expressed an elevated general stress response and *vice versa*. For the cell population in the TCB_S, a minority of cells (3.8%) detached from the main population with a higher median fluorescence intensity of $3.0 \cdot 10^3$ at 448/45 nm compared to the residual cells (92.8%) with a median intensity of $3.8 \cdot 10^2$. Simultaneously, this minor population was characterized by a slightly lower signal intensity of $2.5 \cdot 10^2$ at 660/10 nm compared to the main population with a signal intensity of $4.8 \cdot 10^2$ (Figure 7.15 DGJ).
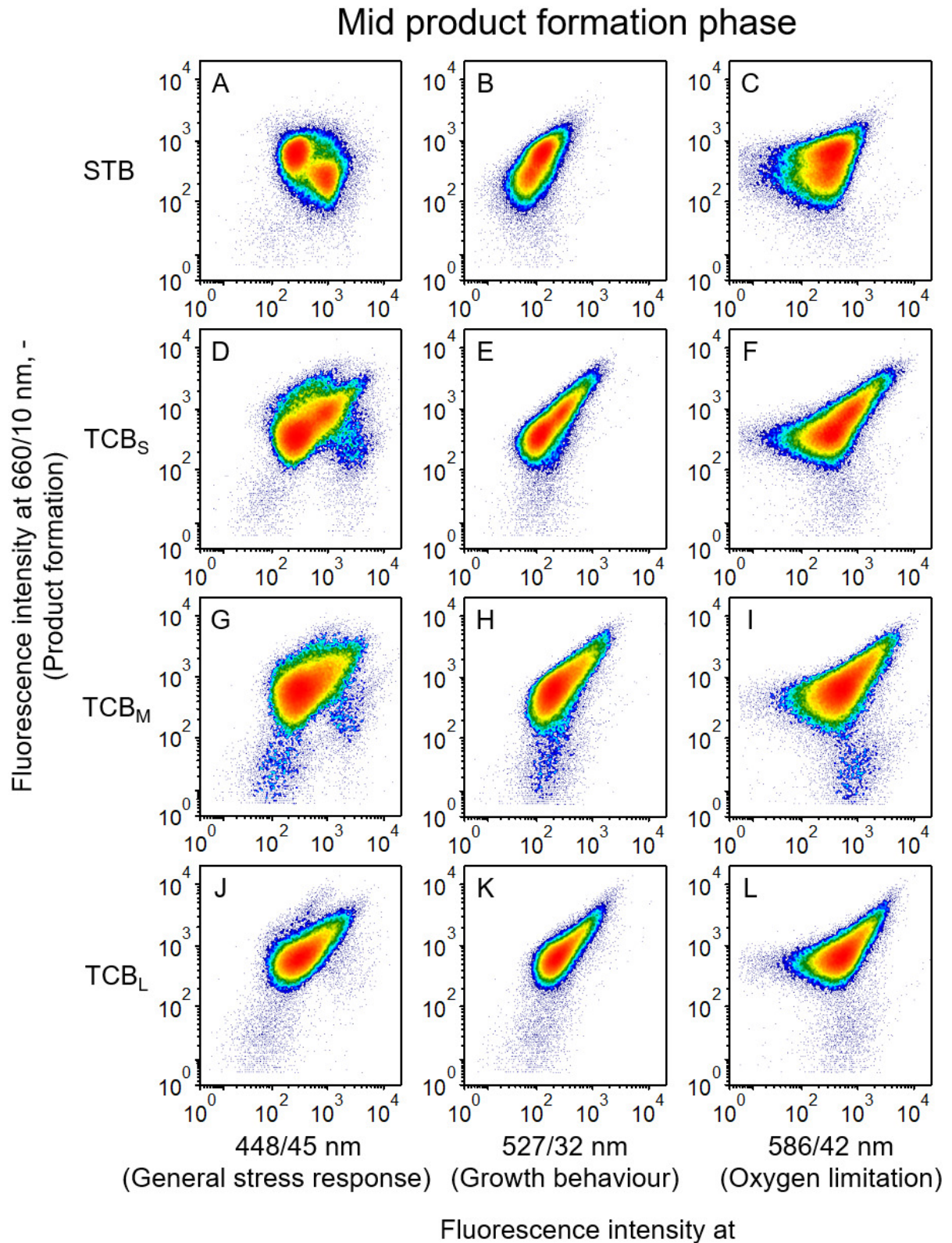
Figure 7.15: Density plots of *Escherichia coli* 4RP cells during the L-phenylalanine production processes at their maximum product formation rates in the stirred-tank bioreactor cultivation (STB, 67.9 h) and two-compartment bioreactor cultivations with short (TCB$_S$, 68.4 h, 102.63 s), medium (TCB$_M$, 69.8 h, 199.50 s) and long (TCB$_L$, 72.3 h, 403.30 s) mean hydraulic residence times. The fluorescence intensities at 660/10 nm (product formation, y-axis) are plotted against the measured intensities at 448/45 nm (general stress response, x-axis), 527/32 nm (growth behaviour, x-axis) and 586/42 nm (oxygen limitation, x-axis).

Conversely, strong producing L-phenylalanine cells in the STB cultivation showed a lower general stress response and *vice versa*, thus exhibiting a rather negative correlation. This was especially exemplified by the two present subpopulations. 53.8% of the cells expressed median fluorescence intensities of $2.9 \cdot 10^2$ and $6.0 \cdot 10^2$ at 448/45 nm and 660/10 nm, whereas the remaining cells (43.3%) had median intensities of $9.5 \cdot 10^2$ and $2.5 \cdot 10^2$ (Figure 7.15 A). Density plots of the expressed product formation and the growth markers (527/32 nm) revealed that cells with a more pronounced growth behaviour generally expressed higher levels of the product formation marker in all L-phenylalanine production processes (Figure 7.15 BEHK). Furthermore, strong L-phenylalanine producing cells also showed high fluorescence intensities of the oxygen limiation marker at 586/42 nm in all TCB cultivations (Figure 7.15 FIL). In contrast, no clear pattern was observed between both cellular characteristics in the STB cultivation (Figure 7.15 C).

Correlation of the general stress response of cells to the growth behaviour, oxygen limitation and product formation at the process end

Last but not least, the general stress response levels of the cells were further elaborated at the process ends, where they most likely faced a stack of unfavourable conditions. Additionally, the previously evaluated histograms showed differences of single-cell fluorescences at 448/45 nm, especially towards the process ends. These were also found in density plots when correlating the fluorescence intensities at 448/45 nm (general stress response) with the measured intensities at 527/32 nm (growth behaviour). In the STB cultivation, no clear coherences were observed, but two almost equally distributed subpopulations occurred. Both showed similar fluorescence intensities at 527/32 nm with 43.7% of the population at $1.2 \cdot 10^2$ and 55.4% of the population at $1.7 \cdot 10^2$. Simultaneously, the former group of cells expressed a higher signal intensity of $1.3 \cdot 10^3$ at 448/45 nm compared to the residual 55.4% of the cells with $2.9 \cdot 10^2$ (Figure 7.16 A). During the TCB cultivations, both cellular characteristics were described by a positive correlation. Again, two populations emerged in all processes. Cultivations with short and medium mean hydraulic residence times had a minority of cells with higher stress response levels compared to the main population. In detail, 11.8% of the cells in the TCB$_S$ had median fluorescence intensities of $2.5 \cdot 10^3$ and $2.4 \cdot 10^2$ at 448/45 nm and 527/32 nm compared to signal intensities of $3.8 \cdot 10^2$ and $1.9 \cdot 10^2$ of the residual population (88.0%). The cell population during the TCB$_M$ cultivation split into two subpopulations containing 6.4% and 93.0% of the cells. These 6.4% showed higher general stress response levels of $3.0 \cdot 10^3$ at 448/45 nm, whereas the other population expressed a median fluorescence intensity of $4.5 \cdot 10^2$. In terms of signal intensities at 527/32 nm, the smaller population expressed an elevated level of $5.3 \cdot 10^2$ compared to $3.3 \cdot 10^2$ of the residual population (Figure 7.16 DG).
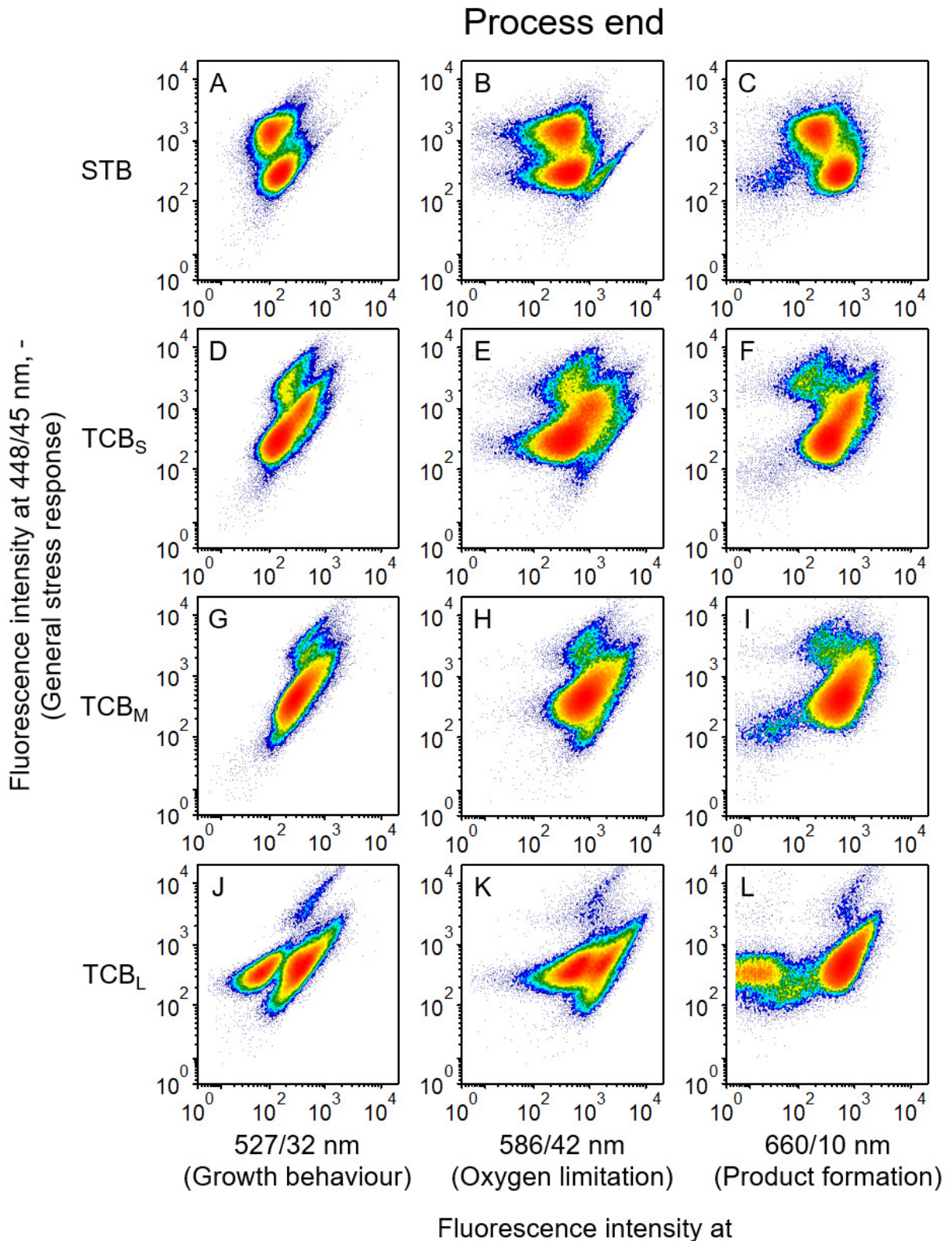
Figure 7.16: Density plots of *Escherichia coli* 4RP cells during the L-phenylalanine production processes at the process ends during the stirred-tank bioreactor cultivation (STB, 89.1 h) and two-compartment bioreactor cultivations with short (TCB$_S$, 92.1 h, 102.63 s), medium (TCB$_M$, 110.0 h, 199.50 s) and long (TCB$_L$, 135.5 h, 403.30 s) mean hydraulic residence times. The fluorescence intensities at 448/45 nm (general stress response, y-axis) are plotted against the measured intensities at 527/32 nm (growth behaviour, x-axis) and 586/42 nm (oxygen limitation, x-axis) and 660/10 nm (product formation, x-axis).

Similarly, the cell population during the TCB_L cultivation separated into two distinct subpopulations, that differed regarding the expressed fluorescence intensities at 527/32 nm. The minority of the cells (32.8%) had a median value of $7.3 \cdot 10^1$, whereas the majority of the population (64.2%) showed a fluorescence intensity of $3.8 \cdot 10^2$. In contrary, the expressed fluorescence intensities at 448/45 nm were approximately similar with median values of the smaller and larger population at $3.4 \cdot 10^2$ and $4.4 \cdot 10^2$ (Figure 7.16 J). All the previously mentioned trends in the STB, TCB_S and TCB_M cultivations were transferable to the density plots correlating the fluorescence intensities at 448/45 nm with the oxygen limitation marker at 586/42 nm (Figure 7.16 BEH) and the product formation marker at 660/10 nm (Figure 7.16 CFI). In detail, the two identified subpopulations during the STB cultivation had slightly different intensities at 586/42 nm with $3.5 \cdot 10^2$ (41.1%) and $4.4 \cdot 10^2$ (53.2%), whereas they strongly differed in signal intensities at 448/45 nm (median values of $1.4 \cdot 10^3$ and $2.9 \cdot 10^2$ for 41.1% and 53.2% of the cells). However, no clear correlation derived from the density plot (Figure 7.16 B). Co-exisiting cell populations were also found when correlating the general stress response to the product formation. A lower signal intensity of $2.3 \cdot 10^2$ at 448/45 nm was expressed by 43.0% of the cell population compared to a signal intensity of $5.7 \cdot 10^2$ of the residual 51.9% of the cells. Further differences were found in their median fluorescence intensities at 660/10 nm, which were at $1.3 \cdot 10^3$ (43.0%) and $2.9 \cdot 10^2$ (51.9%). Again, a clear correlation was not observed (Figure 7.16 C). In contrast, the plotting of signal intensities at 448/45 nm and 586/42 nm in the TCB_S cultivation highlighted a positve correlation. Additionally, two co-existing subpopulations were present. The corresponding median fluorescence intensities of the main population (86.9%) were at $3.8 \cdot 10^2$ and $5.3 \cdot 10^2$ for the detection ranges at 448/45 nm and 586/42 nm, whereas the smaller population had median fluorescence intensities of $2.8 \cdot 10^3$ and $4.5 \cdot 10^2$ (Figure 7.16 E). The same positive correlation with similar subpopulations was observed in the density plot showing the signal intensities at 448/45 nm and 660/10 nm in relation. While 9.9% of the cells had fluorescence intensities of $2.8 \cdot 10^3$ and $2.1 \cdot 10^2$ at 448/45 nm and 660/10 nm, the remaining 87.2% of the cells showed fluorescence intensities of $3.8 \cdot 10^2$ and $4.4 \cdot 10^2$ (Figure 7.16 F). Plotting the measured signal intensities at 448/45 nm and 586/42 nm during the L-phenylalanine production process in the TCB_M also showed a positive correlation with a minority of cells (7.0%) expressing signal intensities of $2.9 \cdot 10^3$ and $8.8 \cdot 10^2$ compared to $4.5 \cdot 10^2$ and $9.0 \cdot 10^2$ of the residual population (92.0%) (Figure 7.16 H). A further positive correlation was revealed when plotting the signal intensities at 448/45 nm and 660/10 nm. In this instance, three subpopulations were observed. One of them contained 3.6% of the cells with median signal intensities of $1.4 \cdot 10^2$ and $3.5 \cdot 10^1$ at 448/45 nm and 660/10 nm, whereas a second subpopulation with 5.0% of the cells had signal intensities of $3.2 \cdot 10^3$ and $3.3 \cdot 10^2$. The main population included 88.6% of the

cells and showed median fluorescence intensities of $4.7 \cdot 10^2$ and $6.4 \cdot 10^2$ (Figure 7.16 I). In contrary, the cell population in the TCB_L cultivation showed tendencies of a positive correlation when plotting the expressed signal intensities at 448/45 nm and 586/42 nm (Figure 7.16 K). Correlating the signal intensities at 448/45 nm and 660/10 nm led to the occurrence of two populations. While most of the cells (59.4%) exhibited a clear positive correlation with median values of $4.9 \cdot 10^2$ and $6.9 \cdot 10^2$ at 448/45 nm and 660/10 nm, the other subpopulation (20.1%) completely detached from the main population. In fact, these cells showed a considerable signal intensity of $3.0 \cdot 10^2$ at 448/45 nm, but expressed a surprisingly low signal intensity of $2.0 \cdot 10^1$ at 660/10 nm (Figure 7.16 L).

Overall, no clear correlations were observed between the expression of the general stress response marker and the remaining three markers in *E. coli* 4RP cells at the process end of the STB cultivation. In contrast, *E. coli* 4RP cells with high general stress response levels consistently showed elevated levels of the growth, oxygen limitation and product formation markers in all TCB cultivations at the process ends. Conversely, cells with low levels of the general stress response marker mostly expressed rather low fluorescence intensities of the remaining three markers. It is also worth mentioning that subpopulations were observed in all processes.

Discussion

Flow cytometry is among the most popular choice for the monitoring of single-cell dynamics of a microbial population, which provides a plethora of morphological and functional information of each cell in large sample pools (Nebe-von-Caron *et al.* 2000, Lundgren *et al.* 2004, Wiacek *et al.* 2006). In combination with reporter strains such as the here established *E. coli* 4RP, it becomes a powerful approach to reveal potential physiological heterogeneities of a bacterial population originating from an isogenic culture (Delvigne *et al.* 2015, Heins *et al.* 2020). To visualize and evaluate the level of population heterogeneity of a cell sample with flow cytometric measurements, histograms are often used. Furthermore, the mean-to-median ratios and the coefficient of variances can support the visual evaluation regarding the extent of population heterogeneity in bioprocesses (Delvigne *et al.* 2015, Heins *et al.* 2020). However, both have their limitations and cannot always display differences of expressed signal intensities of single cells, which was also observed in this study. For example, the mean-to-median ratios are often utilized to highlight bimodal distributions of a cell population. As long as the resulting subpopulations show clearly distinguishable signal intensities, they are accordingly reflected by this indicator. However, the weaker the differences between the subpopulations, the worse the mean-to-median ratio functions, which was also indicated by Delvigne *et al.* (2015).

On the other hand, the coefficient of variance is mainly used for the identification of rather broad histograms. While this works properly for distributions with rather low mean signal intensites, this indicator is increasingly blurred at higher mean signal intensities (Hoang *et al.* 2023a). In any case, there are no reference values for both indicators, which make a generally valid and comparable assessment difficult. Due to the limitations of both supportive indicators, the evaluation of population heterogeneity in bioprocesses should consider as much data and indicators as possible and compare them in a closed study utilizing from the same process and measuring setups.

Considering all the mentioned criteria to evaluate potential differences of cellular physiologies, population heterogeneity was already present during the L-phenylalanine production in the STB. Though it seems counterintuitive to face subpopulations in pure microbial communities that are exposed to well-mixed and controlled process parameters, Delvigne & Goffin (2014) already anticipated the ubiquity of this phenomenon even under homogeneous conditions. In this instance, especially the general stress response and the product formation markers deviated between single cells, mainly at the beginning and process ends of the L-phenylalanine production processes. According to the findings in the literature, the *rpoS* gene seems vulnerable to polymorphism so that this genetic element has higher chances to mutate. The resulting differences at the genotype level transfer to the expressed cellular phenotypes, leading to altered activation pathways and functions of the sigma factor in cells (Ferenci 2003, Price *et al.* 2000). Therefore, the coupled expression levels of mTagBFP2 might have differed due to potentially occurring mutations of the *rpoS* gene in some of the cells, which led to two co-existing populations. Another aspect to consider are potentially deviating intracellular rates on single-cell level. As a result, some cells might have experienced a faster accumulation of toxic by-products compared to others. Such intrinsic differences are inevitable and often observed in microbial communities (Norman *et al.* 2015, Dewachter *et al.* 2019).

In contrast, the deviating single-cell expression levels of the product formation marker might be related to the absolute plasmid numbers in each cell. These most likely vary from cell to cell despite deriving from the same isogenic culture (Rejeb *et al.* 2017). Assuming the unfortunate but present basal expression of mCardinal2, the heterogeneity in plasmid numbers in each cell would automatically result to similarly heterogenic expression levels of mCardinal2 during the STB cultivation. Interestingly, the observed subpopulations particularly emerged after depletion of the residual L-tyrosine. Potentially, the absence of this essential amino acid might have simulated more stressful conditions as cells were not capable to grow anymore. Such unpredictable and uncertain environments often induce

higher mutation rates in microbial cell populations, thus increasing the chances that sub-populations emerge (Tanaka *et al.* 2003, Travis & Travis 2002). It is also important to consider that the omnipresence of stochastic fluctuations of biochemical reactions inside the cells contribute to this phenomenon, as well (Delvigne & Goffin 2014). This includes complex processes such as the transcription and translation. As a result, the identical state between two cells deriving from the same isogenic culture potentially transform to deviating cellular physiologies due to the intrinsic noises (Kœrn *et al.* 2005, Kiviet *et al.* 2014). Nevertheless, extrinsic factors such as dynamic environmental conditions are expected to have an even stronger impact on the level of population heterogeneity. This is because each cell experiences a unique order of microenvironments that promotes the development of different cellular characteristics (Avery 2006, Haringa *et al.* 2016). Indeed, population heterogeneity occurred during the TCB cultivation with short mean hydraulic residence times, again particularly for the general stress response and the product formation markers at the beginning and process end. Surprisingly, the histograms obtained during the other two TCB cultivations showed comparably less pronounced differences in single-cell characteristics.

Nonetheless, the further consideration of density plots at the end of the biomass production phases, mid product formation phases and the process ends of the L-phenylalanine production processes revealed the occurrence of co-existing populations in all cultivations. In general, the higher achieved resolutions of this plot type rely on the coherent presentation of two detection ranges, thus allowing a much more detailed display of the data compared to one-dimensional histograms (Herzenberg *et al.* 2006). With the purpose to find subpopulations with superior cellular characteristics, it was remarkable that cells in the STB cultivation revealed no clear correlations between the fluorescent reporter molecules. In contrast, only positive correlations were found when plotting all four measured cellular characteristics among each other during the conducted TCB cultivations.

To confirm the here observed trends, future studies should consider the sorting of sub-populations paired with selected omics analyses. Precise sorting of certain particles can be achieved by fluorescence-activated cell sorting in flow cytometers (Cho *et al.* 2010, Wu *et al.* 2009). Together with subsequent omics analyses of sorted cell samples, further insights on complex biological networks and dynamic coherences between cells and their surrounding environment can be acquired to contribute to a better mechanistic understanding of population heterogeneity in bioprocesses (Wiacek *et al.* 2006, Zhu *et al.* 2020, He *et al.* 2020). On that note, the further characterization of the subpopulation that occurred during the TCB$_{\mathrm{L}}$ cultivation with suspiciously low fluorescence intensitis at

660/10 nm would be important for the interpretation of this process. A further aspect to consider is the sampling in TCB cultivations. As mentioned previously, samples were taken from the stirred-tank bioreactor in TCB cultivations and had uncertain proportions of cells, whose immediate process conditions they just experienced were not comprehensible. Hence, future experiments should consider the simultaneous sampling at different positions of the TCB, e. g. from the coiled flow inverter.

All in all, dynamic environmental conditions during the L-phenylalanine production with *E. coli* 4RP in the TCB led to a diminished cell growth compared to the STB cultivation, regardless of the applied mean hydraulic residence times in the bypass. While the L-phenylalanine production was not affected in the TCB setup with short mean hydraulic residence times of 102.63 s, the maximum achieved product concentrations were reduced by up to 25% when cells were exposed to limiting conditions in the bypass for 199.50 s or 403.30 s. Although a premature or elevated by-product formation was not observed, all TCB cultivations were characterized by higher carbon dioxide proportions during the initial batch and biomass production phases instead. Besides the targeted production of L-phenylalanine, the *E. coli* quadruple reporter strain also expressed fluorescent reporter molecules to reveal potential single-cell differences regarding their general stress response, growth behaviour, oxygen limitation and product formation. Surprisingly, subpopulations were already present in the STB cultivation under well-mixed and controlled process conditions. Cells especially differed concerning their expressed general stress response and product formation markers at the beginning and the process end. In comparison, population heterogeneity was also present in all conducted L-phenylalanine production processes in the TCB, which was also underlined by the density plots at certain process stages. However, the level of population heterogeneity seemed to be less pronounced compared to the STB cultivation. Consequently, the introduction of dynamic process conditions during the L-phenylalanine production with *E. coli* 4RP rather reduced the differences of selected cellular characteristics and induced a more homogeneous population. Despite this unexpected outcome, this study underlines the increasing importance of reporter strains in combination with flow cytometric measurements as a powerful and noninvasive setup to elucidate potential differences of specific single-cell physiologies during bioprocesses.

8. Summary

Microorganisms can be exploited for the sustainable production of versatile bio-based goods such as biopharmaceuticals or amino acids (Tripathi & Shrivastava 2019, Boodhoo *et al.* 2022). Such microbial bioprocesses are mainly realized in bioreactors, in which ideal bioprocess conditions can be provided for the targeted product forming reactions. To maximize the achieved product amount per unit time and thus meet the globally rising demands for food, drugs and bio-based chemicals, these biotechnological production processes are almost exclusively performed at large scales with typical working volumes between $5\,\mathrm{m}^3$ to $800\,\mathrm{m}^3$ (Chmiel & Weuster-Botz 2018). However, large-scale bioprocesses often suffer from mixing insufficiencies and mass transfer limitations, which prevents the provision of ideal and fully homogenized bioprocesss conditions. Instead, spatio-temporal process gradients prevail and co-exisiting microenvironments evolve (Lara *et al.* 2006, Langheinrich & Nienow 1999, Kuschel & Takors 2020). Each cell experiences an unique but random order of these dynamic conditions that presumably influence its cellular state and expression of certain cellular characteristics (Haringa *et al.* 2017). As a result, subpopulations with heterogeneous cellular phenotypes potentially occur though all cells originated from an isogenic culture. Despite of the increasing attention this phenomenon has received in recent years, there are still plenty of uncertainties regarding the general mechanistic understanding and consequences of population heterogeneity in bioprocesses (Delvigne & Goffin 2014).

With the overall purpose to provide insights and information regarding the impact of fluctuating conditions on the level of cell-to-cell heterogeneity as well as key performance parameters in bioprocesses, this work investigated both mentioned aspects in the L-phenylalanine production process with recombinant *Escherichia coli* FUS4 (pF81$_{kan}$). This process was established by Weiner *et al.* (2016) as a fed-batch cultivation in a stirred-tank bioreactor with a starting volume of 15 L of a chemically defined medium enriched with glycerol as a carbon source. Moreover, it consists of three distinctive phases: an initial batch phase, a biomass production phase and a final product formation phase. The host strain is an optimized variant of the *E. coli* K-12 strain for the targeted L-phenylalanine production. This has been realized by genomic deletions of the *pheA*, *aroF*

and *tyrA* genes making this strain auxotroph towards L-phenylalanine and L-tyrosine. Simultaneously, the *pheA* and *aroF* genes as well as the *aroL* and *aroB* genes are all encoded on the pF81$_{kan}$ plasmid under the control of a tac promoter, thus allowing the inducible recombinant protein expression to ultimately produce L-phenylalanine (Sprenger 2007, Weiner *et al.* 2016).

To add novel insights regarding the level of population heterogeneity during the well-described and robust L-phenylalanine production process of Weiner *et al.* (2016), the first objective of this work was the transformation of the *E. coli* FUS4 (pF81$_{kan}$) host strain to a multiple reporter strain. This was realized by the integration of synthetic copies of reporter molecules into specific genetic units of the host strains' genome or plasmid, which are associated to certain cellular phenotypes of interests. Accordingly, the development of the targeted cellular phenotypes can be representatively followed and analyzed by the recorded fluorescence signals at single-cell level to unveil the presence of potential subpopulations (Heins *et al.* 2020, Hoang *et al.* 2023b). Secondly, the L-phenylalanine production process described by Weiner *et al.* (2016) was transferred to a here established novel two-compartment bioreactor. This is a specialized setup pairing a stirred-tank bioreactor with a helical tube reactor as a bypass, in which dynamic environmental conditions can be simulated by the continuous circulation of the biosuspension between both compartments. As the third and final objective, the impact of fluctuating environmental conditions on the key performance parameters and level of population heterogeneity regarding selected cellular characteristics were investigated by application of the *E. coli* multiple reporter strain for the L-phenylalanine production in two-compartment bioreactor cultivations.

For the initial establishment of an *E. coli* multiple reporter strain, the four fluorescent proteins mTagBFP2, mEmerald, CyOFP1 and mCardinal2 were selected due to their relatively low maturation times, high brightnesses and a monomeric state (Figure 8.1 A). Ideally, they should also show optical compatibility with the available flow cytometer and a low degree of optical cross-talks among each other, which was evaluated in a preliminary screening. Measuring the excitation and emission spectra of mTagBFP2 ($\lambda_{Ex,\ max} = 405\ nm$, $\lambda_{Em,\ max} = 455\ nm$), eGFP (as a substitute for mEmerald, $\lambda_{Ex,\ max} = 480\ nm$, $\lambda_{Em,\ max} = 515\ nm$), CyOFP1 ($\lambda_{Ex,\ max} = 525\ nm$, $\lambda_{Em,\ max} = 590\ nm$) and mCardinal2 ($\lambda_{Ex,\ max} = 605\ nm$, $\lambda_{Em,\ max} = 660\ nm$) approved their compatibility with the here used flow cytometer, which was equipped with three lasers at 405 nm, 480 nm and 640 nm and four matching detection filters at 448/45 nm, 527/32 nm, 586/42 nm and 660/10 nm. Strong fluorescence crossovers between the selected proteins were excluded by flow cytometric measurements of *E. coli* cells expressing one of the four reporter molecules.

The next step was the genetic modification of the *E. coli* FUS4 (pF81$_{kan}$) host strain by integration of synthetic copies of mTagBFP2, mEmerald and CyOFP1 downstream to the *rpoS* gene, into a *rrnB* promoter complex and into the *narGHIJ* operon. This was realized by a series of knock-in recombination reactions utilizing the λ-red mediated Flp/FRT recombination. As a result, the general stress response, growth behaviour and oxygen limitation of cells were reflected by either blue (448/45 nm), green (527/32 nm) or orange fluorescence levels (586/42 nm, Figure 8.1 A). The functionality of this *E. coli* triple reporter strain was verified in two case studies simulating conventional batch cultivations in a stirred-tank bioreactor with either aerobic or anaerobic conditions. While mEmerald levels (marker for growth behaviour) of the cell population especially increased in the early exponential growth phase, mTagBFP2 levels (marker for general stress response) rose particularly after depletion of the carbon source and the transition into the stationary phase. Furthermore, anaerobic conditions were simulated in one of the case studies by interruption of the aeration, which led to a delayed elevation of CyOFP1 levels (marker for oxygen limitation).

After the functional approval of the *E. coli* triple reporter strain, it was enhanced to an *E. coli* quadruple reporter strain by insertion of a synthetic copy of mCardinal2 into the pF81$_{kan}$ plasmid to monitor the product formation of cells by red (660/10 nm) fluorescence (Figure 8.1 A). In preliminary shake flask experiments, IPTG-induced *E. coli* cells with the modified pF81$_{kan}$ plasmid showed remarkably higher fluorescence intensities at 660/10 nm compared to the same *E. coli* cells with the original pF81$_{kan}$ plasmid. However, the novel *E. coli* quadruple reporter strain even expressed red fluorescence levels without the addition of IPTG, which indicated a basal expression of mCardinal2 (marker for product formation).

To ensure that the genetic modifications of the here established *E. coli* triple and quadruple reporter strains had no negative impacts on the cellular integrity and cause no metabolic burden, the original *E. coli* FUS4 (pF81$_{kan}$) strain and both reporter strains were cultivated in a 3.6 L stirred-tank bioreactor for the L-phenylalanine production. This was operated as a fed-batch process with chemically defined minimal medium at a starting volume of 1 L and glycerol as a substrate. The general process strategy was adapted from Weiner *et al.* (2016) with three distinct phases: an initial batch phase, a biomass production phase and a final product formation phase. Maximum biomass and L-phenylalanine concentrations of 29.1 g L^{-1} and 17.09 g L^{-1} were achieved with the original strain, whereas the L-phenylalanine production with the triple reporter strain led to 30.78 g L^{-1} of biomass and 17.59 g L^{-1} of product. In comparison, the quadruple

reporter strain showed maximum biomass amounts of 31.23 g L^{-1} and marginally lower maximum L-phenylalanine concentrations of 16.32 g L^{-1}. Overall, both *E. coli* reporter strains showed similar process performances compared to the original strain so that the cell growth and product formation were not affected by the genetic modifications and the additional expression of fluorescent proteins.

At the same time, the expressed reporter molecules led to reasonable trends that gave a fair approximation of the ongoing process state variables. The general stress response levels indicated by mTagBFP2 expression (measured at 448/45 nm) particularly increased after the cell population entered the biomass production phase, most likely because of the transition from substrate abundance in the initial batch phase to substrate scarcity in the biomass production phase. In comparison, mEmerald was measured at 527/32 nm as the growth marker of the cell population. During the L-phenylalanine production, the growth rates followed the same pattern with their peak at the end of the initial batch phase, reduced intermediate growth rates during the biomass production phase and almost no cell growth at the mid and late product formation phase. This stepwise decrease was also reflected by the expressed mEmerald levels of the cell population. The highest levels of the oxygen limitation marker CyOFP1 (measured at 586/42 nm) coincided with the lowest dissolved oxygen levels of around 30% air saturation at the end of the biomass production phase, whereas the product formation marker mCardinal2 was particularly expressed after the initiation of the product formation phase. Together with the diminished product formation rates of the *E. coli* cells towards the process end, their red fluorescence levels at 660/10 nm decreased, as well. Nevertheless, a premature but comparably lower expression of this marker was observed before the start of the product formation phase.

With the aim to provide a scale-down bioreactor that is capable of simulating dynamic process conditions of large-scale bioreactors, a novel two-compartment bioreactor was established by combining a stirred-tank bioreactor with a coiled flow inverter as a bypass. The latter compartment is a specialized variant of a helical tube reactor with the additional integrations of 90° bends. It was designed and constructed with commercially available components and 3D-printed parts. Using two layers of a hollow square girder frame made out of four PVC pipes and four 3D-printed double pipe sockets with a bend of 90° each, two braided silicone tubes with an inner and outer diameter of 6 mm and 12 mm were winded around these frames. With a distance of 120 mm between both layers, a coil diameter of 118 mm and a pitch distance of 20 mm, up to 4 turns were introduced on each PVC pipe followed by a 90° bend of the tubing. Each tube had a length of 6.615 m, which corresponded to an overall volume of 373 mL.

In step response experiments in the coiled flow inverter using de-ionized water (diH$_2$O) as a mobile phase and 0.025 mg mL^{-1} vitamin B12 as a tracer solution, the application of volumetric flow rates between 1.18 mL s^{-1} to 5.33 mL s^{-1} led to mean hydraulic residence times of 316.10 s to 69.98 s, which covered most of the conventional mixing times of large-scale bioreactors between 10 s to 250 s (Vrábel *et al.* 2000). At the same time, the monitored response curves allowed the approximation of predominant mixing characteristics in the tubes by determination of the dimensionless Bodenstein number (Bo number). Bo numbers of above 100 were paramount to ensure low axial dispersion of flowing fluids in the coiled flow inverter and thus provide narrow residence time distributions (Levenspiel 2012). When diH$_2$O ($\eta = 0.00118$ *Pa s*) was used as a mobile phase, Bo numbers were between 164.20 to 403.03. These were reduced by up to 30% with Bo numbers between 129.10 to 282.13 using a higher viscous 12.5% glycerol solution ($\eta = 0.00176$ *Pa s*) as a mobile phase, which mimicked the viscosity of *E. coli* cell suspensions deriving from the L-phenylalanine production process. Hence, ideal mixing conditions in the coiled flow inverter were confirmed for flow rates between 1.18 mL s^{-1} to 5.33 mL s^{-1} for mobile phases with dynamic viscosities between 0.00118 Pa s to 0.00176 Pa s.

At the end, the *E. coli* quadruple reporter strain was cultivated in the two-compartment bioreactor to investigate the impact of dynamic environmental conditions on the overall process performances during the L-phenylalanine production and the level of population heterogeneity. While the stirred-tank bioreactor had an initial volume of 0.9 L and resembled a well-mixed zone with controlled process parameters, the coiled flow inverter with all connecting tubes had a fixed volume of 0.45 L with no temperature control or supply of oxygen, pH correcting agents or feeding solutions. Therefore, the bypass simulated fluctuating and unfavorable conditions. Three cultivations were conducted in the two-compartment bioreactor with different mean hydraulic residence times of 102.63 s (short), 199.50 s (medium) and 403.30 s (long) in the coiled flow inverter. As a benchmark, the L-phenylalanine production process with the *E. coli* quadruple reporter strain was repeated in the stirred-tank bioreactor, but with an increased starting volume of 1.35 L (Figure 8.1 B).

While the cell growth was not affected by the volumetric adjustment to 1.35 L starting volume in the stirred-tank bioreactor cultivation with a maximum biomass concentration of 33.83 g L^{-1}, the product formation seemed to be enhanced. In fact, the maximum achieved L-phenylalanine concentration was at 21.46 g L^{-1} (Figure 8.1 B), which is approximately equivalent to the maximum achieved product concentrations of the same process described by Weiner *et al.* (2016), but at a higher scale (starting volume of 15 L). How-

ever, compared to the here conducted L-phenylalanine production process in a stirred-tank bioreactor with a starting volume of 1 L, this means a 31.5% higher product concentration.

In contrast, the cell growth was reduced in the two-compartment bioreactor cultivation with short mean hydraulic residence times with a lower maximum biomass concentration of 26.75 g L^{-1}, whereas the L-phenylalanine formation was not affected and led to a maximum concentration of 20.67 g L^{-1}. Prolonging the mean hydraulic residence time in the bypass to 199.50 s resulted in the same lowered cell growth, but also reduced the L-phenylalanine production to a maximum concentration of 14.63 g L^{-1} (Figure 8.1 B). Both processes in the two-compartment bioreactor were characterized by an increased carbon dioxide proportion compared to the stirred-tank bioreactor cultivation. However, a premature or stronger by-product formation was not observed. Suspiciously, the two-compartment bioreactor cultivation with the longest applied mean hydraulic residence time of 403.30 s in the bypass also led to a reduced maximum L-phenylalanine concentration of 15.45 g L^{-1}, but showed an unexplainable increase of biomass concentrations even during the product formation phase. Considering the L-tyrosine auxotrophy of the *E. coli* quadruple reporter strain together with the complete absence of this amino acid at this stage of the bioprocess, a further cell growth was not expected.

The expressed fluorescence intensities of the cell population during the stirred-tank bioreactor cultivation led to the same trends as described previously. Except for the general stress responses of the cells, the exposure of the *E. coli* quadruple reporter strain to dynamic conditions in the two-compartment bioreactor gradually changed the outcoming trends of the growth, oxygen limitation and product formation markers. For example, the oxygen limitation marker was consistently expressed during two-compartment bioreactor cultivations with medium or long mean hydraulic residence times in the coiled flow inverter. This was probably promoted by the prolonged exposure of cells to expectably anoxic conditions in the bypass. In contrast, the observed trends of the growth and product formation markers were rather contradictory to the related process state variables the longer the exposure of the cells to the limiting conditions in the bypass.

Such counterintuitive trends might have been promoted by the observed differences in expressed single-cell fluorescence levels. This was evaluated based on the characteristics of the measured histograms of each fluorescent marker. The presence of particularly broad distributions, skews or the presence of multiple peaks were interpreted as indicators of a prevailing population heterogeneity. Additionally, the mean-to-median ratios and the coefficient of variances of the histograms were also considered for the final assessment.

Despite the expectably homogeneous environmental conditions during the stirred-tank bioreactor cultivation, cells especially differed in their expression levels regarding the general stress response and product formation markers at the beginning and end of the process (Figure 8.1 B).

Similiar findings were also observed in all two-compartment bioreactor cultivations, regardless of the applied mean hydraulic residence times in the bypass. Again, they mainly occurred at the beginning and the process ends. However, the magnitude of monitored single-cell differences seemed lower compared to the level of population heterogeneity observed in the stirred-tank bioreactor cultivation (Figure 8.1 B).

The density plots of all cultivations revealed that cells showing high levels of the growth marker consistently expressed high levels of the other three remaining markers at the end of the biomass production phases. Apart from this, no generally valid correlations were found between the general stress response and the product formation to all the remaining markers during the product formation phases.

All in all, this study uncovered the negative impacts of fluctuating environmental conditions on the cell growth and product formation during the L-phenylalanine production processes with the genetically modifed *E. coli* quadruple reporter strain. In comparison to the L-phenylalanine production in a stirred-tank bioreactor, the maximum achieved biomass concentrations were consistently reduced by more than 20% during the two-compartment bioreactor cultivations with mean hydraulic residence times of 102.63 s or 199.50 s. Simultaneously, the product formation of the cells was diminished by up to 25% at longer exposure times of at least 199.50 s in the coiled flow inverter. In addition, multiple reporter strains proved to be an effective tool to reflect specific cellular characteristics and highlight the presence of population heterogeneity in bioprocesses. Surprisingly, subpopulations were already present during the L-phenylalanine production process in the stirred-tank bioreactor with expectably well-mixed and homogeneous process conditions. *E. coli* cells especially differed regarding their expressed levels of mTagBFP2 (marker for general stress response) and mCardinal2 (marker for product formation) at the beginning and process end. Although population heterogeneity was also present in all two-compartment bioreactor cultivations, the pronounciation of single-cell differences seemed rather reduced compared to the monitored cell population during the stirred-tank bioreactor cultivation. Therefore, as exemplified in the here investigated L-phenylalanine production process, dynamic environmental conditions do not necessarily lead to higher levels of population heterogeneity in bioprocesses, but can have the opposite effect.

A – Engineering of an *Escherichia coli* quadruple reporter strain (*E. coli* 4RP)

Genetic insertion of	→	Monitoring of
mTagBFP2 downstream *rpoS* gene →		General stress response
mEmerald into *rrnB* operon	→	Growth behaviour
CyOFP1 into *narGHIJ* operon	→	Oxygen limitation
mCardinal2 into pF81kan plasmid	→	Product formation

Escherichia coli FUS4 (pF81kan)

Escherichia coli quadruple reporter strain
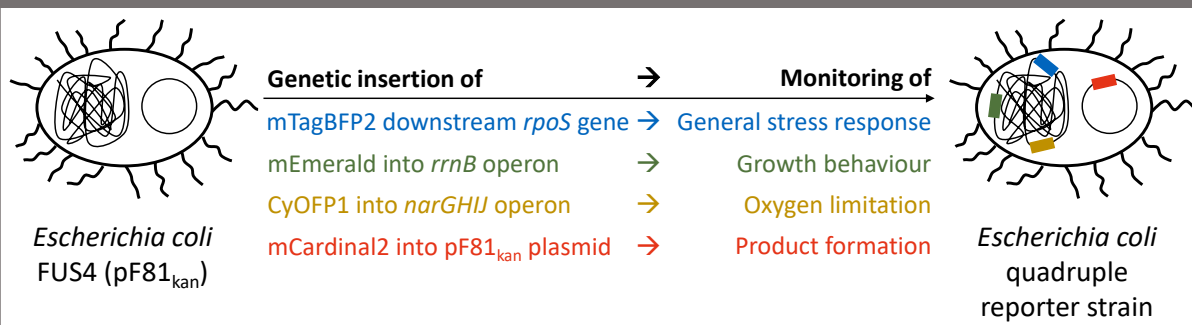
B – L-phenylalanine production with *E. coli* 4RP in two different bioreactor setups

Stirred-tank bioreactor (STB)
Homogeneous environmental conditions

Two-compartment bioreactor (TCB)
Dynamic environmental conditions

I.   Growth and product formation

Cell dry weight: ●   L-phenylalanine: ◐
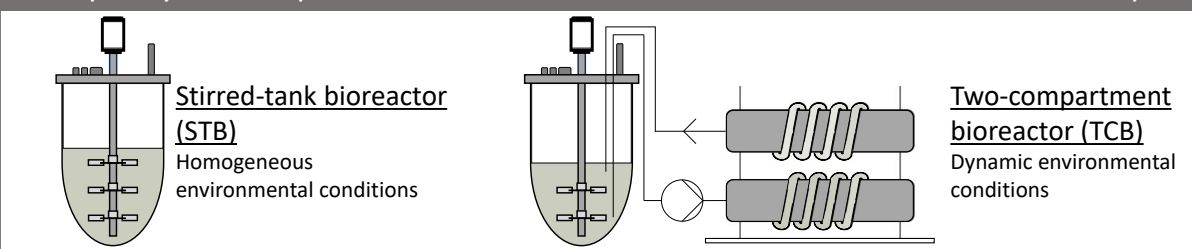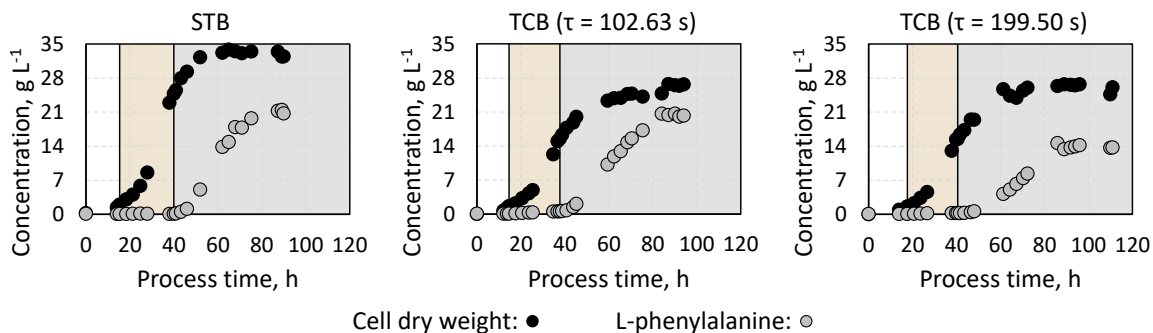
II.   Level of population heterogeneity at process end
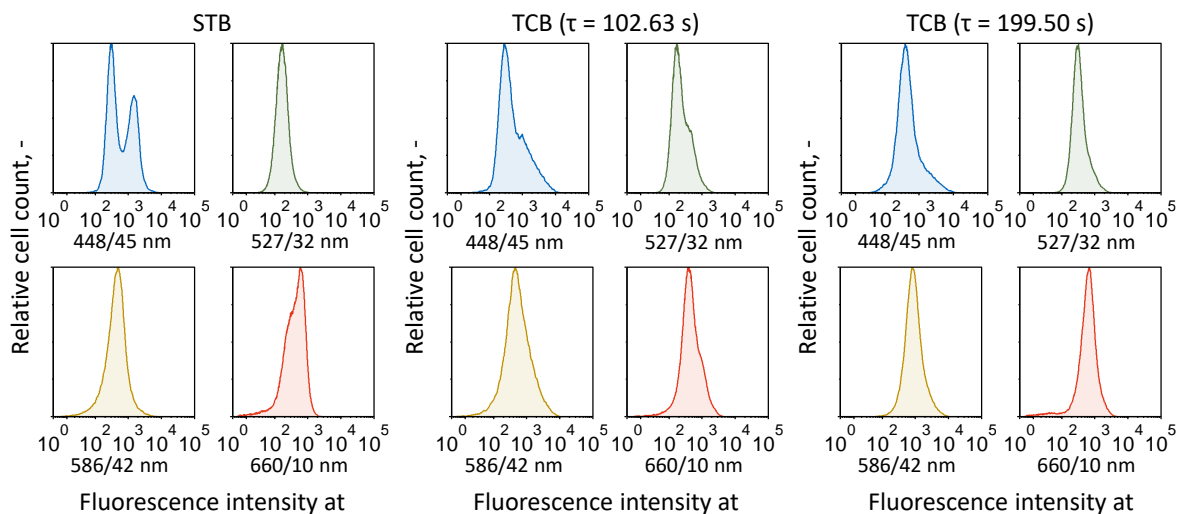
(Full description on next page)

Figure 8.1: Graphical summary of the here conducted L-phenylalanine production processes with recombinant *Escherichia coli*. A shows the transformation of the L-phenylalanine producing *Escherichia coli* FUS4 (pF81$_{kan}$) host strain to an *Escherichia coli* quadruple reporter strain by the genetic insertion of synthetic copies of mTagBFP2 downstream the *rpoS* gene, mEmerald into a *rrnB* promoter complex, CyOFP1 into the *narGHIJ* operon and mCardinal2 into the pF81$_{kan}$ plasmid. As a result, the general stress response, growth behaviour, oxygen limitation and product formation of the cells can be monitored by expression of the corresponding reporter proteins. B displays the L-phenylalanine production processes with the *Escherichia coli* quadruple reporter strain in a stirred-tank bioreactor (STB) or two-compartment bioreactor (TCB) combining a stirred-tank bioreactor with a coiled flow inverter as a bypass. The former provides well-mixed and homogeneous environmental conditions, whereas the latter is characterized by dynamic environmental conditions due to a permanent circulation of the cell suspension between both compartments. The two-compartment bioreactor cultivations were operated at different mean hydraulic residence times of $\tau = 102.63$ s or $\tau = 199.50$ s in the bypass. Section I compares the achieved cell dry weight (●) and L-phenylalanine concentrations (◉) in all performed processes, which were operated as fed-batch processes with the same process strategy. The background colours in the plots highlight the different phases of the L-phenylalanine production process including the initial batch phases (white), the biomass production phases (orange) and the product formation phases (grey). All phases are separated by black verticals. Section II shows the histograms of flow cytometric measurements of the expressed single-cell fluorescence levels at 448/45 nm (mTagBFP2, marker for general stress response, blue histograms), 527/32 nm (mEmerald, marker for growth behaviour, green histograms), 586/42 nm (CyOFP1, marker for oxygen limitation, orange histograms) and 660/10 nm (mCardinal2, marker for product formation, red histograms) at the process ends of each cultivation. (STB: $V_0 = 1.35$ L, T $= 37\,°$C, pH $= 7$, DO $\geq 30\%$; TCB: $V_{0,\,STB} = 0.9$ L, $V_{0,\,CFI} = 0.45$ L, $T_{STB} = 37\,°$C, $pH_{STB} = 7$, $DO_{STB} \geq 30\%$; exponential feeding with $\mu_{set} = 0.1$ h^{-1}, constant feeding of 0.18 g$_{substrate}$ g$_{Biomass}^{-1}$ h^{-1} after induction of the recombinant protein expression with 0.3 mM IPTG).

9. Outlook

The here investigated L-phenylalanine production processes with the *Escherichia coli* quadruple reporter strain in either the stirred-tank bioreactor or two-compartment bioreactor gave valid insights on the general stress response, growth behaviour, oxygen limitation and product formation of the cells. In most of the cases, the trends of the expressed fluorescent proteins matched with the prevailent process state variables, especially in the stirred-tank bioreactor cultivations with presumably controlled process parameters and well-mixed conditions. Additionally, population heterogeneity was revealed in all conducted processes emphasizing the potential role of reporter strains to better comprehend this phenomenon in bioprocesses. Nevertheless, some uncertainties remain and demand for more in-depth studies and optimization of the present experimental setup.

First and foremost, the unwanted basal expression of the product formation marker must be better controlled and reduced. Indeed, the leaky tac promoter can be exchanged with other promoters such as the araBAD expression system to provide a tighter regulation (Terpe 2006, Francis & Page 2010). However, this would completely alter the well-described L-phenylalanine producing *E. coli* FUS4 (pF81$_{kan}$) strain and demand for new extensive studies. Hence, the basal expression of the mCardinal2 protein could be weakened by modifying its ribosome binding site sequence (Salis *et al.* 2009, Seo *et al.* 2013).

To better understand, track and relate the dynamics of the measured fluorescence intensities of the cells to certain events, it is also paramount to estimate the *in vivo* maturation and degradation times of the utilized fluorescent proteins. One interesting approach to measure the *in vivo* maturation times in reporter strains could be the addition of chloramphenicol, which stops the translational events in cells. Therefore, any further increases of the measured fluorescence signals after the addition of the translation inhibiting molecule derive from posttranslational maturations of already translated fluorescent proteins (Hebisch *et al.* 2013). Similarly, the *in vivo* degradation rates can be estimated by monitoring of the decay of fluorescence intensities under the presence of a translational inhibitor such as chloramphenicol or cyclohexemide (Kao *et al.* 2015, Buchanan *et al.* 2016).

Slow degradation rates and a long *in vivo* stability of the used reporter proteins would complicate the reflection of transient and dynamic changes of the cells in real time. In this instance, reporter proteins need to be destablized by extending them with degradation tags. As a result, they are faster recognized by intracellular proteases so that the half-life can be shortened (Andersen *et al.* 1998, Han *et al.* 2013).

Of course, further reporter molecules can be integrated into the existing *Escherichia coli* quadruple reporter strain to gain even more insights to additional cellular characteristics. Especially the monitoring of more specific stress response pathways could be of major interest (Raina *et al.* 1995, Rouvière *et al.* 1995, Shimada *et al.* 2021). However, it is important to ensure that the level of fluorescent crossovers among each other remains at low levels. Furthermore, the more fluorescent proteins are recombinantly expressed, the higher the chance that cells will experience a higher metabolic burden. Hence, this potential trade-off needs to be investigated and considered for the design of a potential quintuple reporter strain.

Moreover, the two-compartment bioreactor should be equipped with devices that allow the monitoring of prevailing process conditions such as the temperature or dissolved oxygen levels at the entrance, center and exit of the coiled flow inverter. This can be achieved by using so-called flow-through cells, which are easily integrable into tubings and allow the *in-line* monitoring of the temperature, pH and dissolved oxygen levels. Implementing these features would also facilitate the simulation of different process gradients in later two-compartment bioreactor cultivations.

Even more complex dynamic environments can be simulated when adding a further compartment to the here established two-compartment bioreactor. Lemoine *et al.* (2015) already established a three-compartment bioreactor, in which they combined a stirred-tank bioreactor with two separate straight tubular reactors. While well-mixed conditions with controlled bioprocess parameters and the supply of oxygen were provided in the stirred-tank bioreactor, the biosuspension was continuously circulated into two separate bypasses. One of them was used to introduce a feeding solution but with no aeration, whereas the other lacked both. Hence, they simulated distinct zones of substrate excess paired with dissolved oxygen limitation (first bypass) together with a combined substrate and dissolved oxygen limitation (second bypass). Both zones are anticipated to occur in large-scale bioreactor cultivations with a feeding and oxygen supply from the bottom of the bioreactor (Lemoine *et al.* 2015). Indeed, targeting other relevant heterogeneous process conditions of large-scale bioprocesses would be of major interest, as well.

Last but not least, the *E. coli* quadruple reporter strain should be further exploited to find rational strategies for the control of phenotypic diversifications during the L-phenylalanine production process. A similar concept was already described by Sassi *et al.* (2019) for gram-negative bacteria. They established a segregostat, which is a continuous cultivation performed in a stirred-tank bioreactor at laboratory scale, but with a feedback controlled supply of glucose pulses based on the *on-line* measured population diversification. This was realized by an integrated online flow cytometry platform that allows an automated sampling and screening of the prevailent phenotypic diversifications within the biosuspension. Interestingly, they were capable of keeping a certain ratio of subpopulations in *E. coli* cultivations regarding their membrane permeabilization dynamics (Sassi *et al.* 2019). Applying a similar strategy for the here established *E. coli* quadruple reporter strains together with a fully automated experimental setup (Heins *et al.* 2022) would tremendeously increase the output of data and allow a better control of the L-phenylalanine production process. Ultimately, these would further elevate the comprehension of population heterogeneity in bioprocesses and highlight potential benefits of diverse microbial populations compared to their homogeneous counterparts.

10. References

Abatenh E, Gizaw B, Tsegaye Z, Wassie M (2017): The Role of Microorganisms in Bioremediation- A Review. *Open J Environ Biol* **2:** 38–46.

Adamberg K, Valgepea K, Vilu R (2015): Advanced continuous cultivation methods for systems microbiology. *Microbiology* **161:** 1707–1719.

Adan A, Alizada G, Kiraz Y, Baran Y, Nalbant A (2017): Flow cytometry: basic principles and applications. *Crit Rev Biotechnol* **37:** 163–176.

Adschiri T, Kanazawa K, Arai K (1992): Rapid and Continuous Hydrothermal Synthesis of Boehmite Particles in Subcritical and Supercritical Water. *J Am Ceram Soc* **75:** 2615–2618.

Ager DJ, Pantaleone DP, Henderson SA, Katritzky AR, Prakash I, Walters DE (1998): Commercial, Synthetic Nonnutritive Sweeteners. *Angew Chem Int Ed* **37:** 1802–1817.

Albermann C, Ghanegaonkar S, Lemuth K, Vallon T, Reuss M, Armbruster W, Sprenger GA (2008): Biosynthesis of the vitamin E compound δ-tocotrienol in recombinant *Escherichia coli* cells. *Chembiochem* **9:** 2524–2533.

Allikian K, Edgar R, Syed R, Zhang S (2019): Fundamentals of Fermentation Media. In Berenjian A: Essentials in Fermentation Technology. Springer, Cham, Switzerland: 41–84.

Andersen JB, Sternberg C, Poulsen LK, Bjørn SP, Givskov M, Molin S (1998): New Unstable Variants of Green Fluorescent Protein for Studies of Transient Gene Expression in Bacteria. *Appl Environ Microbiol* **64:** 2240–2246.

Archer JR, Romero S, Ritchie AE, Hamacher ME, Steiner BM, Bryner JH, Schell RF (1988): Characterization of an Unclassified Microaerophilic Bacterium Associated with Gastroenteritis. *J Clin Microbiol* **26:** 101–105.

Aro N, Ercili-Cura D, Andberg M, Silventoinen P, Lille M, Hosia W, Nordlund E, Landowski CP (2023): Production of bovine beta-lactoglobulin and hen egg ovalbumin by *Trichoderma reesei* using precision fermentation technology and testing of their technofunctional properties. *Food Res Int* **163:** 112131.

Assaf M, Roberts E, Luthey-Schulten Z, Goldenfeld N (2013): Extrinsic noise driven phenotype switching in a self-regulating gene. *Phys Rev Lett* **111:** 58102.

Avery SV (2006): Microbial cell individuality and the underlying sources of heterogeneity. *Nat Rev Microbiol* **4:** 577–587.

Axe DD, Bailey JE (1995): Transport of Lactate and Acetate Through the Energized Cytoplasmic Membrane of *Escherichia coli. Biotechnol Bioeng* **47:** 8–19.

Backman K, O'Connor MJ, Maruya A, Rudd E, McKay D, Balakrishnan R, Radjai M, DiPasquantonio V, Shoda D, Hatch R (1990): Genetic Engineering of Metabolic Pathways Applied to the Production of Phenylalanine. *Ann N Y Acad Sci* **589:** 16–24.

Balleza E, Kim JM, Cluzel P (2018): Systematic characterization of maturation time of fluorescent proteins in living cells. *Nat Methods* **15:** 47–51.

Barghini P, Di Gioia D, Fava F, Ruzzi M (2007): Vanillin production using metabolically engineered *Escherichia coli* under non-growing conditions. *Microb Cell Factories* **6:** 13.

Baronofsky JJ, Schreurs WJA, Kashket ER (1984): Uncoupling by Acetic Acid Limits Growth of and Acetogenesis by *Clostridium thermoaceticum. Appl Environ Microbiol* **48:** 1134–1139.

Bartkiewicz M, Kazazić S, Krasowska J, Clark PL, Wielgus-Kutrowska B, Bzowska A (2018): Non-fluorescent mutant of green fluorescent protein sheds light on the mechanism of chromophore formation. *FEBS Lett* **592:** 1516–1523.

Basan M, Hui S, Okano H, Zhang Z, Shen Y, Williamson JR, Hwa T (2015): Overflow metabolism in *Escherichia coli* results from efficient proteome allocation. *Nature* **528:** 99–104.

Basse NT (2021): Scaling of global properties of fluctuating and mean streamwise velocities in pipe flow: Characterisation of a high Reynolds number transition region. *Phys Fluids* **33:** 101.

Battesti A, Majdalani N, Gottesman S (2011): The RpoS-Mediated General Stress Response in *Escherichia coli. Annu Rev Microbiol* **65:** 189–213.

Becker J, Wittmann C (2012): Systems and synthetic metabolic engineering for amino acid production - the heartbeat of industrial strain development. *Curr Opin Biotechnol* **23:** 718–726.

Beg QK, Vazquez A, Ernst J, Menezes MA de, Bar-Joseph Z, Barabási A-L, Oltvai ZN (2007): Intracellular crowding defines the mode and sequence of substrate uptake by *Escherichia coli* and constrains its metabolic activity. *Proc Natl Acad Sci USA* **104:** 12663–12668.

Behera SS, Ray RC, Das U, Panda SK, Saranraj P (2019): Microorganisms in Fermentation. In Berenjian A: Essentials in Fermentation Technology. Springer, Cham, Switzerland: 1–40.

Bélafi-Bakó K, Koutinas A, Nemestóthy N, Gubicza L, Webb C (2006): Continuous enzymatic cellulose hydrolysis in a tubular membrane bioreactor. *Enzyme Microb Technol* **38:** 155–161.

Bentley WE, Mirjalili N, Andersen DC, Davis RH, Kompala DS (1990): Plasmid-Encoded Protein: The Principal Factor in the "Metabolic Burden" Associated with Recombinant Bacteria. *Biotechnol Bioeng* **35:** 668–681.

Bevis BJ, Glick BS (2002): Rapidly maturing variants of the *Discosoma* red fluorescent protein (DsRed). *Nat Biotechnol* **20:** 83–87.

Birnbaum S, Bailey JE (1991): Plasmid presence changes the relative levels of many host cell proteins and ribosome components in recombinant *Escherichia coli. Biotechnol Bioeng* **37:** 736–745.

Bittorf L, Reichmann F, Schmalenberg M, Soboll S, Kockmann N (2019): Equipment and Separation Units for Flow Chemistry Applications and Process Development. *Chem Eng Technol* **42:** 1985–1995.

Blattner FR, Plunkett G, Bloch CA, Perna NT, Burland V, Riley M, Collado-Vides J, Glasner JD, Rode CK, Mayhew GF, Gregor J, Davis NW, Kirkpatrick HA, Goeden MA, Rose DJ, Mau B, Shao Y (1997): The Complete Genome Sequence of *Escherichia coli* K-12. *Science* **277:** 1453–1462.

Bochner BR (2003): New technologies to assess genotype-phenotype relationships. *Nat Rev Genet* **4:** 309–314.

Bokinsky G, Peralta-Yahya PP, George A, Holmes BM, Steen EJ, Dietrich J, Lee TS, Tullman-Ercek D, Voigt CA, Simmons BA, Keasling JD (2011): Synthesis of three advanced biofuels from ionic liquid-pretreated switchgrass using engineered *Escherichia coli. Proc Natl Acad Sci USA* **108:** 19949–19954.

Bolmanis E, Dubencovs K, Suleiko A, Vanags J (2023): Model Predictive Control—A Stand Out among Competitors for Fed-Batch Fermentation Improvement. *Fermentation* **9:** 206.

Bongaerts J, Krämer M, Müller U, Raeven L, Wubbolts M (2001): Metabolic Engineering for Microbial Production of Aromatic Amino Acids and Derived Compounds. *Metab Eng* **3:** 289–300.

Boodhoo K, Flickinger MC, Woodley JM, Emanuelsson E (2022): Bioprocess intensification: A route to efficient and sustainable biocatalytic transformations for the future. *Chem Eng Process - Process Intensif* **172:** 108793.

Boros I, Pósfai G, Venetianer P (1984): High-copy-number derivatives of the plasmid cloning vector pBR322. *Gene* **30:** 257–260.

Brown GK, Otero LJ, LeGris M, Brown RM (1994): Pyruvate dehydrogenase deficiency. *J Med Genet* **31:** 875–879.

Brown RL (1978): Tubular Flow Reactors With First-Order Kinetics. *J Res Natl Bur Stand* **83:** 1.

Buchanan BW, Lloyd ME, Engle SM, Rubenstein EM (2016): Cycloheximide Chase Analysis of Protein Degradation in *Saccharomyces cerevisiae*. *J Vis Exp* **110:** e53975.

Buron-Moles G, Chailyan A, Dolejs I, Forster J, Mikš MH (2019): Uncovering carbohydrate metabolism through a genotype-phenotype association study of 56 lactic acid bacteria genomes. *Appl Microbiol Biotechnol* **103:** 3135–3152.

Bylund F, Collet E, Enfors S-O, Larsson G. (1998): Substrate gradient formation in the large-scale bioreactor lowers cell yield and increases by-product formation. *Bioprocess Eng* **18:** 171–180.

Bylund F, Guillard F, Enfors S-O, Trägårdh C, Larsson G. (1999): Scale down of recombinant protein production: a comparative study of scaling performance. *Bioprocess Eng* **20:** 377–389.

Calicioglu O, Flammini A, Bracco S, Bellù L, Sims R (2019): The Future Challenges of Food and Agriculture: An Integrated Analysis of Trends and Solutions. *Sustainability* **11:** 222.

Callens M, Rose CJ, Finnegan M, Gatchitch F, Simon L, Hamet J, Pradier L, Dubois M-P, Bedhomme S (2023): Hypermutator emergence in experimental *Escherichia coli* populations is stress-type dependent. *Evol Lett* **7:** 252–261.

Carneiro S, Ferreira EC, Rocha I (2013): Metabolic responses to recombinant bioprocesses in *Escherichia coli*. *J Biotechnol* **164:** 396–408.

Chalfie M, Tu Y, Euskirchen G, Ward WW, Prasher DC (1994): Green fluorescent protein as a marker for gene expression. *Science* **263:** 802–805.

Chandel NS (2021): Glycolysis. *Cold Spring Harb Perspect Biol* **13:** a040535.

Chapman MR, Kwan MHT, King G, Jolley KE, Hussain M, Hussain S, Salama IE, González Niño C, Thompson LA, Bayana ME, Clayton AD, Nguyen BN, Turner NJ, Kapur N, Blacker AJ (2017): Simple and Versatile Laboratory Scale CSTR for Multiphasic Continuous-Flow Chemistry and Long Residence Times. *Org Process Res Dev* **21:** 1294–1301.

Chmiel H, Weuster-Botz D (2018): Bioreaktoren. In Chmiel H, Takors R, Weuster-Botz D: Bioprozesstechnik. Springer Spektrum, Berlin, Germany: 157–230.

Cho SH, Chen CH, Tsai FS, Godin JM, Lo Y-H (2010): Human mammalian cell sorting using a highly integrated micro-fabricated fluorescence-activated cell sorter (μFACS). *Lab Chip* **10:** 1567–1573.

Chu J, Haynes RD, Corbel SY, Li P, González-González E, Burg JS, Ataie NJ, Lam AJ, Cranfill PJ, Baird MA, Davidson MW, Ng H-L, Garcia KC, Contag CH, Shen K, Blau HM, Lin MZ (2014): Non-invasive intravital imaging of cellular differentiation with a bright red-excitable fluorescent protein. *Nat Methods* **11:** 572–578.

Chu J, Oh Y, Sens A, Ataie N, Dana H, Macklin JJ, Laviv T, Welf ES, Dean KM, Zhang F, Kim BB, Tang CT, Hu M, Baird MA, Davidson MW, Kay MA, Fiolka R, Yasuda R, Kim DS, Ng H-L, Lin MZ (2016): A bright cyan-excitable orange fluorescent protein facilitates dual-emission microscopy and enhances bioluminescence imaging *in vivo*. *Nat Biotechnol* **34:** 760–767.

Ciani M, Comitini F, Mannazzu I (2008): Fermentation. In Jørgensen SE, Fath BD: Encyclopedia of ecology. Elsevier B.V., Amsterdam, The Netherlands: 1548–1557.

Citulski J, Farahbakhsh K, Kent F (2009): Optimization of phosphorus removal in secondary effluent using immersed ultrafiltration membranes with in-line coagulant pretreatment — implications for advanced water treatment and reuse applications. *Can J Civ Eng* **36:** 1272–1283.

Cohen BE (2010): Beyond fluorescence. *Nature* **467:** 407–408.

Cormack BP, Valdivia RH, Falkow S (1996): FACS-optimized mutants of the green fluorescent protein (GFP). *Gene* **173:** 33–38.

Cortés JT, Flores N, Bolívar F, Lara AR, Ramírez OT (2016): Physiological effects of pH gradients on *Escherichia coli* during plasmid DNA production. *Biotechnol Bioeng* **113:** 598–611.

Cronan JE, Laporte D (2005): Tricarboxylic Acid Cycle and Glyoxylate Bypass. *EcoSal Plus* **1**.

Croxen MA, Finlay BB (2010): Molecular mechanisms of *Escherichia coli* pathogenicity. *Nat Rev Microbiol* **8:** 26–38.

Croxen MA, Law RJ, Scholz R, Keeney KM, Wlodarska M, Finlay BB (2013): Recent Advances in Understanding Enteric Pathogenic *Escherichia coli*. *Clin Microbiol Rev* **26:** 822–880.

Cubitt AB, Heim R, Adams SR, Boyd AE, Gross LA, Tsien RY (1995): Understanding, improving and using green fluorescent proteins. *Trends Biochem Sci* **20:** 448–455.

Cupples CG, Cabrera M, Cruz C, Miller JH (1990): A Set of *lacZ* Mutations in *Escherichia coli* That Allow Rapid Detection of Specific Frameshift Mutations. *Genetics* **125:** 275–280.

Damodaran S (1996): Amino Acids, Peptides, and Proteins. In Fennema OR: Food Chemistry. Marcel Dekker, New York, United States of America: 321–430.

Darbyshire AG, Mullin T (1995): Transition to turbulence in constant-mass-flux pipe flow. *J Fluid Mech* **289:** 83–114.

Datsenko KA, Wanner BL (2000): One-step inactivation of chromosomal genes in *Escherichia coli* K-12 using PCR products. *Proc Natl Acad Sci USA* **97:** 6640–6645.

Davidson MW, Abramowitz M (2002): Optical microscopy. In Hornak JP: Encyclopedia of Imaging Science and Technology. Wiley-VCH, Weinheim, Germany: 1106–1141.

Dean WR (1927): XVI. Note on the motion of fluid in a curved pipe. *Lond Edinb Dublin Philos Mag J Sci* **4:** 208–223.

Dean WR (1928a): Fluid motion in a curved channel. *Proc R Soc A: Math Phys Eng Sci* **121:** 402–420.

Dean WR (1928b): LXXII. The stream-line motion of fluid in a curved pipe (Second paper). *Lond Edinb Dublin Philos Mag J Sci* **5:** 673–695.

DeFeyter RC, Pittard J (1986): Purification and Properties of Shikimate Kinase II from *Escherichia coli* K-12. *J Bacteriol* **165:** 331–333.

Deindoerfer FH, Gaden EL (1955): Effects of Liquid Physical Properties on Oxygen Transfer in Penicillin Fermentation. *Appl Microbiol* **3:** 253–257.

Delvigne F, Boxus M, Ingels S, Thonart P (2009): Bioreactor mixing efficiency modulates the activity of a *prpoS*::GFP reporter gene in *E. coli*. *Microb Cell Factories* **8:** 15.

Delvigne F, Goffin P (2014): Microbial heterogeneity affects bioprocess robustness: Dynamic single-cell analysis contributes to understanding of microbial populations. *Biotechnol J* **9:** 61–72.

Delvigne F, Baert J, Gofflot S, Lejeune A, Telek S, Johanson T, Lantz AE (2015): Dynamic single-cell analysis of *Saccharomyces cerevisiae* under process perturbation: comparison of different methods for monitoring the intensity of population heterogeneity. *J Chem Technol Biotechnol* **90:** 314–323.

Delvigne F, Baert J, Sassi H, Fickers P, Grünberger A, Dusny C (2017): Taking control over microbial populations: Current approaches for exploiting biological noise in bioprocesses. *Biotechnol J* **12**.

Dewachter L, Fauvart M, Michiels J (2019): Bacterial Heterogeneity and Antibiotic Survival: Understanding and Combatting Persistence and Heteroresistance. *Mol Cell* **76:** 255–267.

Dharmadi Y, Murarka A, Gonzalez R (2006): Anaerobic fermentation of glycerol by *Escherichia coli*: a new platform for metabolic engineering. *Biotechnol Bioeng* **94:** 821–829.

Dias Rodrigues TV, Amore TD, Teixeira EC, Medeiros Burkert JF de (2019): Carotenoid Production by *Rhodotorula mucilaginosa* in Batch and Fed-Batch Fermentation Using Agroindustrial Byproducts. *Food Technol Biotechnol* **57:** 388–398.

Diederichs S, Korona A, Staaden A, Kroutil W, Honda K, Ohtake H, Büchs J (2014): Phenotyping the quality of complex medium components by simple online-monitored shake flask experiments. *Microb Cell Factories* **13:** 1–14.

Dixit PD, Pang TY, Studier FW, Maslov S (2015): Recombinant transfer in the basic genome of *Escherichia coli*. *Proc Natl Acad Sci USA* **112:** 9070–9075.

Dohi N, Takahashi T, Minekawa K, Kawase Y (2004): Power consumption and solid suspension performance of large-scale impellers in gas–liquid–solid three-phase stirred tank reactors. *Chem Eng J* **97:** 103–114.

Dong T, Schellhorn HE (2009): Control of RpoS in global gene expression of *Escherichia coli* in minimal media. *Mol Genet Genom* **281:** 19–33.

Doyle MP, Schoeni JL (1984): Survival and Growth Characteristics of *Escherichia coli* Associated with Hemorrhagic Colitis. *Appl Environ Microbiol* **48:** 855–856.

Drepper T, Eggert T, Circolone F, Heck A, Krauss U, Guterl J-K, Wendorff M, Losi A, Gärtner W, Jaeger K-E (2007): Reporter proteins for in vivo fluorescence without oxygen. *Nat Biotechnol* **25:** 443–445.

Durnin G, Clomburg J, Yeates Z, Alvarez PJJ, Zygourakis K, Campbell P, Gonzalez R (2009): Understanding and harnessing the microaerobic metabolism of glycerol in *Escherichia coli*. *Biotechnol Bioeng* **103:** 148–161.

Durst F, Ray S, Ünsal B, Bayoumi OA (2005): The Development Lengths of Laminar Pipe and Channel Flows. *J Fluids Eng* **127:** 1154–1160.

Eckhardt B, Schneider TM, Hof B, Westerweel J (2007): Turbulence Transition in Pipe Flow. *Annu Rev Fluid Mech* **39:** 447–468.

Ederth J, Mandava CS, Dasgupta S, Sanyal S (2009): A single-step method for purification of active His-tagged ribosomes from a genetically engineered *Escherichia coli. Nucleic Acids Res* **37:** e15.

Elowitz MB, Leibler S (2000): A synthetic oscillatory network of transcriptional regulators. *Nature* **403:** 335–338.

Enfors S-O, Jahic M, Rozkov A, Xu B, Hecker M, Jürgen B, Krüger E, Schweder T, Hamer G, O'Beirne D, Noisommit-Rizzi N, Reuss M, Boone L, Hewitt C, McFarlane C, Nienow A, Kovacs T, Trägårdh C, Fuchs L, Revstedt J, Friberg PC, Hjertager B, Blomsten G, Skogman H, Hjort S, Hoeks F., Lin H-Y, Neubauer P, van der Lans R, Luyben K, Vrabel P, Manelius Å (2001): Physiological responses to mixing in large scale bioreactors. *J Biotechnol* **85:** 175–185.

Enfors S-O (2011): Fermentation Process Engineering. *Royal Institute of Technology.*

Erickson B, Nelson JE, Winters P (2012): Perspective on opportunities in industrial biotechnology in renewable chemicals. *Biotechnol J* **7:** 176–185.

Eyre-Walker A, Keightley PD (2007): The distribution of fitness effects of new mutations. *Nat Rev Genet* **8:** 610–618.

Fazeli E, Roy NH, Follain G, Laine RF, Chamier L von, Hänninen PE, Eriksson JE, Tinevez J-Y, Jacquemet G (2020): Automated cell tracking using StarDist and TrackMate. *F1000Res* **9**.

Ferenci T (2003): What is driving the acquisition of *mutS* and *rpoS* polymorphisms in *Escherichia coli? Trends Microbiol* **11:** 457–461.

Ferguson GP, Tötemeyer S, MacLean MJ, Booth IR (1998): Methylglyoxal production in bacteria: suicide or survival? *Arch Microbiol* **170:** 209–219.

Fernandes BD, Mota A, Teixeira JA, Vicente AA (2015): Continuous cultivation of photosynthetic microorganisms: Approaches, applications and future trends. *Biotechnol Adv* **33:** 1228–1245.

Förster AH, Gescher J (2014): Metabolic Engineering of *Escherichia coli* for Production of Mixed-Acid Fermentation End Products. *Front Bioeng Biotechnol* **2:** 16.

Francis DM, Page R (2010): Strategies to Optimize Protein Expression in *E. coli. Curr Protoc Protein Sci* **Chapter 5:** 5.24.1-5.24.29.

Fürste JP, Pansegrau W, Frank R, Blöcker H, Scholz P, Bagdasarian M, Lanka E (1986): Molecular cloning of the plasmid RP4 primase region in a multi-host-range *tacP* expression vector. *Gene* **48:** 119–131.

Garcia JR, Cha HJ, Rao G, Marten MR, Bentley WE (2009): Microbial *nar*-GFP cell sensors reveal oxygen limitations in highly agitated and aerated laboratory-scale fermentors. *Microb Cell Factories* **8:** 6.

Gaugler L, Mast Y, Fitschen J, Hofmann S, Schlüter M, Takors R (2023): Scaling-down biopharmaceutical production processes via a single multi-compartment bioreactor (SMCB). *Eng Life Sci* **23:** e2100161.

Ghobadi N, Ogino C, Yamabe K, Ohmura N (2017): Characterizations of the submerged fermentation of *Aspergillus oryzae* using a Fullzone impeller in a stirred tank bioreactor. *J Biosci Bioeng* **123:** 101–108.

Giuliodori AM, Gualerzi CO, Soto S, Vila J, Tavío MM (2007): Review on Bacterial Stress Topics. *Ann N Y Acad Sci* **1113:** 95–104.

Göksungur Y, Güvenç U (1997): Batch and Continuous Production of Lactic Acid from Beet Molasses by *Lactobacillus delbrueckii* IFO 3202. *J Chem Technol Biotechnol* **69:** 399–404.

Gomez de Santos P, Hoang MD, Kiebist J, Kellner H, Ullrich R, Scheibner K, Hofrichter M, Liers C, Alcalde M (2021): Functional Expression of Two Unusual Acidic Peroxygenases from *Candolleomyces aberdarensis* in Yeasts by Adopting Evolved Secretion Mutations. *Appl Environ Microbiol* **87:** e0087821.

Gottlieb K, Albermann C, Sprenger GA (2014): Improvement of L-phenylalanine production from glycerol by recombinant *Escherichia coli* strains: the role of extra copies of *glpK*, *glpX*, and *tktA* genes. *Microb Cell Fact* **13:** 1–16.

Grishchenkov VG, Townsend RT, McDonald TJ, Autenrieth RL, Bonner JS, Boronin AM (2000): Degradation of petroleum hydrocarbons by facultative anaerobic bacteria under aerobic and anaerobic conditions. *Process Biochem* **35:** 889–896.

Gur E, Sauer RT (2009): Degrons in protein substrates program the speed and operating efficiency of the AAA+ Lon proteolytic machine. *Proc Natl Acad Sci USA* **106:** 18503–18508.

Guzman L-M, Belin D, Carson MJ, Beckwith J (1995): Tight Regulation, Modulation, and High-Level Expression by Vectors Containing the Arabinose PBAD Promoter. *J Bacteriol* **177:** 4121–4130.

Hammes WP, Brandt MJ, Francis KL, Rosenheim J, Seitter MFH, Vogelmann SA (2005): Microbial ecology of cereal fermentations. *Trends Food Sci Technol* **16:** 4–11.

Han S, Delvigne F, Brognaux A, Charbon GE, Sørensen SJ (2013): Design of Growth-Dependent Biosensors Based on Destabilized GFP for the Detection of Physiological Behavior of *Escherichia coli* in Heterogeneous Bioreactors. *Biotechnol Prog* **29:** 553–563.

Haringa C, Tang W, Deshmukh AT, Xia J, Reuss M, Heijnen JJ, Mudde RF, Noorman HJ (2016): Euler-Lagrange computational fluid dynamics for (bio)reactor scale down: An analysis of organism lifelines. *Eng Life Sci* **16:** 652–663.

Haringa C, Deshmukh AT, Mudde RF, Noorman HJ (2017): Euler-Lagrange analysis towards representative down-scaling of a 22 m³ aerobic *S. cerevisiae* fermentation. *Chem Eng Sci* **170:** 653–669.

Harvey AP, Mackley MR, Seliger T (2003): Process intensification of biodiesel production using a continuous oscillatory flow reactor. *J Chem Technol Biotechnol* **78:** 338–341.

Hattori H, Wada A, Yamamoto M, Yokoo H, Yasunaga K, Kanda T, Hattori K (2022): Experimental study of laminar-to-turbulent transition in pipe flow. *Phys Fluids* **34**.

He X, Memczak S, Qu J, Belmonte JCI, Liu G-H (2020): Single-cell omics in ageing: a young and growing field. *Nat Metab* **2:** 293–302.

Hebisch E, Knebel J, Landsberg J, Frey E, Leisner M (2013): High Variation of Fluorescence Protein Maturation Times in Closely Related *Escherichia coli* Strains. *PLoS One* **8:** e75991.

Heim R, Prasher DC, Tsien RY (1994): Wavelength mutations and posttranslational autoxidation of green fluorescent protein. *Proc Natl Acad Sci USA* **91:** 12501–12504.

Heins A-L, Weuster-Botz D (2018): Population heterogeneity in microbial bioprocesses: origin, analysis, mechanisms, and future perspectives. *Bioprocess Biosyst Eng* **41:** 889–916.

Heins A-L, Reyelt J, Schmidt M, Kranz H, Weuster-Botz D (2020): Development and characterization of *Escherichia coli* triple reporter strains for investigation of population heterogeneity in bioprocesses. *Microb Cell Factories* **19:** 14.

Heins A-L, Hoang MD, Weuster-Botz D (2022): Advances in automated real-time flow cytometry for monitoring of bioreactor processes. *Eng Life Sci* **22:** 260–278.

Heller KB, Lin ECC, Wilson TH (1980): Substrate Specificity and Transport Properties of the Glycerol Facilitator of *Escherichia coli*. *J Bacteriol* **144:** 274–278.

Herman B (1998): Fluorescence microscopy. *Curr Protoc Cell Biol* 4.2.1–4.2.10.

Hernandez VJ, Bremer H (1990): Guanosine Tetraphosphate (ppGpp) Dependence of the Growth Rate Control of *rrnB* P1 Promoter Activity in *Escherichia coli*. *J Biol Chem* **265:** 11605–11614.

Herzenberg, Leonore, A., Tung J, Moore WA, Herzenberg LA, Parks DR (2006): Interpreting flow cytometry data: a guide for the perplexed. *Nat Immunol* **7:** 681–685.

Hirech K, Arhaliass A, Legrand J (2003): Experimental Investigation of Flow Regimes in an SMX Sulzer Static Mixer. *Ind Eng Chem Res* **42:** 1478–1484.

Hlushkou D, Tallarek U (2006): Transition from creeping via viscous-inertial to turbulent flow in fixed beds. *J Chromatogr A* **1126:** 70–85.

Hoang MD, Doan DT, Schmidt M, Kranz H, Kremling A, Heins A-L (2023a): Application of an *Escherichia coli* triple reporter strain for at-line monitoring of single-cell physiology during L-phenylalanine production. *Eng Life Sci* **23:** e2100162.

Hoang MD, Polte I, Frantzmann L, den Eichen N von, Heins A-L, Weuster-Botz D (2023b): Impact of mixing insufficiencies on L-phenylalanine production with an *Escherichia coli* reporter strain in a novel two-compartment bioreactor. *Microb Cell Factories* **22:** 153.

Hobbs DM, Muzzio FJ (1997): The Kenics static mixer: a three-dimensional chaotic flow. *Chem Eng J* **67:** 153–166.

Hodne K, Weltzien F-A (2015): Single-Cell Isolation and Gene Analysis: Pitfalls and Possibilities. *Int J Mol Sci* **16:** 26832–26849.

Hoheisel JD (1989): A cassette with seven unique restriction sites, including octanucleotide sequences: extension of multiple-cloning-site plasmids. *Gene* **80**.

Hoskisson PA, Hobbs G (2005): Continuous culture -making a comeback? *Microbiology* **151:** 3153–3159.

Huang C-J, Lin H, Yang X (2012): Industrial production of recombinant therapeutics in *Escherichia coli* and its recent advancements. *J Ind Microbiol Biotechnol* **39:** 383–399.

Idalia V-MN, Bernardo F (2017): *Escherichia coli* as a Model Organism and Its Application in Biotechnology. In Amidou S: *Escherichia coli* Recent Advances on Physiology, Pathogenesis and Biotechnological Applications. InTech, Rijeka, Croatia: 253–274.

Iizuka R, Yamagishi-Shirasaki M, Funatsu T (2011): Kinetic study of *de novo* chromophore maturation of fluorescent proteins. *Anal Biochem* **414:** 173–178.

Jaibiba P, Vignesh N, Hariharan S (2020): Working principle of typical bioreactors. In Singh L, Yousuf A, Mahapatra DM: Bioreactors. Elsevier B.V., Amsterdam, The Netherlands: 145–173.

Jaroszeski MJ, Radcliff G (1999): Fundamentals of Flow Cytometry. *Mol Biotechnol* **11:** 37–53.

Javelle A, Severi E, Thornton J, Merrick M (2004): Ammonium sensing in *Escherichia coli. J Biol Chem* **279:** 8530–8538.

Jilisen RTM, Bloemen PR, Speetjens MFM (2013): Three-dimensional flow measurements in a static mixer. *AIChE J* **59:** 1746–1761.

Johnson MD, May SA, Calvin JR, Remacle J, Stout JR, Diseroad WD, Zaborenko N, Haeberle BD, Sun W-M, Miller MT, Brennan J (2012): Development and Scale-Up of a Continuous, High-Pressure, Asymmetric Hydrogenation Reaction, Workup, and Isolation. *Org Process Res Dev* **16:** 1017–1038.

Jonkman J, Brown CM, Wright GD, Anderson KI, North AJ (2020): Tutorial: guidance for quantitative confocal microscopy. *Nat Protoc* **15:** 1585–1611.

Junne S, Klingner A, Kabisch J, Schweder T, Neubauer P (2011): A two-compartment bioreactor system made of commercial parts for bioprocess scale-down studies: impact of oscillations on *Bacillus subtilis* fed-batch cultivations. *Biotechnol J* **6:** 1009–1017.

Kampen W (2014): Nutritional Requirements in Fermentation Processes. In Todaro CM, Vogel HC: Fermentation and Biochemical Engineering Handbook. William Andrew, Waltham, United States of America: 37–57.

Kao S-H, Wang W-L, Chen C-Y, Chang Y-L, Wu Y-Y, Wang Y-T, Wang S-P, Nesvizhskii AI, Chen Y-J, Hong T-M, Yang P-C (2015): Analysis of Protein Stability by the Cycloheximide Chase Assay. *Bio Protoc* **5:** e1374.

Karakashev D, Galabova D, Simeonov I (2003): A simple and rapid test for differentiation of aerobic from anaerobic bacteria. *World J Microbiol Biotechnol* **19:** 233–238.

Kargeti M, Venkatesh KV (2017): The effect of global transcriptional regulators on the anaerobic fermentative metabolism of *Escherichia coli. Mol Biosyst* **13:** 1388–1398.

Karimi A, Golbabaei F, Mehrnia MR, Neghab M, Mohammad K, Nikpey A, Pourmand MR (2013): Oxygen mass transfer in a stirred tank bioreactor using different impeller configurations for environmental purposes. *Iran J Environ Health Sci Eng* **10:** 1–9.

Kasli IM, Thomas ORT, Overton TW (2019): Use of a design of experiments approach to optimise production of a recombinant antibody fragment in the periplasm of

Escherichia coli: selection of signal peptide and optimal growth conditions. *AMB Express* **9:** 1–14.

Käß F, Hariskos I, Michel A, Brandt H-J, Spann R, Junne S, Wiechert W, Neubauer P, Oldiges M (2014): Assessment of robustness against dissolved oxygen/substrate oscillations for *C. glutamicum* DM1933 in two-compartment bioreactor. *Bioprocess Biosyst Eng* **37:** 1151–1162.

Kayser A, Weber J, Hecht V, Rinas U (2005): Metabolic flux analysis of *Escherichia coli* in glucose-limited continuous culture. I. Growth-rate-dependent metabolic efficiency at steady state. *Microbiology* **151:** 693–706.

Kazan D, Çamurdan A, Hortaçsu A (1995): The Effect of Glucose Concentration on the Growth Rate and some Intracellular Components of a Recombinant *E. coli* Culture. *Process Biochem* **30:** 269–273.

Kensy F, Engelbrecht C, Büchs J (2009): Scale-up from microtiter plate to laboratory fermenter: evaluation by online monitoring techniques of growth and protein expression in *Escherichia coli* and *Hansenula polymorpha* fermentations. *Microb Cell Factories* **8:** 68.

Khamduang M, Packdibamrung K, Chutmanop J, Chisti Y, Srinophakun P (2009): Production of L-phenylalanine from glycerol by a recombinant *Escherichia coli*. *J Ind Microbiol Biotechnol* **36:** 1267–1274.

Khan SH (2019): Genome-Editing Technologies: Concept, Pros, and Cons of Various Genome-Editing Techniques and Bioethical Concerns for Clinical Application. *Mol Ther Nucleic Acids* **16:** 326–334.

Khot P, Mansour M, Thévenin D, Nigam KD, Zähringer K (2019): Improving the mixing characteristics of coiled configurations by early flow inversion. *Chem Eng Res Des* **146:** 324–335.

Kiley PJ, Reznikoff WS (1991): Fnr Mutants That Activate Gene Expression in the Presence of Oxygen. *J Bacteriol* **173:** 16–22.

Kim T-Y, Yoon T-S, Kang S, Afzal M (2022): Juggling with fluorescent proteins: Spectrum and structural changes of the mCardinal2 variants. *Biochem Biophys Res Commun* **593:** 79–83.

Kimura M, Ohta T (1969): The average number of generations until fixation of a mutant gene in a finite population. *Genetics* **61:** 763–771.

Kirk TV, Szita N (2013): Oxygen transfer characteristics of miniaturized bioreactor systems. *Biotechnol Bioeng* **110:** 1005–1019.

Kiviet DJ, Nghe P, Walker N, Boulineau S, Sunderlikova V, Tans SJ (2014): Stochasticity of metabolism and growth at the single-cell level. *Nature* **514:** 376–379.

Klutz S, Kurt SK, Lobedann M, Kockmann N (2015): Narrow residence time distribution in tubular reactor concept for Reynolds number range of 10–100. *Chem Eng Res Des* **95:** 22–33.

Kœrn M, Elston TC, Blake WJ, Collins JJ (2005): Stochasticity in gene expression: from theories to phenotypes. *Nat Rev Genet* **6:** 451–464.

Kornberg HL (1966): The Role and Control of the Glyoxylate Cycle in *Escherichia coli*. *Biochem J* **99:** 1–11.

Kováts P, Velten C, Mansour M, Thévenin D, Zähringer K (2020): Mixing characterization in different helically coiled configurations by laser-induced fluorescence. *Exp. Fluids* **61:** 1–17.

Kreimer M, Zettl M, Aigner I, Mannschott T, van der Wel P, Khinast JG, Krumme M (2019): Performance Characterization of Static Mixers in Precipitating Environments. *Org Process Res Dev* **23:** 1308–1320.

Kühnen J, Song B, Scarselli D, Budanur NB, Riedl M, Willis AP, Avila M, Hof B (2018): Destabilizing turbulence in pipe flow. *Nat Phys* **14:** 386–390.

Kumar V, Aggarwal M, Nigam K (2006): Mixing in curved tubes. *Chem Eng Sci* **61:** 5742–5753.

Kurt SK, Gelhausen MG, Kockmann N (2015): Axial Dispersion and Heat Transfer in a Milli/Microstructured Coiled Flow Inverter for Narrow Residence Time Distribution at Laminar Flow. *Chem Eng Technol* **38:** 1122–1130.

Kurt SK, Akhtar M, Nigam KDP, Kockmann N (2017): Continuous Reactive Precipitation in a Coiled Flow Inverter: Inert Particle Tracking, Modular Design, and Production of Uniform $CaCO_3$ Particles. *Ind Eng Chem Res* **56:** 11320–11335.

Kuschel M, Takors R (2020): Simulated oxygen and glucose gradients as a prerequisite for predicting industrial scale performance a priori. *Biotechnol Bioeng* **117:** 2760–2770.

Langheinrich C, Nienow AW (1999): Control of pH in Large-Scale, Free Suspension Animal Cell Bioreactors: Alkali Addition and pH Excursions. *Biotechnol Bioeng* **66:** 171–179.

Lapierre FM, Schmid J, Ederer B, Ihling N, Büchs J, Huber R (2020): Revealing nutritional requirements of MICP-relevant *Sporosarcina pasteurii* DSM33 for growth improvement in chemically defined and complex media. *Sci Rep* **10:** 22448.

Lara AR, Galindo E, Ramírez OT, Palomares LA (2006): Living With Heterogeneities in Bioreactors. *Mol Biotechnol* **34:** 355–381.

Lee SY (1996): High cell-density culture of *Escherichia coli*. *Trends Biotechnol* **14:** 98–105.

Lee SY, Kim HU (2015): Systems strategies for developing industrial microbial strains. *Nat Biotechnol* **33:** 1061–1072.

Lehtinen J, Nuutila J, Lilius E-M (2004): Green fluorescent protein-propidium iodide (GFP-PI) based assay for flow cytometric measurement of bacterial viability. *Cytometry A* **60:** 165–172.

Lemoine A, Maya Martínez-Iturralde N, Spann R, Neubauer P, Junne S (2015): Response of *Corynebacterium glutamicum* exposed to oscillating cultivation conditions in a two- and a novel three-compartment scale-down bioreactor. *Biotechnol Bioeng* **112:** 1220–1231.

Leone S, Sannino F, Tutino ML, Parrilli E, Picone D (2015): Acetate: friend or foe? Efficient production of a sweet protein in *Escherichia coli* BL21 using acetate as a carbon source. *Microb Cell Factories* **14:** 106.

Levenspiel O (2012): Tracer Technology. Springer, New York, United States of America.

Li SF, DeMoss JA (1987): Promoter Region of the nar Operon of *Escherichia coli*: Nucleotide Sequence and Transcription Initiation Signals. *J Bacteriol* **169:** 4614–4620.

Li Z, Ji X, Kan S, Qiao H, Jiang M, Lu D, Wang J, Huang H, Jia H, Ouyuang P, Ying H (2010): Past, Present, and Future Industrial Biotechnology in China. In Tsao GT, Ouyang P, Chen J: Biotechnology in China II. Springer, Berlin Heidelberg, Germany: 1–42.

Li F, Hullar MAJ, Beresford SAA, Lampe JW (2011): Variation of glucoraphanin metabolism *in vivo* and *ex vivo* by human gut bacteria. *Br J Nutr* **106:** 408–416.

Lichtman JW, Conchello J-A (2005): Fluorescence microscopy. *Nat Methods* **2:** 910–919.

Lidstrom ME, Konopka MC (2010): The role of physiological heterogeneity in microbial population behavior. *Nat Chem Biol* **6:** 705–712.

Lim HN, Lee Y, Hussein R (2011): Fundamental relationship between operon organization and gene expression. *Proc Natl Acad Sci USA* **108:** 10626–10631.

Limberg MH, Pooth V, Wiechert W, Oldiges M (2016): Plug flow versus stirred tank reactor flow characteristics in two-compartment scale-down bioreactor: Setup-specific influence on the metabolic phenotype and bioprocess performance of *Corynebacterium glutamicum*. *Eng Life Sci* **16:** 610–619.

Ling LS, Mohamad R, Rahim RA, Wan HY, Ariff AB (2006): Improved Production of Live Cells of *Lactobacillus rhamnosus* by Continuous Cultivation using Glucose-yeast Extract Medium. *J Microbiol* **44:** 439–446.

Liu SP, Liu RX, Xiao MR, Zhang L, Ding ZY, Gu ZH, Shi GY (2014): A systems level engineered *E. coli* capable of efficiently producing L-phenylalanine. *Process Biochem* **49:** 751–757.

Liu Y, Xu Y, Ding D, Wen J, Zhu B, Zhang D (2018a): Genetic engineering of *Escherichia coli* to improve L-phenylalanine production. *BMC Biotechnol* **18:** 5.

Liu Q, Schumacher J, Wan X, Lou C, Wang B (2018b): Orthogonality and Burdens of Heterologous AND Gate Gene Circuits in *E. coli. ACS Synth Biol* **7:** 553–564.

Löffler M, Simen JD, Jäger G, Schäferhoff K, Freund A, Takors R (2016): Engineering *E. coli* for large-scale production - Strategies considering ATP expenses and transcriptional responses. *Metab Eng* **38:** 73–85.

Lone SR, Kumar V, Seay JR, Englert DL, Hwang HT (2020): Mass Transfer and Rheological Characteristics in a Stirred Tank Bioreactor for Cultivation of *Escherichia coli* BL21. *Biotechnol Bioprocess Eng* **25:** 766–776.

Long CP, Gonzalez JE, Cipolla RM, Antoniewicz MR (2017): Metabolism of the fast-growing bacterium *Vibrio natriegens* elucidated by 13^C metabolic flux analysis. *Metab Eng* **44:** 191–197.

Longis M, Pereira JC, Högl TH, Neubauer P, Junne S (2023): Plug-flow anaerobic digestion with multi-position sensors: The value of gradient measurement for process monitoring. *Biomass Bioenergy* **173:** 106803.

Lozano Terol G, Gallego-Jara J, Sola Martínez RA, Martínez Vivancos A, Cánovas Díaz M, Diego Puente T de (2021): Impact of the Expression System on Recombinant Protein Production in *Escherichia coli* BL21. *Front Microbiol* **12:** 682001.

Luli GW, Strohl WR (1990): Comparison of Growth, Acetate Production, and Acetate Inhibition of *Escherichia coli* Strains in Batch and Fed-Batch Fermentations. *Appl Environ Microbiol* **56:** 1004–1011.

Lundgren M, Andersson A, Chen L, Nilsson P, Bernander R (2004): Three replication origins in *Sulfolobus* species: Synchronous initiation of chromosome replication and asynchronous termination. *Proc Natl Acad Sci USA* **101:** 7046–7051.

Madar D, Dekel E, Bren A, Zimmer A, Porat Z, Alon U (2013): Promoter activity dynamics in the lag phase of *Escherichia coli. BMC Syst Biol* **7:** 1–13.

Mandenius C-F (2016): Challenges for Bioreactor Design and Operation. In Mandenius C-F: Bioreactors. Wiley-VCH, Weinheim, Germany: 1–34.

Mansour M, Liu Z, Janiga G, Nigam KDP, Sundmacher K, Thévenin D, Zähringer K (2017): Numerical Study of Liquid-Liquid Mixing in Helical Pipes. *Chem Eng Sci* **172:** 250–261.

Martin DK, Vicente O, Beccari T, Kellermayer M, Koller M, Lal R, Marks RS, Marova I, Mechler A, Tapaloaga D, Žnidaršič-Plazl P, Dundar M (2021): A brief overview of global biotechnology. *Biotechnol Biotechnol Equip* **35:** S5–S14.

Martinez KA, Kitko RD, Mershon JP, Adcox HE, Malek KA, Berkmen MB, Slonczewski JL (2012): Cytoplasmic pH response to acid stress in individual cells of *Escherichia coli* and *Bacillus subtilis* observed by fluorescence ratio imaging microscopy. *Appl Environ Microbiol* **78:** 3706–3714.

Martínez-Reyes I, Chandel NS (2020): Mitochondrial TCA cycle metabolites control physiology and disease. *Nat Commun* **11:** 102.

Matic I (2019): Mutation Rate Heterogeneity Increases Odds of Survival in Unpredictable Environments. *Mol Cell* **75:** 421–425.

McGinness KE, Baker TA, Sauer RT (2006): Engineering controllable protein degradation. *Mol Cell* **22:** 701–707.

Meisner JE, Rushmer RF (1963): Eddy Formation and Turbulence in Flowing Liquids. *Circ Res* **12:** 455–463.

Meyer H-P, Leist C, Fiechter A (1984): Acetate formation in continuous culture of *Escherichia coli* K12 D1 on defined and complex media. *J Biotechnol* **1:** 355–358.

Miao H, Ratnasingam S, Pu CS, Desai MM, Sze CC (2009): Dual fluorescence system for flow cytometric analysis of *Escherichia coli* transcriptional response in multi-species context. *J Microbiol Methods* **76:** 109–119.

Mohamed MS, Mohamad R, Ramanan RN, Manan MA, Ariff AB (2009): Modeling of Oxygen Transfer Correlations for Stirred Tank Bioreactor Agitated with Atypical Helical Ribbon Impeller. *Am J Appl Sci* **6:** 848–856.

Mohammadi S, Boodhoo KV (2012): Online conductivity measurement of residence time distribution of thin film flow in the spinning disc reactor. *Chem Eng J* **207-208:** 885–894.

Molotoks A, Smith P, Dawson TP (2021): Impacts of land use, population, and climate change on global food security. *Food Energy Secur.* **10:** e261.

Monaco G, Chen H, Poidinger M, Chen J, Magalhães JP de, Larbi A (2016): flowAI: automatic and interactive anomaly discerning tools for flow cytometry data. *Bioinformatics* **32:** 2473–2480.

Monge F, Aranda V, Millera A, Bilbao R, Alzueta MU (2013): Tubular Flow Reactors. In Battin-Leclerc F, Blurock E, Simmie JM: Cleaner Combustion. Springer, London, United Kingdom: 211–230.

Monod J (1949): The Growth of Bacterial Cultures. *Annu Rev Microbiol* **3:** 371–394.

Mori H, Yano T, Kobayashi T, Shimizu S (1979): High density cultivation of biomass in fed-batch system with DO-stat. *J Chem Eng Japan* **12:** 313–319.

Mørup AJ, Becker J, Christensen PS, Houlberg K, Lappa E, Klemmer M, Madsen RB, Glasius M, Iversen BB (2015): Construction and Commissioning of a Continuous Reactor for Hydrothermal Liquefaction. *Ind Eng Chem Res* **54:** 5935–5947.

Mosberg JA, Lajoie MJ, Church GM (2010): Lambda Red Recombineering in *Escherichia coli* Occurs Through a Fully Single-Stranded Intermediate. *Genetics* **186:** 791–799.

Moser MJ, Holley WR, Chatterjee A, Mian IS (1997): The proofreading domain of *Escherichia coli* DNA polymerase I and other DNA and/or RNA exonuclease domains. *Nucleic Acids Res* **25:** 5110–5118.

Müller S, Harms H, Bley T (2010): Origin and analysis of microbial population heterogeneity in bioprocesses. *Curr Opin Biotechnol* **21:** 100–113.

Munavar H, Zhou Y, Gottesman S (2005): Analysis of the *Escherichia coli* Alp phenotype: heat shock induction in *ssrA* mutants. *J Bacteriol* **187:** 4739–4751.

Muradi NA, Awang Adeni DS, Suhaili N (2020): Enhancement of very high gravity bioethanol production via fed-batch fermentation using sago hampas as a substrate. *Asia Pac J Mol Biol Biotechnol* **28:** 44–51.

Murphy KC (1998): Use of Bacteriophage λ Recombination Functions To Promote Gene Replacement in *Escherichia coli*. *J Bacteriol* **180:** 2063–2071.

Murray HD, Appleman JA, Gourse RL (2003): Regulation of the *Escherichia coli rrnB* P2 Promoter. *J Bacteriol* **185:** 28–34.

Mutanda T, Naidoo D, Bwapwa JK, Anandraj A (2020): Biotechnological Applications of Microalgal Oleaginous Compounds: Current Trends on Microalgal Bioprocessing of Products. *Front Energy Res* **8:** 598803.

Nakai R (2020): Size Matters: Ultra-small and Filterable Microorganisms in the Environment. *Microbes Environ* **35**.

Nakamori S (2017): Early History of the Breeding of Amino Acid-Producing Strains. In Ikeda M, Yokota A: Amino Acid Fermentation. Springer, Tokyo, Japan: 35–54.

Nebe-von-Caron G, Stephens PJ, Hewitt CJ, Powell JR, Badley RA (2000): Analysis of bacterial function by multi-colour fluorescence flow cytometry and single cell sorting. *J Microbiol Methods* **42:** 97–114.

Neubauer P, Junne S (2016): Scale-up and scale-down methodologies for bioreactors. In Mandenius C-F: Bioreactors. Wiley-VCH, Weinheim, Germany: 323–354.

Nieß A, Löffler M, Simen JD, Takors R (2017): Repetitive Short-Term Stimuli Imposed in Poor Mixing Zones Induce Long-Term Adaptation of *E. coli* Cultures in Large-Scale Bioreactors: Experimental Evidence and Mathematical Model. *Front Microbiol* **8:** 1195.

Noorman H (2011): An industrial perspective on bioreactor scale-down: what we can learn from combined large-scale bioprocess and model fluid studies. *Biotechnol J* **6:** 934–943.

Norman TM, Lord ND, Paulsson J, Losick R (2015): Stochastic Switching of Cell Fate in Microbes. *Annu Rev Microbiol* **69:** 381–403.

Ntengwe FW, Chikwa M, Witika LK (2015): Evaluation Of Friction Losses In Pipes And Fittings Of Process Engineering Plants. *Int J Sci Technol Res* **4:** 330–336.

Oller AR, Schaaper RM (1994): Spontaneous Mutation in *Escherichia coli* Containing the *dnaE911* DNA Polymerase Antimutator Allele. *Genetics* **138:** 263–270.

Olson ER (1993): Influence of pH on bacterial gene expression. *Mol Microbiol* **8:** 5–14.

Olsvik E, Kristiansen B (1994): Rheology of filamentous fermentations. *Biotechnol Adv* **12:** 1–39.

Oppenheim AB, Rattray AJ, Bubunenko M, Thomason LC, Court DL (2004): *In vivo* recombineering of bacteriophage λ by PCR fragments and single-strand oligonucleotides. *Virology* **319:** 185–189.

Osella M, Nugent E, Cosentino Lagomarsino M (2014): Concerted control of *Escherichia coli* cell division. *Proc Natl Acad Sci USA* **111:** 3431–3435.

Ow DS-W, Nissom PM, Philp R, Oh SK-W, Yap MG-S (2006): Global transcriptional analysis of metabolic burden due to plasmid maintenance in *Escherichia coli* DH5α during batch fermentation. *Enzyme Microb Technol* **39:** 391–398.

Ozturk SS (1996): Engineering challenges in high density cell culture systems. *Cytotechnology* **22:** 3–16.

Paalme T, Tiisma K, Kahru A, Vanatalu K, Vilu R (1990): Glucose-Limited Fed-Batch Cultivation of *Escherichia coli* with Computer-Controlled Fixed Growth Rate. *Biotechnol Bioeng* **35:** 312–319.

Papagianni M, Mattey M, Kristiansen B (2003): Design of a Tubular Loop Bioreactor for Scale-up and Scale-down of Fermentation Processes. *Biotechnol Prog* **19:** 1498–1504.

Park H-S, Schumacher R, Kilbane JJ (2005): New method to characterize microbial diversity using flow cytometry. *J Ind Microbiol Biotechnol* **32:** 94–102.

Perkel JM (2013): The New Genetic Engineering Toolbox. *Biotechniques* **54:** 185–188.

Pfeifer MJ, Silva SS, Felipe MGA, Roberto Inès C., Mancilha IM (1996): Effect of Culture Conditions on Xylitol Production by *Candida guilliermondii* FTI 20037. *Appl Biochem Biotechnol* **56/57:** 423–430.

Pittard J, Yang J (2008): Biosynthesis of the aromatic amino acids. *EcoSal Plus* **3:** 10–1128.

Plavec TV, Berlec A (2020): Safety Aspects of Genetically Modified Lactic Acid Bacteria. *Microorganisms* **8**.

Price SB, Cheng C-M, Kaspar CW, Wright JC, DeGraves FJ, Penfound TA, Castanie-Cornet M-P, Foster JW (2000): Role of *rpoS* in Acid Resistance and Feca Shedding of *Escherichia coli* O157:H7. *Appl Environ Microbiol* **66:** 632–637.

Priebe X, Hoang MD, Rüdiger J, Turgel M, Tröndle J, Schwab W, Weuster-Botz D (2021): Byproduct-free geraniol glycosylation by whole-cell biotransformation with recombinant *Escherichia coli*. *Biotechnol Lett* **43:** 247–259.

Puskeiler R, Kaufmann K, Weuster-Botz D (2005): Development, Parallelization, and Automation of a Gas-Inducing Milliliter-Scale Bioreactor for High-Throughput Bioprocess Design (HTBD). *Biotechnol Bioeng* **89:** 512–523.

Raina S, Missiakas D, Georgopoulos C (1995): The *rpoE* gene encoding the σE (σ24) heat shock sigma factor of *Escherichia coli*. *EMBO J* **14:** 1043–1055.

Rantasalo A, Vitikainen M, Paasikallio T, Jäntti J, Landowski CP, Mojzita D (2019): Novel genetic tools that enable highly pure protein production in *Trichoderma reesei*. *Sci Rep* **9:** 5032.

Raser JM, O'Shea EK (2005): Noise in Gene Expression: Origins, Consequences, and Control. *Science* **309:** 2010–2013.

Reggeti F, Bienzle D (2011): Flow Cytometry in Veterinary Oncology. *Vet Pathol* **48:** 223–235.

Reis N, Gonçalves CN, Vicente AA, Teixeira JA (2006): Proof-of-Concept of a Novel Micro-Bioreactor for Fast Development of Industrial Bioprocesses. *Biotechnol Bioeng* **95:** 744–753.

Reis MH, Varner TP, Leibfarth FA (2019): The Influence of Residence Time Distribution on Continuous-Flow Polymerization. *Macromolecules* **52:** 3551–3557.

Rejeb SB, Lereclus D, Slamti L (2017): Analysis of abrB Expression during the Infectious Cycle of *Bacillus thuringiensis* Reveals Population Heterogeneity. *Front Microbiol* **8:** 2471.

Renggli S, Keck W, Jenal U, Ritz D (2013): Role of Autofluorescence in Flow Cytometric Analysis of *Escherichia coli* Treated with Bactericidal Antibiotics. *J Bacteriol* **195:** 4067–4073.

Riedel TE, Berelson WM, Nealson KH, Finkel SE (2013): Oxygen Consumption Rates of Bacteria under Nutrient-Limited Conditions. *Appl Environ Microbiol* **79:** 4921–4931.

Riesenberg D, Schulz V, Knorre WA, Pohl H-D, Korz D, Sanders EA, Roß A, Deckwer W-D (1991): High cell density cultivation of *Escherichia coli* at controlled specific growth rate. *J Biotechnol* **20:** 17–28.

Rinke C, Lee J, Nath N, Goudeau D, Thompson B, Poulton N, Dmitrieff E, Malmstrom R, Stepanauskas R, Woyke T (2014): Obtaining genomes from uncultivated environmental microorganisms using FACS-based single-cell genomics. *Nat Protoc* **9:** 1038–1048.

Rodriguez A, Martínez JA, Flores N, Escalante A, Gosset G, Bolivar F (2014): Engineering *Escherichia coli* to overproduce aromatic amino acids and derived compounds. *Microb Cell Factories* **13:** 126.

Romano AH, Conway T (1996): Evolution of carbohydrate metabolic pathways. *Res Microbiol* **147:** 448–455.

Rossi D, Gargiulo L, Valitov G, Gavriilidis A, Mazzei L (2017): Experimental characterization of axial dispersion in coiled flow inverters. *Chem Eng Res Des* **120:** 159–170.

Rothfus RR, Monrad CC, Senecal VE (1950): Velocity Distribution and Fluid Friction in Smooth Concentric Annuli. *Ind Eng Chem* **42:** 2511–2520.

Rouvière PE, Las Peñas A de, Mecsas J, Lu CZ, Rudd KE, Gross CA (1995): *rpoE*, the gene encoding the second heat-shock sigma factor, σE, in *Escherichia coli. EMBO J* **14:** 1032–1042.

Rugbjerg P, Myling-Petersen N, Porse A, Sarup-Lytzen K, Sommer MOA (2018): Diverse genetic error modes constrain large-scale bio-based production. *Nat Commun* **9:** 787.

Rugbjerg P, Sommer MOA (2019): Overcoming genetic heterogeneity in industrial fermentations. *Nat Biotechnol* **37:** 869–876.

Saint-Ruf C, Pesut J, Sopta M, Matic I (2007): Causes and Consequences of DNA Repair Activity Modulation During Stationary Phase in *Escherichia coli*. *Crit Rev Biochem Mol Biol* **42:** 259–270.

Salis HM, Mirsky EA, Voigt CA (2009): Automated design of synthetic ribosome binding sites to control protein expression. *Nat Biotechnol* **27:** 946–950.

Santacesaria E, Turco R, Tortorelli M, Russo V, Di Serio M, Tesser R (2012): Biodiesel Process Intensification by Using Static Mixers Tubular Reactors. *Ind Eng Chem Res* **51:** 8777–8787.

Santos-Moreno J, Schaerli Y (2019): A framework for the modular and combinatorial assembly of synthetic gene circuits. *ACS Synth Biol* **8:** 1691–1697.

Sarkar D, Le Meur N, Gentleman R (2008): Using flowViz to visualize flow cytometry data. *Bioinformatics* **24:** 878–879.

Sassi H, Nguyen TM, Telek S, Gosset G, Grünberger A, Delvigne F (2019): Segregostat: a novel concept to control phenotypic diversification dynamics on the example of Gram-negative bacteria. *Microb Biotechnol* **12:** 1064–1075.

Saxena AK, Nigam KDP (1981): Axial Dispersion in Laminar Flow of Polymer Solutions through Coiled Tubes. *J Appl Polym Sci* **26:** 3475–3486.

Saxena AK, Nigam KDP (1983): Effect of coil pitch and cross-sectional ellipticity on RTD for diffusion-free laminar flow in coiled tubes. *Chem Eng Commun* **23:** 277–289.

Saxena AK, Nigam KDP (1984): Coiled Configuration for Flow Inversion and Its Effect on Residence Time Distribution. *AIChE J* **30:** 363–368.

Schlichting H, Gersten K (2017): Boundary-Layer Theory. Springer, Berlin Heidelberg, Germany.

Schoppel K, Trachtmann N, Korzin EJ, Tzanavari A, Sprenger GA, Weuster-Botz D (2022): Metabolic control analysis enables rational improvement of *E. coli* L-tryptophan producers but methylglyoxal formation limits glycerol-based production. *Microb Cell Factories* **21:** 201.

Schweizer HP (2003): Applications of the *Saccharomyces cerevisiae* Flp-FRT system in bacterial genetics. *J Mol Microbiol Biotechnol* **5:** 67–77.

Seo SW, Yang J-S, Kim I, Yang J, Min BE, Kim S, Jung GY (2013): Predictive design of mRNA translation initiation region to control prokaryotic translation efficiency. *Metab Eng* **15:** 67–74.

Shaner NC, Campbell RE, Steinbach PA, Giepmans BNG, Palmer AE, Tsien RY (2004): Improved monomeric red, orange and yellow fluorescent proteins derived from *Discosoma sp.* red fluorescent protein. *Nat Biotechnol* **22:** 1567–1572.

Shaner NC, Steinbach PA, Tsien RY (2005): A guide to choosing fluorescent proteins. *Nat Methods* **2:** 905–909.

Shaner NC, Patterson GH, Davidson MW (2007): Advances in fluorescent protein technology. *J Cell Sci* **120:** 4247–4260.

Sharkey TD (2021): Pentose Phosphate Pathway Reactions in Photosynthesizing Cells. *Cells* **10:** 1547.

Shehata TE, Marr AG (1975): Effect of Temperature on the Size of *Escherichia coli* Cells. *J Bacteriol* **124:** 857–862.

Shemiakina II, Ermakova GV, Cranfill PJ, Baird MA, Evans RA, Souslova EA, Staroverov DB, Gorokhovatsky AY, Putintseva EV, Gorodnicheva TV, Chepurnykh TV, Strukova L, Lukyanov S, Zaraisky AG, Davidson MW, Chudakov DM, Shcherbo D (2012): A monomeric red fluorescent protein with low cytotoxicity. *Nat Commun* **3:** 1204.

Shibai A, Takahashi Y, Ishizawa Y, Motooka D, Nakamura S, Ying B-W, Tsuru S (2017): Mutation accumulation under UV radiation in *Escherichia coli. Sci Rep* **7:** 14531.

Shimada T, Furuhata S, Ishihama A (2021): Whole set of constitutive promoters for RpoN sigma factor and the regulatory role of its enhancer protein NtrC in *Escherichia coli* K-12. *Microb Genom* **7**.

Shu C-H, Liao C-C (2002): Optimization of L-phenylalanine production of *Corynebacterium glutamicum* under product feedback inhibition by elevated oxygen transfer rate. *Biotechnol Bioeng* **77:** 131–141.

Sieben M, Steinhorn G, Müller C, Fuchs S, Ann Chin L, Regestein L, Büchs J (2016): Testing Plasmid Stability of *Escherichia coli* Using the Continuously Operated Shaken BIOreactor System. *Biotechnol Prog* **32:** 1418–1425.

Silva F, Passarinha L, Sousa F, Queiroz JA, Domingues FC (2009): Influence of growth conditions on plasmid DNA production. *J Microbiol Biotechnol* **11:** 1408–1414.

Simen JD, Löffler M, Jäger G, Schäferhoff K, Freund A, Matthes J, Müller J, Takors R (2017): Transcriptional response of *Escherichia coli* to ammonia and glucose fluctuations. *Microb Biotechnol* **10:** 858–872.

Singer C (1914): Notes on the Early History of Microscopy. *Proc R Soc Med* **7:** 247–279.

Smith AM, Bidochka MJ (1998): Bacterial fitness and plasmid loss: the importance of culture conditions and plasmid size. *Can J Microbiol* **44:** 351–355.

Sniegowski PD, Gerrish PJ, Lenski RE (1997): Evolution of high mutation rates in experimental populations of *E. coli. Nature* **387:** 703–705.

Soomro AH, Masud T, Anwaar K (2002): Role of Lactic Acid Bacteria (LAB) in Food Preservation and Human Health - A Review. *Pak J Nutr* **1:** 20–24.

Sprenger GA (1995): Genetics of pentose-phosphate pathway enzymes of *Escherichia coli* K-12. *Arch Microbiol* **164:** 324–330.

Sprenger GA (2007): From scratch to value: engineering *Escherichia coli* wild type cells to the production of L-phenylalanine and other fine chemicals derived from chorismate. *Appl Microbiol Biotechnol* **75:** 739–749.

Stark JC, Huang A, Nguyen PQ, Dubner RS, Hsu KJ, Ferrante TC, Anderson M, Kanapskyte A, Mucha Q, Packett JS, Patel P, Patel R, Qaq D, Zondor T, Burke J, Martinez T, Miller-Berry A, Puppala A, Reichert K, Schmid M, Brand L, Hill LR, Chellaswamy JF, Faheem N, Fetherling S, Gong E, Gonzalzles EM, Granito T, Koritsaris J, Nguyen B, Ottman S, Palffy C, Patel A, Skweres S, Slaton A, Woods T, Donghia N, Pardee K, Collins JJ, Jewett MC (2018): BioBits™ Bright: A fluorescent synthetic biology education kit. *Sci Adv* **4:** eaat5107.

Stincone A, Prigione A, Cramer T, Wamelink MMC, Campbell K, Cheung E, Olin-Sandoval V, Grüning N-M, Krüger A, Tauqeer Alam M, Keller MA, Breitenbach M, Brindle KM, Rabinowitz JD, Ralser M (2015): The return of metabolism: biochemistry and physiology of the pentose phosphate pathway. *Biol Rev Camb Philos Soc* **90:** 927–963.

Subach OM, Cranfill PJ, Davidson MW, Verkhusha VV (2011): An Enhanced Monomeric Blue Fluorescent Protein with the High Chemical Stability of the Chromophore. *PLoS One* **6:** e28674.

Summers DK (1991): The kinetics of plasmid loss. *Trends Biotechnol* **9:** 273–278.

Sun W, Ding D, Bai D, Lin Y, Zhu Y, Zhang C, Zhang D (2023): Transcriptomics and metabolomics analysis of L-phenylalanine overproduction in *Escherichia coli. Microb Cell Factories* **22:** 65.

Sun-Gu L, Liao JC (2008): Control of Acetate Production Rate in *Escherichia coli* by Regulating Expression of Single-Copy pta Using *lacIQ* in Multicopy Plasmid. *J Microbiol Biotechnol* **18:** 334–337.

Surek D, Stempin S (2014): Technische Strömungsmechanik. Springer Fachmedien, Wiesbaden, Germany.

Surre J, Saint-Ruf C, Collin V, Orenga S, Ramjeet M, Matic I (2018): Strong increase in the autofluorescence of cells signals struggle for survival. *Sci Rep* **8:** 12088.

Swain PS, Elowitz MB, Siggia ED (2002): Intrinsic and extrinsic contributions to stochasticity in gene expression. *Proc Natl Acad Sci USA* **99:** 12795–12800.

Sweere APJ, Luyben, K. Ch. A. M., Kossen NWF (1987): Regime analysis and scaledown: tools to investigate the performance of bioreactors. *Enzyme Microb Technol* **9:** 386–398.

Swings T, van den Bergh B, Wuyts S, Oeyen E, Voordeckers K, Verstrepen KJ, Fauvart M, Verstraeten N, Michiels J (2017): Adaptive tuning of mutation rates allows fast response to lethal stress in *Escherichia coli. eLife* **6:** e22939.

Tabatabaei M, Aghbashlo M, Dehhaghi M, Panahi HKS, Mollahosseini A, Hosseini M, Soufiyan MM (2019): Reactor technologies for biodiesel production and processing: A review. *Prog Energy Combust Sci* **74:** 239–303.

Takors R, Weuster-Botz D (2018): Prozessmodelle. In Chmiel H, Takors R, Weuster-Botz D: Bioprozesstechnik. Springer Spektrum, Berlin, Germany: 71–106.

Tanaka MM, Bergstrom CT, Levin BR (2003): The Evolution of Mutator Genes in Bacterial Populations: The Roles of Environmental Change and Timing. *Genetics* **164:** 843–854.

Teichmann S, Efremova M (2020): Method of the Year 2019: Single-cell multimodal omics. *Nat Methods* **17:** 2020.

Telford WG, Hawley T, Subach F, Verkhusha V, Hawley RG (2012): Flow cytometry of fluorescent proteins. *Methods* **57:** 318–330.

Teng Y-M, Wu K-S (2019): Sustainability Development in Hospitality: The Effect of Perceived Value on Customers' Green Restaurant Behavioral Intention. *Sustainability* **11:** 1987.

Terpe K (2006): Overview of bacterial expression systems for heterologous protein production: from molecular and biochemical fundamentals to commercial systems. *Appl Microbiol Biotechnol* **72:** 211–222.

Thompson BG, Kole M, Gerson DF (1985): Control of Ammonium Concentration in *Escherichia coli* Fermentations. *Biotechnol Bioeng* **27:** 818–824.

Tonin F, Tieves F, Willot S, van Troost A, van Oosten R, Breestraat S, van Pelt S, Alcalde M, Hollmann F (2021): Pilot-Scale Production of Peroxygenase from *Agrocybe aegerita. Org Process Res Dev* **25:** 1414–1418.

Tonouchi N, Ito H (2017): Present Global Situation of Amino Acids in Industry. In Ikeda M, Yokota A: Amino Acid Fermentation. Springer, Tokyo, Japan: 3–14.

Travis JMJ, Travis ER (2002): Mutator dynamics in fluctuating environments. *Proc R Soc B: Biol Sci* **269:** 591–597.

Tripathi NK, Shrivastava A (2019): Recent Developments in Bioprocessing of Recombinant Proteins: Expression Hosts and Process Development. *Front Bioeng Biotechnol* **7:** 420.

Trivedi RN, Vasudeva K (1975): Axial dispersion in laminar flow in helical coils. *Chem Eng Sci* **30:** 317–325.

Trivedi J, Atray N, Agrawal D (2021): Enhanced biomass production of *Scenedesmus obliquus* in a flat-panel photobioreactor, grown in photoautotrophic mode. *Biofuels* **12:** 53–59.

Tsien RY (1998): The green fluorescent protein. *Annu Rev Biochem* **67:** 509–544.

Tsien RY (2009): Constructing and exploiting the fluorescent protein paintbox (Nobel Lecture). *Angew Chem Int Ed* **48:** 5612–5626.

Usmani Z, Sharma M, Awasthi AK, Sivakumar N, Lukk T, Pecoraro L, Thakur VK, Roberts D, Newbold J, Gupta VK (2021): Bioprocessing of waste biomass for sustainable product development and minimizing environmental impact. *Bioresour Technol* **322:** 124548.

Utagawa T (2004): Production of Arginine by Fermentation. *J Nutr* **134:** 2854S–2857S.

van den Bergh B, Fauvart M, Michiels J (2017): Formation, physiology, ecology, evolution and clinical importance of bacterial persisters. *FEMS Microbiol Rev* **41:** 219–251.

van Elsas JD, Semenov AV, Costa R, Trevors JT (2011): Survival of *Escherichia coli* in the environment: fundamental and public health aspects. *ISME J* **5:** 173–183.

van Heeswijk WC, Westerhoff HV, Boogerd FC (2013): Nitrogen Assimilation in *Escherichia coli*: Putting Molecular Data into a Systems Perspective. *Microbiol Mol Biol Rev* **77:** 628–695.

Veal DA, Deere D, Ferrari B, Piper J, Attfield PV (2000): Fluorescence staining and flow cytometry for monitoring microbial cells. *J Immunol Methods* **243:** 191–210.

Vrábel P, van der Lans RGJM, Luyben, Karel Ch. A. M., Boon L, Nienow AW (2000): Mixing in large-scale vessels stirred with multiple radial or radial and axial up-pumping impellers: modelling and measurements. *Chem Eng Sci* **55:** 5881–5896.

Wang L, Jackson WC, Steinbach PA, Tsien RY (2004): Evolution of new nonantibody proteins via iterative somatic hypermutation. *Proc Natl Acad Sci USA* **101:** 16745–16749.

Wang Z, Sun J, Yang Q, Yang J (2020): Metabolic Engineering *Escherichia coli* for the Production of Lycopene. *Molecules* **25:** 3136.

Watkins JJ, McCarty TJ (1995): Polymer/Metal Nanocomposite Synthesis in Supercritical CO_2. *Chem Mater* **7:** 1991–1994.

Watson JD, Crick FH (1953): Molecular structure of nucleic acids. *Nature* **171:** 737–738.

Weber H, Polen T, Heuveling J, Wendisch VF, Hengge R (2005): Genome-wide analysis of the general stress response network in *Escherichia coli*: sigmaS-dependent genes, promoters, and sigma factor selectivity. *J Bacteriol* **187:** 1591–1603.

Wei Y, Lee JM, Smulski DR, LaRossa RA (2001): Global Impact of *sdiA* Amplification Revealed by Comprehensive Gene Expression Profiling of *Escherichia coli*. *J Bacteriol* **183:** 2265–2272.

Wei P, Haringa C, Portela LM, Noorman HJ (2023): Metabolic-fluid dynamics model construction and scale-down design for an industrial penicillin chrysogenum fermentation with combined dissolved oxygen and glucose concentration dynamics. *Chem Eng Sci* **276:** 118770.

Weiner M, Albermann C, Gottlieb K, Sprenger GA, Weuster-Botz D (2014a): Fed-batch production of l-phenylalanine from glycerol and ammonia with recombinant *Escherichia coli*. *Biochem Eng J* **83:** 62–69.

Weiner M, Tröndle J, Albermann C, Sprenger GA, Weuster-Botz D (2014b): Carbon Storage in Recombinant *Escherichia coli* During Growth on Glycerol and Lactic Acid. *Biotechnol Bioeng* **111:** 2508–2519.

Weiner M, Tröndle J, Albermann C, Sprenger GA, Weuster-Botz D (2016): Perturbation Experiments: Approaches for Metabolic Pathway Analysis in Bioreactors. In Bao J, Ye Q, Zhong J-J: Bioreactor Engineering Research and Industrial Applications II. Springer, Berlin Heidelberg, Germany: 91–136.

Weuster-Botz D (2000): Experimental Design for Fermentation Media Development: Statistical Design or Global Random Search? *J Biosci. Bioeng* **90:** 473–483.

Weuster-Botz D, Takors R (2018): Wachstumskinetik. In Chmiel H, Takors R, Weuster-Botz D: Bioprozesstechnik. Springer Spektrum, Berlin, Germany: 45–70.

White CM (1929): Streamline flow through curved pipes. *Proc R Soc A: Math Phys Eng Sci* **123:** 645–663.

Wiacek C, Müller S, Benndorf D (2006): A cytomic approach reveals population heterogeneity of *Cupriavidus necator* in response to harmful phenol concentrations. *Proteomics* **6:** 5983–5994.

Wiedenmann J, Schenk A, Röcker C, Girod A, Spindler K-D, Nienhaus GU (2002): A far-red fluorescent protein with fast maturation and reduced oligomerization tendency

from *Entacmaea quadricolor* (Anthozoa, Actinaria). *Proc Natl Acad Sci USA* **99:** 11646–11651.

Wielgoss S, Barrick JE, Tenaillon O, Wiser MJ, Dittmar WJ, Cruveiller S, Chane-Woon-Ming B, Médigue C, Lenski RE, Schneider D (2013): Mutation rate dynamics in a bacterial population reflect tension between adaptation and genetic load. *Proc Natl Acad Sci USA* **110:** 222–227.

Wilkerson MJ (2012): Principles and applications of flow cytometry and cell sorting in companion animal medicine. *Vet Clin: Small Anim Pract* **42:** 53–71.

Winn M, Casey E, Habimana O, Murphy CD (2014): Characteristics of *Streptomyces griseus* biofilms in continuous flow tubular reactors. *FEMS Microbiol Lett* **352:** 157–164.

Wolf L, Cummings T, Müller K, Reppke M, Volkmar M, Weuster-Botz D (2021): Production of β-carotene with *Dunaliella salina* CCAP19/18 at physically simulated outdoor conditions. *Eng Life Sci* **21:** 115–125.

Wong K-L, Bünzli J-CG, Tanner PA (2020): Quantum yield and brightness. *J Lumin* **224:** 117256.

Woo AC, Faure L, Dapa T, Matic I (2018): Heterogeneity of spontaneous DNA replication errors in single isogenic *Escherichia coli* cells. *Sci Adv* **4:** eaat1608.

Wu Z, Willing B, Bjerketorp J, Jansson JK, Hjort K (2009): Soft inertial microfluidics for high throughput separation of bacteria from human blood cells. *Lab Chip* **9:** 1193–1199.

Xiong L, Du X, Shi B, Bi J, Kleitz F, Qiao SZ (2015): Tunable Stellate Mesoporous Silica Nanoparticles for Intracellular Drug Delivery. *J Mater Chem B* **3:** 1712–1721.

Yang Z, Matsumoto S, Goto H, Matsumoto M, Maeda R (2001): Ultrasonic micromixer for microfluidic systems. *Sens Actuators A: Phys* **93:** 266–272.

Yazdani SS, Gonzalez R (2007): Anaerobic fermentation of glycerol: a path to economic viability for the biofuels industry. *Curr Opin Biotechnol* **18:** 213–219.

Yazdani SS, Gonzalez R (2008): Engineering *Escherichia coli* for the efficient conversion of glycerol to ethanol and co-products. *Metab Eng* **10:** 340–351.

Yee L, Blanch HW (1992): Recombinant protein expression in high cell density fed-batch cultures of *Escherichia coli*. *Nat Biotechnol* **10:** 1550–1556.

You ST, Raman AAA, Shah RSSRE, Mohamad Nor MI (2014): Multiple-impeller stirred vessel studies. *Rev Chem Eng* **30:** 323–336.

Yu JS, Pertusi DA, Adeniran AV, Tyo KEJ (2017): CellSort: a support vector machine tool for optimizing fluorescence-activated cell sorting and reducing experimental effort. *Bioinformatics* **33:** 909–916.

Zhang J, Greasham R (1999): Chemically defined media for commercial fermentations. *Appl Microbiol Biotechnol* **51:** 407–421.

Zhang J, Reddy J, Salmon P, Buckland B, Greasham R (1998a): Process Characterization Studies To Facilitate Validation of a Recombinant Protein Fermentation. In Kelley BD, Ramelmeier RA: Validation of Biopharmaceutical Manufacturing Processes. American Chemical Society, Washington D. C., United States of America: 12–27.

Zhang Y, Buchholz F, Muyrers JP, Stewart AF (1998b): A new logic for DNA engineering using recombination in *Escherichia coli. Nat Genet* **20:** 123–128.

Zhang L, Patel HN, Lappe JW, Wachter RM (2006): Reaction Progress of Chromophore Biogenesis in Green Fluorescent Protein. *J Am Chem Soc* **128:** 4766–4772.

Zhang J, Li F, Yang D (2019): DNA: From Carrier of Genetic Information to Polymeric Materials. *Trans Tianjin Univ* **25:** 301–311.

Zhao D, Yuan S, Xiong B, Sun H, Ye L, Li J, Zhang X, Bi C (2016): Development of a fast and easy method for *Escherichia coli* genome editing with CRISPR/Cas9. *Microb Cell Factories* **15:** 205.

Zhong J-J (2010): Recent advances in bioreactor engineering. *Korean J Chem Eng* **27:** 1035–1041.

Zhu F, Lu L, Fu S, Zhong X, Hu M, Deng Z, Liu T (2015): Targeted engineering and scale up of lycopene overproduction in *Escherichia coli. Process Biochem* **50:** 341–346.

Zhu C, Preissl S, Ren B (2020): Single-cell multimodal omics: the power of many. *Nat Methods* **17:** 11–14.

Ziegler M, Zieringer J, Takors R (2021): Transcriptional profiling of the stringent response mutant strain *E. coli* SR reveals enhanced robustness to large-scale conditions. *Microb Biotechnol* **14:** 993–1010.

Zilberstein D, Agmon V, Schuldiner S, Padan E (1984): *Escherichia coli* Intracellular pH, Membrane Potential, and Cell Growth. *J Bacteriol* **158:** 246–252.

Zlokarnik M (1999): Rührtechnik: Theorie und Praxis. Springer, Berlin Heidelberg, Germany.

Other references:

IGEM 2014: https://2014.igem.org/Safety/Risk_Group_Guide (Last access: 31/08/2023)

Infors AG 2019: Operating manual Labfors 5 (Last access: 29/12/2023)

Supplementary material

A. Supporting data

A.1. Chemicals, enzymes, buffers, consumables and devices

Table A.1: Chemicals used in this work.

Chemical	Article number	Supplier or manufacturer
3-(N-morpholino)propanesulfonic acid (MOPS)	6979.2	Carl Roth GmbH & Co. KG
3-mercaptopropionic acid	63768-25ML	Sigma Aldrich
Acetic acid 60%	LC-10071.2	LabChem Inc.
Acetone $\geq$ 99.8%	9372.1	Carl Roth GmbH & Co. KG
Acetonitrile $\geq$ 99%	200-835-2	Thermo Fisher Scientific Inc.
Agar	6494.3	Carl Roth GmbH & Co. KG
Agarose	2267.5	Carl Roth GmbH & Co. KG
Aluminium chloride hexahydrate	1.010.841.000	Merck KGaA
Ammonia 25%		CLN GmbH
Ammonium sulfate	9218.2	Carl Roth GmbH & Co. KG
Ampicillin sodium salt	K029.2	Carl Roth GmbH & Co. KG
Bicine	9162.1	Carl Roth GmbH & Co. KG
Boric acid	6943.2	Carl Roth GmbH & Co. KG
Calcium chloride dihydrate	5239.1	Carl Roth GmbH & Co. KG
Citric acid monohydrate	SFD1890	Fachdrogerie St. Florian
Cobalt(II) chloride hexahydrate	1.025.390.250	Merck KGaA
Copper(II) chloride dihydrate	CN82.2	Carl Roth GmbH & Co. KG
Diammonium phosphate	LC-10018.1	LabChem Inc.
Dipotassium phosphate	J0320	Honeywell International Inc.
Disodium phosphate	P030.3	Carl Roth GmbH & Co. KG
Ethanol $\geq$ 99.9%	1.009.832.500	Merck KGaA
Ethanol denatured	1004725721001	CLN GmbH

Continued on next page

Table A.1 – continued from previous page

Chemical	Article number	Supplier or manufacturer
Ethylenediaminetetraacetic acid	141026.1211	AppliChem GmbH
Glucose monohydrate	6887.5	Carl Roth GmbH & Co. KG
Glycerol		CLN GmbH
Hydrochloric acid 37%	4625.2	Carl Roth GmbH & Co. KG
Immersion oil	X899.2	Carl Roth GmbH & Co. KG
Iodoacetic acid	I4386-10G	Sigma Aldrich
Iron(II) sulfate heptahydrate	3722.1	Carl Roth GmbH & Co. KG
Iron(III) citrate	9435.2	Carl Roth GmbH & Co. KG
Isopropanol (LC-MS grade)	AE73.2	Carl Roth GmbH & Co. KG
Isopropanol (technical grade)	LC-7339.1	LabChem Inc.
Isopropyl ß-d-1-thiogalacto-pyranoside (IPTG)	CN08.4	Carl Roth GmbH & Co. KG
Kanamycin sulfate	T832.3	Carl Roth GmbH & Co. KG
Lactic acid calcium salt	4071.1	Carl Roth GmbH & Co. KG
L-phenylalanine	1709.2	Carl Roth GmbH & Co. KG
L-tryptophane	T0254-25G	Sigma Aldrich
L-tyrosine	1741.2	Carl Roth GmbH & Co. KG
Magnesium chloride	KK36.2	Carl Roth GmbH & Co. KG
Magnesium sulfate heptahydrate	T888.2	Carl Roth GmbH & Co. KG
Malic acid	112577-100G	Sigma Aldrich
Manganese(II) chloride tetra-hydrate	A2087,1000	AppliChem GmbH
Manganese(II) sulfate mono-hydrate	4.487	Carl Roth GmbH & Co. KG
Methanol	P717.1	Carl Roth GmbH & Co. KG
Monopotassium phosphate	3904.1	Carl Roth GmbH & Co. KG
Monosodium phosphate monohydrate	K300.3	Carl Roth GmbH & Co. KG
ortho-phtalaldehyde	5980.1	Carl Roth GmbH & Co. KG
Peptone caseine	61B87AD1	neoFroxx GmbH
Phosphoric acid $\geq 85\%$	LC-7052.2	LabChem Inc.
Potassium acetate	T874.3	Carl Roth GmbH & Co. KG
Potassium chloride	6781.1	Carl Roth GmbH & Co. KG
Potassium hydroxide $\geq 85\%$	221473-2.5KG	Sigma Aldrich
Rubidium chloride	4471.1	Carl Roth GmbH & Co. KG

Table A.1 – continued from previous page

Chemical	Article number	Supplier or manufacturer
Sodium acetate	6773.2	Carl Roth GmbH & Co. KG
Sodium hydroxide	6771.1	Carl Roth GmbH & Co. KG
Sodium L-glutamate mono-hydrate	1.06445-1000	Merck KGaA
Sodium molybdate dihydrate	274.2	Carl Roth GmbH & Co. KG
Succinic acid	2725.2	Carl Roth GmbH & Co. KG
Sulfuric acid $\geq 95\%$	231-598-3	Thermo Fisher Scientific Inc.
Trisodium citrate dihydrate	102289386	Sigma Aldrich
Vitamin B12	V2876-1G	Sigma Aldrich
Water (DEPC treated, sterile, nuclease-free, autoclaved)	T143	Carl Roth GmbH & Co. KG
Yeast extract	253.3	Ohly GmbH
Zinc acetate dihydrate	P035.1	Carl Roth GmbH & Co. KG
Zinc sulfate heptahydrate	1.088.830.500	Merck KGaA

Table A.2: Enzymes, buffers and kits used in this work.

Enzymes, buffers or kits	Article number	Supplier or manufacturer
Ammonia assay	11112732035	R-Biopharm AG
Antifoam AF 204	A6426-500G	Sigma Aldrich
Buffer pH 4	20062.1000PE	CLN GmbH
Buffer pH 7	10315026	Honeywell International Inc.
Buffer pH 9	LC-4695.3	LabChem Inc.
CutSmart buffer (10x)	B7204S	New England Biolabs
dNTP mix (10 mM each)	N0447S	New England Biolabs
DpnI (20 000 U mL^{-1})	R0176S	New England Biolabs
FastGene® Optima Hotstart with loading dye (2x)	212110	Nippon Genetics Europe GmbH
HiFi DNA assembly master mix (2x)	M5520A	New England Biolabs
HindIII HF (20 000 U mL^{-1})	R3104S	New England Biolabs
Loading dye without SDS (6x)	B7025S	New England Biolabs
Midori green	MG04	Nippon Genetics Europe GmbH
Monarch® DNA gel extraction kit	T1020L	New England Biolabs

Table A.2 – continued from previous page

Enzymes, buffers or kits	Article number	Supplier or manufacturer
Monarch® PCR & DNA cleanup kit	T1030L	New England Biolabs
OneTaq (5000 U mL^{-1})	M0480S	New England Biolabs
OneTaq master mix with standard buffer (2x)	M0482S	New England Biolabs
Q5 polymerase (2 000 U mL^{-1})	M0480S	New England Biolabs
Q5 reaction buffer (5x)	B9027S	New England Biolabs
QIAprep spin miniprep kit	27104	Qiagen
Quick-Load® 1 kb extend DNA ladder	N3239S	New England Biolabs
rCutSmart buffer (10x)	B6004S	New England Biolabs
RNAse A (151.5 U mg^{-1})	A2760,0100	AppliChem GmbH
Rotiphorese® TAE buffer (10x)	T845.2	Carl Roth GmbH & Co. KG
T4 DNA ligase (400 000 U mL^{-1})	M0202S	New England Biolabs
T4 DNA ligase buffer (10x)	B0202S	New England Biolabs

Table A.3: Disposables used in this work.

Vessels and disposables	Specification	Supplier or manufacturer
Autoclave tape	Steriking®	Wipak oy
Beaker	Different sizes	Schott AG
		Thermo Fisher Scientific Inc.
		Kavalierglass a.s.
Bottle-top filter	Steritop® 45 mm neck-size, millipore express®, 0.22 µm	Merck KGaA
Cable ties	Different sizes	Carl Roth GmbH & Co. KG
Cell spreader	L-shaped, sterile	VWR International
Centrifuge tubes	CellStar™ tubes, PP, conical bottom, different sizes	Greiner Bio-One
Check valve	-	B. Braun SE
Cover glass	21x26 mm	Carl Roth GmbH & Co. KG
Crimp caps with bore hole	ND20 septum, Butyl/PTFE	Carl Roth GmbH & Co. KG

Table A.3 – continued from previous page

Vessels and disposables	Specification	Supplier or manufacturer
Crimp caps with bore hole	N11 silver, centerhole, NR/Butyl/TEF	Macherey Nagel
Crimp neck vials	ND20, flat bottom	Carl Roth GmbH & Co. KG
Cultivation tubes	100x16 mm, PP, sterile	Sarstedt AG & Co. KG
Cuvettes	10x10x45, semi-micro	Greiner Bio-One
Electroporation cuvette	1 mm gap	Biozym Biotech Trading GmbH
Erlenmeyer flask	Different sizes	Schott AG
		VWR International
Examination gloves	Nitril® NextGen®	Meditrade UK Ltd
Filter	Chromafil® PET 20/25, 0.2 µm	Macherey Nagel
	Chromafil® RC-20/15 MS, 0.2 µm	Macherey Nagel
Filter tips	TipOne®, different sizes	Starlab GmbH
Glass pasteur pipettes	7477 15	Brand GmbH & Co. KG
Graduated cylinder	Different sizes	Kavalierglass a.s.
		Brand GmbH & Co. KG
Hose barb valved coupling body	Male plug, PP, different sizes	Colder Products Company
	Female plug, PP, different sizes	Colder Products Company
Inoculation membrane	19 mm	Infors HT
Laboratory bottles	Round, different sizes	Schott AG
		VWR International
		Kavalierglass a.s.
Laboratory screw joins	GL14, 6 mm	Carl Roth GmbH & Co. KG
Luer connector	Male plug, different sizes	neoLab Migge GmbH
	Female plug, different sizes	neoLab Migge GmbH
Measuring beaker	Differenz sizes	VITLAB GmbH
Membrane valve	Safeflow	B. Braun SE
Microfiber wipes	Kimtech® Science, 7558	Kimberly-Clark Corporation
	Kimtech® Science, 05511	Kimberly-Clark Corporation
Microscopy slide	76x26 mm, pre-cleaned	R. Langenbrinck GmbH

Table A.3 – continued from previous page

Vessels and disposables	Specification	Supplier or manufacturer
Microreaction tube	Round-bottom, 2 mL	Eppendorf SE
	Conical-bottom, safe-lock, 1.5 mL	Eppendorf SE
Microtiter plate	96-well, flat-bottom	Thermo Fisher Scientific Inc.
Multiple distributor for bottle	GL45, PP	Carl Roth GmbH & Co. KG
Parafilm	PM-996	Bemis
PCR cap	0.2 mL, flat-cap	Starlab GmbH
PCR tube	0.2 mL, thinwalled	Eppendorf SE
Petri dish	94x16 mm with vents	Greiner Bio-One
Pipette tip	Different sizes	Brand GmbH & Co. KG
Pouring ring	GL45	Schott AG
PTFE sealing tape	12x12x0.1 mm	Landefeld Druckluft und Hydraulik GmbH
Pumping tube	Masterflex®, Norprene® L/S 16®	Cole-Parmer Instrument Company LTD
Round-bottom tubes	Polystyrene, 12x75 mm	Corning Inc.
Rubber pipette bulb	-	neoLab Migge GmbH
Screw cap	GL45	Schott AG
Shake flask	Duran®, different sizes	Schott AG
Silicone tube	3x6 mm	neoLab Migge GmbH
	4x8 mm	neoLab Migge GmbH
Sterilisation container	Steriset®	WAGNER GmbH
Stirrer bar	Different sizes	Cowie Technology Group Ltd.
Syringe	Different sizes	B. Braun SE
Syringe filter	Minisart®, NML, 0.2 µm	Sartorius AG
Syringe needle	Sterican®, different sizes	B. Braun SE
T piece	TS6	Norma Group
Three-way valve	LF-KHTC3/14L	db-shop 24
Volumetric flask	Different sizes	Schott AG
		Brand GmbH & Co. KG
Weighing boats	Different sizes	Heathrow Scientific
		neoLab Migge GmbH
Y piece	Rotilabo®, PP	Carl Roth GmbH & Co. KG

Table A.4: Devices used in this work.

Device	Specification	Supplier or manufacturer
3D printer	i3 MK3	Prusa Research a.s.
ÄKTApilot™	1474726	GE Healthcare Technologies Inc.
Autoclave	Varioklav® 500 EC-Z	HP Labortechnik GmbH
	VX-150	Systemc GmbH & Co. KG
Balance	Explorer™ E1 M212	OHAUS Europe GmbH
Benchtop centrifuge	Mikro 20	Andreas Hettich GmbH & Co. KG
	5424R	Eppendorf SE
Centrifuge	Rotixa 50 RS	Andreas Hettich GmbH & Co. KG
Clean bench	BDK Klasse 1	Luft- und Reinraumtechnik GmbH
Cooling chamber		FRIESS-TECHNIK Friess GmbH
Drying and heating chamber	Model E 28	Binder GmbH
Drying chamber	Model FD240-230V	Binder GmbH
	UN 260	Memmert GmbH
Electroporator	Gene pulser Xcell™	Bio-Rad Laboratories Inc.
Flow cytometer	FACSMelody™	Becton Dickinson
Fridge	GSS22E420	Siemens
	GS29	Siemens
	freezer	Bosch
	Ultralow temperature freezer, MDF-193	Sanyo
	Premium biofresh	Liebherr-Hausgeräte GmbH
Fume hood	Variolab Mobilien W90	Waldner Laboreinrichtungen GmbH & Co. KG
High performance liquid chromatography	Smartline	Knauer Wissenschaftliche Geräte GmbH
	Prominence-i LC-2030C Plus	Shimadzu
Ice flake machine	AF 80	Scotsterm

Table A.4 – continued from previous page

Device	Specification	Supplier or manufacturer
Imaging chamber	Intas Gel iX Imager	Intas Science Imaging Instruments GmbH
Induction plate	Ambiano	Amazon.com Inc.
Magnetic stirrer plate	Electronicrührer Monotherm	Variomag USA
	D-6010	neoLab Migge GmbH
Microcentrifuge	PerfectSpin mini	PEQLAB Biotechnologie GmbH
Microplate reader	Infinite® M200	Tecan Group
Microscope	Axiolab drb KT, lense: ACHROPLAN 100x/1.25 oil	Carl Zeiss AG
Microwave	MW781	Clatronic
Nanodrop	Nanophotometer® N120	Implen GmbH
Orbital shaker	Multitron	Infors HT
Peristaltic pump	BVP ISM 444	Ismatec SA
	Masterflex® Model 07525- 40	Cole-Parmer
Power supply	peqPOWER 300	PEQLAB Biotechnologie GmbH
	Power source 300V	VWR International
Precision balance	Explorer$^{\text{TM}}$ E12145	OHAUS Europe GmbH
	ADB 200.4	KERN & SOHN GmbH
	XA204 DeltaRange®	Mettler Toledo
Spectrophotometer	Genesys$^{\text{TM}}$ 10S-UV-Vis	Thermo Fisher Scientific Inc.
Thermocycler	Labcycler 48	SensoQuest GmbH
Thermoshaker	Thermomixer comfort	Eppendorf SE
Ultrasonic bath	Model USC 2100	VWR International
	Sonorex Super RK 510 H	Reichmann Industrieservice
Viscosimeter	Rheolab QC	Anton Paar GmbH
Vortexer	D-0612	neoLab Migge GmbH
	Model 7-2020	neoLab Migge GmbH
Water bath	Model ME	Julabo GmbH

Table A.5: Equipment of the 3.6 L stirred-tank bioreactor (Labfors 5, Infors HT).

Component	Specification	Supplier or manufacturer
DO electrode	VisiFerm DO Arc 325 H0	Hamilton Bonaduz AG
Inlet filter	Acro® 50 with 0.2 µm, Emflon™	Pall Corporation
Off-gas sensor	BlueVary	BlueSens gas sensor GmbH
Outlet filter	Acro® 50 with 0.2 µm, PTFE	Pall Corporation
	AcroPak™ 300, PTFE membrane	Pall Corporation
pH electrode	EasyFerm Plus PHI Arc 325	Hamilton Bonaduz AG
Software Labfors 5 station	iMC-Board controller version 2.04 LAF5	Infors HT
	Touchfors version 3.3.1.0	Infors HT

Table A.6: Equipment of the coiled flow inverter.

Component	Specification	Supplier or manufacturer
Braided silicone tubing	6x12 mm	Landefeld Druckluft und Hydraulik GmbH
Double pipe socket	3D printed	-
Hollow spacer cylinder	3D printed	-
Hose clamp brackets	6-way, 11.6 mm	Landefeld Druckluft und Hydraulik GmbH
Mounting foot	3D printed	-
PVC pipe	110 mm	Landefeld Druckluft und Hydraulik GmbH
PVC plate	495x495 mm	nattmann GmbH
Threaded rod	M10	-

Table A.7: Equipment of the flow cytometer (FACSMelody™, Becton Dickinson).

Component	Specification	Supplier or manufacturer
Accudrop beads	345249	Becton Dickinson
CS&T beads	661414	Becton Dickinson
Rinse solution	FACSRinse™	Becton Dickinson
Sheath fluid	FACSFlow™	Becton Dickinson
Sorting nozzle	Nozzle Assy 10 µm, square cuvette aligned	Becton Dickinson
Software operation	FACSChorus™	Becton Dickinson
Software post-analysis	FCSExpress™ version 7.18.0015	De Novo Software

Table A.8: Equipment of the high performance liquid chromatography (Smartline, Knauer Wissenschaftliche Geräte GmbH).

Component	Specification	Supplier or manufacturer
Autosampler	Midas Model 3900	Spark Holland B.V.
Column	Gemini 5 µm, C18, 110 Å	Phenomenex Inc.
Fluorescence detector	RF-20 A	Shimadzu
Oven	Jetstream Plus	JASCO Inc.
Precolumn	SecurityGuard™ AJ0-7597	Phenomenex Inc.
Precolumn cartridge kit	SecurityGuard™ KJ0-4282	Phenomenex Inc.
Sampling needle	AST 101.367	Techlab GmbH
Syringe	AST 103.664	Techlab GmbH
Software	ChromGate® version 3.1	Knauer Wissenschaftliche Geräte GmbH

Table A.9: Equipment of the high performance liquid chromatography (Prominence-i LC-2030C Plus, Shimadzu).

Component	Specification	Supplier or manufacturer
Column	Aminex HPX-87H	Bio-Rad Laboratories Inc.
Precolumn	Micro-Guard Cation H+ Cartridges	Bio-Rad Laboratories Inc.
Refractive index detector	RID-20A	Shimadzu
Software	LabSolutions version 5.98	Bio-Rad Laboratories Inc.

Table A.10: Equipment of the viscosimeter (Rheolab QC, Anton Paar GmbH).

Component	Specification	Supplier or manufacturer
Standard measuring system	DG42/SS/QC-LTD	Anton Paar GmbH
Temperature control system	G-LTD80/QC	Anton Paar GmbH
Water bath	rheotherm 115	Contraves
Software	Rheoplus I32 version 3.62	Anton Paar GmbH

Table A.11: Equipment for the preparation of agarose gels.

Component	Specification	Supplier or manufacturer
Chamber	MGU-402T	CBS Scientific
Empty gel cassette combs	23-well, 1.5 mm, MBU-1518	CBS Scientific
Handcast station	GCT-10-111	CBS Scientific

Table A.12: Equipment of the imaging chamber (Intas Gel iX Imager, Intas Science Imaging Instruments GmbH).

Component	Specification	Supplier or manufacturer
Camera	EOS 80D	Canon
LED light pad	Model A5	reflecta GmbH
Software operation	EOS utility version 3	Canon
Software post-analysis	Digital photo professional version 4	Canon

A.2. L-tyrosine data

Table A.13: L-tyrosine (L-tyr) concentration during the L-phenylalanine production processes in a 3.6 L stirred-tank bioreactor (STB) or two-compartment bioreactor (TCB) with the *Escherichia coli* quadruple reporter strain as a fed-batch cultivation. Two-compartment bioreactor cultivations were conducted with either short (TCB$_S$), medium (TCB$_M$) or long (TCB$_L$) mean hydraulic residence times of 102.63 s (4.71 mL s^{-1}), 199.50 s (2.36 mL s^{-1}) or 403.30 s (1.18 mL s^{-1}) in the bypass. Phase 1 resembles the initial batch phase, phase 2 the biomass production phase and phase 3 the final product formation phase.

STB		TCB$_S$		TCB$_M$		TCB$_L$	
L-tyr, g L^{-1}	Process time, h	L-tyr, g L^{-1}	Process time, h	L-tyr, g L^{-1}	Process time, h	L-tyr, g L^{-1}	Process time, h
Phase 1							
0.0	0.07	0.0	0.05	0.0	0.03	0.0	0.05
14.0	0.01	12.0	0.02	13.8	0.00	13.8	0.01
		13.7	0.01				
Phase 2							
15.3	0.00	14.6	0.00	17.6	0.00	16.2	0.00
18.3	0.04	17.6	0.05	20.6	0.03	19.2	0.03
21.3	0.09	20.6	0.10	23.6	0.09	22.2	0.11
24.7	0.15	23.6	0.16	26.6	0.16	25.2	0.16
27.9	0.13	25.4	0.17	37.8	0.20	34.2	0.22
38.0	0.17	34.7	0.18	39.8	0.19	36.3	0.20
		36.7	0.19			38.3	0.19
Phase 3							
39.9	0.11	37.8	0.18	40.6	0.18	39.1	0.16
40.9	0.20	38.8	0.17	41.6	0.16	40.1	0.14
43.3	0.11	40.8	0.11	43.6	0.12	42.1	0.10
45.9	0.05	43.8	0.07	46.6	0.05	45.1	0.04
51.9	0.00	45.3	0.02	48.1	0.00	46.6	0.00
62.1	0.00	59.4	0.00	61.3	0.00	60.8	0.00
64.9	0.00	62.4	0.00	64.3	0.00	63.8	0.00
67.9	0.00	65.4	0.00	67.3	0.00	66.8	0.00
70.9	0.00	68.4	0.00	70.3	0.00	69.8	0.00
75.3	0.00	70.4	0.00	72.3	0.00	71.8	0.00
87.3	0.00	75.4	0.00	86.0	0.00	85.5	0.00
89.1	0.00	84.1	0.00	89.0	0.00	88.5	0.00
89.9	0.00	87.1	0.00	92.0	0.00	91.5	0.00
		90.1	0.00	94.0	0.00	95.5	0.00
		92.1	0.00	96.0	0.00	109.5	0.00
		94.1	0.00	110.0	0.00	113.5	0.00
				111.0	0.00	117.5	0.00
						121.5	0.00
						135.5	0.00
						136.5	0.00

A.3. Integral carbon balances

Table A.14: Integral carbon balance of the L-phenylalanine production process in a 3.6 L stirred-tank bioreactor with the *Escherichia coli* quadruple reporter strain as a fed-batch cultivation. The biomass production phase started at 15.3 h, whereas the product formation phase was initiated at 39.9 h. By-products include acetate, ethanol, malate, lactate and succinate. Other amino acids (AA) include L-tyrosine, L-tryptophane and L-glutamate. L-phe represents L-phenylalanine, whereas carbon dioxide is abbreviated with CO_2.

Process time, h	Biomass, mol%	Glycerol, mol%	Citrate, mol%	L-phe, mol%	Other AA, mol%	By-products, mol%	CO_2, mol%	Sum, mol%
0.0	5.4	71.7	14.6	2.6	2.0	2.2	0.0	98.5
14.0	29.9	16.7	14.9	1.8	0.9	2.8	29.1	96.0
15.3	42.0	0.6	14.8	1.5	0.3	2.8	36.4	98.4
18.3	43.7	0.4	9.5	1.0	1.1	1.9	38.0	95.6
21.3	40.8	0.2	6.4	1.3	1.8	1.6	39.6	91.7
24.7	43.3	0.2	4.7	1.4	1.5	1.1	42.0	94.2
27.9	41.2	0.2	3.0	0.7	1.1	0.9	48.6	95.6
38.0	37.0	0.1	0.8	0.2	0.6	0.6	61.5	100.7
39.9	35.1	0.1	1.6	0.2	0.6	0.5	64.8	102.7
40.9	34.3	0.1	1.3	0.3	0.6	0.6	66.2	103.4
43.3	34.0	0.1	0.9	0.8	0.5	0.5	67.5	104.3
45.9	32.1	0.0	0.7	1.7	0.4	0.5	68.0	103.4
51.9	29.1	0.0	0.4	6.3	0.3	0.4	67.7	104.2
62.1	23.7	0.1	0.3	13.4	0.3	0.4	67.0	105.0
64.9	22.6	0.1	0.3	13.5	0.2	0.2	66.9	103.9
67.9	21.1	0.1	0.2	15.4	0.3	0.2	67.0	104.1
70.9	19.7	0.1	0.2	14.4	0.2	0.3	67.2	102.1
75.3	18.5	0.1	0.3	14.9	0.2	0.7	67.5	102.2
87.3	15.9	0.2	0.3	13.8	0.3	3.9	67.4	101.7
89.1	15.0	0.3	0.3	13.5	0.3	5.2	66.8	101.4
89.9	14.9	0.4	0.3	13.0	0.3	5.6	66.6	101.1

Table A.15: Integral carbon balance of the L-phenylalanine production process in a two-compartment bioreactor with the *Escherichia coli* quadruple reporter strain as a fed-batch cultivation. The mean hydraulic residence time in the bypass was set to 102.63 s (4.71 mL s^{-1}). The biomass production phase started at 14.6 h, whereas the product formation phase was initiated at 37.8 h. By-products include acetate, ethanol, malate, lactate and succinate. Other amino acids (AA) include L-tyrosine, L-tryptophane and L-glutamate. L-phe represents L-phenylalanine, whereas carbon dioxide is abbreviated with CO_2.

Process time, h	Biomass, mol%	Glycerol, mol%	Citrate, mol%	L-phe, mol%	Other AA, mol%	By-products, mol%	CO_2, mol%	Sum, mol%
0.0	1.2	75.8	14.8	3.2	1.6	1.7	0.0	98.2
12.0	16.8	34.4	14.9	3.8	0.6	1.9	21.8	94.1
13.7	28.2	11.6	14.7	4.1	0.4	2.0	33.6	94.5
14.6	38.0	0.3	14.8	4.1	0.0	1.9	41.0	100.1
17.6	36.5	0.2	9.8	4.1	1.4	1.6	45.2	98.9
20.6	39.4	0.2	7.0	4.2	1.7	1.3	49.2	102.8
23.6	40.1	0.2	5.2	4.3	2.1	1.0	53.3	106.3
25.4	38.1	0.1	3.6	3.8	2.5	1.4	54.5	104.0
34.7	38.3	0.1	1.0	2.3	0.9	0.8	63.0	106.4
36.7	38.6	0.1	0.8	2.0	0.9	0.6	64.8	107.8
37.8	37.7	0.1	2.2	2.0	0.9	0.7	66.1	109.7
38.8	37.3	0.1	1.9	2.1	0.9	0.7	66.1	109.3
40.8	36.5	0.0	1.5	2.2	0.7	0.7	66.3	107.9
43.8	34.0	0.0	1.3	3.7	0.4	0.6	67.1	107.1
45.3	33.6	0.0	1.2	4.9	0.3	0.5	66.7	107.2
59.4	25.9	0.0	0.8	15.4	0.1	0.3	66.5	109.0
62.4	24.6	0.0	0.7	16.7	0.1	0.3	66.8	109.3
65.4	23.1	0.0	0.7	17.1	0.2	0.3	67.2	108.6
68.4	22.4	0.1	0.7	18.3	0.1	0.4	67.5	109.5
70.4	21.6	0.1	0.6	18.5	0.1	0.6	67.8	109.3
75.4	19.3	0.1	0.5	18.7	0.3	0.8	68.6	108.2
84.1	17.1	0.1	0.5	19.4	0.2	1.8	69.2	108.2
87.1	17.6	0.1	0.5	18.2	0.2	3.3	68.8	108.7
90.1	16.7	0.1	0.5	17.7	0.2	4.7	68.1	108.0
92.1	16.1	0.1	0.5	16.7	0.3	5.9	67.6	107.1
94.1	15.9	0.1	0.5	16.4	0.3	7.1	66.9	107.2

Table A.16: Integral carbon balance of the L-phenylalanine production process in a two-compartment bioreactor with the *Escherichia coli* quadruple reporter strain as a fed-batch cultivation. The mean hydraulic residence time in the bypass was set to 199.50 s (2.36 mL s^{-1}). The biomass production phase started at 17.6 h, whereas the product formation phase was initiated at 40.6 h. By-products include acetate, ethanol, malate, lactate and succinate. Other amino acids (AA) include L-tyrosine, L-tryptophane and L-glutamate. L-phe represents L-phenylalanine, whereas carbon dioxide is abbreviated with CO_2.

Process time, h	Biomass, mol%	Glycerol, mol%	Citrate, mol%	L-phe, mol%	Other AA, mol%	By-products, mol%	CO_2, mol%	Sum, mol%
0.0	0.0	92.4	0.0	2.8	1.0	2.2	0.0	98.3
13.8	26.0	52.1	0.0	2.5	0.0	1.9	24.3	105.9
17.6	45.2	0.0	0.0	2.4	0.0	2.6	54.6	104.7
20.6	40.8	0.0	0.0	2.3	0.7	1.5	55.1	100.4
23.6	42.3	0.2	0.0	2.5	1.6	1.0	58.2	105.8
26.6	43.2	0.1	0.0	2.6	2.1	1.0	62.4	111.4
37.8	37.0	0.1	0.0	0.9	1.1	0.5	67.5	107.1
39.8	35.9	0.1	0.0	0.8	0.9	0.9	67.6	106.2
40.6	35.8	0.1	0.0	0.8	1.0	0.5	68.9	107.0
41.6	36.2	0.0	0.0	0.7	0.9	0.5	69.3	107.6
43.6	35.0	0.0	0.0	0.8	0.9	0.4	69.8	106.9
46.6	35.1	0.0	0.0	1.0	0.5	0.3	70.9	107.8
48.1	33.1	0.0	0.0	1.4	0.8	0.5	71.3	107.1
61.3	30.8	0.1	0.0	6.8	0.2	0.4	72.3	110.5
64.3	27.3	0.1	0.1	7.8	0.2	0.5	72.6	108.6
67.3	25.2	0.1	0.1	8.9	0.4	0.6	72.7	107.9
70.3	25.3	0.1	0.1	10.0	0.3	0.6	72.7	109.0
72.3	24.9	0.1	0.1	10.9	0.3	0.6	72.6	109.4
86.0	20.7	0.1	0.2	15.7	0.5	1.8	71.7	110.5
89.0	20.1	0.2	0.2	13.7	0.6	2.7	71.3	108.7
92.0	19.3	0.2	0.2	13.6	0.5	3.7	70.6	108.0
94.0	18.7	0.2	0.1	13.4	0.6	4.3	70.1	107.5
96.0	18.3	0.2	0.1	13.3	0.7	5.0	69.5	107.1
110.0	14.3	0.2	0.0	10.8	1.0	11.9	64.6	102.9
111.0	15.0	0.2	0.0	10.7	1.0	12.3	64.2	103.4

Table A.17: Integral carbon balance of the L-phenylalanine production process in a two-compartment bioreactor with the *Escherichia coli* quadruple reporter strain as a fed-batch cultivation. The mean hydraulic residence time in the bypass was set to 403.30 s (1.18 mL s^{-1}). The biomass production phase started at 16.2 h, whereas the product formation phase was initiated at 39.1 h. By-products include acetate, ethanol, malate, lactate and succinate. Other amino acids (AA) include L-tyrosine, L-tryptophane and L-glutamate. L-phe represents L-phenylalanine, whereas carbon dioxide is abbreviated with CO_2.

Process time, h	Biomass, mol%	Glycerol, mol%	Citrate, mol%	L-phe, mol%	Other AA, mol%	By-products, mol%	CO_2, mol%	Sum, mol%
0.0	0.0	78.5	15.0	2.9	1.4	0.6	0.0	98.4
13.8	26.4	29.5	15.4	2.1	0.2	2.1	27.8	103.5
16.2	36.2	0.2	15.6	1.8	0.0	1.0	46.0	100.9
19.2	39.3	0.1	10.1	1.7	0.8	0.7	49.1	101.7
22.2	39.5	0.1	7.0	1.9	1.6	0.5	54.1	104.8
25.2	36.9	0.1	5.2	1.8	1.8	0.4	58.8	105.0
34.2	25.8	0.8	1.3	0.7	1.2	4.4	59.6	93.8
36.3	30.3	0.9	1.0	0.5	0.8	2.1	61.4	97.0
38.3	31.3	0.2	0.6	0.4	0.8	0.9	63.4	97.6
39.1	32.2	0.2	1.7	0.3	0.8	0.6	62.8	98.6
40.1	32.2	0.2	1.4	0.4	0.8	0.5	64.0	99.5
42.1	32.2	0.1	0.9	0.6	0.7	0.4	65.9	100.8
45.1	31.9	0.1	0.5	1.1	0.4	0.3	67.8	102.1
46.6	31.4	0.1	0.4	1.8	0.4	0.3	68.4	102.9
60.8	24.7	0.1	0.1	8.8	0.1	0.3	71.3	105.4
63.8	24.2	0.1	0.3	10.0	0.1	0.3	71.9	106.9
66.8	22.8	0.1	0.3	10.5	0.1	0.3	72.5	106.7
69.8	22.2	0.1	0.4	12.0	0.2	0.3	73.0	108.1
71.8	22.1	0.1	0.4	11.8	0.2	0.3	73.2	108.1
85.5	20.4	0.1	0.4	14.0	0.2	0.3	74.5	109.8
88.5	20.5	0.1	0.4	14.9	0.2	0.4	74.7	111.1
91.5	19.3	0.1	0.4	15.0	0.3	0.4	74.9	110.4
95.5	20.6	0.1	0.4	14.7	0.2	0.6	75.1	111.6
109.5	22.2	0.1	0.3	12.8	0.2	0.7	76.2	112.4
113.5	20.8	0.1	0.3	12.0	0.2	0.7	76.6	110.7
117.5	20.8	0.1	0.2	11.4	0.1	1.5	77.0	111.1
121.5	20.2	0.1	0.3	10.8	0.1	2.0	77.3	110.9
135.5	19.7	0.5	0.3	8.1	0.1	4.3	76.8	109.7
136.5	19.9	0.8	0.3	7.7	0.1	5.0	76.6	110.3

A.4. Mean-to-median ratios and coefficient of variances

Table A.18: Mean-to-median ratios (MMR) of the expressed fluorescence intensities at 448/45 nm (general stress response), 527/32 nm (growth behaviour), 586/42 nm (oxygen limitation) and 660/10 nm (product formation) during the L-phenylalanine production process in a stirred-tank bioreactor with the *Escherichia coli* quadruple reporter strain. The biomass production phase started at 15.3 h, whereas the product formation phase was initiated at 39.9 h.

Process time, h	MMR 448/45 nm, -	MMR 527/32 nm, -	MMR 586/42 nm, -	MMR 660/10 nm, -
14.0	1.61 ± 0.04	1.35 ± 0.01	1.49 ± 0.01	2.74 ± 0.04
15.3	1.68 ± 0.02	1.37 ± 0.01	1.54 ± 0.02	2.92 ± 0.02
18.3	1.30 ± 0.01	1.30 ± 0.01	1.32 ± 0.00	2.27 ± 0.01
21.3	1.29 ± 0.00	1.37 ± 0.01	1.32 ± 0.00	2.39 ± 0.02
24.7	1.19 ± 0.01	1.28 ± 0.01	1.24 ± 0.00	2.02 ± 0.01
27.9	1.15 ± 0.00	1.23 ± 0.00	1.22 ± 0.01	2.02 ± 0.03
38.0	1.11 ± 0.00	1.18 ± 0.00	1.19 ± 0.00	1.89 ± 0.00
39.9	1.08 ± 0.00	1.15 ± 0.00	1.18 ± 0.01	1.68 ± 0.00
40.9	1.11 ± 0.00	1.17 ± 0.00	1.23 ± 0.01	1.68 ± 0.01
43.3	1.08 ± 0.00	1.14 ± 0.00	1.18 ± 0.00	1.41 ± 0.01
45.9	1.09 ± 0.00	1.12 ± 0.00	1.13 ± 0.00	1.19 ± 0.00
51.9	1.32 ± 0.02	1.10 ± 0.00	1.12 ± 0.00	1.05 ± 0.00
62.1	1.49 ± 0.02	1.10 ± 0.00	1.13 ± 0.01	1.07 ± 0.00
64.9	1.44 ± 0.01	1.12 ± 0.01	1.11 ± 0.00	1.10 ± 0.00
67.9	1.50 ± 0.01	1.13 ± 0.01	1.11 ± 0.00	1.11 ± 0.00
70.9	1.49 ± 0.00	1.12 ± 0.00	1.11 ± 0.00	1.12 ± 0.01
75.3	1.52 ± 0.01	1.14 ± 0.00	1.15 ± 0.02	1.16 ± 0.00
87.3	1.77 ± 0.02	1.13 ± 0.00	1.18 ± 0.01	1.11 ± 0.00
89.1	1.68 ± 0.01	1.14 ± 0.00	1.23 ± 0.02	1.13 ± 0.01
89.9	1.72 ± 0.07	1.13 ± 0.01	1.24 ± 0.00	1.12 ± 0.02

Table A.19: Coefficient of variances (CV) of the expressed fluorescence intensities at 448/45 nm (general stress response), 527/32 nm (growth behaviour), 586/42 nm (oxygen limitation) and 660/10 nm (product formation) during the L-phenylalanine production process in a stirred-tank bioreactor with the *Escherichia coli* quadruple reporter strain. The biomass production phase started at 15.3 h, whereas the product formation phase was initiated at 39.9 h.

Process time, h	CV 448/45 nm, -	CV 527/32 nm, -	CV 586/42 nm, -	CV 660/10 nm, -
14.0	2.01 ± 0.67	1.22 ± 0.05	1.73 ± 0.07	2.14 ± 0.11
15.3	2.21 ± 0.61	1.44 ± 0.21	2.22 ± 0.43	2.09 ± 0.05
18.3	1.21 ± 0.04	1.12 ± 0.02	1.49 ± 0.02	1.92 ± 0.01
21.3	1.55 ± 0.67	3.13 ± 3.03	1.54 ± 0.09	1.87 ± 0.08
24.7	1.17 ± 0.02	1.18 ± 0.04	1.23 ± 0.01	1.44 ± 0.01
27.9	1.00 ± 0.02	1.02 ± 0.05	1.12 ± 0.02	1.37 ± 0.02
38.0	0.84 ± 0.07	0.90 ± 0.11	1.06 ± 0.09	1.14 ± 0.01
39.9	0.71 ± 0.01	0.81 ± 0.17	0.97 ± 0.09	1.02 ± 0.01
40.9	1.13 ± 0.34	1.24 ± 0.47	1.83 ± 0.71	1.10 ± 0.02
43.3	0.63 ± 0.01	0.71 ± 0.05	1.10 ± 0.17	1.00 ± 0.01
45.9	0.66 ± 0.00	0.62 ± 0.02	0.87 ± 0.02	0.77 ± 0.00
51.9	0.88 ± 0.11	0.61 ± 0.02	0.96 ± 0.16	0.61 ± 0.00
62.1	1.34 ± 0.43	1.16 ± 0.48	1.69 ± 0.66	0.67 ± 0.06
64.9	0.88 ± 0.06	0.95 ± 0.43	1.60 ± 0.82	0.64 ± 0.01
67.9	1.08 ± 0.40	2.65 ± 3.46	0.94 ± 0.06	0.83 ± 0.35
70.9	0.86 ± 0.01	0.72 ± 0.15	1.33 ± 0.65	1.63 ± 0.00
75.3	0.94 ± 0.12	0.87 ± 0.40	1.65 ± 0.91	0.65 ± 0.00
87.3	0.94 ± 0.01	0.61 ± 0.02	1.08 ± 0.12	0.64 ± 0.01
89.1	0.92 ± 0.00	0.64 ± 0.04	1.17 ± 0.11	0.66 ± 0.00
89.9	0.92 ± 0.01	0.65 ± 0.04	1.25 ± 0.04	0.66 ± 0.02

Table A.20: Mean-to-median ratios (MMR) of the expressed fluorescence intensities at 448/45 nm (general stress response), 527/32 nm (growth behaviour), 586/42 nm (oxygen limitation) and 660/10 nm (product formation) during the L-phenylalanine production process in a two-compartment bioreactor with the *Escherichia coli* quadruple reporter strain. The mean hydraulic residence time in the bypass was set to 102.63 s (4.71 mL s^{-1}). The biomass production phase started at 14.6 h, whereas the product formation phase was initiated at 37.8 h.

Process time, h	MMR 448/45 nm, -	MMR 527/32 nm, -	MMR 586/42 nm, -	MMR 660/10 nm, -
12.0	1.23 ± 0.00	1.19 ± 0.01	1.19 ± 0.01	1.55 ± 0.06
13.7	1.25 ± 0.02	1.19 ± 0.01	1.18 ± 0.00	1.47 ± 0.02
14.6	1.26 ± 0.00	1.19 ± 0.00	1.18 ± 0.01	1.48 ± 0.01
17.6	1.28 ± 0.00	1.21 ± 0.00	1.20 ± 0.00	1.43 ± 0.02
20.6	1.32 ± 0.01	1.22 ± 0.01	1.20 ± 0.00	1.49 ± 0.00
23.6	1.27 ± 0.00	1.24 ± 0.00	1.21 ± 0.00	1.52 ± 0.02
25.4	1.30 ± 0.00	1.25 ± 0.01	1.23 ± 0.00	1.42 ± 0.02
34.7	1.40 ± 0.01	1.28 ± 0.00	1.25 ± 0.00	1.48 ± 0.02
36.7	1.36 ± 0.01	1.31 ± 0.00	1.30 ± 0.00	1.63 ± 0.04
37.8	1.37 ± 0.00	1.29 ± 0.00	1.27 ± 0.00	1.53 ± 0.00
38.8	1.33 ± 0.01	1.28 ± 0.00	1.27 ± 0.00	1.55 ± 0.01
40.8	1.30 ± 0.00	1.28 ± 0.00	1.27 ± 0.00	1.51 ± 0.01
43.8	1.31 ± 0.00	1.26 ± 0.00	1.25 ± 0.00	1.39 ± 0.00
45.3	1.33 ± 0.00	1.25 ± 0.01	1.25 ± 0.00	1.36 ± 0.00
59.4	1.50 ± 0.02	1.28 ± 0.00	1.30 ± 0.00	1.31 ± 0.01
62.4	1.71 ± 0.02	1.39 ± 0.01	1.37 ± 0.00	1.40 ± 0.02
65.4	1.80 ± 0.01	1.45 ± 0.01	1.42 ± 0.00	1.42 ± 0.01
68.4	1.85 ± 0.01	1.44 ± 0.01	1.41 ± 0.01	1.42 ± 0.01
70.4	1.83 ± 0.01	1.45 ± 0.01	1.43 ± 0.02	1.41 ± 0.02
75.4	1.72 ± 0.02	1.35 ± 0.02	1.42 ± 0.01	1.33 ± 0.01
84.1	1.96 ± 0.01	1.45 ± 0.00	1.54 ± 0.02	1.36 ± 0.01
87.1	2.04 ± 0.01	1.45 ± 0.01	1.56 ± 0.02	1.34 ± 0.00
90.1	2.11 ± 0.02	1.43 ± 0.01	1.56 ± 0.02	1.33 ± 0.01
92.1	2.11 ± 0.01	1.41 ± 0.00	1.55 ± 0.01	1.31 ± 0.00
94.1	2.16 ± 0.01	1.40 ± 0.01	1.57 ± 0.01	1.31 ± 0.00

Table A.21: Coefficient of variances (CV) of the expressed fluorescence intensities at 448/45 nm (general stress response), 527/32 nm (growth behaviour), 586/42 nm (oxygen limitation) and 660/10 nm (product formation) during the L-phenylalanine production process in a two-compartment bioreactor with the *Escherichia coli* quadruple reporter strain. The mean hydraulic residence time in the bypass was set to 102.63 s (4.71 mL s^{-1}). The biomass production phase started at 14.6 h, whereas the product formation phase was initiated at 37.8 h.

Process time, h	CV 448/45 nm, -	CV 527/32 nm, -	CV 586/42 nm, -	CV 660/10 nm, -
12.0	1.24 ± 0.68	1.18 ± 0.88	0.84 ± 0.02	1.11 ± 0.04
13.7	0.86 ± 0.01	0.71 ± 0.01	0.81 ± 0.01	1.04 ± 0.02
14.6	0.86 ± 0.00	0.71 ± 0.01	0.83 ± 0.00	1.06 ± 0.01
17.6	0.85 ± 0.01	0.71 ± 0.01	0.81 ± 0.00	0.99 ± 0.02
20.6	1.27 ± 0.45	1.03 ± 0.37	1.12 ± 0.30	1.09 ± 0.13
23.6	0.91 ± 0.01	0.71 ± 0.01	0.79 ± 0.00	1.01 ± 0.01
25.4	0.92 ± 0.00	0.73 ± 0.01	0.80 ± 0.01	0.91 ± 0.02
34.7	1.15 ± 0.15	1.34 ± 0.79	0.83 ± 0.01	0.96 ± 0.02
36.7	1.01 ± 0.01	0.86 ± 0.02	0.92 ± 0.04	1.05 ± 0.02
37.8	1.03 ± 0.01	0.83 ± 0.03	0.85 ± 0.01	1.00 ± 0.01
38.8	1.09 ± 0.17	0.81 ± 0.04	0.89 ± 0.08	1.00 ± 0.01
40.8	0.98 ± 0.00	0.85 ± 0.02	0.97 ± 0.17	0.98 ± 0.00
43.8	0.98 ± 0.00	0.81 ± 0.01	0.83 ± 0.01	0.92 ± 0.00
45.3	1.00 ± 0.01	0.84 ± 0.05	0.84 ± 0.01	0.89 ± 0.01
59.4	1.07 ± 0.01	0.85 ± 0.02	0.98 ± 0.06	0.84 ± 0.01
62.4	1.20 ± 0.02	0.91 ± 0.02	1.05 ± 0.01	0.91 ± 0.01
65.4	1.26 ± 0.02	0.93 ± 0.01	1.12 ± 0.08	0.92 ± 0.01
68.4	1.31 ± 0.01	0.92 ± 0.02	1.14 ± 0.06	0.92 ± 0.01
70.4	1.32 ± 0.02	0.95 ± 0.02	1.19 ± 0.06	0.91 ± 0.02
75.4	1.20 ± 0.02	0.89 ± 0.12	1.18 ± 0.23	0.83 ± 0.01
84.1	1.35 ± 0.01	0.95 ± 0.02	1.33 ± 0.13	0.87 ± 0.01
87.1	1.42 ± 0.01	0.90 ± 0.01	1.28 ± 0.07	0.85 ± 0.01
90.1	1.44 ± 0.01	0.88 ± 0.02	1.23 ± 0.00	0.83 ± 0.01
92.1	1.40 ± 0.02	0.85 ± 0.02	1.17 ± 0.00	0.82 ± 0.01
94.1	1.44 ± 0.02	0.83 ± 0.01	1.21 ± 0.01	0.81 ± 0.00

Table A.22: Mean-to-median ratios (MMR) of the expressed fluorescence intensities at 448/45 nm (general stress response), 527/32 nm (growth behaviour), 586/42 nm (oxygen limitation) and 660/10 nm (product formation) during the L-phenylalanine production process in a two-compartment bioreactor with the *Escherichia coli* quadruple reporter strain. The mean hydraulic residence time in the bypass was set to 199.50 s (2.36 mL s^{-1}). The biomass production phase started at 17.6 h, whereas the product formation phase was initiated at 40.6 h.

Process time, h	MMR 448/45 nm, -	MMR 527/32 nm, -	MMR 586/42 nm, -	MMR 660/10 nm, -
13.8	1.34 ± 0.02	1.27 ± 0.01	1.33 ± 0.01	2.09 ± 0.02
17.6	1.34 ± 0.01	1.23 ± 0.00	1.27 ± 0.01	1.76 ± 0.03
20.6	1.28 ± 0.01	1.22 ± 0.00	1.22 ± 0.01	1.60 ± 0.01
23.6	1.27 ± 0.00	1.23 ± 0.00	1.20 ± 0.00	1.52 ± 0.00
26.6	1.27 ± 0.01	1.25 ± 0.00	1.22 ± 0.01	1.44 ± 0.01
37.8	1.30 ± 0.00	1.37 ± 0.00	1.31 ± 0.01	1.55 ± 0.01
39.8	1.29 ± 0.01	1.39 ± 0.01	1.34 ± 0.01	1.63 ± 0.01
40.6	1.28 ± 0.00	1.35 ± 0.01	1.34 ± 0.00	1.57 ± 0.02
41.6	1.25 ± 0.01	1.32 ± 0.00	1.31 ± 0.00	1.55 ± 0.01
43.6	1.28 ± 0.01	1.32 ± 0.00	1.30 ± 0.01	1.48 ± 0.00
46.6	1.40 ± 0.00	1.38 ± 0.00	1.33 ± 0.00	1.43 ± 0.01
48.1	1.40 ± 0.00	1.46 ± 0.01	1.41 ± 0.01	1.43 ± 0.02
61.3	1.58 ± 0.01	1.41 ± 0.01	1.35 ± 0.01	1.29 ± 0.01
64.3	1.59 ± 0.01	1.41 ± 0.01	1.34 ± 0.01	1.28 ± 0.01
67.3	1.57 ± 0.01	1.42 ± 0.01	1.37 ± 0.01	1.29 ± 0.03
70.3	1.61 ± 0.02	1.37 ± 0.00	1.34 ± 0.00	1.23 ± 0.00
72.3	1.61 ± 0.02	1.37 ± 0.01	1.34 ± 0.02	1.23 ± 0.01
86.0	1.60 ± 0.03	1.36 ± 0.01	1.37 ± 0.02	1.19 ± 0.01
89.0	1.59 ± 0.04	1.31 ± 0.01	1.33 ± 0.00	1.18 ± 0.02
92.0	1.60 ± 0.01	1.31 ± 0.00	1.33 ± 0.01	1.16 ± 0.00
94.0	1.65 ± 0.01	1.28 ± 0.01	1.33 ± 0.02	1.15 ± 0.01
96.0	1.70 ± 0.03	1.28 ± 0.02	1.34 ± 0.02	1.15 ± 0.01
110.0	1.73 ± 0.03	1.27 ± 0.00	1.30 ± 0.00	1.13 ± 0.00
111.0	1.74 ± 0.01	1.26 ± 0.00	1.29 ± 0.00	1.12 ± 0.00

Table A.23: Coefficient of variances (CV) of the expressed fluorescence intensities at 448/45 nm (general stress response), 527/32 nm (growth behaviour), 586/42 nm (oxygen limitation) and 660/10 nm (product formation) during the L-phenylalanine production process in a two-compartment bioreactor with the *Escherichia coli* quadruple reporter strain. The mean hydraulic residence time in the bypass was set to 199.50 s (2.36 mL s^{-1}). The biomass production phase started at 17.6 h, whereas the product formation phase was initiated at 40.6 h.

Process time, h	CV 448/45 nm, -	CV 527/32 nm, -	CV 586/42 nm, -	CV 660/10 nm, -
13.8	0.99 ± 0.02	0.86 ± 0.03	1.18 ± 0.04	1.57 ± 0.05
17.6	1.60 ± 1.21	1.02 ± 0.44	1.51 ± 0.71	1.49 ± 0.12
20.6	0.79 ± 0.01	0.70 ± 0.01	0.99 ± 0.01	1.23 ± 0.03
23.6	0.79 ± 0.01	0.69 ± 0.01	0.90 ± 0.01	1.10 ± 0.01
26.6	0.82 ± 0.01	0.71 ± 0.01	0.89 ± 0.01	1.02 ± 0.01
37.8	0.87 ± 0.01	0.88 ± 0.01	0.99 ± 0.06	1.04 ± 0.01
39.8	0.92 ± 0.04	0.94 ± 0.02	1.15 ± 0.28	1.17 ± 0.00
40.6	0.95 ± 0.03	0.93 ± 0.03	1.38 ± 0.10	1.15 ± 0.00
41.6	0.95 ± 0.06	0.93 ± 0.07	1.50 ± 0.32	1.12 ± 0.00
43.6	0.93 ± 0.01	0.89 ± 0.01	1.02 ± 0.13	1.10 ± 0.00
46.6	1.01 ± 0.04	0.95 ± 0.05	1.21 ± 0.43	1.04 ± 0.01
48.1	1.01 ± 0.02	1.05 ± 0.04	1.34 ± 0.05	1.06 ± 0.03
61.3	1.41 ± 0.25	1.31 ± 0.52	1.66 ± 0.37	0.91 ± 0.01
64.3	1.28 ± 0.02	0.97 ± 0.02	1.21 ± 0.12	0.91 ± 0.01
67.3	1.24 ± 0.02	1.04 ± 0.04	1.51 ± 0.19	0.92 ± 0.05
70.3	1.38 ± 0.14	0.94 ± 0.02	1.18 ± 0.09	0.86 ± 0.01
72.3	1.33 ± 0.03	0.96 ± 0.03	1.29 ± 0.22	0.84 ± 0.01
86.0	1.40 ± 0.20	1.28 ± 0.73	1.11 ± 0.08	0.75 ± 0.01
89.0	1.28 ± 0.02	0.90 ± 0.04	1.30 ± 0.06	0.77 ± 0.03
92.0	1.34 ± 0.03	0.86 ± 0.02	1.11 ± 0.11	0.72 ± 0.01
94.0	1.36 ± 0.01	0.83 ± 0.03	1.14 ± 0.12	0.72 ± 0.01
96.0	1.43 ± 0.07	0.80 ± 0.02	1.05 ± 0.05	0.71 ± 0.01
110.0	1.42 ± 0.02	0.75 ± 0.02	0.94 ± 0.08	0.69 ± 0.00
111.0	1.46 ± 0.01	0.75 ± 0.01	0.92 ± 0.02	0.68 ± 0.00

Table A.24: Mean-to-median ratios (MMR) of the expressed fluorescence intensities at 448/45 nm (general stress response), 527/32 nm (growth behaviour), 586/42 nm (oxygen limitation) and 660/10 nm (product formation) during the L-phenylalanine production process in a two-compartment bioreactor with the *Escherichia coli* quadruple reporter strain. The mean hydraulic residence time in the bypass was set to 403.30 s (1.18 mL s^{-1}). The biomass production phase started at 16.2 h, whereas the product formation phase was initiated at 39.1 h.

Process time, h	MMR 448/45 nm, -	MMR 527/32 nm, -	MMR 586/42 nm, -	MMR 660/10 nm, -
13.8	1.29 ± 0.00	1.23 ± 0.00	1.25 ± 0.00	1.82 ± 0.00
16.2	1.22 ± 0.00	1.20 ± 0.00	1.19 ± 0.01	1.57 ± 0.02
19.2	1.21 ± 0.00	1.20 ± 0.00	1.16 ± 0.00	1.45 ± 0.01
22.2	1.17 ± 0.00	1.20 ± 0.00	1.14 ± 0.00	1.38 ± 0.01
25.2	1.17 ± 0.00	1.20 ± 0.00	1.14 ± 0.01	1.31 ± 0.01
34.2	1.16 ± 0.00	1.22 ± 0.00	1.16 ± 0.00	1.30 ± 0.00
36.3	1.25 ± 0.00	1.28 ± 0.00	1.22 ± 0.00	1.43 ± 0.01
38.3	1.25 ± 0.00	1.30 ± 0.00	1.25 ± 0.00	1.51 ± 0.01
39.1	1.22 ± 0.00	1.27 ± 0.00	1.25 ± 0.00	1.50 ± 0.01
40.1	1.20 ± 0.00	1.26 ± 0.00	1.24 ± 0.00	1.48 ± 0.00
42.1	1.24 ± 0.00	1.27 ± 0.00	1.24 ± 0.00	1.39 ± 0.01
45.1	1.35 ± 0.00	1.33 ± 0.01	1.25 ± 0.01	1.36 ± 0.01
46.6	1.38 ± 0.00	1.34 ± 0.01	1.25 ± 0.00	1.35 ± 0.00
60.8	1.32 ± 0.01	1.33 ± 0.01	1.25 ± 0.00	1.26 ± 0.01
63.8	1.35 ± 0.01	1.31 ± 0.00	1.24 ± 0.00	1.26 ± 0.00
66.8	1.35 ± 0.00	1.32 ± 0.00	1.26 ± 0.01	1.27 ± 0.03
69.8	1.36 ± 0.00	1.29 ± 0.00	1.23 ± 0.00	1.23 ± 0.00
71.8	1.36 ± 0.01	1.29 ± 0.00	1.24 ± 0.01	1.23 ± 0.01
85.5	1.36 ± 0.01	1.28 ± 0.01	1.24 ± 0.01	1.16 ± 0.01
88.5	1.40 ± 0.01	1.26 ± 0.00	1.23 ± 0.01	1.16 ± 0.00
91.5	1.40 ± 0.01	1.27 ± 0.00	1.24 ± 0.01	1.15 ± 0.00
95.5	1.41 ± 0.01	1.27 ± 0.00	1.25 ± 0.00	1.14 ± 0.01
109.5	1.49 ± 0.01	1.24 ± 0.01	1.27 ± 0.01	1.06 ± 0.01
113.5	1.48 ± 0.01	1.23 ± 0.00	1.26 ± 0.00	1.05 ± 0.00
117.5	1.47 ± 0.01	1.24 ± 0.01	1.33 ± 0.01	1.04 ± 0.00
121.5	1.45 ± 0.02	1.24 ± 0.00	1.35 ± 0.01	1.04 ± 0.00
135.5	1.49 ± 0.02	1.24 ± 0.00	1.39 ± 0.01	1.07 ± 0.01
136.5	1.47 ± 0.04	1.25 ± 0.01	1.37 ± 0.01	1.11 ± 0.01

Table A.25: Coefficient of variances (CV) of the expressed fluorescence intensities at 448/45 nm (general stress response), 527/32 nm (growth behaviour), 586/42 nm (oxygen limitation) and 660/10 nm (product formation) during the L-phenylalanine production process in a two-compartment bioreactor with the *Escherichia coli* quadruple reporter strain. The mean hydraulic residence time in the bypass was set to 403.30 s (1.18 mL s^{-1}). The biomass production phase started at 16.2 h, whereas the product formation phase was initiated at 39.1 h.

Process time, h	CV 448/45 nm, -	CV 527/32 nm, -	CV 586/42 nm, -	CV 660/10 nm, -
13.8	1.50 ± 0.81	0.80 ± 0.07	1.69 ± 0.67	1.78 ± 0.01
16.2	0.88 ± 0.01	0.70 ± 0.01	1.08 ± 0.02	1.49 ± 0.05
19.2	0.75 ± 0.03	0.68 ± 0.02	0.98 ± 0.01	1.25 ± 0.03
22.2	0.67 ± 0.01	0.63 ± 0.01	0.87 ± 0.01	1.04 ± 0.01
25.2	0.65 ± 0.02	0.64 ± 0.03	0.84 ± 0.02	0.91 ± 0.01
34.2	0.65 ± 0.01	0.69 ± 0.00	0.75 ± 0.00	0.81 ± 0.01
36.3	0.73 ± 0.00	0.76 ± 0.00	0.85 ± 0.01	0.99 ± 0.01
38.3	0.75 ± 0.00	0.80 ± 0.00	0.91 ± 0.01	1.16 ± 0.01
39.1	0.78 ± 0.04	0.81 ± 0.01	1.17 ± 0.40	1.23 ± 0.01
40.1	0.76 ± 0.00	0.82 ± 0.01	0.93 ± 0.02	1.26 ± 0.01
42.1	0.82 ± 0.01	0.84 ± 0.00	0.96 ± 0.01	1.17 ± 0.01
45.1	0.86 ± 0.00	0.87 ± 0.02	0.93 ± 0.06	1.03 ± 0.01
46.6	0.89 ± 0.01	0.88 ± 0.02	0.92 ± 0.02	0.98 ± 0.01
60.8	0.98 ± 0.19	0.82 ± 0.02	0.86 ± 0.02	0.77 ± 0.01
63.8	0.93 ± 0.03	0.83 ± 0.01	1.03 ± 0.24	0.78 ± 0.01
66.8	0.92 ± 0.01	0.82 ± 0.01	0.83 ± 0.02	0.81 ± 0.04
69.8	0.97 ± 0.01	0.81 ± 0.02	0.86 ± 0.03	0.75 ± 0.00
71.8	0.99 ± 0.02	0.79 ± 0.01	0.84 ± 0.01	0.75 ± 0.01
85.5	1.07 ± 0.01	0.79 ± 0.01	0.88 ± 0.04	0.73 ± 0.01
88.5	1.12 ± 0.02	0.78 ± 0.01	0.82 ± 0.03	0.73 ± 0.01
91.5	1.20 ± 0.08	0.82 ± 0.09	0.90 ± 0.16	0.75 ± 0.01
95.5	1.48 ± 0.45	0.78 ± 0.01	0.94 ± 0.03	0.74 ± 0.01
109.5	1.44 ± 0.04	0.79 ± 0.01	0.89 ± 0.12	0.83 ± 0.01
113.5	1.61 ± 0.07	0.82 ± 0.01	0.85 ± 0.02	0.90 ± 0.00
117.5	1.67 ± 0.09	1.01 ± 0.14	1.13 ± 0.13	0.95 ± 0.01
121.5	1.79 ± 0.06	0.95 ± 0.01	0.96 ± 0.01	1.05 ± 0.00
135.5	1.81 ± 0.04	0.99 ± 0.01	0.00 ± 0.06	1.10 ± 0.01
136.5	1.79 ± 0.10	0.96 ± 0.01	0.97 ± 0.04	1.11 ± 0.00

B. List of abbreviations

Table B.1: List of abbreviations with their description.

Abbreviation	Description
3DHQ	3-dehydroquinate
3DHS	3-dehyroshikimate
5EPS3P	5-enolpyruvylshikimate 3-phosphate
6PG	6-phosphate gluconate
µF	Microfarad
µL	Microliter
Ω	Ohm
Å	Angström
AA	Amino acid
AAA	Aromatic amino acid
AcCoA	Acetyl-Coenzym A
ATP	Adenosine triphosphate
Bo	Bodenstein
C	Carbon
CDW	Cell dry weight
CER	Carbon dioxide evolution rate
CFI	Coiled flow inverter
CO_2	Carbon dioxide
CRISPR	Clustered regularly interspaced short palindromic repeats
CV	Coefficient of variance
DAHP	3-deoxy-D-arabino-heptulosonate 7-phosphate
DHA	Dihydroxyacetone
DHAP	Dihydroxyacetone phosphate
diH_2O	De-ionized water
Dn	Dean
DNA	Deoxyribonucleic acid
dNTP	Deoxynucleotide triphosphate
DO	Dissolved oxygen
dsDNA	Double-stranded DNA
E curve	Exit age distribution curve
E. coli	*Escherichia coli*
E. coli 3RP	*Escherichia coli* triple reporter strain
E. coli 4RP	*Escherichia coli* quadruple reporter strain
E4P	Erythrose 4-phosphate
EMP	Embden-Meyerhof-Parnas

Table B.1 – continued from previous page

Abbreviation	Description
exo	Exonuclease
F curve	Cumulative distribution curve
F6P	Fructose 6-phosphate
FACS	Fluorescence-activated cell sorting
$FADH_2$	Flavin adenine dinucleotide
fbr	feedback resistant
Flp	Flippase recombinase
FRT	Flippase recognition target
FSC	Forward scatter
g	Gram
G3P	Glyceraldehyde 3-phosphate
G6P	Glucose 6-phosphate
g_{CDW}	Grams of cell dry weight
GFP	Green fluorescent protein
Gly	Glycine
GLY3P	Glycerol 3-phosphate
GMP	Good manufacturing practice
h	Hour
H_2O	Water
H_2O_2	Hydrogen peroxide
HCl	Hydrochloric acid
HF	High fidelity
His	Histidine
HPLC	High performance liquid chromatography
HPP	4-hydroxyphenylpyruvate
IPTG	Isopropyl ß-D-1-thiogalactopyranoside
kb	Kilobase
kg	Kilogram
KOH	Potassium hydroxide
L	Liter
LB	Lysogeny broth
L-phe	L-phenylalanine
L-tyr	L-tyrosine
m	Meter
mA	Milliampere
MCS	Multiple cloning site
M	Molar
min	Minute
mL	Milliliter
mM	Millimolar
mm	Millimeter
MMR	Mean-to-median ratio
MOPS	3-(N-morpholino)propanesulfonic acid
mRNA	Messenger RNA
N	Nitrogen
NADH	Nicotinamide adenine dinucleotide
NADPH	Nicotinamide adenine dinucleotide phosphate

Table B.1 – continued from previous page

Abbreviation	Description
NaOH	Sodium hydroxide
ng	Nanogram
nm	Nanometer
O_2	Oxygen
OD_{600}	Optical density at 600 nm
OUR	Oxygen uptake rates
Pa	Pascal
PCR	Polymerase chain reaction
PBS	Phosphate-buffered saline
PEP	Phosphoenolpyruvate
PHPYR	Phenylpyruvate
PMT	Photomultiplier tubes
PPP	Pentose phosphate pathway
PRE	Prephenate
PYR	Pyruvate
R5P	Ribose 5-phosphate
RBS	Ribosome binding site
RNA	Ribonucleic acid
rpm	Revolutions per minute
rRNA	Ribosomal RNA
RTD	Residence time distribution
Ru5P	Ribulose 5-phosphate
s	Second
S7P	Sedoheptulose 7-phosphate
SDS	Sodium dodecyl sulfate
Ser	Serine
SHK	Shikimate
SHK3P	3-phosphoshikimate
SOC	Super optimal broth with catabolite repression
SSC	Side scatter
ssDNA	Single-stranded DNA
STB	Stirred-tank bioreactor
SuCCoA	Succinyl-Coenzym A
TAE	Tris-acetate-ethylenediaminetetraacetic acid
TCA	Tricarboxylic acid cycle
TCB	Two-compartment bioreactor
TCB_L	Two-compartment bioreactor with long mean hydraulic residence times of 403.30 s in the bypass
TCB_M	Two-compartment bioreactor with medium mean hydraulic residence times of 199.50 s in the bypass
TCB_S	Two-compartment bioreactor with short mean hydraulic residence times of 102.63 s in the bypass
Tfb I	Transformation buffer I
Tfb II	Transformation buffer II
Tyr	Tyrosine
U	Units

Table B.1 – continued from previous page

Abbreviation	Description
UTR	Untranslated region
UV	Ultraviolet
V	Volt
W	Watt
X5P	Xylulose 5-phosphate

C. List of symbols

Table C.1: List of symbols with their description and unit.

Symbol	Description	Unit
α_b	Bend angle	$^\circ$
ϵ_λ	Molar extinction coefficient at a wavelength λ	$m^2\ mol^{-1}$
η	Dynamic viscosity	$Pa\ s$
θ	Dimensionless time	$-$
λ_{Em}	Emission wavelength	nm
$\lambda_{Em,max}$	Maximum emission wavelength	nm
λ_{Ex}	Excitation wavelength	nm
$\lambda_{Ex,max}$	Maximum excitation wavelength	nm
μ	Specific growth rate	h^{-1}
μ_{max}	Maximum growth rate	h^{-1}
μ_{set}	Set growth rate	h^{-1}
ρ	Density of the fluid	$kg\ m^{-3}$
σ	Standard deviation of a distribution	-
σ^2	Variance	s^2
τ	Mean hydraulic residence time	s
A	Cross-sectional area of a tube	m^2
A_λ	Absorbance at a wavelength λ	$-$
Bo	Bodenstein number	$-$
c	Concentration	$mol\ L^{-1}$
$c(t)$	Tracer concentration	$mol\ L^{-1}$
CER	Carbon dioxide evolution rate	$mol\ L^{-1}\ h^{-1}$
c_i	Concentration of component i	$g\ L^{-1}$
$c_{i,0}$	Concentration of component i in feeding solution	$g\ L^{-1}$
c_{max}	Maximum tracer concentration	$mol\ L^{-1}$
c_S	Substrate concentration	$g\ L^{-1}$
$c_{S,0}$	Substrate concentration in feeding solution	$g\ L^{-1}$
CV	Coefficient of variance	-
c_X	Biomass concentration	$g\ L^{-1}$
$c_{X,0}$	Initial biomass concentration	$g\ L^{-1}$
d	Characteristic length	m
d_c	Coil diameter	m
d_{cuv}	Thickness of the cuvette	m
D_i	Dispersion coefficient	$m^2\ s^{-1}$
d_i	Inner tube diameter	m
Dn	Dean number	$-$

Continued on next page

Table C.1 – continued from previous page

Symbol	Description	Unit
d_o	Outer tube diameter	m
$E(t)$	Exit age distribution	s^{-1}
$F(\theta)$	Dimensionless concentration	$-$
H	Distance between the levels	mm
I	Transmitted intensity	$W\ m^{-2}$
I_0	Incident intensity	$W\ m^{-2}$
K_S	Saturation constant	$g\ L^{-1}$
L	Length of the tube	m
m_0	Mass of empty tube	g
m_1	Mass of filled tube	g
MMR	Mean-to-median ratio	-
m_S	Substrate consumption for maintenance	$g\ g_{CDW}^{-1}\ h^{-1}$
N	Number of turns in one coil	-
n_{bends}	Number of bends	-
OUR	Oxygen uptake rate	$mol\ L^{-1}\ h^{-1}$
p	Pitch distance	m
q_P	Biomass specific product formation rate	$g\ g_{CDW}^{-1}\ h^{-1}$
q_S	Substrate uptake rate	$g\ g_{CDW}^{-1}\ h^{-1}$
$q_{S,\mu}$	Substrate uptake rate for growth	$g\ g_{CDW}^{-1}\ h^{-1}$
$q_{S,m}$	Substrate uptake rate for maintenance	$g\ g_{CDW}^{-1}\ h^{-1}$
$q_{S,p}$	Substrate uptake rate for product formation	$g\ g_{CDW}^{-1}\ h^{-1}$
Re	Reynolds number	$-$
r_i	Reaction rate of component i	$g\ L^{-1}\ h^{-1}$
r_S	Reaction rate of substrate	$g\ L^{-1}\ h^{-1}$
t	Time	h
T	Torsion parameter	-
$T*$	Modified torsion parameter	-
t_0	Starting time	h
$t_{theoretical}$	Theoretical residence time	s
u	Superficial velocity	$m\ s^{-1}$
V	Working volume	L
$V_{0,STB}$	Initial working volume in stirred-tank bioreactor of two-compartment bioreactor	L
V_{CFI}	Working volume in coiled flow inverter of two-compartment bioreactor	L
V_L	Volume	L
V_M	Molar volume of ideal gas	$L\ mol^{-1}$
V_R	Bioreactor volume	L
$V_{R,0}$	Initial bioreactor volume	L
$\dot{V}$	Volumetric flow rate	$L\ s^{-1}$
$\dot{V}_{in}$	Volumetric flow of feed medium into the bioreactor	$L\ h^{-1}$
$\dot{V}_{g,in}$	Inlet gas flow rate	$L\ h^{-1}$
$\dot{V}_{out}$	Volumetric flow of culture medium out of the bioreactor	$L\ h^{-1}$
x_i	Value of sample i	-
$\overline{x}$	Mean of a distribution	-
$\widetilde{x}$	Median of a distribution	-

Table C.1 – continued from previous page

Symbol	Description	Unit
$Y_{CO_2,in}$	Molar fraction of carbon dioxide in inlet flow	-
$Y_{CO_2,out}$	Molar fraction of carbon dioxide in exhaust	-
$Y_{O_2,in}$	Molar fraction of oxygen in inlet flow	-
$Y_{O_2,out}$	Molar fraction of oxygen in exhaust	-
$Y_{P/S}$	Product yield	$g\ g^{-1}$
$Y_{X/S}$	Biomass yield	$g\ g^{-1}$
z	Axial distance	m

D. List of Figures

E. List of Tables